



UNIVERSITÀ DI SIENA 1240

Dipartimento di Scienze fisiche, della Terra e dell'ambiente

Dottorato in Scienze e tecnologie ambientali, geologiche e polari

33° Ciclo

Coordinatore: Prof. Simone Bastianoni

A NEW APPROACH TO ASSESS THE SUSCEPTIBILITY TO SHALLOW LANDSLIDES AT REGIONAL SCALE AS INFLUENCED BY BEDROCK GEO-MECHANICAL PROPERTIES

Settore scientifico disciplinare: GEO/05

Candidato

D'Addario Enrico

DSFTA, Università di Siena

Tutore

Prof. Aggr. Leonardo Disperati

DSFTA, Università di Siena

Co-tutore

Josè Luis Zezerè

IGOT, Universidad de Lisboa

Anno accademico di conseguimento del titolo di Dottore di ricerca

2019/2020

Università degli Studi di Siena
Dottorato in Scienze e tecnologie ambientali, geologiche e polari
33° Ciclo

Data dell'esame finale

22/04/2021

Commissione giudicatrice

Bateira	Carlos	Prof. Associato	Univ. do Porto	Departamento de Geografia	cbateira@letras.up.pt
Tejerina	Juan Remondo	Prof. Titular	Univ. de Cantabria	Departamento de Ciencias de la Tierra y Física de la Materia Condensada	juan.remondo@unican.es
Fantozzi	Pier Lorenzo	Prof. Associato	Univ. di Siena	Dipartimento di Scienze fisiche, della Terra e dell'ambiente	pierlorenzo.fantozzi@unisi.it

Supplenti

Meisina	Claudia	Prof. Ordinario	Univ. di Pavia	Dipartimento di Scienze della Terra e dell'ambiente	claudia.meisina@unipv.it
---------	---------	-----------------	----------------	---	--------------------------

Acknowledgements

Before proceeding with the presentation of the thesis, I would like to dedicate a few lines to all those who have been close to me on this path of personal and professional growth.

First of all, I would like to thank my tutor Prof. Leonardo Disperati, who has followed me and been available for every step of the process, starting from the initial planning of the PhD.

I would also like to thank my co-tutor Prof. José Luis Zezerè and all the RISKam staff at the University of Lisbon for setting me at ease during my research period abroad. His advice and suggestions were fundamental to the development of the thesis.

I would also like to thank my colleagues at the Geomatics Laboratory of the University of Siena, who were always available for mutual support and professional and personal exchange.

I would like to thank my whole family for their constant moral support and patience, especially during the last year.

To my friends, thanks to their light-heartedness and moments of fun that allowed me to "recharge" my battery.

Finally, a special thanks goes to my partner Valina, for the beautiful moments and the encouragements and, especially, for putting up with me during the months of pandemic, the period in which I wrote my final paper. Thank you for listening to me and being there when I was lost, especially considering the difficult time we were going through.

Abstract	9
1 Introduction	12
1.1 Structure of the thesis	13
1.2 State of the art	14
1.2.1 Shallow landslides and slope deposits	14
1.2.2 Landslide inventories	18
1.2.3 Shallow landslides susceptibility modelling	21
1.3 Aim of the thesis	25
2 Methods - A new way to approach shallow landslides and susceptibility assessment by means well-established tools	28
2.1 Workflow of the method	29
2.2 Data collection strategy	32
2.3 Visual interpretation of orthophoto maps	33
2.4 Engineering geological characterization of Slope Deposits	36
2.4.1 Field survey data acquisition	36
2.4.1.1 Depth of slope deposits	36
2.4.1.2 Fabric and grain size estimation	37
2.4.2 Sampling and laboratory analysis	41
2.4.2.1 Grain size estimation and plasticity analysis	41
2.4.2.2 Unit weight	43
2.4.3 Classification of morphometric variables	44
2.4.4 Slope Deposits Engineering Geological Map	46
2.4.4.1 Slope deposits depth	47
2.4.4.2 Shear strength parameters assessment	47
2.4.4.3 Slope Deposits Engineering Geological Units	52
2.5 Bedrock geomechanical characterization	54
2.5.1 Rock mass geo-mechanical survey	54
2.5.1.1 Schmidt hammer rebound value test	54

2.5.1.2	Normalization of SH rebound values	57
2.5.1.3	Discontinuity analysis	59
2.5.1.4	Geological Strength Index	59
2.5.2	Unit weight determination	62
2.5.3	Cluster and Outlier Analysis (Anselin Local Moran's Index)	63
2.5.4	Multi-variate cluster analysis	64
2.5.5	Determination of Uniaxial Compressive Strength	66
2.5.6	Estimation of shear strength of a rock mass	70
2.5.7	Bedrock Geo-mechanical Units Map	76
2.6	Shallow landslides susceptibility models	77
2.6.1	SHALSTAB and PROBSS	77
2.6.2	Information Value	80
2.7	Accuracy assessment methods	81
3	Study area	83
3.1	Data available from the literature	84
3.2	Geographic outline	85
3.3	Geological outline	89
4	Results - Processing and spatialization of data	94
4.1	Landslide inventory	95
4.1.1	Landslide inventory accuracy assessment	95
4.1.2	General statistics of the landslide inventory	96
4.1.3	Characterization of visited landslides	98
4.2	Engineering Geological characterization of Slope Deposits	104
4.2.1	Extraction of Morphometric units	106
4.2.2	Depth classes	109
4.2.2.1	Slope deposits depth maps	112
4.2.3	Grain size analysis	126
4.2.3.1	Laboratory results	126

4.2.3.2	Grain size field estimation results	128
4.2.4	Unit weight results	131
4.2.5	Engineering Geological Map of Slope Deposits	131
4.2.5.1	Friction angle of gravelly SD	131
4.2.5.2	Friction angle assessment using NAVFAC diagram	133
4.2.5.3	Engineering Geological Units parameters	134
4.3	Bedrock Geo-mechanical characterization	138
4.3.1	Descriptive statistics of bedrock geo-mechanical properties	140
4.3.2	Uni-variate spatial cluster analysis of bedrock properties	143
4.3.3	Multi-variate cluster analysis	150
4.3.4	Bedrock Geo-mechanical Units	155
5	Results - Shallow landslide susceptibility modeling	161
5.1	Shallow landslide susceptibility analysis: a comparison between PROBSS and Information Value	162
5.1.1	Shallow landslide inventory	162
5.1.2	PROBSS input data	163
5.1.3	Information value input data	163
5.1.4	Susceptibility maps and accuracy assessment	166
5.1.5	Discussion	171
5.2	Exploring differences between shallow landslides involving slope deposits and/or bedrock by means of Information Value method	174
5.2.1	Information value input data and weighs determination	175
5.2.2	Susceptibility maps and accuracy assessment	176
5.2.3	Discussion	180
5.3	Physically based modelling of shallow landslides involving bedrock	183
5.3.1	PROBSS input data	185
5.3.2	Susceptibility maps and accuracy assessment	187
5.3.3	Discussion	190

6	General discussion	198
6.1	Shallow landslide inventory	199
6.2	Slope deposits features at regional scale	205
6.3	Assessment of bedrock Geo-mechanical properties and regionalization	213
6.4	Shallow landslides susceptibility modelling	218
7	Conclusions	223
	Appendix A	227
	Appendix B	229
	Appendix C	251
	References	258

Abstract

Due to high velocity, high frequency and the lack of warning signs, shallow landslides represent a major hazardous factor in mountain regions. Moreover, increasing urbanisation and climate changes triggering intense rainfall events make shallow landslides a source of widespread risk. The interest of the scientific community in this process has grown in the last three decades with the aim to perform robust shallow landslide hazard assessment at regional scale.

Generally, these slope failures involve relatively small volumes of material sliding along with a planar shallow rupture surface. In the literature it is widely accepted that shallow landslides involve only slope deposit (or colluvium) and the sliding surface correspond to the discontinuity between bedrock and the overlying loose material. The fieldwork conducted in this thesis highlighted that often shallow landslides involve also the weathered and fractured portion of bedrock. In this framework, the implementation of shallow landslides susceptibility modelling should take into account the engineering geological properties of slope deposits, as well as of the underlying bedrock. In this thesis a fieldwork-based method is proposed to acquire, process and spatialize engineering geological properties of slope deposits and bedrock. The aims of this thesis were to compile a new multi-temporal shallow landslide inventory, characterize the engineering geological properties of slope deposits and bedrock, implement and compare shallow landslide susceptibility modelling by means a physically-based and a data-driven methods and explore the role of bedrock in shallow slope failures. The study area corresponds to a 242 km² portion of the Garfagnana basin (Northern Apennines), a mountainous region where the elevation ranges between 150 and 2000 m a.s.l. characterized by an incised and rugged morphology with steep slopes (average 28° degrees) and a mean annual rainfall between 1500 and 2500 mm/year. From a geological point of view, the Garfagnana basin is a narrow intra-mountainous valley, interposed between the Alpi Apuane metamorphic complex to the east and the sedimentary northern Apennine's ridge to the west.

The fieldwork and laboratory tasks carried out to map engineering geology characters of slope deposits consisted on a set of hundreds of field sampling points, with the acquisition of depth to the bedrock, geotechnical horizons, unit weight, as well as soil samples for lab analysis. The distribution of points was chosen by observing that engineering geology properties of slope deposits depend on both bedrock lithology and morphometric conditions. In order to obtain the map distribution of engineering geology parameters, we implemented a spatial analysis by clustering morphometric variables stratified as a function of bedrock lithological units. In order to investigate the engineering geology characteristics of the bedrock, a field survey aimed to classify rock masses was conducted. For each survey site, 200-400 Schmidt hammer rebound measures, bedding and joint data, GSI (Geological Strength Index) and samples for laboratory analyses (unit weight and slake durability test) were collected. The field data were processed and spatially analyzed by means uni-variate and multi-variate cluster analysis in order to

delineate domains with different bedrock geo-mechanical properties. The shallow landslide susceptibility analysis was performed using both data-driven, Information Value, and physically-based, a modified version of SHALSTAB model (PROBSS), methods.

The numerical modelling faced three issues: a) the comparison of PROBSS and Information value (IV) in the prediction of shallow landslides involving SD; b) the training and cross-validation of IV models using shallow landslides involving bedrock or not; c) implementation of a physically-based model to predict involving bedrock shallow landslides. First of all, the results highlight that the field-based methods proposed here to evaluate engineering geological properties of slope deposits and bedrock are adequate for the implementation of regionalised physically-based susceptibility models.

The comparison between PROBSS and IV highlights that the simplification of shallow landslides adopted by the infinite slope model which do not take into account the occurrence of a sliding surface located below the slope deposits / bedrock discontinuity, may affect the performance of physically-based susceptibility models. The accuracy of IV model is slightly better than PROBSS model. Having implemented two data-driven susceptibility models using two different training datasets highlighted the different characteristics that slope deposits and bedrock involving shallow landslides have, suggesting and demonstrating that the latter occur in conditions that the physically based model cannot predict. By placing the slip surface below the discontinuity between slope deposits and bedrock and providing shear strength parameters compatible with a weathered and fractured rock material, satisfactory accuracy result was obtained with PROBSS model.

ACRONYMS AND SYMBOLS

%FS	Percentage of SH low full-scale values
ϕ	Friction angle
BLU	Bedrock Geological Units
BMU	Bedrock Geo-mechanical Units
BR	Bedrock
BRL	Landslides involving bedrock
c'	Effective cohesion
DEM	Digital Elevation Model
EGU	Engineering Geological Units
GSI	Geological Strength Index
IV	Information value model
J_v	Joint Volume Count
LI	Landslide inventory
NVS	Not Visited landslides
OLd / Ld	Overall / landslide density
PDF	Probability density function
R	Schmidt Hammer rebound value
Rh / Rv	Normalized Schmidt Hammer rebound value
SD	Slope deposits
SDd	Slope deposits depth
SDL	Landslides involving slope deposits
SH	Schmidt Hammer
PROBSS	Modified Shalstab model
UCS	Uniaxial Compressive Strength
VS	Visited landslides

1 INTRODUCTION

1.1 STRUCTURE OF THE THESIS

Geology, geomorphology, geological engineering and statistical analysis applied to shallow landslide susceptibility assessment are the main topics of this thesis.

The thesis has a similar structure of a method-centric type scientific article, the core of this work lies in the detailed description of data acquisition and processing methods for the implementation of shallow landslide susceptibility models. The methodology is then applied to a study area whose results are presented and discussed.

After a brief introduction describing the data available at the beginning of the PhD thesis, the state of the art of knowledge, different approaches to assess landslide susceptibility and the objectives of this work, an exhaustive chapter describing the phases of data acquisition in the field, their processing and statistical analysis is presented. The study area in which the methodology was applied is identified and a description of the geographical and geological characteristics is provided.

In the next chapter, the results of the data acquired are presented and implemented in shallow landslide susceptibility models. Three different ways of approaching slope stability are described, analysed and discussed.

Finally, a chapter dedicated to general discussions which integrates considerations, critical points and strengths of the methodology, results and modelling is presented.

The thesis ends with a chapter of conclusions, appendices and bibliography.

1.2 STATE OF THE ART

1.2.1 *Shallow landslides and slope deposits*

A landslide is defined as the movement of a mass of rock, debris, or earth down a slope, under the influence of gravity (Cruden, 1991). The classification of landslide was a challenging issue since geologists and geotechnical engineers started to handle the problem. In the literature several landslide classification systems exist, introduced by different experts as geologists, geomorphologists and engineers, but a universal and comprehensive description of the phenomenon was firstly introduced by Sharpe (1938) recognizing type of movement, material and movement velocity. This classification was then expanded by Varnes (1958, 1978), then completed with velocity rates (Cruden and Varnes, 1996), making it the most used classification at global scale (Figure 1-1). In a recent update (Hungr et al., 2014), the authors aim was to introduce modifications reflecting recent advances in understanding landslide phenomena and the materials and mechanisms involved. The starting point of the modifications is the 1978 version of the classification (Varnes 1978), taking also into account concepts introduced by Cruden and Varnes (1996). The most important features that the work of Hungr et alii (2014) have introduced is a more detailed characterization of materials. The authors adopt a geotechnical material terminology, as it relates best to the mechanical behaviour of the landslide, replacing the Varnes's terms "debris" and "earth" with other terms which describe the texture and composition (Figure 1-2). The resulting landslide classification is represented in Figure 1-3 and was adopted in this thesis. As will be shown in the following paragraphs of this thesis, this update resulted to be very suitable for the purpose of this work because some of the information needed to accurately classified landslide was necessarily collected to implement the landslide susceptibility models.

Even if in the paper of Hungr et alii (2014) a detailed description of a wide number of slope failures types is provided, a widely accepted definition of shallow landslide is lacking. Nevertheless, the landslide type which most closely resembles what is usually identified as a shallow landslide is the "gravel/sand/debris slide", defined as "*Sliding of a mass of granular material on a shallow, planar surface parallel with the ground. Usually, the sliding mass is a veneer of colluvium, weathered soil, or pyroclastic deposits sliding over a stronger substrate*" (Hungr et al., 2014). Milledge et alii (2014) provide a quantitative analysis based on 6 landslide inventory, affirming that shallow landslides: have a scar areas between 30 and 300 m², are generally longer than they are wide, wider than they are deep with a slip surface that rarely extend beyond a few meters deep, and the majority are between 0.1 and 1 m deep. In the definition of shallow landslide of Hungr et al. (2014), the sliding mass is called "colluvium" or "weathered soil". In this thesis we call slope deposits (SD) what in the literature other authors call for example "colluvium", "soil" or "regolith" (Goudie, 2004; Leopold and Völkel, 2007; Scott and Pain, 2008; Miller and Juilleret, 2020). The definition adopted in this thesis correspond to the definition proposed by Trefolini (2015), defining slope deposits as "a deposit obtained

from the actual or recent alteration and/or disruption of substratum and eventually the transport and sedimentation along the hillslope by unchannelized flux or gravity-dominated processes, independently of texture, structure, cementation and consistence”. Slope deposits are bounded below by an unconformity which defines the border between them and the underlying bedrock. In this thesis, the term “bedrock” is attributed to a material which may consist of a hard or weak rock, or even to a more or less cemented sedimentary deposit, which maintain their structure and hardness, and formed in a geological and morphoclimatic environment different from the current one (Figure 1-4).

Shallow landslides characteristics listed above make these slope processes suitable for modeling by means the infinite slope method (Taylor, 1948), in which the slip surface corresponds to the bedrock-slope deposits interface, working as a mechanical and hydraulic discontinuity. The role and, eventually, the involvement of weathered and fractured bedrock in shallow landsliding has been poorly investigated while, when dealing with deep-seated landslides or rockfalls, bedrock properties are deeply taken into consideration. For this kind of slope failure, the degree of weathering, fracturing and bedding play a fundamental role and are crucial information in order to obtain site specific susceptibility models (Grelle et al., 2011; Jaboyedoff et al., 2011; Brideau and Roberts, 2014; Marchesini et al., 2015; Stead and Wolter, 2015; Huang et al., 2016). Instead, in regional data-driven landslide susceptibility modeling some bedrock-related predisposing factors, such as distance from faults and layers bedding, are often taken into account (Donati and Turrini, 2002; Guzzetti et al., 2008; Blahut et al., 2010; Goswami et al., 2011; Migoń et al., 2017). Nevertheless, in the literature the “typical” shallow landslide does not involve bedrock, for this reason there is no interest on the investigation of bedrock properties during shallow landslide susceptibility analysis. In light of what has been seen in the fieldwork carried out in this thesis, the author does not exclude *a priori* involvement of bedrock and the role that the weathering and fracturing degree has in the distribution of shallow landslides. In this work, involving bedrock shallow landslides (BRL) are defined as landslides in which the sliding surface is located under the slope deposits/bedrock discontinuity (Figure 1-5). Unlike the SD / bedrock interface, this surface is not tangible and defined by an abrupt discontinuity, however it usually corresponds to a transition zone between bedrock with different degrees of weathering and fracturing.

Movement type	Rock	Debris	Earth
Fall	1. Rock fall	2. Debris fall	3. Earth fall
Topple	4. Rock topple	5. Debris topple	6. Earth topple
Rotational sliding	7. Rock slump	8. Debris slump	9. Earth slump
Translational sliding	10. Block slide	11. Debris slide	12. Earth slide
Lateral spreading	13. Rock spread	—	14. Earth spread
Flow	15. Rock creep	16. Talus flow	21. Dry sand flow
		17. Debris flow	22. Wet sand flow
		18. Debris avalanche	23. Quick clay flow
		19. Solifluction	24. Earth flow
		20. Soil creep	25. Rapid earth flow
			26. Loess flow
Complex	27. Rock slide-debris avalanche	28. Cambering, valley bulging	29. Earth slump-earth flow

Figure 1-1 A summary of Varnes' 1978 classification system (from Hungr et alii, 2014)

Material name	Character descriptors (if important)	Simplified field description for the purposes of classification	Corresponding unified soil classes	Laboratory indices (if available)
Rock	Strong	Strong—broken with a hammer		UCS>25 MPa
	Weak	Weak—peeled with a knife		2<UCS<25 MPa
Clay	Stiff	Plastic, can be molded into standard thread when moist; has dry strength	GC, SC, CL, MH, CH, OL, and OH	$I_p > 0.05$
	Soft			
	Sensitive			
Mud	Liquid	Plastic, unsorted remolded, and close to Liquid Limit	CL, CH, and CM	$I_p > 0.05$ and $I_L > 0.5$
Silt, sand, gravel, and boulders	Dry	Nonplastic (or very low plasticity), granular, sorted. Silt particles cannot be seen by eye	ML, SW, SP, and SM, GW, GP, and GM	$I_p < 0.05$
	Saturated			
	Partly saturated			
Debris	Dry	Low plasticity, unsorted and mixed	SW-GW, SM-GM, CL, CH, and CM	$I_p < 0.05$
	Saturated			
	Partly saturated			
Peat		Organic		
Ice		Glacier		

Figure 1-2 Landslide-forming material types (from Hungr et al., 2014)

Type of movement	Rock	Soil
Fall	1. Rock/ice fall ^a	2. Boulder/debris/silt fall ^a
Topple	3. Rock block topple ^a	5. Gravel/sand/silt topple ^a
	4. Rock flexural topple	
Slide	6. Rock rotational slide	11. Clay/silt rotational slide
	7. Rock planar slide ^a	12. Clay/silt planar slide
	8. Rock wedge slide ^a	13. Gravel/sand/debris slide ^a
	9. Rock compound slide	14. Clay/silt compound slide
	10. Rock irregular slide ^a	
Spread	15. Rock slope spread	16. Sand/silt liquefaction spread ^a
		17. Sensitive clay spread ^a
Flow	18. Rock/ice avalanche ^a	19. Sand/silt/debris dry flow
		20. Sand/silt/debris flowslide ^a
		21. Sensitive clay flowslide ^a
		22. Debris flow ^a
		23. Mud flow ^a
		24. Debris flood
		25. Debris avalanche ^a
		26. Earthflow
		27. Peat flow
		Slope deformation
29. Rock slope deformation	31. Soil creep	
	32. Solifluction	

Figure 1-3 Summary of the Hungr (2014) version of the Varnes classification system (from Hungr et alii, 2014)

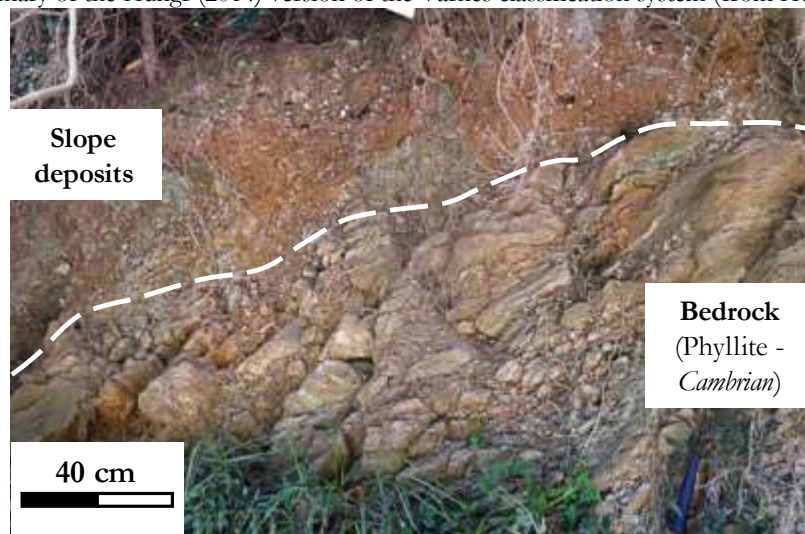


Figure 1-4 A natural trench exposing slope deposits above the bedrock, divided by the unconformity (white dashed line).

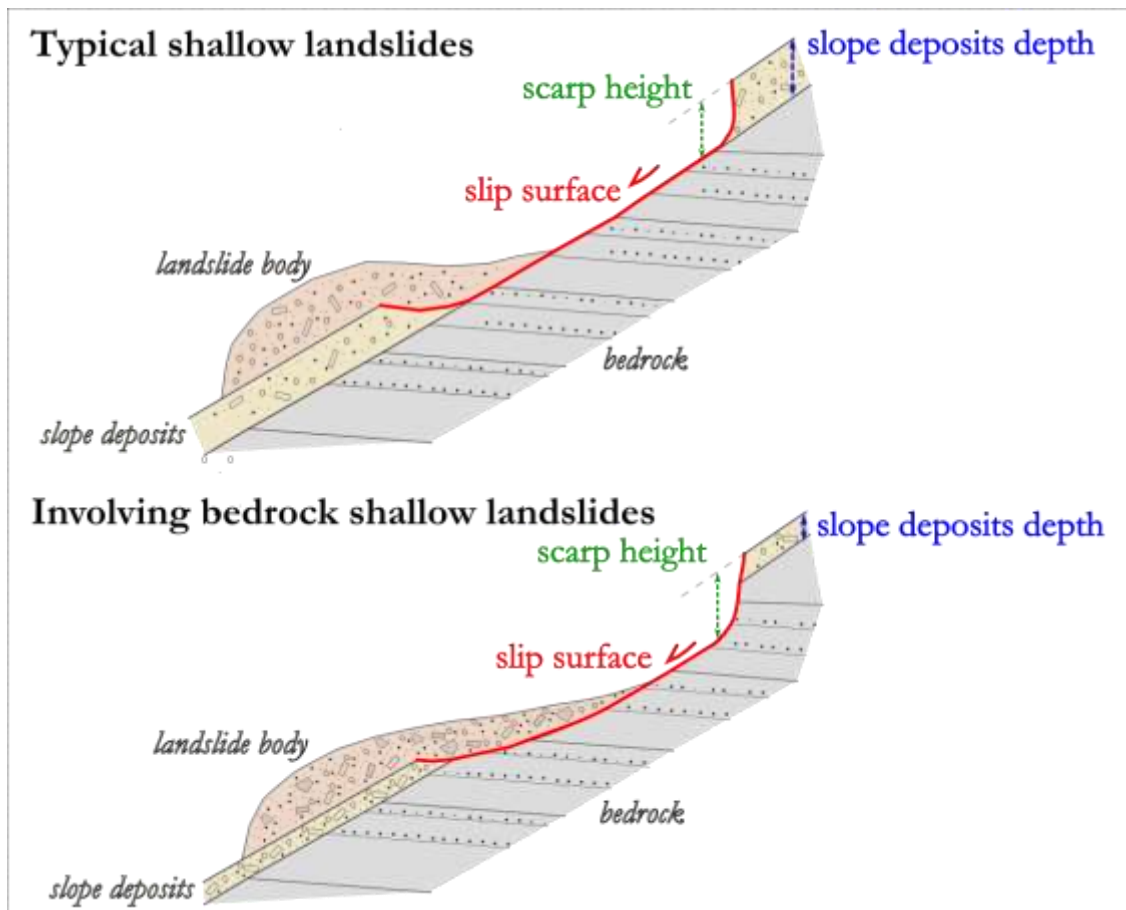


Figure 1-5 Simplified scheme of a typical shallow landslide and an involving bedrock shallow landslide

1.2.2 Landslide inventories

A landslide susceptibility analysis, regardless of which method is used to define it, cannot disregard a landslide inventory. A landslide inventory (LI) is a record of landslides, combined with their attributes, recognized in a particular area. These attributes should ideally provide information on the type of landslide, date of occurrence or relative age, size, current state of activity, and causes. The method to be used to prepare a landslide inventory should depend on purpose of the inventory, the extent of the study area, the scale of the base maps and resolution of remote sensing images (Guzzetti et al., 2012). LIs have usually been produced by using geomorphological field mapping and visual interpretation of aerial photographs. Today, innovative techniques are rising including analysis of (very-high resolution) digital elevation models (DEMs), interpretation and (semi-automated) analysis of satellite images (Drăguț and Blaschke, 2006; Booth et al., 2009; Joyce et al., 2009; Guzzetti et al., 2012; Jaboyedoff et al., 2012; Martha et al., 2012; Casagli et al., 2016; Z. Li et al., 2016; Disperati et al., 2016; Plank and Martinis, 2016; DeWitt et al., 2017). Depending on the purpose, the landslide inventory can be classified as historical, event, seasonal or multi-temporal inventories. An historical inventory shows the cumulative effects of many landslide events over a period of tens, hundreds or thousands of years. Instead, an event-based LI is prepared following a well-defined trigger event (e. g., heavy rainfall, earthquake, snowmelt). Multi-

temporal and seasonal inventories are prepared investigating multiple sets of aerial or satellite images of different dates. A seasonal inventory shows landslides triggered by single or multiple events during a single season, or a few seasons, whereas multi-temporal inventories show landslides triggered by multiple events over longer periods (Guzzetti et al., 2012).

Due to different methods, different scale of analysis and different purposes, for these reasons defining the accuracy of a landslide inventory is not straightforward, and standards do not exist (Galli et al., 2008). Several difficulties arise in building a good landslide database and many types of imprecision can affect the database (Trigila et al., 2010; Guzzetti et al., 2012). For instance, common errors can be related to the boundary and position of landslides (cartographic errors) or in discerning the source from the runout area (interpretation errors). Furthermore, the use of different source of information (e.g. newspapers, remote sensing and field surveys) can generate landslide records with different reliability (Trigila et al., 2010).

An important feature to consider in order to characterize a landslide inventory is the landslide size distribution (Malamud et al., 2004). In the literature it is widely accepted that whilst large landslides are perceived to be the most hazardous, small landslides occur most frequently. For this reason, assess landslide size distribution for a specific landslide event or to assess the completeness of a landslide inventory is an important tool to evaluate landslide hazard and risk zoning (Malamud et al., 2004; Fell et al., 2008; Corominas et al., 2014).

Several studies have proposed that the non-cumulative size-frequency distribution of landslides follows a negative power-law relationship for medium to large landslides (Hovius et al., 1997; Pelletier, 1997; C. P. Stark and Hovius, 2001; Ardizzone et al., 2002; Malamud et al., 2004). The non-cumulative frequency-density of a landslide inventory is given by the number of landslides dN over the range of areas dA . Probability density function (pdf) can be estimated normalizing the frequency-density to the total number of landslides in the inventory:

Equation 1-1

$$pdf = \frac{1}{N_{CL}} \frac{\delta N_{CL}}{\delta A_L}$$

where N_{CL} is the non-cumulative number of landslides and A_L the landslide area. To construct the pdf, firstly divide the interval covered by the data values into sub-intervals (bins). The division may be linear or logarithmic. Then count the number of landslides within each interval and normalized the number of landslides to the width of the bin and to the total of landslides.

Once the pdf has been estimated, it is possible to fit a function for data distribution using the Double Pareto distribution (Stark and Hovius, 2001) or Inverse Gamma (Malamud et al., 2004).

Power-law relationship exponent estimation usually varies from $\alpha = 1.4$ to $\alpha = 3.3$ (Van Den Eeckhaut et al., 2007). This scaling exponent may vary with underlying geology (Guzzetti et al., 2008; Frattini and Crosta, 2013a; Hurst, Ellis, et al., 2013) or with the failure type (Brunetti et al., 2009; Hurst, Ellis, et al., 2013). As previously noted, landslide size-distribution exhibit a negative power-law relationship for medium to large events, meanwhile pdf shows a rollover to a positive power-law relationship for smaller landslides. In the literature, there's no agreement about the definition of the rollover. Some authors defined the rollover as the modal value of pdf distribution (C. P. Stark and Hovius, 2001; Stark and Guzzetti, 2009a; L. Li et al., 2016) while other authors consider the rollover approximately as the point of departure of the data from the power-law (Guthrie and Evans, 2004; Guthrie et al., 2008). Regarding physical meaning of rollover, three hypotheses have been proposed. The first is ascribed to the interplay of cohesion and friction, stating that these parameters resist landsliding for small and large landslides respectively (Pelletier, 1997; Guzzetti et al., 2002; Malamud et al., 2004; Stark and Guzzetti, 2009). Alternatively it concerns the completeness of the inventory, because erosion, reworking of deposits and fast vegetation regrowth may be responsible for the concealing of small and shallow landslides, resulting in a under sampling of the landslide inventory (Brardinoni and Church, 2004). Another issue regards the resolution and the scale of the remotely sensed data used to acquire landslides that may lead to the small and shallow slope failures under sampling (Galli et al., 2008; Guzzetti et al., 2012). For the reason listed above, the most likely to be incomplete are historical inventories, on the contrary, event-based are the most complete.

The Italian Landslide Inventory (IFFI) Project was launched in 1999 with the aim of identifying and mapping landslides throughout Italy on the basis of standardized criteria. This huge database is an historical landslide inventory containing 620.808 slope failures covering an area of 23.700 km² (7,9 % of Italian territory). In Trigila et alii (2010), the authors carried out an analysis of the IFFI database, despite excellent results of accuracy, the frequency-magnitude distribution highlighted a rollover around 10000 m², suggesting an underestimation of shallow and small landslide (Figure 1-6). However, high frequency, high velocity rate and lack of predictive indicators, make shallow landslides source of hazard and risk. In this thesis, by means visual interpretation of orthophoto maps, a new multi-temporal inventory of shallow landslide triggered by intense rainfall was prepared for the study area.

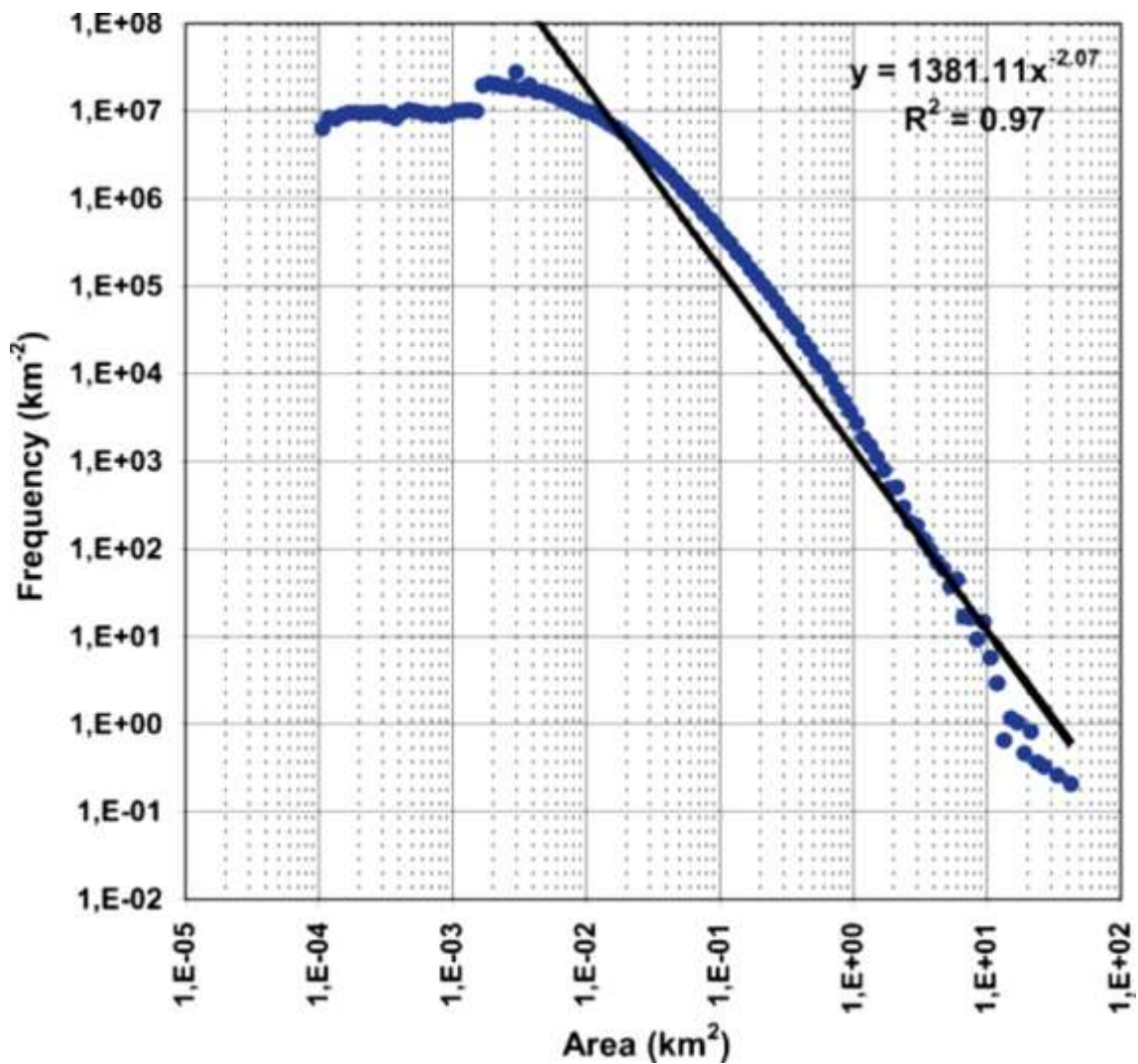


Figure 1-6 Magnitude-frequency distribution of the IFFI (from Trigila et al., 2010)

1.2.3 Shallow landslides susceptibility modelling

Landslide susceptibility is defined as a quantitative or qualitative assessment of the classification, volume (or area), and spatial distribution of landslides which exist or potentially may occur in an area (Fell et al., 2008). Landslide susceptibility modelling is a key tool to assess hazard and risk zoning of a slope failures prone area. It is the first step to accomplish and it is the starting point for a correct risk management and design of mitigation works for the protection of public health and property.

Landslide susceptibility modelling can be developed at the site-specific or regional level. Site-specific analyses are related to a specific landslide or a specific limited area, usually deep-seated landslides that threaten man-made environments such as the stability analysis of a reservoir bank slope, slope stability assessment related to specific facility, buildings or infrastructures such as railways, roads or pipelines. By contrast, regional assessment is not generally motivated by the needs of man-made structures but is mainly oriented to the evaluation of probability of occurrence of slope failures in a wide area. The outcomes of regional assessment are fundamental tools in regional planning and can be followed by site-

specific studies. A regional-scale study is mainly based on the evaluation of predisposing factors causing slope instability such as geology, structural setting, land use and morphometric variables derived from the DEM (e.g. slope steepness, curvatures, upslope contributing area, slope aspect and so on).

Regional landslide susceptibility assessment can be performed by means both a qualitative approach, with knowledge driven methods, or with a quantitative approach, with data-driven (statistical) and physically-based (deterministic) methods. Knowledge-driven or heuristic methods rely on the subjective judgment of experts, landslide susceptibility map can be prepared by means geomorphological survey by expert geomorphologists or created in the office as a derivative map of a geological/geomorphological map. In knowledge-driven or heuristic methods, the method is direct, as the expert interprets the susceptibility of the terrain directly in the field, based on the observed phenomena and the geomorphological/geological setting. The data acquired in the field may be digitalized using a GIS software, without extensive modelling. Knowledge-driven methods can also be applied indirectly using a GIS, by combining several factor maps that are considered to be important for landslide occurrence. On the basis of his/her expert knowledge on past landslide occurrences and their causal factors within a given area, an expert assigns particular weights to certain combinations of factors (Corominas et al., 2014).

The concept behind data-drive methods is that the condition at which landslides occurred in the past, will be similar to the condition at which landslides will occur in the future (Reichenbach et al., 2018). Therefore, these methods consist on the combinations of predisposing factors that have conditioned landslides in the past are evaluated statistically, obtaining a quantitative prediction for current non-landslide-affected areas with similar geological, topographical and land-cover conditions. Moreover, with statistical methods is possible to use a large variety of input parameters (without limitation) and, at the same time, do not require *a priori* knowledge of relationships between predisposing factors and slope stability.

In the literature exists a lot of data-driven methods that can be grouped in: classical statistical (logistic regression, discriminant analysis etc.), index-based (weigh of evidence, information value), machine learning (fuzzy logic, support vector machines, forest trees), multi criteria decision analysis and neural networks. Reichenbach el alii (2018) provide an extensive review on data-driven susceptibility methods and on their evolution in the last decades. In this paper, the authors showed that although the advent of new complex statistical techniques applied to landslide susceptibility is spreading, as well as the increased availability of a wide range of classification tools in open source, classical statistics and index-based methods are used in around 70% of the works published from 2010 to 2018 (Reichenbach et al., 2018). An interesting reflection the authors do in their paper is that “the use of more complex classification methods – a trend observed in the literature in the recent years – does not guarantee better susceptibility models and sound terrain zonations necessarily. Rather, the opposite is true; the use of complex modelling techniques requires a full understanding of the model constrains, not all of which may be

obvious to a non-expert user.” This reflection should encourage in experimenting new techniques comparing them with methods well established. The only two main drawbacks data-drive methods have, are the requirement of a good landslide inventory and their inability to model a scenario that has not happened yet. In Figure 1-7, a table extracted from the work of Corominas et alii (2014), which shows the recommended data-driven methods.

	Method	References
Bivariate statistical methods	Likelihood ratio model (LRM)	Lee (2005)
	Information value method	Yin and Yan (1988)
	Weights of evidence modelling	van Westen (1993), Bonham-Carter (1994), Suzen and Doyuran (2004)
	Favourability functions	Chung and Fabbri (1993), Luzi (1995)
Multivariate statistical method	Discriminant analysis	Carrara (1983), Gorsevski et al. (2000)
	Logistic regression	Ohlmacher and Davis (2003), Gorsevski et al. (2006a)
ANN	Artificial neural networks	Lee et al. (2004), Ermini et al. (2005), Kanungo et al. (2006)

Figure 1-7 Recommended methods for data-driven landslide susceptibility (from Corominas et al., 2014)

Deterministic methods rely upon simplified, physically-based landslide modelling schemes to analyse the stability/instability conditions, often using simple limit equilibrium model coupled with a hydrological infiltration model. The infiltration model, such as TOPOG (O’Loughlin, 1986) and TOPMODEL (Beven and Kirkby, 1979), simulates infiltration and groundwater flow processes and is used to evaluate the pore pressure in the section under analysis. The slope stability model, such as the infinite slope model (Taylor, 1948; Skempton and Delory, 1984), simulates the slope safety factor (FS) defined as the ratio of stabilizing to destabilizing forces. In Table 1.1, some of the most used models in the literature are listed. The parameters commonly used to perform a stability analysis are topographic (e.g. slope, upslope contributing area), hydrogeological (e.g. hydraulic conductivity), geotechnical (e.g. cohesion, friction angle, unit weight) and geological (depth).

The simplifications and assumptions of models adopted and the representation of slope deposits geotechnical properties is a key problem in the use of physically based slope stability models (Cervi et al., 2010; Corominas et al., 2014). Due to infinite slope model assumption that the sliding surface correspond to the slope deposit/bedrock discontinuity, the slope deposit depth, defined as the depth from the surface to a consolidated material (usually bedrock), plays a key role on the accuracy of regional susceptibility

analysis. Soil thickness can be modelled using physically based methods that model rates of weathering, denudation and accumulation (Dietrich et al., 1995; D’Odorico, 2000) or empirical methods that determine correlations with topographical factors such as slope, or it can be predicted using geostatistical methods (Tsai et al., 2001; Florinsky et al., 2002; Catani et al., 2007; Kuriakose, Devkota, et al., 2009; Kim et al., 2016). Slope deposits geotechnical properties are generally affected by great uncertainty. This is due to the cost associated with field surveys, laboratory tests and *in situ* tests, but also for the SD natural variability, due to a complex geological evolution. Furthermore, the reliability of geotechnical properties maps for slope deposits are also a source of uncertainty (van Westen et al., 2008). In order to consider the above-mentioned uncertainty of input data, many authors have adopted a probabilistic approach (Gorsevski et al., 2006; Liu and Wu, 2008; van Westen et al., 2008; Kuriakose, van Beek, et al., 2009; Park et al., 2013; Raia et al., 2014). The probabilistic approach makes it possible to model the variability of input parameters by means of probability distribution functions; as a result, the model response is expressed by probability laws, which are for example, numerically obtained by means of Monte Carlo sampling methods. Unlike data-driven methods, physically-based models are applicable to areas with incomplete landslide inventories and permit making predictions based on different triggering factors such as rainfall, land use change, earthquake and snowmelt.

Table 1.1 A few physically-based models available in the literature

Model name	Reference
dSLAM	Wu and Sidle 1995
SHALSTAB	Dietrich et al. 1998
SINMAP	Pack et al. 1998
SHETRAN	Ewen et al. 2000
PROBSTAB	van Beek 2002
TRIG-RS / TRIG-RS-P	Baum et al. 2002; Raia et al. 2014
GEOtop-FS	Simoni et al. 2008

1.3 AIM OF THE THESIS

In the last decades, due to climatic changes and increasing frequency of intense rainfall events, studies about landslide distribution and predisposing factors have experienced an extensive development (Gariano and Guzzetti, 2016; Reichenbach et al., 2018). Many researchers have focused on landslide susceptibility as well as hazard and risk zoning in order to provide tools to mitigate human and economic losses (Fell et al., 2008; Corominas et al., 2014). Moreover, landslides are a major hazard causing human and large economic losses worldwide and, in the last twenty years, an increasing trend of fatal landslides in Europe has been observed (Figure 1-6, Haque et al. 2016).

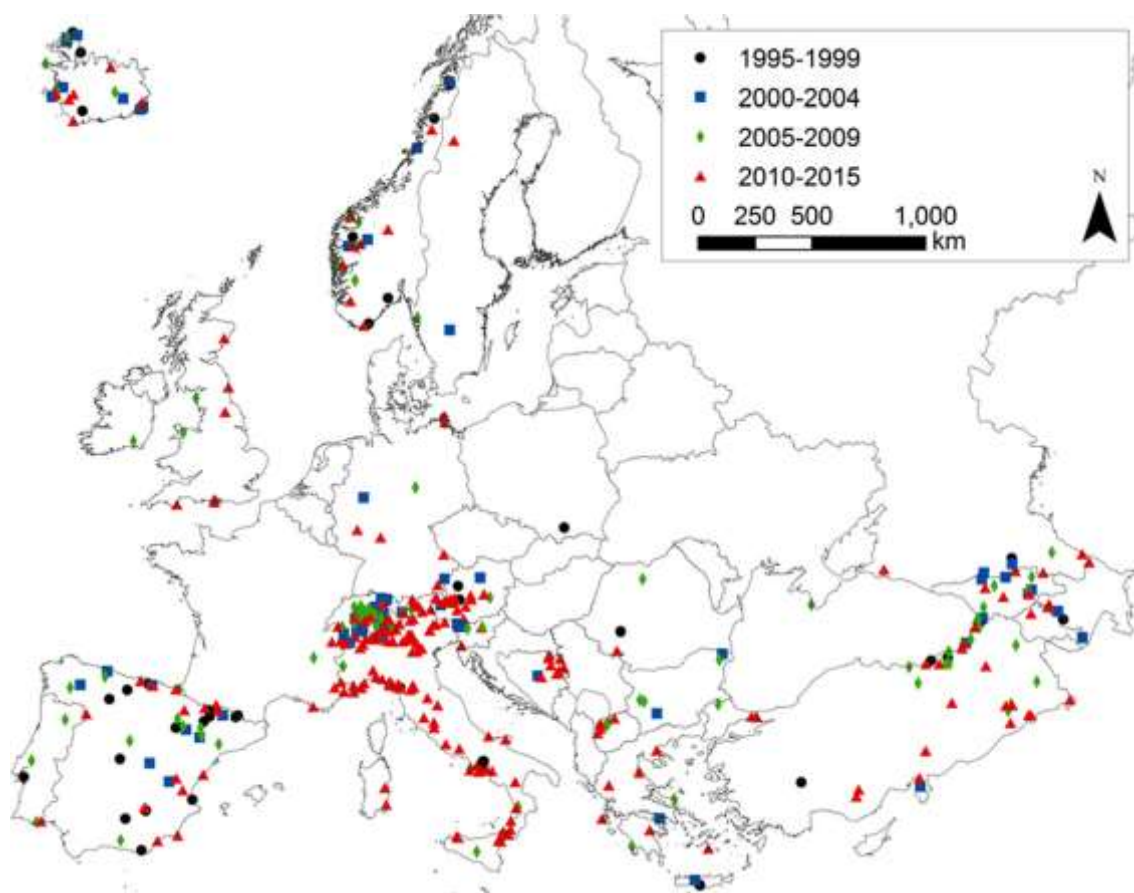


Figure 1-8 Spatial distribution of fatal (death, injury, and missing) landslides (from Haque et al. 2016)

Italy is the European country most affected by fatal landslides and in the recent past was hit by disastrous landslide events occurred in Piemonte Region in 1994, in Versilia (Tuscany) in 1996, in Sarno and Quindici (Campania Region) in 1998, in a large sector of Northern Italy in 2000, in Val Canale (Friuli Venezia Giulia Region) in 2003, Messina (Sicily) in 2009 and in Liguria/Northern Tuscany in 2014 (Trigila et al., 2010; Giordan et al., 2017). The majority of these events share an intense rainfall triggering a great number of shallow landslides evolved in more-or-less concentrated debris flows hitting densely populated or man-modified areas. In this framework, shallow landslides distribution, characterization and

susceptibility analyses are fundamental tasks in order to implement a reasonable spatial planning and decrease hazard and risk.

However, the predictive capacity of a shallow landslide susceptibility model substantially depends in the cases of the physically based models on the quality of the input data and on the quality of the landslide inventory for data-driven models. One of the most important challenges for physically based models is the accurate definition of geo-technical parameters of materials involved in the landsliding, consequently the predictive ability of these methods is closely linked to the degree of detail with which they are characterized. For this reason, physically based models are inadequate in cases where a small-scale regionalized slope stability analysis is required (Corominas et alii, 2014; study area > 1000 km²). Furthermore, since physically based models assume that the sliding surface is located at the interface between the slope deposits and the underlying bedrock, determining the depth of this interface is also a difficulty to be taken into consideration. Numerous studies highlight how the depth of the slide influences the probability of a landslide occurring, in fact, with equal morphological and geo-technical conditions, the deeper the sliding surface the more likely it is to fail. For this reason, having the availability or building a map that describes the trend of the depth of the slope deposits/bedrock interface is a fundamental input for a physically based susceptibility model. It is also true that considering slope deposits/bedrock interface as the surface where sliding can occur is a simplification of reality. The fieldwork experience gained in this thesis has highlighted that a large part of the shallow landslides has a sliding surface which is located just below the slope deposits/bedrock interface, thus affecting the most superficial portion of the rock mass characterized by varying degrees of alteration and fracturing. Not considering the possibility that a landslide could affect the bedrock inevitably leads to an underestimation of the probability of a landslide occurring in certain areas. Taking this aspect into account also means knowing the geo-mechanical characteristics of the rock mass that lies beneath the slope deposit, which will not be the characteristic of an undisturbed or tunneled rock mass but rather are characteristics that depend on the degree of weathering and fracturing of the first 1-3 meters below the interface with the slope deposit. This is because as the depth increases, the mechanical characteristics of the rock masses increase, the more superficial portions always tend to have worse characteristics due to their proximity and / or direct contact with the biosphere, atmosphere and hydrosphere.

Data-driven models, having a different approach than physically based models, i.e. the basic assumption consists in the concept that new landslides should take place in the same conditions in which past landslides took place, can have a greater predictive performance for landslides involving bedrock with respect to deterministic models. The reason is that a physically based model should also include the difficult task of geotechnical parameters characterization of the bedrock undergoing failure.

However, being the data-driven approach a black box model, if the occurrence and frequency of shallow landslides involving bedrock is not known as an input information, they cannot discriminate between

areas where landslides are more likely to involve either slope deposits only, or slope deposits and the underlying bedrock.

As a consequence of what it is stated above, the aims of this PhD thesis are:

- To characterize shallow landslides identifying the differences between slope deposits landslides and landslides also involving bedrock
- To define and apply a method to estimate the variability of geotechnical properties both for SD and bedrock involved in shallow landslides
- To define and apply a method to spatialize the above properties at regional scale
- To explore the performance of both data-drive and physically based models for the assessment of shallow landslide susceptibility also considering the involvement of bedrock in the failure processes
- To discuss the role of bedrock for shallow landslides development

**2 METHODS - A NEW WAY TO APPROACH
SHALLOW LANDSLIDES AND
SUSCEPTIBILITY ASSESSMENT BY
MEANS WELL-ESTABLISHED TOOLS**

This chapter focuses on the methodological approach developed in this thesis. The workflow used in the field to investigate and characterize the geotechnical properties of both slope deposits and bedrock, the statistical methods adopted to process and spatialize field data for the evaluation of shallow landslides susceptibility and the numerical models are presented.

2.1 WORKFLOW OF THE METHOD

In Figure 2-1, the flowchart summarizes the workflow proposed in this thesis in order to characterize slope deposits (SD) and bedrock (BR) and their implementation in shallow landslide susceptibility assessment. The input data needed in the initial phase of the work are tools that are now available for most of the globe, namely a Digital Elevation Model (DEM), a geological map and orthophoto maps. As demonstrated by the application and confirmed by the literature (Johnson and Johnston, 1995; Kühni and Pfiffner, 2001; Chelli et al., 2010; Heckman and Rasmussen, 2011; Kirby and Whipple, 2012; Allen et al., 2013; Hurst et al., 2013; Nsangou Ngapna et al., 2018; Bernard et al., 2019; Glaus et al., 2019), the basic assumption on which this method is founded is that different lithologies have different response to erosion, weathering and tectonic deformation giving, in turn, place to specific morphology and geotechnical properties of materials. Therefore, the geological map (1:10000 scale) it is simplified by grouping the formations on a lithological and stratigraphic basis (Bedrock Lithological Units, BLU).

The DEM is used to calculate morphometric variables which are a fundamental input data for both the data driven and physically based modelling approaches, as well as, they are used to compute through unsupervised classification (described in detail in the next chapter) morphometric units for each BLU. Nevertheless, the whole method proposed and developed in this thesis could not be completed without the compilation of a new shallow landslides inventory, obtained here through the visual interpretation of orthophotos. With the aim of assessing the accuracy of the landslide inventory and collecting data both in areas involved by landslides and in stable areas, the field work is controlled by the shallow landslide distribution (data collection strategy details are described in the next chapter). During the field work, both SD and BR properties are investigated. In the SD there may be an intrinsic variability of properties (depth to the bedrock, texture, grain size, unit weight) depending on morphology and the underlying BLU. Hence, field work site observations and laboratory analysis have been performed and analysed according to morphometric units and BLU, and then a set of geotechnical parameters (SD depth, friction angle, unit weight) have been assigned. An accuracy assessment is then performed for the SD depth map. Finally, in order to regionally spatialize SD properties, the Engineering Geological SD map (SDEG map) is obtained joining the geotechnical parameters to the raster of morphometric units of each BLU. The last operation consists on the merging of SDEG maps of each BLU into a single map.

In order to understand the role played by bedrock in shallow landslides, it is necessary to characterize and verify the geo-mechanical properties of the surficial portion of rock masses. The workflow of the field work consisted in analyzing rock mass outcrops ranging in size from a minimum of 4-5 meters up to 20 meters, deeper less than 4 meters from the surface. The first phase of the rock mass analysis consisted on the description of lithology, structure, layering and texture. The second phase of the field work is aimed to the quantitative characterization of the outcrop, and involves three steps: Schmidt hammer rebound value, discontinuities analysis and "Geological Strength Index" (GSI) estimation. In order to explore the distribution of bedrock properties and variability, a descriptive statistical analysis is performed. Then, to verify the presence of a spatial variability of bedrock properties at regional scale, uni-variate and multi-variate cluster analysis are carried out (detailed description in the next chapter). As well as for slope deposits, the regionalization of geotechnical parameters is executed assigning a range of geotechnical parameters for each pre-defined Geo-mechanical Bedrock Unit (GMU). In this case, the definition of Geo-mechanical Bedrock Units is not ruled by morphometric units but the spatial variability of bedrock properties. If the spatial analysis identifies clusters with similar characteristics, on expert basis, using tectonic features, drainage network and morphology, the GMUs are identified by mapping the edges of the clusters. The shallow landslide susceptibility modelling is then performed by means both a data driven and physically based models. The data driven approach is made up combining the landslide inventory with morphometric variables, SD depth map and BLU. The physically based approach instead is made up performing a Monte Carlo simulation of SD and BR properties. The output susceptibility maps are then subjected to the accuracy assessment, compared and combined.

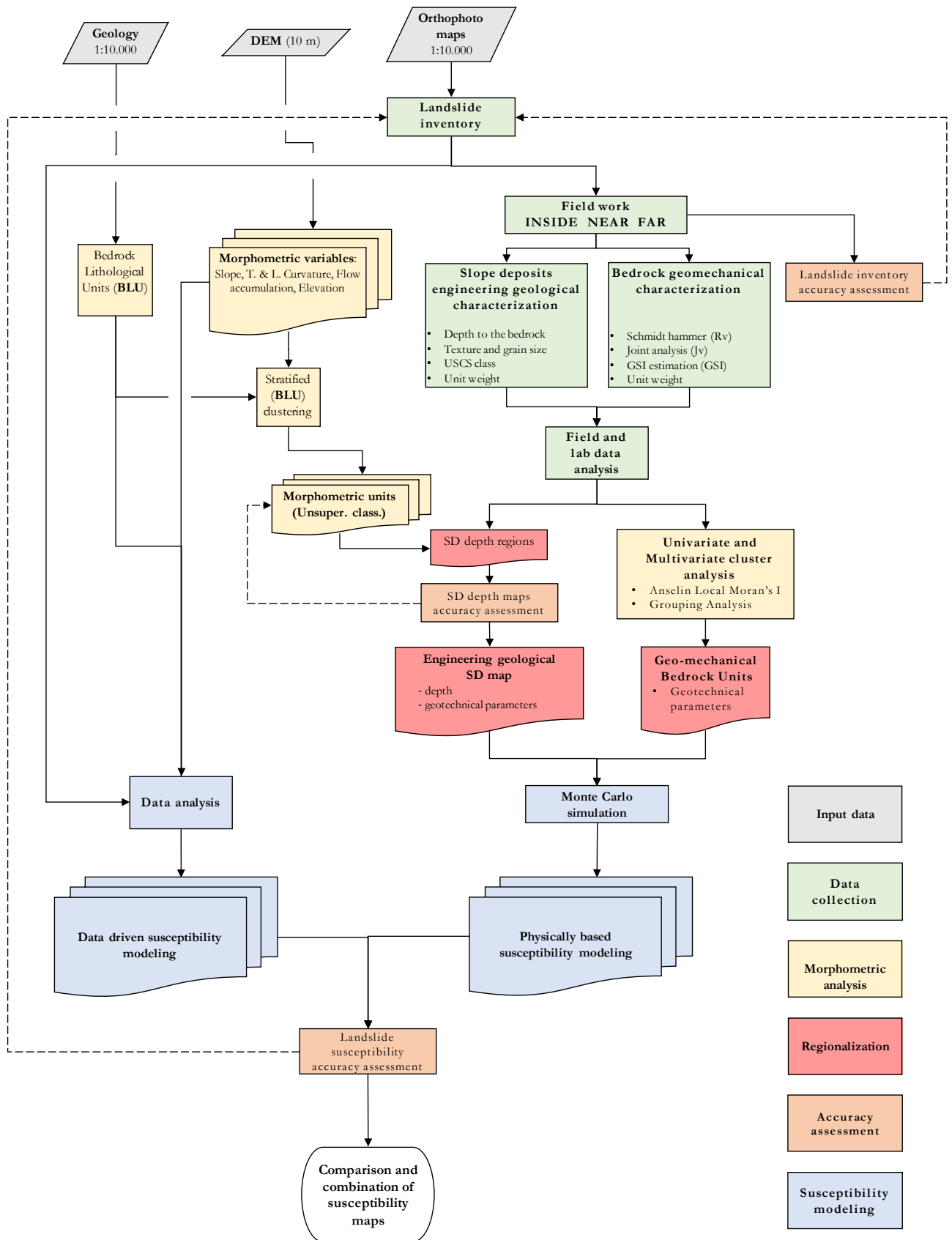


Figure 2-1 Workflow of the method proposed in this PhD thesis

2.2 DATA COLLECTION STRATEGY

Given the workflow described above, the planning of sampling is a key feature in order to have a comprehensive framework of both SD and BR variability. Moreover, it is important to characterize not only landslide areas, but also sites not yet characterized by slope instability. For this reason, the role of a detailed landslide inventory is fundamental because the data collection strategy was based on performing observation sites for the characterization of both the SD and BR inside, near and far from the previously detected landslides (Figure 2-2). According to this strategy, the analysis of SD and BR was conducted both in correspondence of the landslide scarp (inside) and in the surroundings of the landslides, usually within 50 meters (near). All the other site observations are considered as “far”.

Of course, sampling density is strictly related to the extension of the study area and frequency and spatial distribution of landslides. On the basis of the extension of the study area chosen in this thesis ($>200 \text{ km}^2$) and the landslide density resulted from the new shallow landslide inventory, the data collection lasted about a year.

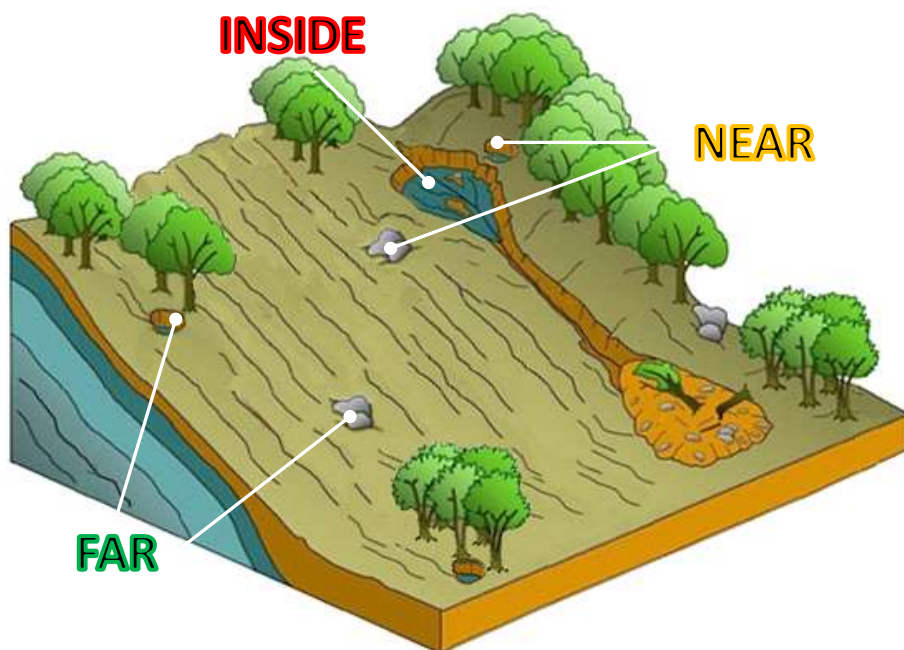


Figure 2-2 Schematic sketch representing the data collection strategy

2.3 VISUAL INTERPRETATION OF ORTHOPHOTO MAPS

In this thesis, the visual interpretation of orthophoto maps was used to compile a new multi-temporal shallow landslide inventory (LI) for the study area. By using this method, the older image (2000) is considered as the basic image, that is, the initial stage of the territory, from which all the later images were compared. The digital multitemporal visual interpretation was focused at identifying and delineating, as polygonal features, small-scale shallow landslides occurred during the analyzed period. These slope failures essentially triggered by intense rainfall events correspond to decameter-scale scars where either the residual slope deposits or underlying bedrock crop out. The comparison of aerial images from different epochs allowed us to identify abrupt local-scale variations in texture and tone/color, sharp interruption of vegetation and cultivated fields, disruption of linear patterns, and occurrence of U-shaped elongated features (Figure 2-3). These clues have led to the hypothesis that these forms may be labelled as landslides.



Figure 2-3 Example of multi-temporal investigation of orthophoto maps and delineated landslide polygons

A visual topographic and land use analysis may help to confirm or deny the hypothesis.

Nevertheless, in addition to the delineation of polygons classified as landslides, areas displaying similar features to those described above were also mapped as polygons and labelled as stable areas. In other words, there are some instances, as well landslides, which differ from the neighbouring areas for texture, tone and color, that are not necessarily landslides. The need to identify these sites and discriminate them from the polygons classified as landslides is aimed at evaluating the quality of the work of visual interpretation to recognize both unstable and stable areas. The quality was quantitatively evaluated by means of sensitivity and specificity executing the accuracy assessment tasks. Polygons classified as “stable areas” are subjected to validation such as polygons classified as landslides. In Figure 2-4 an example of unstable (landslide) and stable areas is provided.

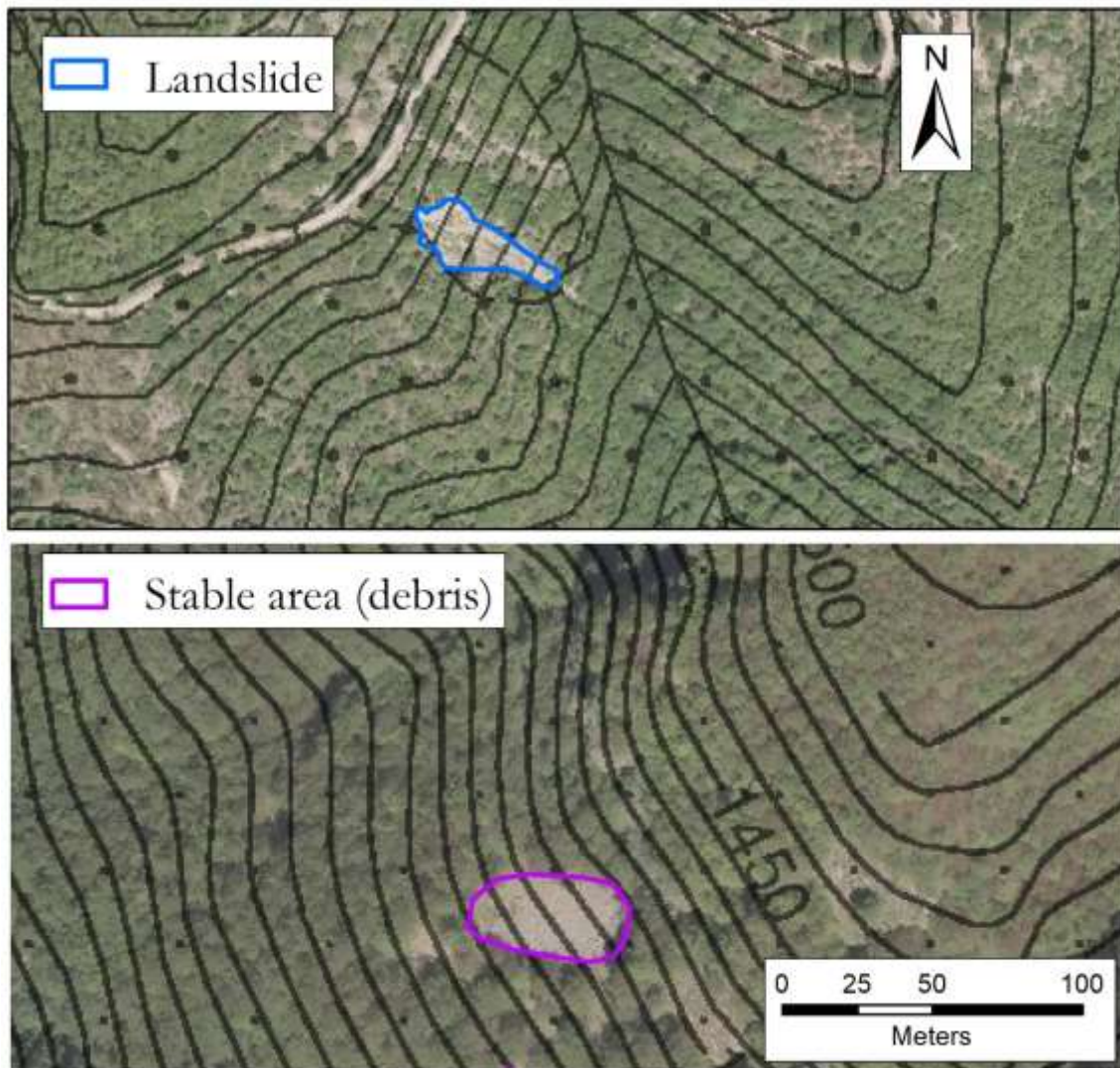


Figure 2-4 Delineated polygons of a landslide area (blue line) and a stable area (violet line). The lack of vegetation, tone, colour and shape are similar, but the violet polygon is inferred to represent a debris area

In this thesis, the polygonal Shape File (ESRI ArcGIS®) is accompanied by an attribute table and the fields are briefly described below:

- The field YEAR_OUTL (numeric) indicates the oldest orthophoto where the shape is recognized and has been delineated.
- The field GEO_LABEL (text) indicates the geological formation in which the landslides has occurred.
- The fields ORTHO_xxxx (where xxxx is referred to the epoch of the orthophoto maps) are numeric fields that indicate whether the form is visible (1) or not (0) in the orthophoto of the respective acquisition period. Consequently, the oldest period of the ORTHO_xxxx field for which the value is equal to 1 coincides with the value in the field YEAR_OUTL.

- The field UNCERT is a numeric field (1-3, certain-very uncertain) indicating the degree of uncertainty of the delineated features, as qualitatively estimated by the interpreter. It describes how confident the operator is that the delineated shape is a landslide.
- The field “POLY_TYP” (text) indicates if the polygon is classified as “landslide” or “stable area”

The visual interpretation of orthophoto maps has few limitations, but some of these needs to be discussed. Even if aerial images are generally acquired during the spring/summer period, the acquisition time may vary. At mid-day, the sun is closest to the zenith position, providing homogeneous lighting and minimum shadowing. Nevertheless, when images are acquired during the morning, northern slopes are shaded hindering the detection. More often, when solar lighting is nearly parallel to the ground surface, in sites where vegetation is lacking (rock outcrops, e.g.) it is not possible to exclude the presence of a landslide and vice versa. Another issue involving visual interpretation of orthophoto maps regards identifying slow-moving landslides since recent aerial images have a spatial resolution that usually ranges between 1 m to 0.2 m, which is the same order of magnitude of slow-moving landslides displacement rate, defined as less than 1.6 m/year (IUGS-International Working Group, 1995; Cruden and Varnes, 1996). Due to the small size and shallow depth of rupture surface, the post-failure vegetation re-growth is another issue occurring during visual interpretation of orthophoto maps (Rib and Liang, 1978). This issue is well known especially in tropical and equatorial regions where vegetation may grows rapidly obliterating the slope failure in a matter of months or seasons. Moreover, in the mid-latitude cultivated areas, agricultural practices can easily cancel the morphological and land cover signature of landslides (Guzzetti et al., 2012).

Nevertheless, this problem occurs even when geomorphological field mapping is performed, or imagery is processed by means of classification. Instead, using a very high spatial resolution digital elevation model captured by LiDAR sensors to map landslide may help to bypass the problem (Guzzetti et al., 2012). Beyond the limits described above, interpretation of the aerial photographs remains the most common method to recognize landslides, and to prepare landslide inventories (Guzzetti et al., 2012).

2.4 ENGINEERING GEOLOGICAL CHARACTERIZATION OF SLOPE DEPOSITS

2.4.1 Field survey data acquisition

2.4.1.1 Measuring the depth of slope deposits

The SD field survey was performed after the manual opening of digs until reaching either the bedrock unconformity or getting as deep as possible under the ground surface. In fact, in some cases, it is not possible to reach the bedrock due to the presence of roots or cobbles. In order to verify the identification of the bedrock, the dig is repeatedly enlarged and cleaned using a trowel. By the field experience, a common investigation depth limit is around 2 m.

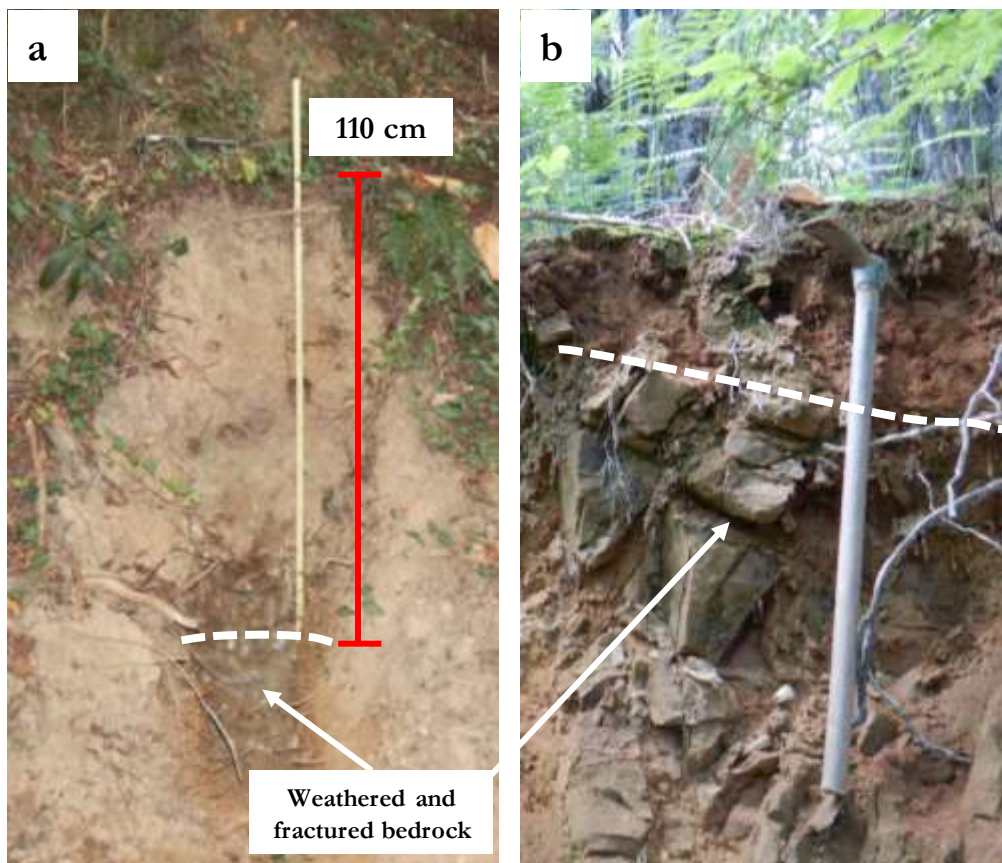


Figure 2-5 Examples of a medium thick (a) and a thin (b) slope deposits. Pickaxe length 100 cm.

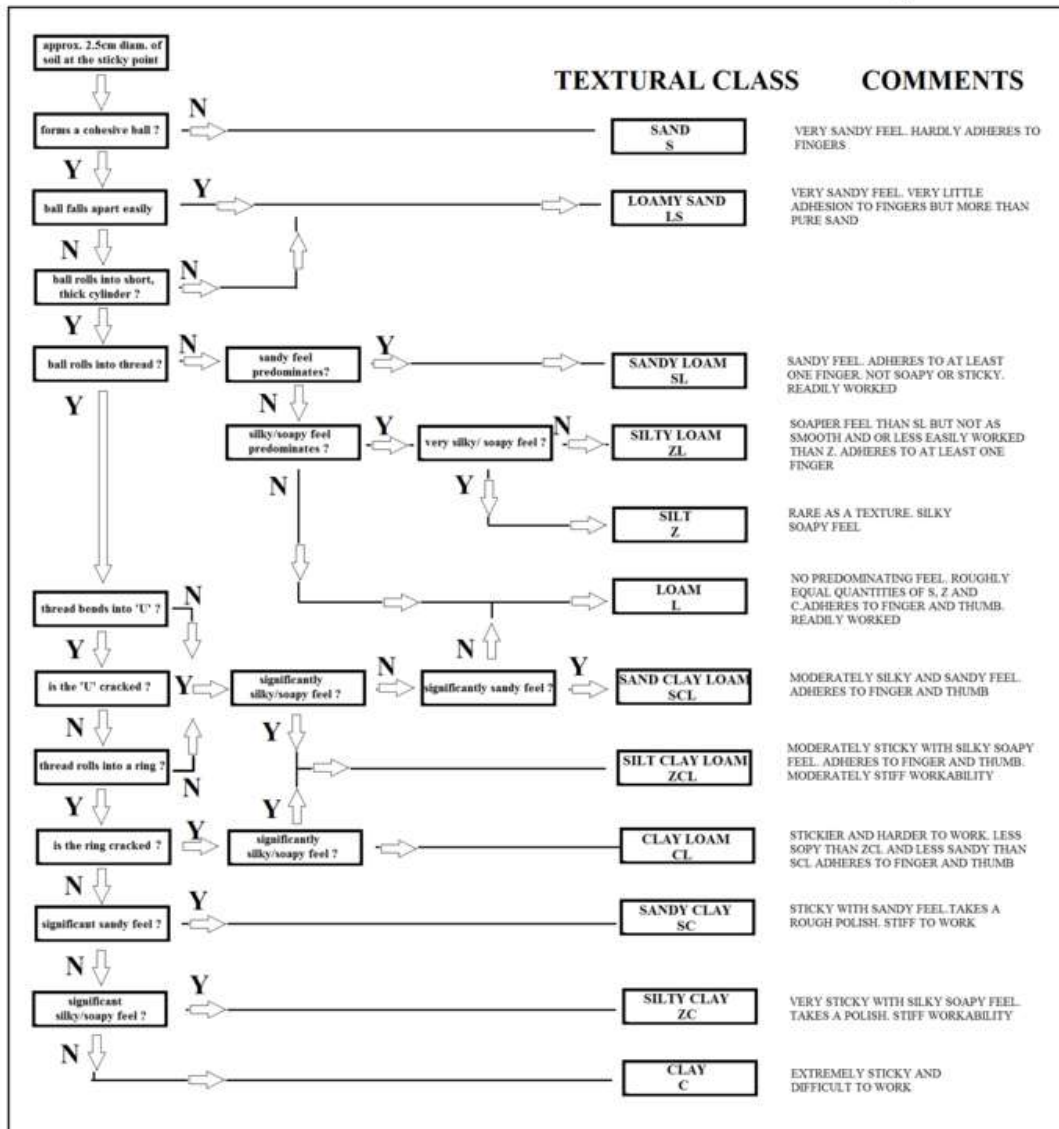
2.4.1.2 Fabric and grain size estimation

Once the dig is completed or if a natural trench allows to conduct a detailed observation down to the bedrock, the analysis of horizons is conducted. For each horizon, grain size and structure are evaluated. To estimate the grain size distribution of clay, silt and sand the USDA procedure have been used (USDA, 1987; Figure 2-6). This method of soil texture classification is particularly well suited to field applications. It requires answering a set of questions about the soil behaviour, which leads to an assessment of the textural class. The classification process can be formulated as a flow chart, which is shown in Figure 2-6. It is hence convenient to express the textural classes in terms of their fraction of sand, silt or clay on a trilinear diagram Figure 2-7.

Since the USDA classification does not take into account the quantity of grains larger than two millimetres, the visual scheme proposed by Terry and Chilingar (1955, Figure 2-8) has been used to assess the percentage of gravel and blocks.

Another information collected is the fabric of the deposits. In sedimentology and pedology, a deposit or a soil can be matrix-supported, grain-supported or variably clast- to matrix- supported (Terzaghi et al., 1996; Blair and McPherson, 1999). Figure 2-9 shows the scheme proposed by Ricci Lucchi (1980) to assess this property. An example of the two end-members is provided in Figure 2-10a-b.

Hand Identification Chart for Soil Texture Analysis



Sticky point: moisture content at which dry soil being wetted just begins to adhere to fingers

Workability: easy with which soil can be moulded between the fingers. Because consistence varies greatly with moisture, samples must be properly and uniformly wetted up

Cylinder: approx 5cm long and 1.5cm diameter

Thread: approx 13cm long and 0.6cm diameter

Ring: approx 2.5cm diameter formed from about 8cm of above thread.

Figure 2-6 Flow chart for USDA soil classification (USDA, 1987)

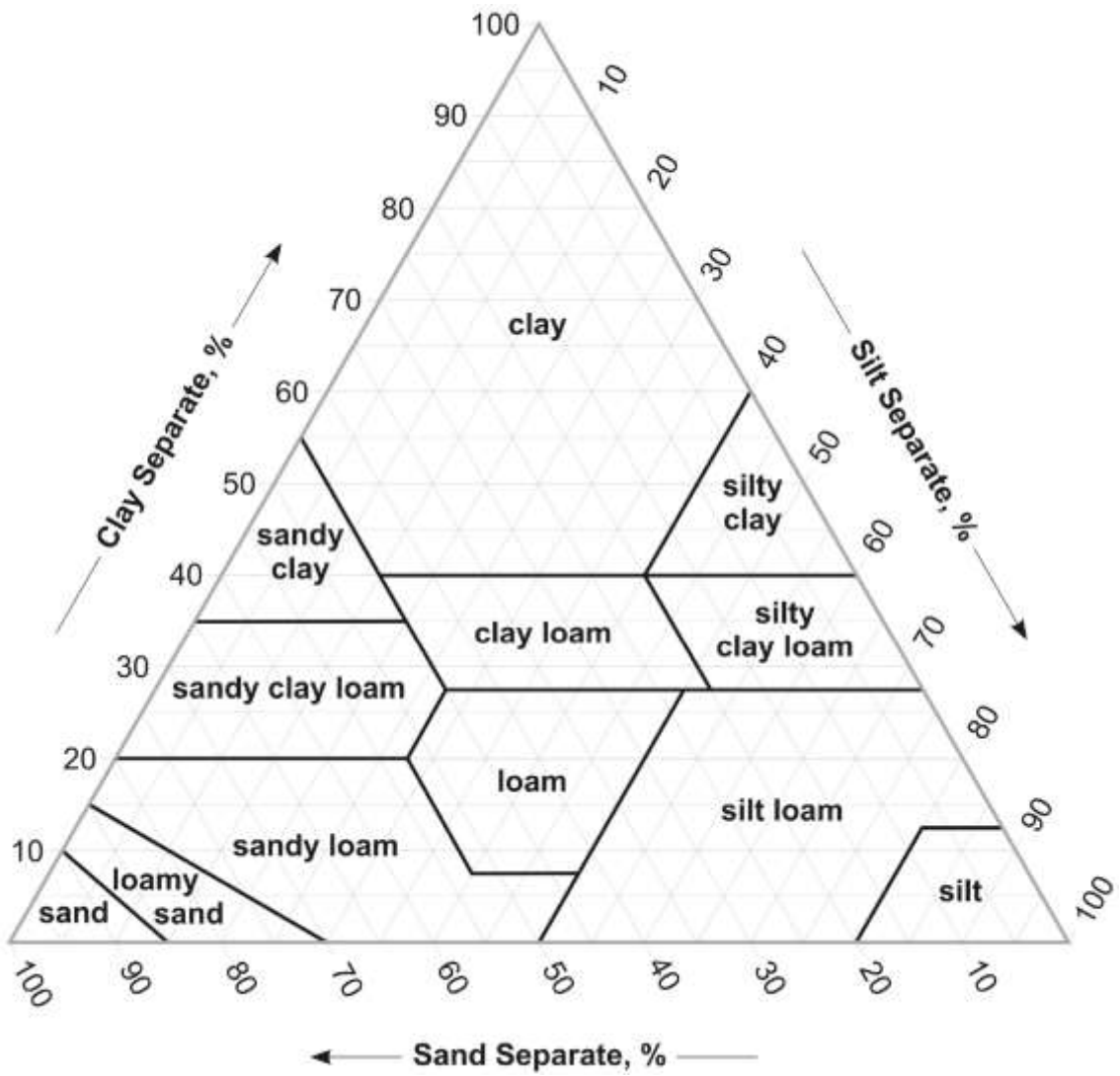


Figure 2-7 Soil Textural Triangle, from USDA (USDA, 1987)

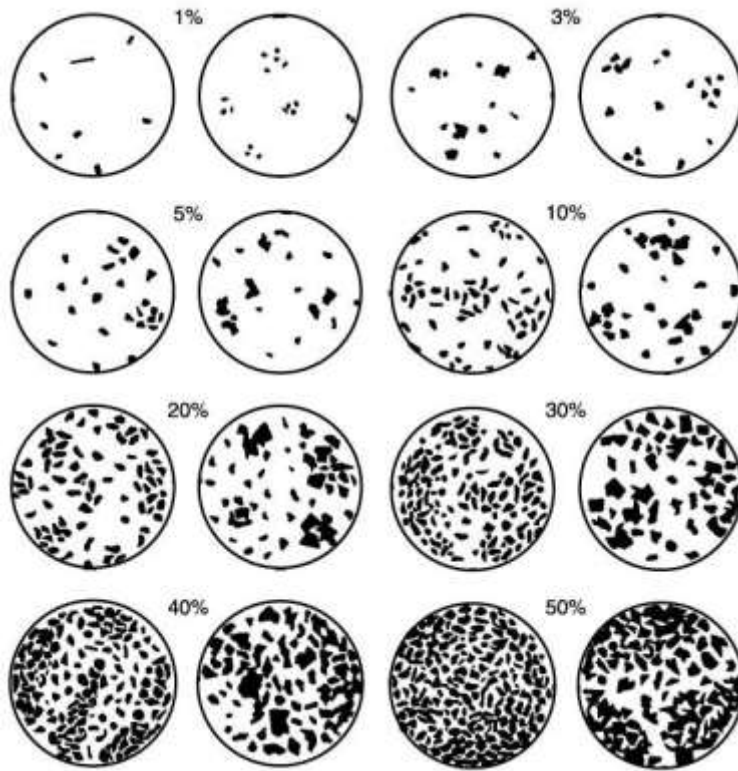


Figure 2-8 Visual estimation of coarse-grained particle size (Terry & Chilingar, 1955)

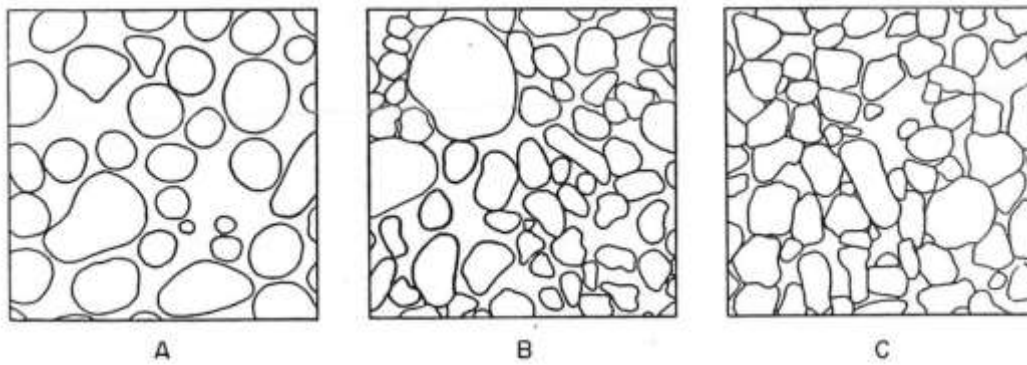


Figure 2-9 Structure analysis proposed by Ricci Lucchi (1980). A and C represent matrix- and clast- supported structure, while B is a transition among them.



Figure 2-10 a. Grain supported deposit. b. Matrix supported deposit.

2.4.2 Sampling and laboratory analysis

2.4.2.1 Grain size estimation and plasticity analysis

Remoulded samples are collected in order to evaluate grain size composition and Atterberg limits in the laboratory. This information is useful to assign the deposits to USCS class (Unified Soil Classification System - ASTM D2487-17, 2017). The USCS is a tool for classifying mineral and organo-mineral soils for engineering purposes based on laboratory determination of particle-size characteristics, liquid limit, and plasticity index. Generally, in accordance with Head and Epps (1980), the mass of soil to be sampled to conduct the analysis is about 2 kg when the largest particle size of the soil is about 20 mm. Hence gravel is estimated only through a field visual approach above mentioned. The laboratory particle size analyses are carried out using wet sieves for coarse material (ASTM C136 / C136M-14, 2014), while for the fine fraction (particle size <0.075 mm) the sedimentation process (ASTM D422-63 2007) is used. To obtain the USCS class of the fine grained samples (<0.075 mm), the Atterberg limits must be defined and plotted in the plasticity chart as shown in Figure 2-11.

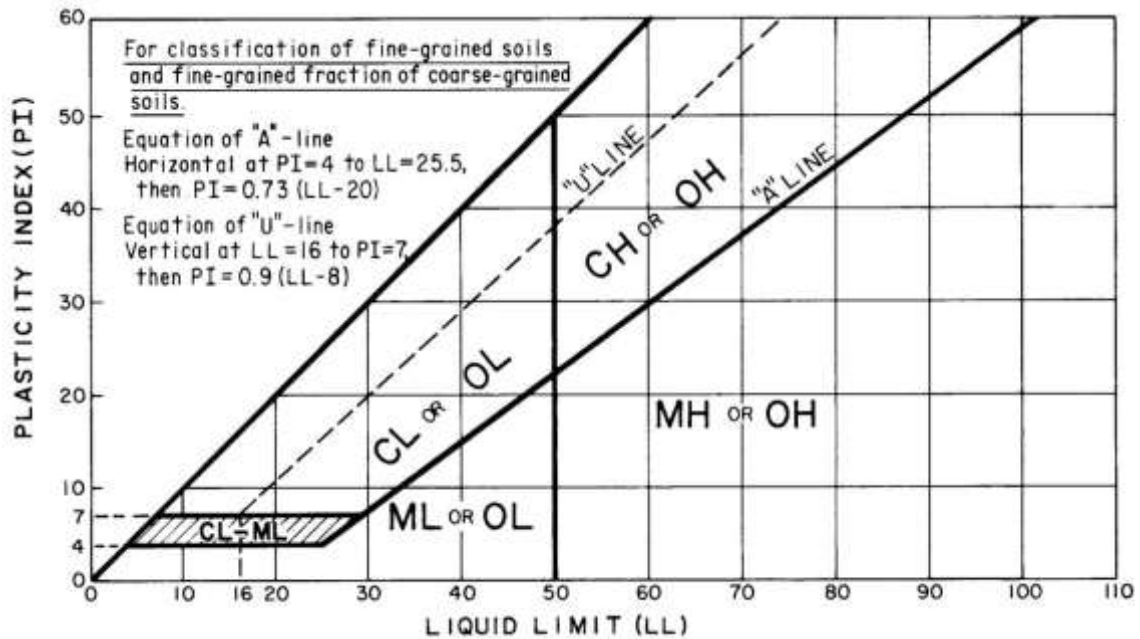


Figure 2-11 Plasticity chart used to determine USCS classes (ASTM D2487-17)

Coarse-grained slope deposits are classified basing on:

- C_u , coefficient of uniformity, the ratio D_{60}/D_{10} , where D_{60} and D_{10} are the particle diameters corresponding to 60 and 10 % finer on the cumulative particle-size distribution curve respectively,
- C_c , coefficient of curvature, the ratio $(D_{30})^2/(D_{10} \cdot D_{60})$, where D_{60} , D_{30} , and D_{10} are the particle sizes corresponding to 60, 30, and 10 % finer on the cumulative particle-size distribution curve, respectively.

In Figure 2-12, the classification chart to assess USCS class is shown.

Criteria for Assigning Group Symbols and Group Names Using Laboratory Tests ^a				Soil Classification		
				Group Symbol	Group Name ^b	
COARSE-GRAINED SOILS	Gravels	Clean Gravels	$C_u \geq 4$ and $1 \leq C_c \leq 3^c$	GW	Well-graded gravel ^d	
	More than 50% retained on No. 200 sieve	More than 50% of coarse fraction retained on No. 4 sieve	$C_u < 4$ and/or $1 > C_c > 3^c$	GP	Poorly graded gravel ^d	
		Gravels with Fines	Fines classify as ML or MH	GM	Silty gravel ^{d, f, g}	
		More than 12% fines ^f	Fines classify as CL or CH	uncl.1>GC	Clayey gravel ^{d, f, g}	
		Sands	$C_u \geq 6$ and $1 \leq C_c \leq 3^c$	SW	Well-graded sand ^d	
	50% or more of coarse fraction passes No. 4 sieve	Clean Sands	$C_u < 6$ and/or $1 > C_c > 3^c$	SP	Poorly graded sand ^d	
		Sands with Fines	Fines classify as ML or MH	SM	Silty sand ^{d, f, h}	
		More than 12% fines ^f	Fines classify as CL or CH	SC	Clayey sand ^{d, f, h}	
	FINE-GRAINED SOILS	Silts and Clays	inorganic	$P_I > 7$ and plots on or above "A" line ⁱ	CL	Lean clay ^{k, l, m}
		50% or more passes the No. 200 sieve	Liquid limit less than 50	$P_I < 4$ or plots below "A" line ⁱ	ML	Silt ^{k, l, m}
		organic	Liquid limit - oven dried ⁿ $> < 0.75$	OL	Organic clay ^{k, l, m, n}	
			Liquid limit - not dried	OL	Organic silt ^{k, l, m, n}	
		Silts and Clays	inorganic	P_I plots on or above "A" line ⁱ	CH	Fat clay ^{k, l, m}
		Liquid limit 50 or more	organic	P_I plots below "A" line	MH	Elastic silt ^{k, l, m}
			organic	Liquid limit - oven dried ⁿ < 0.75	OH	Organic clay ^{k, l, m, n}
				Liquid limit - not dried	OH	Organic silt ^{k, l, m, n}
HIGHLY ORGANIC SOILS	Primarily organic matter, dark in color, and organic odor			PT	Peat	

- ^a Based on the material passing the 3-in. (75-mm) sieve.
- ^b If field sample contained cobbles or boulders, or both, add "with cobbles or boulders, or both" to group name.
- ^c $C_u = D_{60}/D_{10}$; $C_c = (D_{30})^2 / (D_{10} \times D_{60})$
- ^d If soil contains $\geq 15\%$ sand, add "with sand" to group name.
- ^e Gravels with 5 to 12% fines require dual symbols:
GW-GM well-graded gravel with silt
GW-GC well-graded gravel with clay
GP-GM poorly graded gravel with silt
GP-GC poorly graded gravel with clay
- ^f If fines classify as CL-ML, use dual symbol GC-GM, or SC-SM.
- ^g If fines are organic, add "with organic fines" to group name.
- ^h If soil contains $\geq 15\%$ gravel, add "with gravel" to group name.
- ⁱ Sands with 5 to 12% fines require dual symbols:
SW-SM well-graded sand with silt
SW-SC well-graded sand with clay
SP-SM poorly graded sand with silt
SP-SC poorly graded sand with clay
- ^j If Atterberg limits plot in hatched area, soil is a CL-ML, silty clay.
- ^k If soil contains 15 to 29% plus No. 200, add "with sand" or "with gravel," whichever is predominant.
- ^l If soil contains $\geq 30\%$ plus No. 200, predominantly sand, add "sand" to group name.
- ^m If soil contains $\geq 30\%$ plus No. 200, predominantly gravel, add "gravelly" to group name.
- ⁿ $P_I \geq 4$ and plots on or above "A" line.
- ^o $P_I < 4$ or plots below "A" line.
- ^p P_I plots on or above "A" line.
- ^q P_I plots below "A" line.

Figure 2-12 Soil classification chart according to ASTM D2487-17

2.4.2.2 Unit weight

When possible according to the particle size of deposits, samples were collected for the determination of the unit weight. Slope deposits sampling took place in this case on non-disturbed material through the manual insertion of a ring with a diameter of 53 mm and with a volume of 100 cm³: the ring is inserted inside the deposits using a rubber mallet (Figure 2-13). This procedure was carried out within those horizons where the coarse fraction is not very large thus allowing the insertion of the ring. The samples have been protected in order to preserve the conditions of humidity in situ, after which they were weighed in the laboratory: the volumetric water content was then determined θ ($\theta = V_w / V_T$, where V_w and V_T represent the volume of water and the total volume of the soil sample, respectively), natural unit weight γ_n (kN / m³) and dry unit weight γ_d (kN / m³), after drying of the sample at 110 ° C for 24 hours in the oven (ASTM - D2937; BS 1377-2, 1990).



Figure 2-13 The collection of undisturbed samples for unit weight determination

2.4.3 Classification of morphometric variables

The shape of ground surface influences the drainage network, transport of sediments, colluvium/slope deposits production and affects the climate on local and regional scales. This is the reason of interest on landform recognition and analysis by Earth sciences and neighbouring disciplines (Mokarram et al., 2015). Landforms have a wide range of application domains, including geomorphological mapping, small scale lithological mapping, landslide mapping, prediction of soil/colluvium/slope deposits at regional scale, vegetation and land cover mapping and precision agriculture (MacMillan and Shary 2009; Evans 2012; Mokarram et al. 2015; Mokarram and Sathyamoorthy 2018 and references therein).

The recognition of landforms was initially performed by heuristic interpretation of terrain, but the increasing availability and resolution of Digital Elevation Models nowadays allows for much more accurate, automated and objective representation of forms, including their boundaries (Wieczorek and Migoń, 2014), by means of digital classification.

Landform classification can be performed with different approaches; the choice depends on the criteria used for classification, the number of variables, spatial scale of inquiry, resolution of input data, and algorithms used in the procedure. GIS-based approaches generally use morphometric variables such as slope steepness, aspect and profile/plan curvatures (Evans, 1972; Dikau, 1989; Guth, 1995; Wood, 1996; Fisher et al., 2004).

Popular automated methods to landform classification are those which implement data mining, such as the, fuzzy k-mean algorithm (Roberts et al., 1997; Burrough et al., 2000; Schmidt and Hewitt, 2004; Summerell et al., 2005; Deng et al., 2006; Arrell et al., 2007; Benito-Calvo et al., 2009), k-median algorithm (Wieczorek and Migoń, 2014; Szypuła and Wieczorek, 2020), ISODATA algorithm (Niemann and Howes, 1991; Irvin et al., 1997; Adediran et al., 2004; Liu and Tang, 2006; Zhong et al., 2009; Trefolini,

2015), Self-Organizing maps (Zhang et al., 2009; Ehsani et al., 2010; Kohonen, 2012), Support Vector Machine (SVM) (Stepinski et al., 2006) and combination between them (Brown et al., 1998; Iwahashi and Pike, 2007; Vilorio et al., 2016). Niemann and Howes (1991) proposed an unsupervised classification to assess slope stability and risk assessment. The procedure consisted of creating groups by using the k-mean cluster analysis for each variable independently, starting with slope gradient. After processing the full dataset, they introduced upslope drainage area as a second variable. In the last step, profile and plan curvatures were used to distinguish sub-groups within the previously created groups. The classification procedure finally revealed 44 groups. In Irvin et al. (1997) the authors showed that the classification of landforms using both the ISODATA and fuzzy k-mean methods can yield quick and useful results. The difference between results obtained from the two algorithms is that in the ISODATA classification pixels are assigned to only one landform group, while in the fuzzy classification each data point can have partial membership in several groups.

An example of using a different unsupervised classification method was one by Brown et al. (1998) who used maximum likelihood classification and neural network. Five morphometric variables were considered as basic input data: elevation, slope gradient, local relative relief, local roughness and upslope area. The support vector machine (SVM) is a group of theoretically superior machine learning algorithms (Huang et al., 2002). It was developed to be competitive with the best available machine learning algorithms in classifying high dimensional data sets (Mangai et al., 2010). For example, Stepinski et al. (2006) used SVMs for a test site on Mars to produce the most accurate results as compared to other conventional techniques of classifying topographic objects. Mangai et al. (2010) used SVMs to classify landforms and to identify a wide variety of landforms in the subcontinent of India.

Beyond the algorithm chosen to conduct the landforms classification, Dikau (1989) claimed that an accurate morphometric classification may be performed using four basic parameters obtained from a DEM: slope, aspect, plan and profile curvatures. However, this set of basic parameters can be extended, using variables such as roughness, relative height and topographic wetness index or upslope contributing area (Brown et al., 1998; Burrough et al., 2000; Deng et al., 2006).

The unsupervised classification is the method used in this work in order to classify the terrain. This clustering procedure allows to extract regions of contiguous pixels and is based on the analysis of a certain number of continuous variables. This technique is often used for remote sensing image interpretation (Abburu and Babu Golla, 2015) as well as for the geomorphological classification of landscapes using DEM derivatives (Irvin et al., 1997). The tool beyond the classification is the Iterative Self-organizing Data Analysis (ISODATA) technique (Tou and Gonzalez, 1974) which uses a maximum-likelihood decision rule to calculate class means that are evenly distributed in the data space and then iteratively clusters the remaining pixels, using minimum-distance techniques. Each iteration recalculates means and reclassifies pixels with respect to the new means. This process continues until the number of pixels in each class

changes by less than a selected pixel change threshold or until a specified maximum number of iterations is reached (Melesse and Jordan, 2002). This kind of approach is suitable for the classification on landforms starting from the DEM of an area in order to obtain clusters corresponding to the Morphometric Units. In this thesis, the term "Morphometric Unit" refers to spatial units with similar morphometric characteristics. In the literature, terms such as "landforms", "terrain units" and "homogenous units" are often used. As already stated, the assumption behind the Engineering Geological SD map is that, within the same bedrock lithology area, each cluster corresponds to a landform or Morphometric Unit. Therefore, the Engineering Geological SD map is then obtained assigning to Morphometric Units a set of engineering geological parameters.

The Unsupervised Classification is implemented in ESRI ArcGIS™ as a tool which combines the functionalities of the Iso Cluster and Maximum Likelihood Classification tools. The number of clusters must be defined before running the code, the minimum value is two classes, while there is not a maximum value.

The number of clusters for our purpose is ruled by the number of observations collected and the natural variability of the landscape in the subset of the study area under classification. Classifying the landscape in too many morphometric units provides a detailed characterization, but the sample frequency needed to describe all unit may be insufficient. On the contrary, taking few classes would lead to a rough description of the landscape.

A statistical method useful to determine the number of clusters to be used for the analysis, consists on the calculation of the Sum of Square Error (SSE) (Richards and Xiuping, 2006) assessing the data dispersion for each cluster for different clustering solutions. However, this method does not take into account the sampling density and the SSE results must be subjectively analyzed.

In our experience, a classification based on 5 to 15 classes turned out to be a good compromise.

The efficiency of clustering depends on some pre-processing procedures, like data stretching. A min-max stretching approach was implemented, as suggested by ESRI guidelines on Unsupervised Classification.

2.4.4 Slope Deposits Engineering Geological Map

For each BLU a Slope Deposits Engineering Geological Map is obtained by integrating field and laboratory results with morphometric units. According to the geographic position of observation sites, these results are grouped for each morphometric units. The statistical analysis of engineering geological properties is conducted at morphometric unit scale, in order to assign a dataset of slope deposits depth, USCS class and dry unit weight.

2.4.4.1 Slope deposits depth

Likewise geo-technical parameters, the depth of SD (SDd) is a fundamental input parameter to assess shallow landslide susceptibility at regional scale using physically based models (Wu and Sidle, 1995; Dietrich et al., 1998; Segoni et al., 2012; D. W. Park et al., 2013; Disperati et al., 2018). Even if some authors have shown the influence of SD depth on determining both the uncertainty and reliability of susceptibility maps (Ho et al. 2012; Kuriakose et al. 2009; Meisina and Scarabelli 2007), this information is generally missing at the map scale, and authors assume a constant value for SDd when performing stability analyses (Dietrich et al., 1998; Guimaraes et al., 2003; Teixeira et al., 2015).

In other studies, the SD depth maps are obtained as statistical relation with single or multiple morphometric variables (Dietrich et al., 1995; Kuriakose, Devkota, et al., 2009; Pelletier and Rasmussen, 2009; Schulz et al., 2009; Tesfa et al., 2009; Lanni et al., 2012; Segoni et al., 2012), or by means physically based approach, focusing on the temporal evolution of the soil thickness or basing on the conservation of mass equation (Mudd and Furbish, 2004; Saco et al., 2006; Nicótina et al., 2011). Nevertheless, all authors agree that the spatial distribution of soil depth is controlled by complex interactions of many factors such as topography, parent material, climate, biological, chemical and physical processes, resulting in a difficult prediction due to its high spatial variability. Given the above general framework, the method used in this thesis is based on the concept that the slope deposits depth is related to lithology of the underlying bedrock and morphometric variables. The method here adopted is an improvement of the method developed by Trefolini, (2015), Trefolini et al., (2015), Venturini et al., (2016) and Disperati et al., (2018).

In this PhD thesis, SD depth is represented by a system based on categorical depth classes instead of continuous representations, given the intrinsic local variability of SD depth. As described in paragraph 2.6.1, in the physically based model used for shallow landslides susceptibility assessment, the range of each class was used as input variability for depth executing the Monte Carlo simulation.

The number of depth classes may depend on the number of field observations, the maximum depth value reached and the expected degree of detail. Moreover, the width of the classes may be constant or follow a different rule depending on depth. This, in turn depends on the number of field observations as well as the statistical distribution of SD depth values.

Hence, a method to determine the number and the width of SD depth classes is to plot the cumulative frequency distribution of depth measures of the whole fieldwork dataset.

2.4.4.2 Shear strength parameters assessment

The cohesion c and friction angle ϕ are the parameters used to describe shear strength parameters of SD by means of the Mohr-Coulomb shear strength criterion (Lambe and Whitman, 1991).

When working at specific site scale or in small study areas, the shear strength of soils can be estimated in laboratory by testing representative undisturbed samples to triaxial or direct shear tests. Moreover the same goal may be reached by performing in situ tests, such as penetrometric tests (Lambe and Whitman, 1991; Lancellotta, 2001; Ameratunga et al., 2016). Although generally regarded as accurate and reliable, these procedures are costly, logistically complex and time consuming. Furthermore, collecting an undisturbed sample in non-cemented granular deposits is difficult, as it is almost impossible to perform on-site tests in predominantly gravelly materials.

In this work, the workflow and the method described are addressed to study multi-scale areas wider than 100 km², so a large number of investigation sites is requested. For this reason, the estimation of shear strength parameters of slope deposits, as well as of bedrock that will be presented later, is assessed by means of empirical and experimental correlations.

In this section relevant empirical correlations are discussed for both cohesive and granular slope deposits. The SD are materials made up of mixtures of granulometric fractions ranging from clays to gravels, passing through the sands. Furthermore, being SD formed in recent times outside the alluvial depositional areas they can be regarded as are normally consolidated without cementation. This implies also that cohesion of SD is apparent, depending on water content, matrix suction properties and type/density of vegetated root systems (Terzaghi and Peck, 1967; Terzaghi et al., 1996).

Soil suction can vary among different soils, moreover, due to its dependence on water content, it also considerably varies over time. However, the soil suction is negligible when the soil is completely saturated. When performing stability analysis, the contribution of soil suction to the slope stability is neglected (Lambe and Whitman, 1991).

The role of roots cohesion has been investigated during the last decades by several authors (Watson et al., 2000; Roering et al., 2003; Schwarz et al., 2010; Arnone et al., 2016; Marzini et al., 2019).

Marzini et alii (2019) evaluated the stabilizing effects of root systems in shallow landslides. They conclude that in certain conditions the root cohesion is a relevant parameter for shear strength, estimating a maximum value of about 5 kPa. Moreover, they highlight that root reinforcement is exerted principally in the main and lateral scarps, acting to a depth less than 1 m.

Due to the reasons mentioned above, one of the most effective ways to evaluate the cohesion of SDs is to derive it by back-analysis while implementing physically based models. Initial effective cohesion values can be assigned by referring to the literature; then, having available an inventory of landslides to validate the model, depending on the accuracy results, the cohesion can be calibrated according to the stability scenario obtained from the modelling (Disperati et al., 2018). In the case of SHALSTAB (Montgomery and Dietrich, 1994; Montgomery et al., 1998), for example, unconditionally unstable areas (UU) are those being unstable when piezometric surface does not develop. The occurrence of stable SD within the UU areas is an obvious paradox. Consequently, in order to reduce the extent of UU areas, the expert can

proceed to increase the effective cohesion value. Likewise, unconditionally stable areas (US) are areas that are never susceptible to landslide. However, if landslides occur in those areas, there the effective cohesion may be reduced until this issue is solved. After such an expert-driven process of back analysis, the outcome cohesion values ranges, which depends on the integration of numerical stability model with the landslide inventory, have to be compared with values known from the literature.

In Table 2.1, typical c' and ϕ' values according to Australian Standard - 4678 (2002) are reported.

Table 2.1 Typical c' and ϕ' values according to Australian Standard - 4678 (2002)

Soil group	Typical soils in group	Soil parameters	
		c' (kPa)	ϕ' (degrees)
Poor	Soft and firm clay of medium to high plasticity; silty clays; loose variable clayey fills; loose sandy silts	0–5	17–25
Average	Stiff sandy clays; gravelly clays; compact clayey sands and sandy silts; compacted clay fills	0–10	26–32
Good	Gravelly sands, compacted sands, controlled crushed sandstone and graveled fills, dense well graded sands	0–5	32–37
Very good	Weak weathered rock, controlled fills of road base, gravel and recycled concrete	0–25	36–43

Regarding cohesive SD, the literature reports a clear evidence that increasing plasticity leads to a reduction in the peak of friction angle. The increasing of plasticity is related to the increasing clay content, the latter having low frictional resistance (Ameratunga et al., 2016). Sorensen and Okkels (2013) analysed an extensive database of normally consolidated reconstituted and undisturbed natural clays from the Danish Geotechnical Insititute, along with other data from the literature (Kenney, 1959; Bjerrum and Simons, 1960; Brooker and Ireland, 1965; Terzaghi et al., 1996) and proposed two correlations in order to estimate the friction angle from plasticity index (Figure 2-14).

They suggested that for a cautious lower bound estimate, the friction angle can be estimated as:

Equation 2-1

$$\phi = 39 - 11 \log PI$$

Where PI is the plasticity index. Instead, the best estimate of the peak friction angle is given by:

Equation 2-2

$$\phi = 43 - 10 \log PI$$

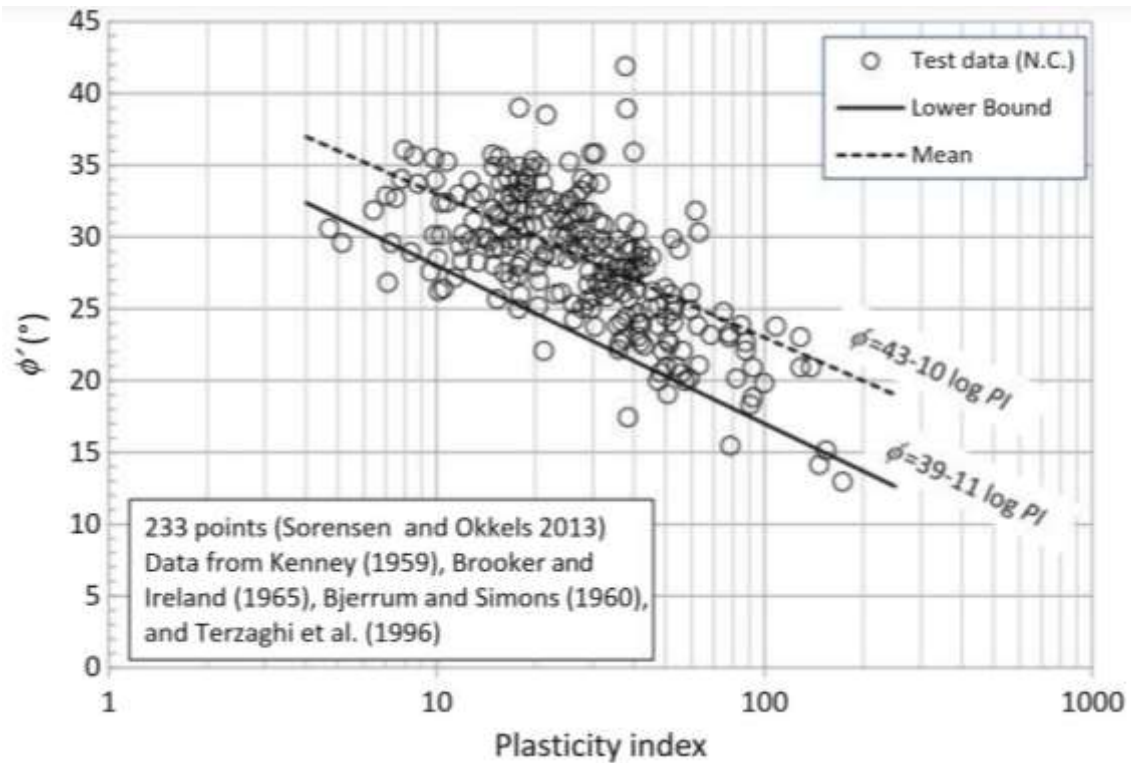


Figure 2-14 Correlations between plasticity index and friction angle (from Sorensen and Okkels, 2013)

In general, the friction angle of a granular materials increases with the angularity of the grains, surface roughness and relative density. Well graded granular materials usually have higher friction angle than poorly graded ones. In Table 2.2, some representative friction angle values of sands and silts provided by Terzaghi et al. (1967) are reported. In the work of Schmertmann et alii (1978), the friction angle of granular soils was determined from triaxial compression tests and related to relative density, as shown in Figure 2-15.

Table 2.2 Representative values of friction angle for sands and silts (Terzaghi et alii, 1967)

Soil	ϕ' (Degrees)	
	Loose	Dense
Sand, round grains, uniform	27.5	34
Sand, angular grains, well graded	33	45
Sandy gravels	35	50
Silty sand	27–33	30–34
Inorganic silt	27–30	30–35

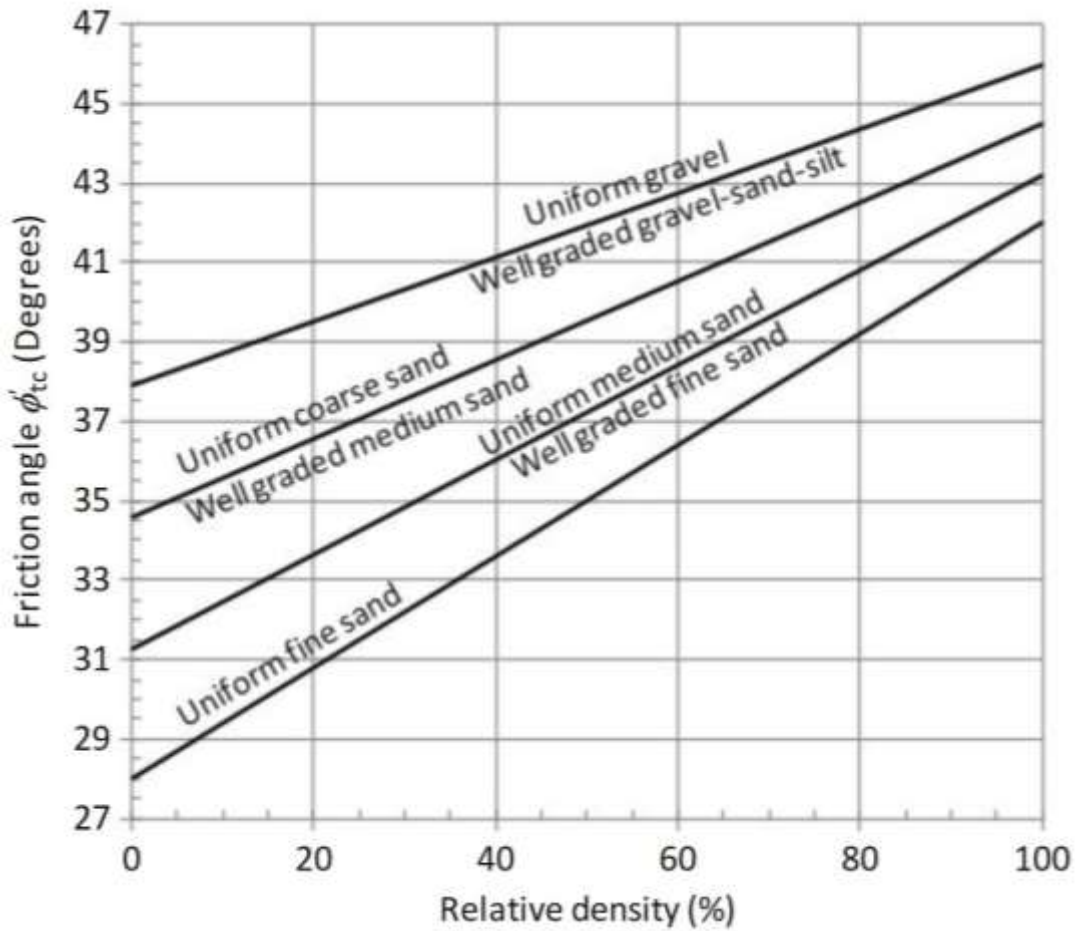


Figure 2-15 Relations between friction angle and relative density according to Schmertmann et alii (1978)

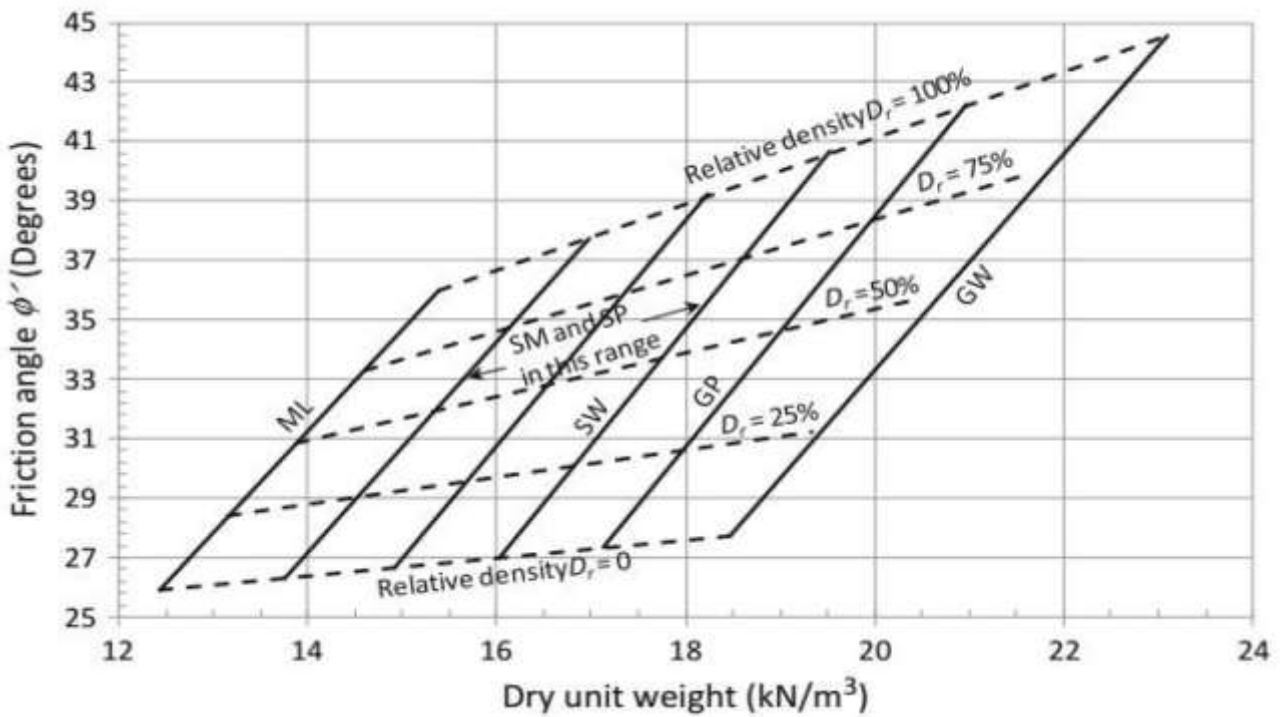


Figure 2-16 Relations between USCS class, unit weight and friction angle according to NAVFAC (1986)

Figure 2-16 shows the friction angle determined from triaxial compression tests for different granular soils without plastic fines. Here, the friction angle is related to the USCS class, relative density and unit weight (NAVFAC, 1986). Since sampling for the grain size laboratory analysis as well as determination of the unit weight are logistically feasible even at regional scale, in this work the angle of friction was estimated using the diagram proposed by NAVFAC (1986).

2.4.4.3 Slope Deposits Engineering Geological Units

The Slope Deposits Engineering Geological Units map is a raster format file summarizing all the geotechnical information for the implementation of the physically based model of shallow landslide susceptibility. As previously described, each BLU was split into clusters on morphometric basis to which a depth class, a range of friction angle and a range of dry unit weight are assigned. The depth class is attributed on the basis of the frequency of field measurements, i.e. by crossing the depth measurements acquired in situ with the morphometric units assigning the most frequently measured depth class. Since laboratory results are not enough to adequately populate each morphometric unit, the approach that is used involves also the grain size estimated in the field. Once from the laboratory analyses for each observation site the USCS class has been determined, the statistical distribution at BLU scale is analysed, in order to obtain a simplified classification consisting of the three most frequent USCS classes of gravels, sand and fine. Even though this grouping process implies losing some detail, it allows to integrate the laboratory data with the field data based on the USDA estimations and obtain a larger dataset. In fact, for each grain size estimation performed on the field, one of the three classes are attributed according to the percentages of gravel, sand and fine material.

From the laboratory results the range of variability of the friction angle (NAVFAC) and dry unit weight for each of the three simplified USCS classes are calculated.

At this point, having available the simplified USCS classes resulting from both the laboratory analyses and those of the field estimates, these data are intersected with the morphometric classes, building a matrix in which each column represents a morphometric unit and each row a simplified USCS class. This table is populated by counting the frequency of occurrence of simplified USCS classes for each morphometric unit coupling laboratory and field data. To obtain the friction angle and dry unit weight values for each morphometric unit, a weighted average is made between the frequency of the simplified USCS class and the range of variability of the parameters obtained from laboratory analyses.

An example of the attribute table of the EGU map is may be structured as follows (Table 2.3).

Table 2.3 Example of attribute table of the EGU map

EGU	Depth class (min)	Depth class (max)	Friction Angle (min)	Friction Angle (max)	Dry Unit weight (min)	Dry Unit weight (max)
1	30	60	28	30	1850	1920
2	90	120	27	31	1820	1980
n	

2.5 BEDROCK GEOMECHANICAL CHARACTERIZATION

2.5.1 Rock mass geo-mechanical survey

2.5.1.1 Schmidt hammer rebound value test

The Schmidt Hammer (SH), manufactured by Proceq in Zurich, Switzerland (S. Proceq, 1977), is one of the most popular, portable and non/destructive tools for the determination of rock hardness. Since the last century, this tool was correlated with the Uniaxial Compressive Strength (UCS) in order to obtain easier, rapid and cheaper UCS value in respect to laboratory tests (Deere and Miller, 1966; Aufmuth, 1973; Beverly et al., 1979; Haramy and DeMarco, 1985; Karaman et al., 2002; Aydin and Basu, 2005; Karaman and Kesimal, 2015).

The apparatus consists of a spring-loaded piston which is released when a plunger is pressed against a surface (Figure 2-17a-b). Here, the spring energy is transferred to the material through the impact of a piston onto the plunger. The extent to which this energy is recovered depends on the hardness of the material, which is expressed as a percentage of the maximum stretched length of the key spring before the release of the piston to its length after the rebound (R) (Aydin and Basu, 2005). Part of the piston energy is consumed by deformation within rock while the remain energy represents the impact penetration resistance (the hardness) of the surface. The measurable hardness (R value) ranges between 10 and 100. When the rock is too weak, the instrument goes full scale without returning values, thus censoring the values $R < 10$. Basing on impact energy and therefore the different kind of material (hardness) to be measured, there are two types of Schmidt Hammer, the L-type, with 0.735 Nm impact energy, and N-type, 2.207 Nm. If most of the rocks to be investigated are not very hard rocks (UCS > 100 Mpa; ISRM, 2007), the L-type SH should be preferred, according to ASTM D5873-14.

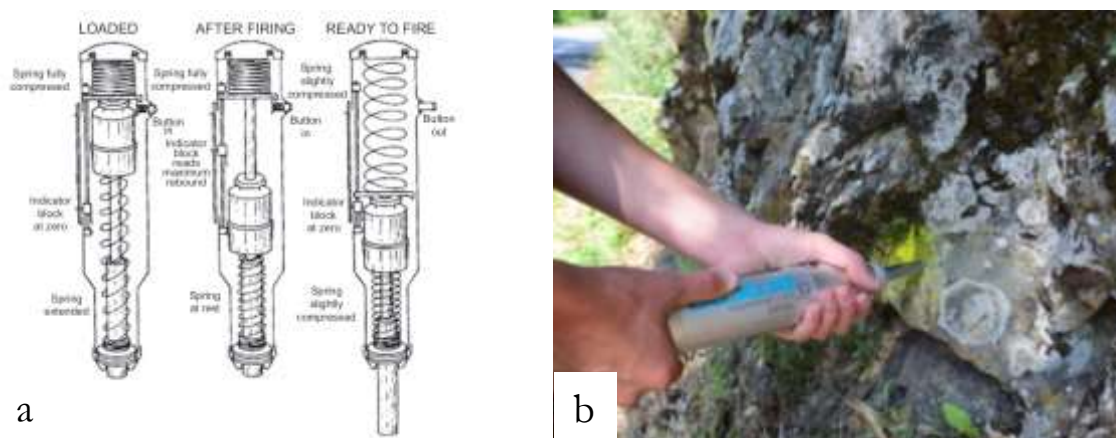


Figure 2-17 Schmidt Hammer. a. Working principles (from Adnan Aydin, 2008). b. Execution of the test in a natural outcrop

There are various Schmidt hammer measurements recording methods in the literature. Some existing Schmidt hammer test procedures are listed in Table 2.4. Most authors have proposed test procedures based on single impacts, while other authors have recommended test procedures based on repeated impacts at a point. While some methods consider the average of the R upper values. In the work of Goktan and Gunes (2005), who studied the correlation between the SH test procedures and the UCS of some rock type obtained by laboratory tests, it was found that incorporating all the measured values rather than selecting only the peak values gives a better representation of overall rock hardness and hence a better prediction of the UCS, provided the outliers are statistically discarded. In detail, these authors performed the test on tunnel faces using a Proceq N-type hammer. They applied a repeated impact method for each point, collecting 15-20 impacts and discarding the lowest value only if it satisfied Chauvenet's criterion and they compared this results with other 2 different test procedures selecting the peak rebound value from continuous impacts at a point and discarding the rest. Their results showed that the SH test procedures that are based on continuous impacts at a point provide more reliable and accurate predictions of the UCS than those that are based on single impacts and they also suggest that incorporating all the measurements at one point gives better results in predicting the UCS rather than using only the higher values.

A similar approach has been used by Karaman and Kesimal (2015) in which they perform the measurements with the SH on laboratory samples by proposing three different procedures for acquiring the rebound values and comparing them with four of the procedures most used in the literature. The statistical test results show that a strong relationship ($R^2 > 0.9$) was found between the rebound value and the UCS value for all the procedures adopted. This means that, for analyzes conducted on rock specimens in laboratory, different procedures can lead to negligible differences.

In Karaman et alii (2002), using a N-type Schmidt hammer and analyzing hard rocks, the authors investigate the differences between the rebound values acquired in the field and in the laboratory on rock specimens. The results show that the correlation between the measurements acquired in the field and those acquired in laboratory has a correlation value close to or greater than 0.9. These authors, since a slight discrepancy between the two tests exists, propose to use their correlation equation to correct the rebound values if the test is performed in the field or laboratory.

Since the aim of the method proposed here is not to characterize a rock specimen or an intact portion of the rock mass but the entire mass composed of more or less intact portions, as well as discontinuities, to take into account natural variability of a rock outcrop, the testing strategy consisted on the design of a grid, made up of 20 nodes arranged at a distance of about one metre from each other (Figure 2-18).

Table 2.4 Some recommended Schmidt hammer test procedures (from Karaman and Kesimal, 2015)

Author	Test procedure
ISRM (1978, 2007)	Record 20 rebound values from single impacts separated by at least a plunger diameter, and average the upper ten values
ASTM (2001)	Record ten rebound values from single impacts separated by at least the diameter of the piston, and discard readings differing from the average of ten readings by more than seven units and determine the average of the remaining readings
USBR (1998)	Ten readings at various locations on each surface. Discard the five lowest readings, and average the highest five
Sumner and Nel (2002)	Take 15 readings at different points and discard five great outliers to obtain a mean value from the remaining ten values
Aydin (2009)	20 Rebound values should be recorded from single impacts separated by at least a plunger diameter. The test may be stopped when any ten subsequent readings differ only by four (corresponding to R repeatability range of ± 2)
Soiltest Inc. (1976)	Record 15 rebound values from single impacts and average the highest ten. The maximum deviation from the mean should be less than 2.5
Kazi and Al-Mansour (1980)	Record at least 35 rebound readings, drop the ten lowest readings and average the remaining 25
Goktan and Ayday (1993)	Record 20 rebound values from single impacts separated by at least a plunger diameter. Reject outlier values by using Chauvenet's criterion, and average the remaining readings.
Katz et al. (2000)	Perform 32–40 individual impacts and average the upper 50 %
Deere and Miller (1966)	Record three readings along the length of an NX-size core for each 45° rotation. Average a total of 24 readings, disregarding the erroneous readings
Fowell and McFeath Smith (1976)	Take the mean of the last five values from ten continuous impacts at a point.

For each node, 20 SH single impact measures of R were acquired, following the procedure suggested by Aydin (2009). Therefore, for each outcrop, about 400 measures of R distributed all over the outcrop were acquired and reported in the database. Of course, when the outcrop was too small (4-5 meters), a smaller number of nodes were tested, with a minimum of 12 nodes.

All the testing procedures listed in Table 2.4, reject the low full-scale values. When a rock is weak due to its nature or weathering, the SH rebound values may be often lower than 10. Usually, these measures are discarded, and this implies a general overestimation of the rock quality. In this work, if a rock mass displays local weaknesses and the SH provides low full-scale rebound values, the % of measurements $R < 10$ is recorded. The motivation lies in the fact that by registering the number of times for each node

in which SH goes to low full-scale, it is possible to identify local weakness zones with a worse mechanical behaviour. In doing so, the tendency is to be prudential in determining the hardness of the rock mass.



Figure 2-18 An example of testing grid with 20 nodes

2.5.1.2 Normalization of SH rebound values

Rock surfaces in the field generally have a direction that is not vertical. Rebound values of the SH are influenced by the gravitational force if the hammer has a non-horizontal impact direction. In this case, rebound values should be normalized using the correction curves provided by the manufacturer.

Barton and Choubey (1977) proposed a correction chart for the L-type hammer based on data furnished by the manufacturer. According to Kolaiti and Papadopoulos (1994) the corrections provided by the SH manufacturers were derived empirically for a certain material with a relatively narrow range of mechanical properties, and their application was limited to two or four impact directions. A new, more accurate normalization method was proposed by Basu and Aydin (2004) where the authors verify its applicability to a wider range of rocks.

The assumption of this method is that the square of the rebound velocity is proportional to the impact energy. In the horizontal impact direction, energy released by the key spring is equal to the piston's kinetic energy with which it is released onto the plunger:

Equation 2-3

$$0.5kx_1^2 = 0.5MV_1^2$$

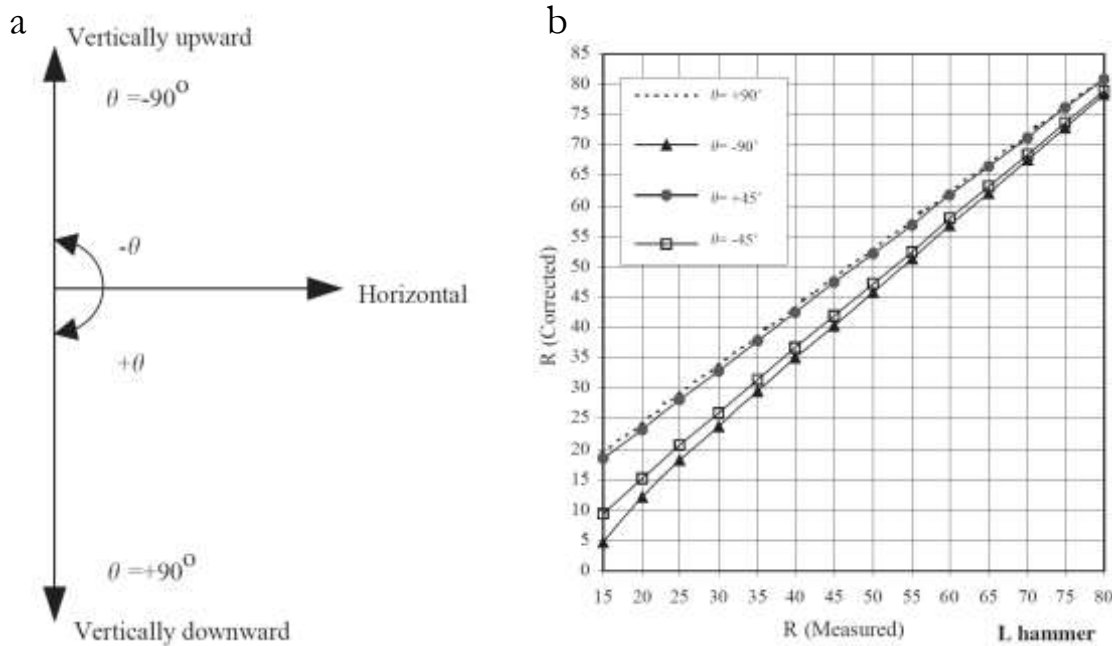


Figure 2-19 a. Schmidt hammer impact direction. b. Normalization curves with reference to horizontal direction (Basu and Aydin, 2004)

in which k is the key spring constant, x_1 the maximum stretch of the spring, M is mass of the piston and V_1 the velocity of the piston when it touches the plunger.

Likewise, the piston's kinetic energy at the instant rebound starts must be equal to the energy of the key spring stretched by x_2 at maximum rebound position:

Equation 2-4

$$0.5kx_2^2 = 0.5MV_2^2$$

Combining the above equations, we have:

Equation 2-5

$$R_h = \frac{x_2}{x_1 * 100}$$

In Figure 2-19 the normalization curves referred to the horizontal direction are reported. Normalized rebound values were used to calculate the average for each node ($\overline{R_n}$), in turn used to calculate site (rock mass) statistics (average, standard dev., median, quartiles, interquartile range,).

2.5.1.3 Discontinuity analysis

The term discontinuity or joint is used widely in rock engineering to describe any measurable interruption of a rock mass. It is often used to the exclusion of geologically more acceptable terms such as bedding, lamination, fault and joint, in order to emphasize the importance of the existence of discontinuities in controlling the engineering behavior of rock masses, rather than their genesis (Farmer, 1983).

The frequency, persistence and conditions of discontinuities affect directly the strength and stability of rock mass (Hack, 1997). For this reason, the recognition and the recording of major discontinuity sets is an important information to collect in the field. The main discontinuities that can be recognized in a rock outcrop are layering or schistosity planes, joints and fractures, metric scale shear planes and faults. When these structures are recognized in the rock mass under examination, through the use of a compass, the orientation, inclination and spacing are measured.

Joints data are subsequently processed for the calculation of the J_v (Volumetric Joint Count), introduced by Palmstrom (1982). The volumetric joint count is an estimate for the number of joints intersecting a volume of 1 m^3 of rock mass. It is defined as number of joints per m^3 and is calculated as follows:

$$J_v = \frac{1}{S_1} + \frac{1}{S_2} \dots + \frac{1}{S_n}$$

where S is the average spacing (m) of discontinuities.

2.5.1.4 Geological Strength Index

The strength of a jointed rock mass depends on the properties of the intact rock pieces, the freedom of these pieces to slide and rotate under different stress conditions and the properties of discontinuities. The freedom of pieces is controlled by their geometrical shape as well as the condition of the surfaces separating the pieces. Angular rock pieces with clean, rough discontinuity surfaces will result in a much stronger rock mass than one which contains rounded particles surrounded by weathered and altered material (Hoek, 2000). In order to semi-quantitatively classify rock masses the Geological Strength Index (GSI) was used, introduced by Hoek (1994), Hoek et al. (1995) and Hoek and Brown (1997). It provides a system for estimating the reduction in rock mass strength for different geological conditions as identified by field observations (Figure 2-20).

The GSI started with a purely qualitative assessment of the rock mass properties (Hoek, 1994; Hoek and Brown, 1997; Marinos and Hoek, 2000) and it was later modified and improved by many authors towards a semi-quantitative classification (Marinos and Hoek, 2001; Cai et al., 2004, 2007; Hoek and Brown, 2019). When working with flysch and heterogenous rock masses, the revised GSI classification (Figure

2-21) should be adopted (Marinos, 2019) together with original GSI chart (Figure 2-20). From the GSI classification it is possible to obtain an index expressed as a range of values, which is defined by the combination of the degree of jointing and/or the composition of the rock mass with the weathering grade of the surface of discontinuities.

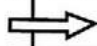
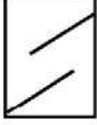





<p>GEOLOGICAL STRENGTH INDEX FOR JOINTED ROCKS</p> <p>From the lithology, structure and surface conditions of the discontinuities, estimate the average value of GSI. Do not try to be too precise. Quoting a range from 33 to 37 is more realistic than stating that GSI = 35. Note that the table does not apply to structurally controlled failures. Where weak planar structural planes are present in an unfavourable orientation with respect to the excavation face, these will dominate the rock mass behaviour. The shear strength of surfaces in rocks that are prone to deterioration as a result of changes in moisture content will be reduced if water is present. When working with rocks in the fair to very poor categories, a shift to the right may be made for wet conditions. Water pressure is dealt with by effective stress analysis</p>		SURFACE CONDITIONS				
		<p>VERY GOOD Very rough, fresh, unweathered surfaces</p>	<p>GOOD Rough, slightly weathered, iron stained surfaces</p>	<p>FAIR Smooth, moderately weathered and altered surfaces</p>	<p>POOR Slickensided, highly weathered surfaces with compact coating or fillings of angular fragments</p>	<p>VERY POOR Slickensided, highly weathered surfaces with soft clay coatings or fillings</p>
STRUCTURE		DECREASING SURFACE QUALITY 				
	INTACT OR MASSIVE- Intact rock specimens or massive in-situ rock with few widely spaced discontinuities	90			N/A	N/A
	BLOCKY - Well interlocked undisturbed rock mass consisting of cubical blocks formed by three intersecting discontinuity sets	80	70			
	VERY BLOCKY - Interlocked, partially disturbed mass with multi-faceted angular blocks formed by 4 or more joint sets		60	50		
	BLOCKY/DISTURBED/SEAMY - Folded with angular blocks formed by many intersecting discontinuity sets. Persistence of bedding planes or schistosity			40		
	DISINTEGRATED - Poorly interlocked, heavily broken rock mass with mixture of angular and rounded rock pieces				30	
	LAMINATED/SHEARED - Lack of blockiness due to close spacing of the weak schistosity or shear planes					20
						10
		N/A	N/A			

Figure 2-20 Geological Strength Index proposed by Marinos & Hoek (2000)

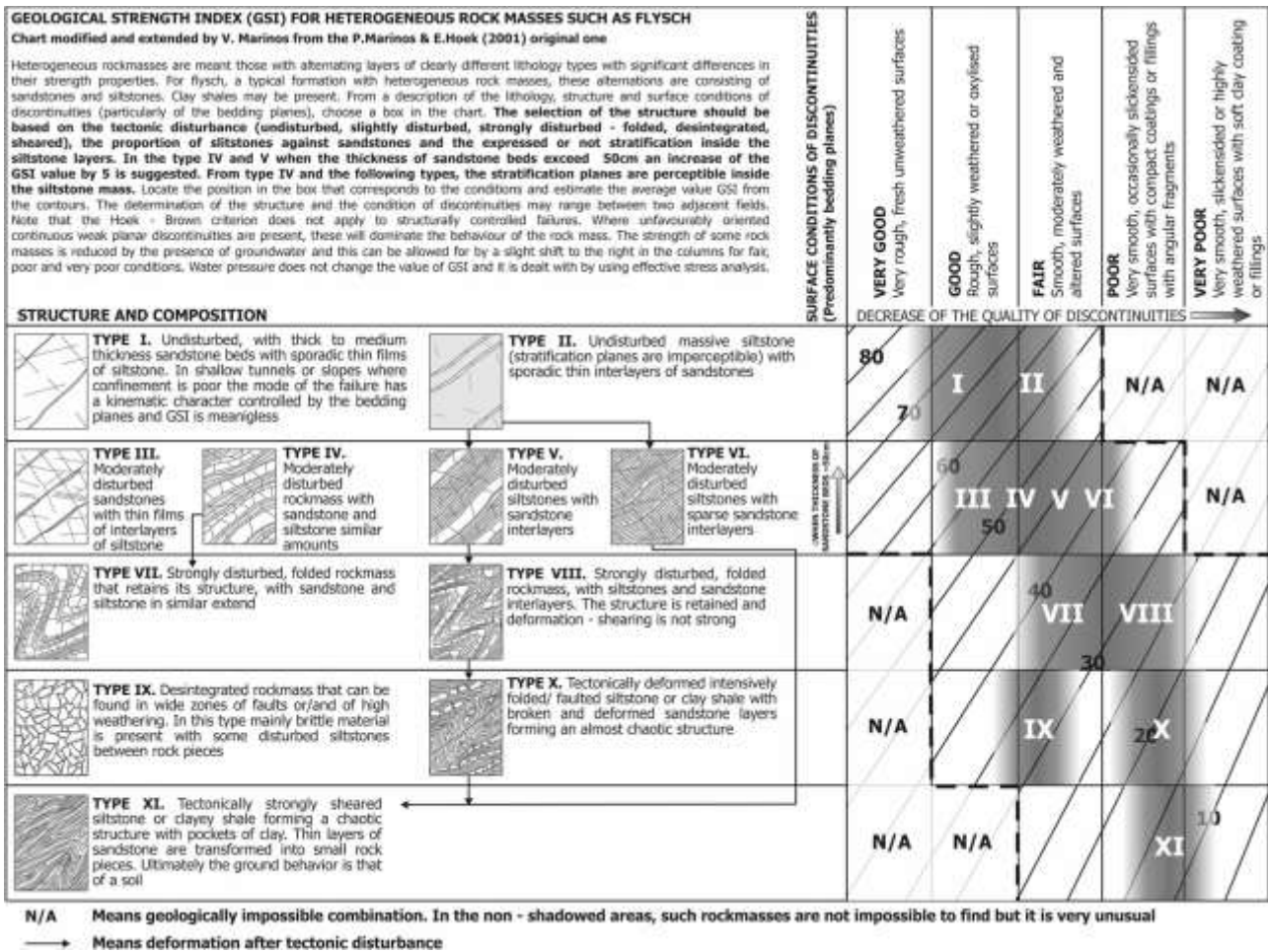


Figure 2-21 The new, revised, geotechnical classification GSI system for tectonically disturbed heterogeneous rock masses, such as flysch.

2.5.2 Unit weight determination

The last phase of rock mass field survey consists on the collection of rock samples for the unit weight laboratory determination. In this work, the unit weight is determined using the Hydrostatic Weighing method, according to ASTM - D2937.

The weight of the sample in air is compared to the weight of the sample immersed in a liquid of known density (usually water). Generally, the sample is divided in about 10 fragments having mass not less than 50 g and minimum size not less than 10 times the maximum diameter of the rock grains constituents. After weighing the sample in air, it is dried in an oven at 110°, in order to determine the dry unit weight. Then, the sample surface is sealed with wax coating and then weighed in water. Each sample is divided in 5 small blocks and for each block a series of 5 repeated weigh are performed in order to test repeatability of the laboratory testing.

2.5.3 Cluster and Outlier Analysis (*Anselin Local Moran's Index*)

Local Moran's Index (LMI) is a local spatial autocorrelation statistics based on the Moran's Index (Moran, 1948). It was developed by Anselin (1995) as a local indicator of spatial association. The Local Moran's I for each observation gives an indication of the extent of significant spatial clustering of similar values around that observation; the sum of LMI for all observations is proportional to a global indicator of spatial association (Global Moran's Index). The Local Moran's Index estimates the similarity in x (the variable to be spatialized) between observation i and observations j in the neighbourhood of i defined by a matrix of weights w_{ij} . The statistics, provided by Anselin (1995), is calculated as:

Equation 2-6

$$I_i = \left[\frac{z_i}{\left(\frac{\sum_i z_i^2}{n} \right)} \right] \sum_j w_{ij} \times z_j$$

Where $z_i = x_i - \bar{x}$

In essence, Equation 2-6 standardizes value x for observation i to determine if it is high or low relative to the mean, and standardizes values of x for j to determine if the neighbourhood is high or low relative to the mean. The standardization operates in a similar manner as a statistical z-score that compares observations to the mean in order to determine the observations' relative position within a distribution. In the absence of such standardization, the resulting Moran's I values would be disproportionately influenced by extreme values of severity. Multiplying the standardized value x for observation i and the neighbourhood j produces a scalar Moran's I value (Bone et al., 2013). A positive value for I indicates that a feature has neighbouring features with similarly high or low attribute values; this feature is part of a cluster. A negative value for I indicates that a feature has neighbouring features with dissimilar values; this feature is an outlier. The output of the computation consists of four categories representing the relationship between each point and its neighbours: Low/Low, High/Low, Low/High, and High/High. The clusters are two, Low/Low and High/High, while High/Low and Low/High are the outliers. Note that not all Moran's I values are significant: a test of significance is computed for each point to determine if the spatial relationship is significant given a specified level of confidence, e.g. in the function implemented in ArcGIS®, statistical significance is set at the 95 percent confidence level (Mitchell, 2005). The output of this tool is a new output feature class with the following attributes for each feature in the input feature class: local Moran's I index, z-score, p-value, and the COType (cluster/outlier type) (ESRI, 2013).

In respect to bedrock properties, SD properties are often linked with morphometry (Florinsky et al., 2002; Guimaraes et al., 2003; Seibert et al., 2007; Zhang et al., 2012). Nevertheless, bedrock properties are not spatially constant, therefore it is useful to conduct an objective spatial analysis in order to verify large regions with different bedrock properties.

The Anselin Local Moran's clustering method allows to spatially verify if each bedrock property display a dispersed or a clustered pattern. In order to attribute spatially distributed geotechnical parameters, if a variable does not show a spatial autocorrelation, this should be excluded from multivariate cluster analysis (described in paragraph 2.5.4) as it is irrelevant. On the contrary, if the variables give a positive outcome to spatial autocorrelation, these must be taken into account for multivariate analysis. If two or more variables show an almost identical clustering in multivariate analysis, it would be necessary to exclude them and keep only one. Finally, if no variable shows clustering, the geotechnical parameters can be the same for the whole survey area.

2.5.4 Multi-variate cluster analysis

The multi-variate spatial cluster analysis can be performed using the Grouping Analysis tool implemented in ESRI ArcGIS™, which groups features based on feature attributes and spatial constraints.

The theory of minimum spanning tree (Boruvka, 1926; Kruskal, 1956; Prim, 1957) is used in order to split the dataset into clusters. A minimum spanning tree can be defined as a subset of edges connecting vertices of a connectivity graph, in which the sum of the weights of the edges is the minimum possible. Given a set of points in space, each vertex (v) is connected to the nearest vertices by edges (l), each edge has a weight (or cost) which depends on how much the attribute of each vertex is dissimilar from the adjacent one. The cost $d(i,j)$ between the edges i and j is the square of the Euclidean distance between the attribute vectors x_i and x_j (Assunção et al., 2006):

Equation 2-7

$$d(i,j) = \sum_{l=1}^n (x_{il} - x_{jl})^2$$

A minimum spanning tree (MST) is the resulting connectivity graph of the edges with minimum cost, where the cost is measured as the sum of the dissimilarities over all the edges of the tree. In order to obtain clusters, the MST must be split removing the edges with the maximum cost.

The ArcGIS™ tool Grouping Analysis is implemented in this way: suppose you want to split a dataset into four spatially contiguous groups. The tool will create a minimum spanning tree reflecting both the spatial structure of features and their associated analysis field values. The tool then determines the best place to cut the tree to create two separate groupings. Next, it decides which one of the two resultant

groups should be divided to yield the best three group solution. One of the two groups will be divided, the other group remains intact. Finally, it determines which of the resultant three groupings should be divided in order to provide the best four group solutions. For each step, the best solution is the one that maximizes both within-group similarity and between-group difference (ESRI, 2016). In order to constrain spatial relationships among features in the groups created, the Grouping Analysis tool allow to specify a spatial constrain. In this thesis the K nearest neighbours spatial constrain was used. The published method employed in Grouping Analysis is called SKATER (Spatial "K"luster Analysis by Tree Edge Removal), proposed by Assunção et alii (2006).

The grouping effectiveness is measured using the Calinski-Harabasz pseudo F-statistic (Caliński and Harabasz, 1974), which is a ratio reflecting within-group similarity and between-group difference:

Equation 2-8

$$\frac{\left(\frac{R^2}{n_c - 1}\right)}{\left(\frac{1 - R^2}{n - n_c}\right)}$$

Where

$$R^2 = \frac{SST - SSE}{SST}$$

The SST represents between-group differences while SSE within group similarity, and these are respectively expressed as:

Equation 2-9

$$SST = \sum_{x=1}^{n_c} \sum_{y=1}^{n_x} \sum_{k=1}^{n_v} (V_{xy}^k - \bar{V}^k)^2$$

$$SSE = \sum_{x=1}^{n_c} \sum_{y=1}^{n_x} \sum_{k=1}^{n_v} (V_{xy}^k - \bar{V}_t^k)^2$$

Where

n the number of features

n_x the number of features in group x

n_c the number of classes (groups)

n_v the number of variables used to group features

V_{xy}^k the value of the k th variable of the y th feature in the x th group

V^k the mean value of the k th variable

V_i^k the mean value of the k th variable in group x

The output of the Grouping Analysis tool is a new output feature class containing the fields used in the analysis plus a new Integer field named SS_GROUP identifying which group each feature belongs to (ESRI, 2016). A report file can be generated, in which statistical properties of clusters are described.

Using as input data the variables showing a uni-variate spatial clustering, this tool allows to identify groups of investigation sites with similar geo-mechanical features (e.g. SH rebound value, GSI and Jv). In other words, each cluster represents a domain, namely a Bedrock Geo-mechanical Unit (GMU), to which a set of geotechnical parameters (friction angle and cohesion) will be assigned (Figure 2-22).

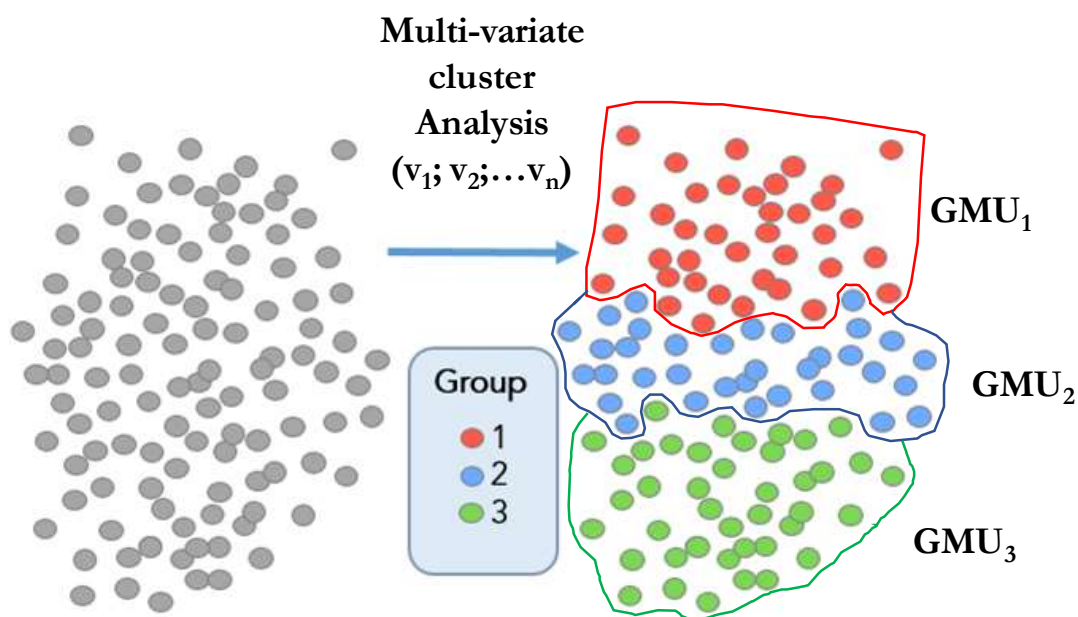


Figure 2-22 A visualization of ESRI's Grouping Analysis Tool (ESRI ArcGIS documentation). The letter "v" stands for variable.

2.5.5 Determination of Uniaxial Compressive Strength

Since the 1960s, various authors have tried to use SH to quickly, easily and economically estimate the uniaxial compressive strength (UCS) of rock masses, for different purposes (Deere and Miller, 1966; Aufmuth, 1973; Beverly et al., 1979; Haramy and DeMarco, 1985; Katz et al., 2000; Karaman et al., 2002; Yaşar and Erdoğan, 2004; Aydin and Basu, 2005; Fener et al., 2005; Shalabi et al., 2007; Kılıç and Teymen, 2008; Yilmaz, 2009a; Aydin, 2009; Moomivand, 2011; Mishra and Basu, 2013; Karaman and Kesimal, 2015; Armaghani et al., 2016; Hebib et al., 2017; Kong and Shang, 2018; Wang and Wan, 2019a). These studies have correlated the rebound value with the UCS measured by laboratory tests on rock samples..

The great advantage of using the SH to calculate the UCS of a rock mass is due to its easy and rapid execution, and if measurements follow an acquisition scheme as described in the previous chapter, the UCS statistics may describe the outcrop as a whole.

In fact, laboratory tests give accurate and acceptable results of the uniaxial compressive strength but are sample-specific estimations for rock mass assessments. A rock mass is inhomogeneous and uniaxial compressive strength of rock can vary at meter-scale (Moomivand, 2011): parameters such as mineral composition, rock compaction, weathering, and tectonic are likely to have a major influence on the results (Aydin, 2009; Hebib et al., 2017). Therefore, the measured uniaxial compressive strength of limited number of specimens tested in the laboratory can't describe the variability of UCS for all parts of in-situ rock mass. The SH rebound test is a useful method of estimating the variability of rock mass strength particularly in situations where large numbers of laboratory tests would be necessary.

In Table 2.5, a few R-UCS correlations from the literature are presented. This table includes the works where the L-type Schmidt's hammer was used and the test was performed on various rock types or, for the same lithology, different degrees of weathering. For other correlations, please consult Aydin and Basu (2005), Karaman and Kesimal (2015) and Wang and Wan (2019), and references therein.

The relationships are expressed by power, exponential or linear functions. In a number of these functions, rebound value (the main independent variable) is multiplied with dry density (introduced as a second variable) in an effort to improve the correlations. For example, in Figure 2-23, using the correlation proposed by Deere and Miller (1966), three synthetic exponential curves are calculated varying the dry unit weight value. It is worth to note that unit weight influences the obtained value of UCS, increasing SH rebound value, increase UCS variability for different unit weight.

All the proposed correlation listed in Table 2.5 are experimentally determined, except for the last one, proposed by Wang and Wan (2019), where the authors collect laboratory data from 18 references and apply a regression analysis in order to obtain the best fit curve. In Figure 2-24 the proposed correlation listed in Table 2.5 are plotted.

Table 2.5 Relations of rebound value with uniaxial compressive strength. UCS (uniaxial compressive strength, MPa); γ (Unit weight, gr/cm³). Hammer inclination: V, vertical; H, horizontal. When the data is not specified, n.s. is written.

References	Tested rocks	Hammer inclination	Proposed correlations	r / R ²	Validity range	
					UCS	R
Deere and Miller (1966)	28	V	$UCS = 9.97 * e^{(0.02*R*\gamma)}$	0.94	22-358	23-59
Aufmuth (1973)	25	n.s.	$UCS = 0.33 * (R * \gamma)^{1.35}$	0.80	12-362	10-54
Beverly et al. (1979)	20	n.s.	$UCS = 12.74 * e^{(0.02*R*\gamma)}$	n.s.	38-218	n.s.
Aydin and Basu (2005)	Granites	H	$UCS = 1.45 * e^{(0.07*R)}$	0.92	6-196	20-65
Torabi et al. (2011)	Sedimentary	V	$UCS = 0.046R^2 - 0.175R + 27.7$	0.86	25-224	16-67
Moomivand (2011)	104	n.s.	$UCS = 11.324 * e^{(0.0175*R*\gamma)}$	0.92	25-370	n.s.
Mishra and Basu (2013)	Schists, sandstones, granites	V	$UCS = 2.38 * e^{0.065*R}$	0.87	20-180	25-65
Karaman and Kesimal (2015)	47	V	$UCS = 0.138 * R^{1.743}$	0.91	8-215	10-64
Selçuk and Yabalak (2015)	11	V	$UCS = 0.007 * R^{2.443}$	0.92	5-120	10-43
Hebib et al. (2017)	19 sedimentary	n.s.	$UCS = 3.98 * e^{0.023*R*\gamma}$	0.87	5-140	15-60
Wang and Wan (2019)	18 references	-	$UCS = \left(\frac{6222}{88.15 - R} \right) - 70.38$	0.6	n.s.	n.s.

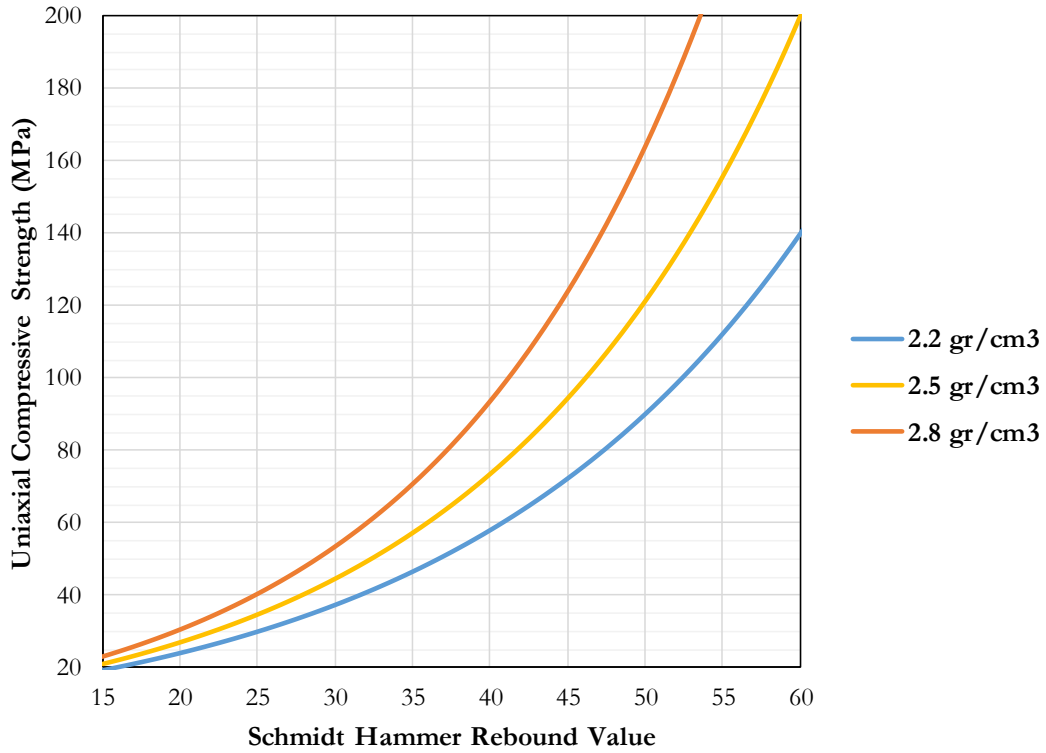


Figure 2-23 Rebound value and UCS correlation varying the dry unit weight, according to Deere And Miller (1966) correlation.

Some Rv and UCS correlations available in the literature

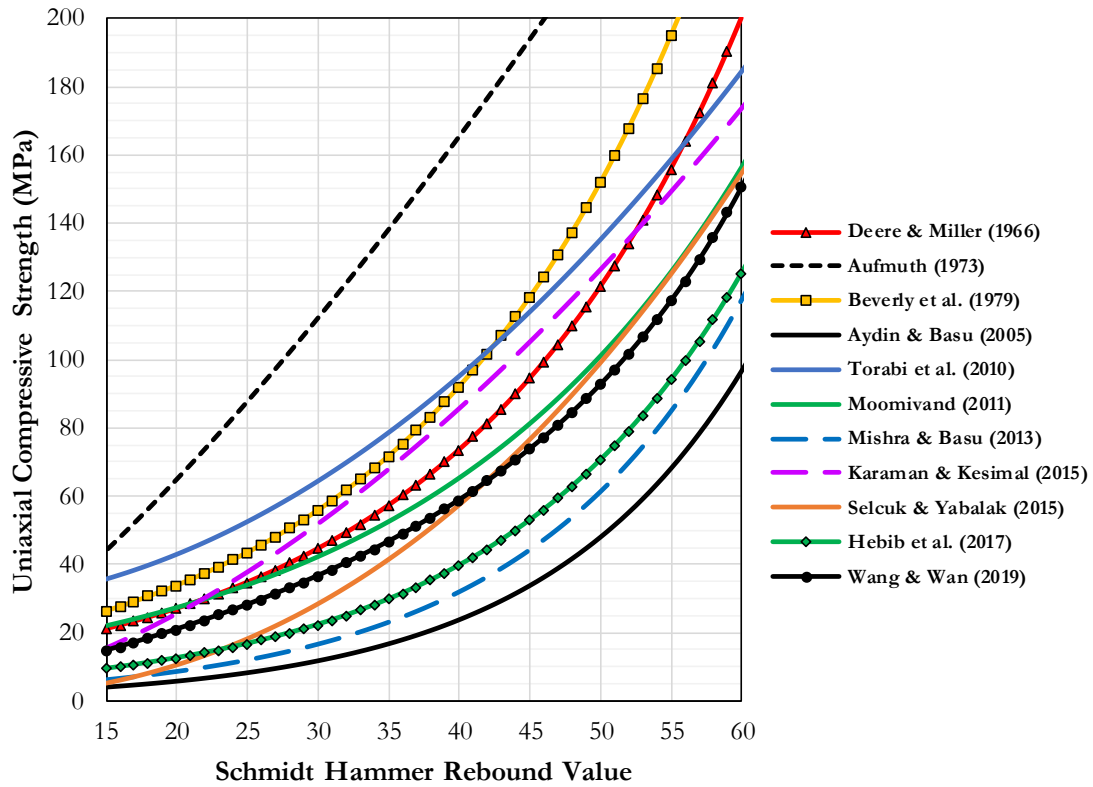


Figure 2-24 Bibliographic correlation curves for UCS prediction from rebound value.

In this work, the correlation proposed by Deere and Miller (1966) have been used to calculate the UCS, using the \overline{Rv} value, obtained averaging 400 measures and site-specific dry unit weight.

2.5.6 Estimation of shear strength of a rock mass

A widely used criterion to estimate rock mass strength is the non-linear Generalized Hoek–Brown (GHB) failure criterion (Hoek et al., 2002) since it is able to estimate the shear strength of various types of intact rock and rock masses (Priest, 2005). If the GHB criterion is used in conjunction with limit equilibrium method for analyzing the slope stability, methods are required to determine the equivalent MC shear strength parameters cohesion and angle of friction at the specified normal stress σ_n from the GHB criterion (Shen et al., 2012).

The original non-linear- Hoek—Brown criterion (Hoek & Brown, 1980) has been widely used for rock engineering for the past three decades, and it was renewed by Hoek et alii (2002), as:

Equation 2-10

$$\sigma_1 = \sigma_3 + \sigma_{ci} \left(\frac{m_b \sigma_3}{\sigma_{ci}} + s \right)^a$$

where σ_1 and σ_3 are the major and minor principal stresses, σ_{ci} is the uniaxial compressive strength of the intact rock mass and m_b , s and a are the Hoek–Brown input parameters which can be estimated from the GSI for the rock mass, given by:

Equation 2-11

$$m_b = m_i e^{\frac{GSI-100}{28-14D}}$$

Equation 2-12

$$s = e^{\frac{GSI-100}{9-3D}}$$

Equation 2-13

$$a = 0.5 + \frac{e^{\frac{-GSI}{15}} - e^{\frac{-20}{3}}}{6}$$

in which m_i is the Hoek–Brown constant for intact rock mass (Figure 2-25), D is the disturbance factor (Figure 2-26). In Figure 2-27 and Figure 2-28 the relationships between GSI, m_b , a and s are reported.

Rock type	Class	Group	Texture			
			Coarse	Medium	Fine	Very fine
SEDIMENTARY	Clastic		Conglomerates (21 ± 3) Breccias (19 ± 5)	Sandstones 17 ± 4	Siltstones 7 ± 2 Greywackes (18 ± 3)	Claystones 4 ± 2 Shales (6 ± 2) Marls (7 ± 2)
		Non-Clastic	Carbonates	Crystalline Limestone (12 ± 3)	Sparitic Limestones (10 ± 2)	Micritic Limestones (9 ± 2)
	Evaporites			Gypsum 8 ± 2	Anhydrite 12 ± 2	
	Organic					Chalk 7 ± 2
METAMORPHIC	Non Foliated		Marble 9 ± 3	Hornfels (19 ± 4) Metasandstone (19 ± 3)	Quartzites 20 ± 3	
	Slightly foliated		Migmatite (29 ± 3)	Amphibolites 26 ± 6	Gneiss 28 ± 5	
	Foliated*			Schists 12 ± 3	Phyllites (7 ± 3)	Slates 7 ± 4
IGNEOUS	Plutonic	Light	Granite 32 ± 3 Diorite 25 ± 5 Granodiorite (29 ± 3)			
		Dark	Gabbro 27 ± 3 Norite 20 ± 5	Dolerite (16 ± 5)		
	Hypabyssal			Porphyries (20 ± 5)	Diabase (15 ± 5)	Peridotite (25 ± 5)
	Volcanic	Lava		Rhyolite (25 ± 5) Andesite 25 ± 5	Dacite (25 ± 3) Basalt (25 ± 5)	
		Pyroclastic	Agglomerate (19 ± 3)	Volcanic breccia (19 ± 5)	Tuff (13 ± 5)	

* These values are for intact rock specimens tested normal to bedding or foliation. The value of m_i will be significantly different if failure occurs along a weakness plane.

Figure 2-25 Values of the constant m_i for intact rock, by rock group. (from Marinos and Hoek 2001)


The disturbance factor D should never be applied to the entire rock mass surrounding an excavation		
Appearance of rock mass	Description of rock mass	Suggested value of D
	Excellent quality-controlled blasting or excavation by a road-header or tunnel boring machine results in minimal disturbance to the confined rock mass surrounding a tunnel. The blasting designs for this tunnel is discussed in http://www.rncscience.com/assets/resources/learning/hoek/Practical-Rock-Engineering-Chapter-16-Blasting-Damage-in-Rock.pdf	$D = 0$
	Mechanical or manual excavation in poor quality rock masses gives minimal disturbance to the surrounding rock mass. Where squeezing problems result in significant floor heave, disturbance can be severe unless a temporary invert, as shown in the photograph, is placed.	$D = 0$ $D = 0.5$ with no invert
	Poor control of drilling alignment, charge design and detonation sequencing results in very poor blasting in a hard rock tunnel with severe damage, extending 2 or 3 m, in the surrounding rock mass.	$D = 1.0$ at surface with a linear decrease to $D = 0$ at ± 2 m into the surrounding rock mass
	Small-scale blasting in civil engineering slopes results in modest rock mass damage when controlled blasting is used, as shown on the left-hand side of the photograph. Uncontrolled production blasting can result in significant damage to the rock face.	$D = 0.5$ for controlled presplit or smooth wall blasting with $D = 1.0$ for production blasting
	In some weak rock masses, excavation can be carried out by ripping and dozing. Damage to the slopes is due primarily to stress relief. Very large open pit mine slopes suffer significant disturbance due to heavy production blasting and stress relief from overburden removal.	$D = 0.7$ for mechanical excavation effects of stress reduction damage $D = 1.0$ for production blasting A transitional D relationship incorporating the effects of stress relaxation can be derived from the disturbance rating*

Figure 2-26 Guidelines for estimating disturbance factor D due to stress relaxation and blasting damage. (from Hoek and Brown 2019)

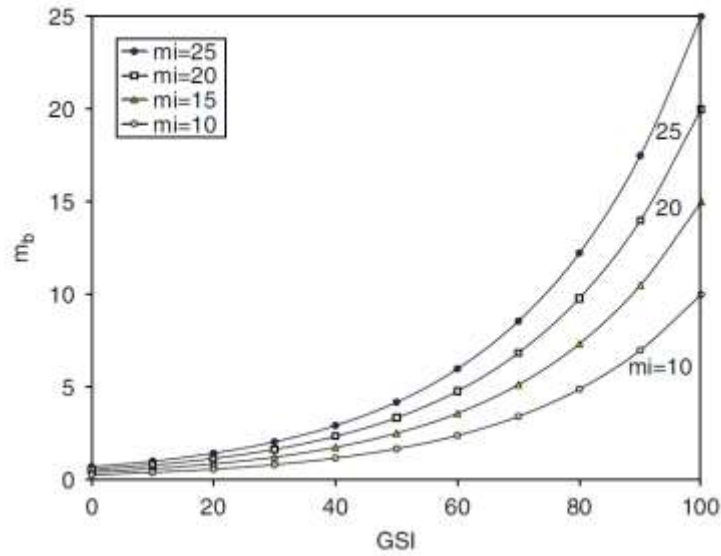


Figure 2-27 Relationship between GSI and m_b for different m_i values. (from Cai et al. 2007)

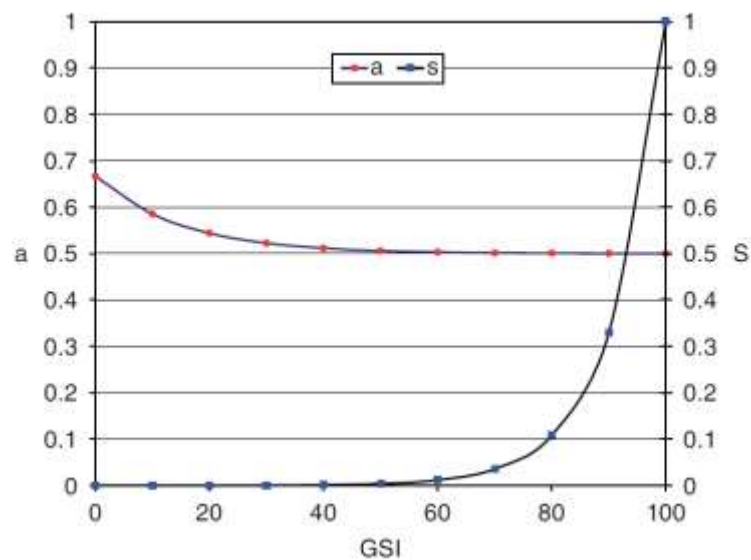


Figure 2-28 Relationship between GSI, a and s . (from Cai et al. 2007)

The GHB criterion (Equation 2-10) can also be expressed in terms of normal stress σ_n and shear stress τ on the failure plane. Figure 2-29 gives a graphical representation of the HB criterion expressed by (a) major and minor principal stresses and (b) normal and shear stresses. The equivalent MC shear strength parameters can be calculated by locating the tangent of the HB envelope with the specified normal stress σ_n , as illustrated in Figure 2-29b. The MC criterion is expressed by the equation:

Equation 2-14

$$\tau = c' + \sigma \tan \phi'$$

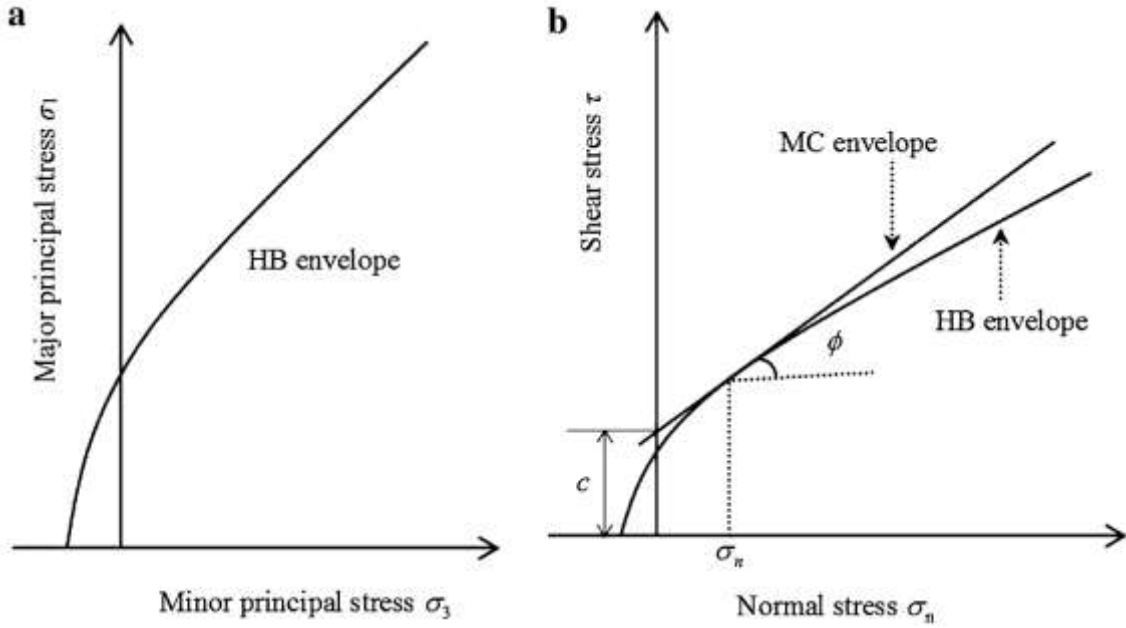


Figure 2-29 a. Major and minor principal stresses for the HB criterion. b. normal and shear stresses for the HB criterion

The Mohr-Coulomb shear strength τ , for a given normal stress σ , is found by substitution of these values of c' and ϕ' into the equation (Hoek and Brown, 1997):

Equation 2-15

$$\sigma'_1 = \frac{2c' \cos \phi'}{1 - \sin \phi'} + \frac{1 + \sin \phi'}{1 - \sin \phi'} \sigma'_3$$

According to the description above, friction angle and cohesion are calculated as follows:

Equation 2-16

$$\phi' = \sin^{-1} \left[\frac{6am_b(s + m_b \sigma'_{3n})^{a-1}}{2(1+a)(2+a) + 6am_b(s + m_b \sigma'_{3n})^{a-1}} \right]$$

Equation 2-17

$$c' = \frac{\sigma_{ci} [(1+2a)s + (1-a)m_b \sigma'_{3n}] (s + m_b \sigma'_{3n})^{a-1}}{(1+a)(2+a) \sqrt{1 + (6am_b(s + m_b \sigma'_{3n})^{a-1} / (1+a)(2+a))}}$$

Where $\sigma'_{3n} = \sigma'_{3max} / \sigma_{ci}$, and:

Equation 2-18

$$\sigma'_{cm} = \sigma_{ci} \frac{[m_b + 4s - a(m_b - 8s)] * [\frac{m_b}{4+s}]^{a-1}}{2(1+a)(2+a)}$$

Equation 2-19

$$\frac{\sigma_{3max}'}{\sigma_{cm}'} = 0.72 \left(\frac{\sigma_{cm}'}{\gamma H} \right)^{-0.91}$$

Cai et al. (2007) discussed about the calculation of equivalent residual strength parameters. Guidelines given by the GSI system are for the estimation of the peak strength of jointed rock masses. In general, rock masses, except when highly disturbed, exhibit strain-softening post-peak behaviour, the gradual loss of load-bearing capacity of a material, so that the residual strength parameters are lower than the peak parameters. The authors proposed a method to extend the GSI system for the estimation of a rock mass's residual strength. It is proposed to adjust the peak GSI to the residual GSI_r value based on the two major controlling factors in the GSI system, the residual block volume V_r^b and the residual joint condition factor J_r^c, comparing and validating the results with in-situ block shear test data from three large-scale cavern construction sites and data from a back-analysis of rock slopes. The results obtained by Cai et al. (2007) shows that the estimated residual strengths, calculated using the reduced residual GSI_r value, are in good agreement with field test or back-analyzed data.

The relation between peak GSI and residual GSI used to calculate residual strength parameters is then provided:

Equation 2-20

$$GSI_r = GSI e^{-0.0134GSI}$$

In this work, the equations reported above were implemented in a MATLAB™ code, also enabling to perform a Monte Carlo simulation of the input parameters, such as, GSI, m_i, D and σ_{ci}.

2.5.7 Bedrock Geo-mechanical Units Map

A Bedrock Geo-Mechanical Units (BMU) is a portion of the study area where the semi-quantitative data acquired in the field (R_v , GSI and J_v) have similar values of average and standard deviation, and therefore a range of Mohr-Coulomb equivalent parameters, which are significantly different to other BMU.

The BMUs are defined taking into account the result of the multivariate clustering and the expert analysis of the geological map. In practice, the clusters of observation sites are delineated following morphological characteristics, such as the drainage network and basins watersheds, tectonic feature such as faults and thrusts, and lithological characters.

Few works in the literature perform the regional spatialization of geo-mechanical characteristics of rock masses by using geostatistical methods (Ferrari, 2013; Ferrari et al., 2014; Kaewkongkaew et al., 2015; Pinheiro et al., 2016; Mammoliti, 2020). However, these methods ignore the major regional structures due to tectonic activity, past and recent, and assume that there is a gradual transition to different conditions.

The structure of the attribute table of the Bedrock Geo-mechanical Units Map implemented in this work is quite similar to the EGU map presented in Table 2.3. In this case, the fields consist on: the id code of the GMU, the range of friction angle and the effective cohesion.

2.6 SHALLOW LANDSLIDES SUSCEPTIBILITY MODELS

Assessing shallow landslide susceptibility by using data driven or physically based methods may provide different results due to the conceptually different approaches they are based on. The former is sustained by the assumption that landslides tend to occur more likely in locations with predisposing factors similar to those of areas where landslides occurred in the past, whereas the latter are based on the balancing between destabilizing forces and soil/rock strengths. In the literature, comparing between different methods to assess landslide susceptibility is not a new research topic when performed exclusively between either different data-driven (Yilmaz, 2009b; Akgun, 2012; Francipane et al., 2014; Regmi et al., 2014; Goetz et al., 2015; Pham et al., 2016; Zêzere et al., 2017) or different physically based methods (Zizioli et al., 2013; Teixeira et al., 2015; Formetta et al., 2016; Pradhan and Kim, 2016). Regarding the comparison between the predictive capability of data driven and physically based methods, less works exist (Carrara et al., 2008; Frattini et al., 2008; Cervi et al., 2010; Goetz et al., 2011). Some authors have combined the results obtained by data driven and physically based approaches obtaining interesting results (Chang and Chiang, 2009; Goetz et al., 2011; Oliveira et al., 2016). For this reasons, this thesis compares and combines the susceptibility maps obtained by using a data driven and a physically based method also introducing new insights about the relevance of bedrock geo-mechanical characterization, slope deposits depth and geotechnical characterization, and the evaluation of their uncertainty and natural variability by means of Monte Carlo simulation.

In this paragraph the theory behind landslide susceptibility models adopted in this thesis is provided.

2.6.1 SHALSTAB and PROBSS

The SHALSTAB model (Montgomery and Dietrich, 1994) is based on coupling a hydrological model to a limit-equilibrium slope stability model to calculate the critical steady-state rainfall necessary to trigger slope instability at any point in a landscape (Montgomery et al., 1998). The hydrological model consists on the analysis of upslope contributing area (flow accumulation), soil transmissivity and local slope (O'Loughlin, 1986), and is based on the assumption that water infiltrate still reaching a low conductivity layer following topographically determined flow paths. Local wetness (W) is calculated as following:

Equation 2-21

$$W = \frac{Qa}{bT\sin \theta}$$

Where Q is the steady-state rainfall (m/day), a is the contributing area (m²), b is the cell size (m), T is the SD transmissivity (m²/day) and θ is the slope steepness (degrees). If the saturated conductivity is constant with depth, the previous equation is simplified as:

Equation 2-22

$$W = \frac{h}{z}$$

Combining Equation 2-21 and Equation 2-22:

Equation 2-23

$$\frac{h}{z} = \frac{Qa}{bT \sin \theta}$$

Where h is the saturated thickness of SD layer and z is SD depth.

The infinite slope stability model adopted by the authors do not consider arching and lateral root reinforcement, for this reason the slope failure is expressed by the following limit equilibrium equation (Skempton and Delory, 1984):

Equation 2-24

$$\rho_s g z \sin \theta \cos \theta = C' + \left[\rho_s - \left(\frac{h}{z} \right) \rho_w \right] g z \cos^2 \theta \tan \varphi$$

Where

ρ_s is the bulk density of slope deposit

g is gravitational acceleration

z is soil depth

C' is effective cohesion

ρ_w is water bulk density

φ is the friction angle

Combining Equation 2-23 and Equation 2-24, and rearranging in order to obtain the critical steady-state rainfall (Q_c) needed to trigger slope failure, the SHALSTAB model equation results to be:

Equation 2-25

$$Q_c = \frac{T \sin \theta}{a/b} \left[\frac{C'}{\rho_w g z \cos^2 \theta \tan \varphi} + \frac{\rho_s}{\rho_w} \left(1 - \frac{\tan \theta}{\tan \varphi} \right) \right]$$

The SHALSTAB model provides other two scenarios, the Unconditional Stability (Unconditionally Stable, US) and the Unconditional Instability (Unconditionally Unstable, UU). A slope is considered as US when they are stable even when $W = 1$, this occur when the slope deposit layer reaches saturation and water in excess develops run-off as overland flow. This scenario is described as:

Unconditionally Stable disequation 1

$$\tan \theta < \frac{C'}{\rho_s g z \cos^2 \theta} + \left(1 - \frac{\rho_w}{\rho_s}\right) \tan \varphi$$

Instead, the UU scenario is a slope which is predicted to be unstable even without rainfall ($W = 0$). These areas are probably rock outcrops, because the slope steepness is too high to allow sediment accumulation (Montgomery et al., 1998). For this reason, a detailed and accurate slope deposit depth map is an important tool to obtain reliable results by the SHALSTAB model. The UU is expressed as:

Unconditionally Unstable disequation 2

$$\tan \theta \geq \frac{C'}{\rho_s g z \cos^2 \theta} + \tan \varphi$$

In this thesis the output susceptibility value is calculated pixel-by-pixel as the logarithm of the ratio between Q_c and T (transmissivity, m/day), as suggested by Montgomery et alii (1998). Moreover, in pixels with the Q_c or $\log Q_c/T$ is lower, these areas are interpreted as more susceptible to shallow landsliding. Conversely, where Q_c or $\log Q_c/T$ is higher, those areas are interpreted as more stable, as a less frequent rainfall event would be required to cause instability (Montgomery and Dietrich, 1994). In order to represent the effects of the natural variability and uncertainty of geotechnical parameters (ρ_s , C' and φ) as well as slope deposits depth (z), and US and UU disequations were implemented in MATLAB™ by means a Monte-Carlo simulation (Binder et al., 1993). For each pixel_i, for a large number n of iterations (ex., $n=10,000$), sets of parameters are randomly selected from ranges of values defined according to lithology, morphometric unit, field observations and laboratory analyses. As a first step, for the pixel_i the code verifies if either the US or UU inequalities are satisfied. When the sets of parameters satisfy either the US or UU more than 99% of the iterations, the pixel_i is classified as US or UU, respectively. On the contrary, when the same inequalities are satisfied less than the above-mentioned threshold, stability is assumed to depend on the rainfall intensity Q because a critical value Q_c may be found causing to get the limit equilibrium. Hence, the pixel_i is classified as “ Q_c -dependent” and n values of the indicator of shallow landslide susceptibility ($\log Q_c/T$) are iteratively calculated. Then, the statistical distribution of this indicator is obtained for the dataset of the Q_c -dependent pixels. Finally, the analysis of these distributions allows to choose a fixed quantile (median) in order represent the spatial distribution of shallow landslide susceptibility. In order to distinguish the original SHALSTAB model with the probabilistic implementation proposed in this thesis, from now on we will refer to PROBSS.

2.6.2 Information Value

The Information Value (IV, Yin and Yan 1988) is a bivariate statistical method which is based on the assumption that future landslides tend to occur in sites with similar predisposing factors where past and present landslides were already occurred. For this reason, a detailed, accurate and complete landslide inventory is the most important input, which affects directly the model accuracy (Corominas et al., 2014). Practically, the IV method consists on assigning to each class variable a weigh (IV_i) depending on the landslide density, it is expressed as:

Equation 2-26

$$IV_i = \ln \left(\frac{S_i/N_i}{S/N} \right)$$

where

S_i : the number of pixels with landslides and the presence of variable X_i

N_i : the number of pixels with variable X_i

S : the total number of pixels with landslides

N : the total number of pixels

S/N is the a priori probability. It is the probability for each pixel to have a landslide without considering predisposing factors.

S_i/N_i is the conditional probability. It is the probability to have a landslide given the presence of variable X_i .

Negative IV_i means that the presence of the variable is favourable to slope stability. Positive IV_i indicates a relevant relationship between the presence of the variable and landslide distribution; the higher the score, the stronger the relationship (Yin and Yan, 1988). IV_i equal zero means no clear relationship between variable and landslide occurrence. In this thesis, the classes of each variable not containing any landslide have a conditioned probability equal to lower IV_i in the respective class.

The susceptibility map is then obtained by the sum of the IV_i of each variable present in each pixel:

Equation 2-27

$$IV_j = \sum_{i=1}^m X_{ji} IV_i$$

where m is the number of variables and X_{ji} is either 0 if the variable is not present in the pixel j , or 1 if the variable is present.

2.7 ACCURACY ASSESSMENT METHODS

The landslide inventory accuracy assessment was made using a binary classification test. Given a classifier and an instance, there are four possible outcomes. If the instance is positive and it is classified as positive, it is counted as a true positive; if it is classified as negative, it is counted as a false negative. If the instance is negative and it is classified as negative, it is counted as a true negative; if it is classified as positive, it is counted as a false positive. Given a classifier and a set of instances (the test set), a two-by-two confusion matrix (also called a contingency table, Figure 2-30) can be constructed representing the dispositions of the set of instances (Fawcett, 2006).

		Actual	
		Actual positive	Actual negative
Labelled by classifier	Labelled positive	TP	FP
	Labelled negative	FN	TN

Figure 2-30 Confusion matrix of binary classification (modified from Fawcett 2006)

In the context of visual interpretation of orthophoto maps, the binary classification test is executed for polygons (instances) classified as shallow landslides or not, which are subsequently verified by field work, allowing to evaluate the proportion classified polygons. Therefore, the binary classification of the confusion matrix consists on:

- True positives (TP): polygons classified as landslides effectively corresponding to landslides in the field;
- True negatives (TN): polygons identifying features similar to landslides but classified as no landslide areas effectively corresponding to stable areas in the field;
- False positives (FP): polygons classified as landslides but actually corresponding to stable areas in the field;

- False negatives (FN): can be undetected/unclassified landslides, as well as polygons classified as stable areas but actually corresponding to landslides in the field.

Sensitivity, specificity, precision and accuracy are statistical measures of the classification performance, defined as:

$$\text{Sensitivity or True Positive rate (TPR)} = \frac{TP}{TP + FN}$$

$$\text{Specificity or True Negative rate (TNR)} = \frac{TN}{TN + FP}$$

$$\text{Precision or Positive Predictive rate (PPR)} = \frac{TP}{TP + FP}$$

$$\text{Accuracy (ACC)} = \frac{TP + TN}{TP + TN + FP + FN}$$

Also the accuracy of the SD depth map is evaluated. To this aim, the SD depth sites observations were randomly split in training dataset (70%) and test dataset (30%). The accuracy assessment of the SD depth maps is calculated for both the training and test dataset and is expressed in terms of success rate for different steps of SD depth error. In other words, the frequency percentage of well classified observations sites (success rate) is calculated. Then, the success rate is calculated assuming an incorrect classification of one class step, then two and so on. Since in this thesis the depth of the SD is divided into classes with constant amplitude, it is possible to evaluate what is the maximum error of depth (cm) between the predicted and the measured.

The predictive capacity of susceptibility models was evaluated and compared by using the receiver-operating characteristic (ROC) plot, introduced by Hanley and McNeil (1982). In the ROC plot, the sensitivity (true positive rate, TPR) of the model is plotted against 1-specificity (true negatives rate, TNR): sensitivity is the number of correctly predicted landslide cells (True Positives) over the total number of predicted landslide cells (True Positives + False Negatives), whereas the specificity is the number of correctly predicted non-landslides cells (TN, True Negatives) over the total number of predicted non-landslides cells (False Positives + True Negatives). The area-under-ROC (AUROC) is used to assess the global accuracy statistics of the model. The value of AUROC varies between 0.5 (no improvement over random assignment, represented by the diagonal straight line) and 1 (perfect discrimination). For each landslide, if it consists of more than one cell, the cell with the highest susceptibility value was selected to calculate the accuracy. Thus, a landslide consisting of both stable and unstable cells is considered unstable, since it is sufficient that there is one unstable cell to consider the area unstable. Non-predicted landslides are polygons consisting only of unstable cells.

3 STUDY AREA

Northern Tuscany is characterized by high landslide susceptibility due to geological, geomorphological and climatic characteristics. This is one of the rainiest areas in the whole country due to the proximity of Ligurian sea to the Northern Apennines ridges and, in the period 2008-2014, 45 intense rainfall events were recorded (Lavorini et al., 2015). According to the authors, the concept of intense rainfall events is strictly related with return period and therefore, is site specific. Nevertheless, in the study area were classified as intense rainfall event a daily cumulative precipitation above 50 mm/day. In Figure 3-5 some of the most severe rainfall events occurred in the study area in the period 2010-2016 are reported.

The Serchio river valley, the main basin in Northern Tuscany (1565 km²), was affected by intense rainfall events triggering shallow landslides and causing victims in 2009, 2010 and 2014 (Giannecchini et al., 2012; Giordan et al., 2017). In this thesis, an area of 242 km² including several Serchio sub-basins has been selected in order to apply the methodology described in the previous chapter and to perform slope stability analysis.

3.1 DATA AVAILABLE FROM THE LITERATURE

In Table 3.1 data available from the literature are listed. Geological information, the digital elevation model and orthophotomaps are data that Tuscany Regional Authority makes available for free to the public through the online portal “Geoscopio” (<https://www.regione.toscana.it/-/geoscopio>).

In order to collect homogeneous and detailed data from field observations, Microsoft Access Databases were developed by Geomatica Lab of Department of Environmental, Physical and Earth Science, University of Siena.

Table 3.1. Available data in the literature

Name	Description	Data type	Source	Resolution / scale
Continuum Geologico della Regione Toscana	Geologic database of Tuscany region.	Vector data. Esri Shapefile	http://www502.regione.toscana.it/geoscopio/geologia.html	1:10000 scale
DEM	Digital elevation model.	Raster float	http://www502.regione.toscana.it/wmsraster/com.rt.wms.RTmap/wms?map=wmsmorfologia&map_resolution=91&	Cell size: 10x10 meters
Orthophoto maps	Aerial orthorectified images	Raster	http://www502.regione.toscana.it/geoscopio/ortofoto.html	Cell size: from 0.2 to 1 m
Slope deposits Database	Database used to slope deposits field observations	Microsoft Access Database	Lab. Geomatica, DSFTA UNISI	
Bedrock Database	Database used to bedrock field observations	Microsoft Access Database	Lab. Geomatica, DSFTA UNISI	

The aerial images used to detect landslides cover a period from 2000 to 2016: images acquired in 2000 and 2005 are panchromatic (pixel size 1 m), while 2007, 2009, 2010 and 2013 are multispectral visible - near infrared (pixel size 0.5 m) images. The 2016 multispectral visible - near infrared images have instead a higher resolution (pixel size 0.2 m).

3.2 GEOGRAPHIC OUTLINE

The study area of this thesis is located in Northern Tuscany, Central Italy. The area is included in the upper part of the Serchio Valley, known also as Garfagnana valley, an intermountain basin which develops with a NW-SE orientation and parallel to the Northern Apennines main ridges. Serchio river hydrographic basin extends for 1565 km², while the area investigated in this thesis is composed by 5 sub-basins covering an extension of 242 km². From North to the South the sub-basin included are: Corfino, Castiglione, Sillico, Ceserano and Tùrrite Secca.

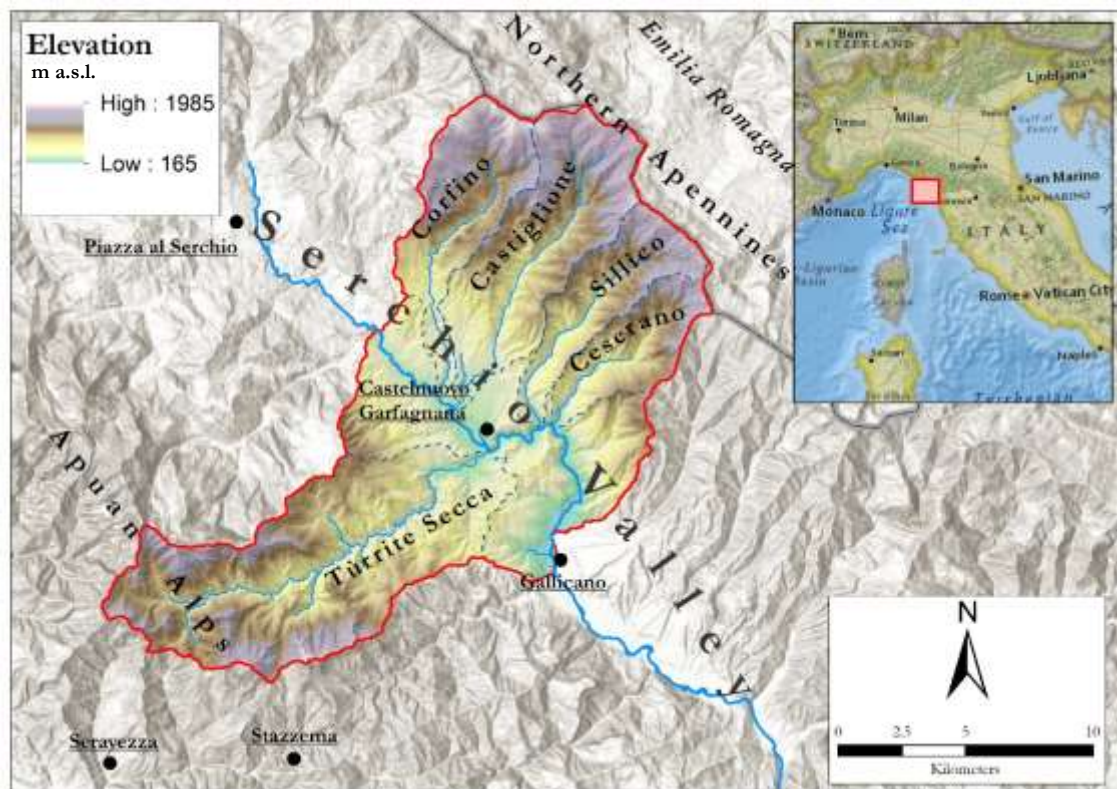


Figure 3-1 Geographical outline of the study area. The red line is the border of the study area. Light blue lines are the stream network. Dark blue dashed lines are watersheds. Grey-black line is the Tuscany-Emilia-Romagna border.

This area was chosen due to the wide variability from morphological and geological point of view. In fact, this valley is located between two main ridges, the Apuan Alps in the south western part, and the Northern Apennines in the North East. These two mountain ranges have a very different morphology, mainly because their different lithology and tectonic evolution (see paragraph 3.3 for more details).

The elevation ranges from 165 m a.s.l. of the valley bottom, close to the town of Gallicano, to the 1985 m a.s.l. of Monte Vecchio, located in the northern end of the area. To the SW, Apuan Alps ridges reach an altitude of more than 1700 m a.s.l..

The average slope steepness is 27 degrees but is slightly different if considering separately the hydrographic left and right of Serchio basin, displaying an average of 25 and 28 degrees respectively. The low slope steepness ($<15^\circ$) in the bottom of the valley is due to the widespread outcrop of continental Villafranchian deposits and terraced alluvial deposits, whose low resistance to erosion led to the formation of a sub-flat morphology interrupted by fluvial scarps of $25-45^\circ$ of steepness. In the high altitude area, the steepness is usually higher than 35° , often reaching more than 70 degrees in slopes where carbonate rocks crop out. The Figure 3-2 describes the distribution of land use in the study area, which is dominated by the presence of woods.

Land use distribution of the study area

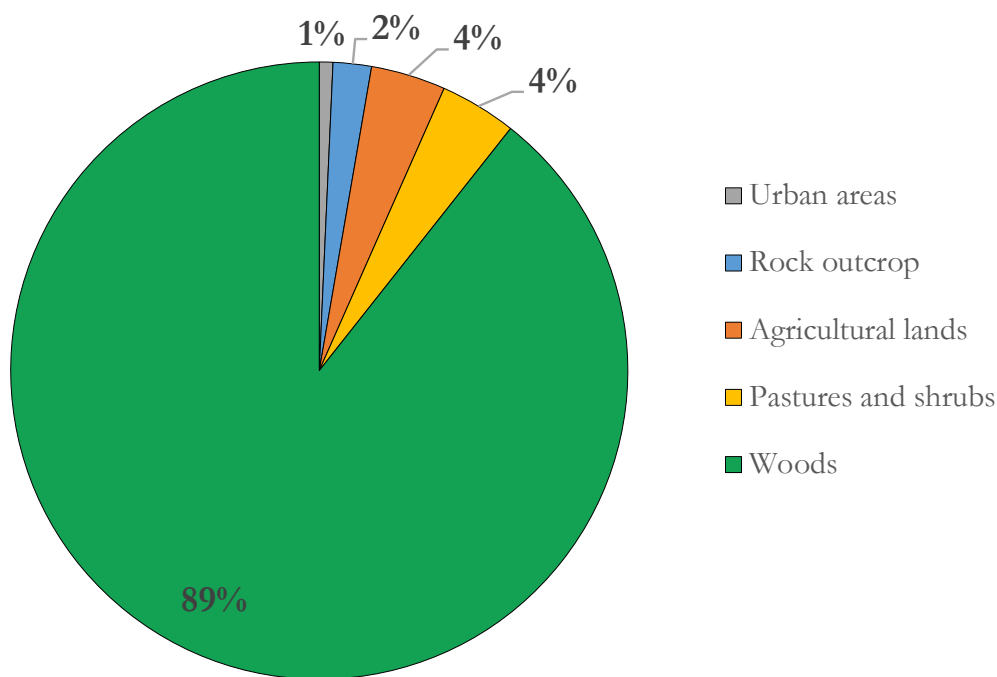


Figure 3-2 Pie chart of land use distribution (data from Corine Land Cover, 2006)

Due to the relative proximity to the Ligurian Sea (around 30 km) and Apuan Alps and Apennines ridge, the area displays a wide variety of climate (Beck et al., 2018) and a high amount of rainfall (Maracchi et al., 2005). In Figure 3-3a is presented a new Köppen-Geiger climate classification map (Beck et al., 2018) with a resolution of 1 km^2 which highlights that in the study area the climate ranges from Mediterranean (Csa and Csb) to Oceanic (Cfb) and Continental Humid or Cold (Dfb and Dfc) in the higher zones. Moreover, the mean annual precipitation map (Figure 2-3, Maracchi et al. 2005) highlights that the study

area is located where the rainfall rate is the highest in the region, ranging from 1500 mm/year to 2300 mm/year. In Figure 3-4 are plotted the cumulative annual rainfalls for the period 2004-2019 of three rain gauges located in the study area.

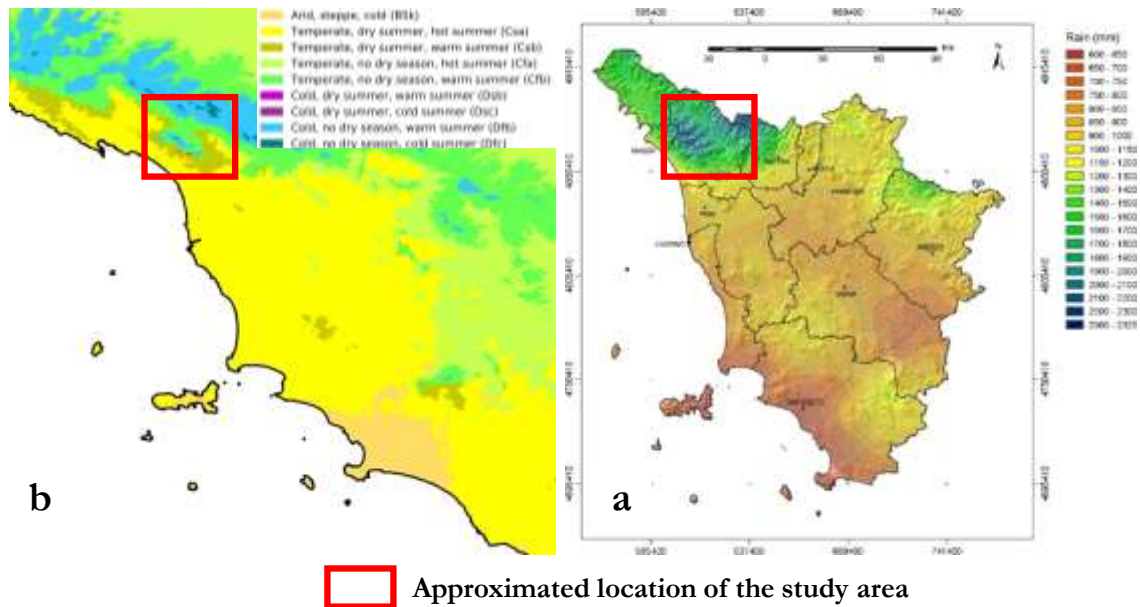


Figure 3-3 a. Sample of Köppen-Geiger climate classification map for Italy (modified from Beck et al. 2018). b. Mean annual precipitation in Tuscany (Maracchi et al., 2005).

Ponte di Campia rain gauge is in the bottom of the valley, close to Galliciano town, Campagrina rain gauge is located at the top of Tùrrite Secca sub-basin while Casone di Profecchia rain gauge is at the top of Castiglione sub-basin. In respect to the Serchio valley and Apennine chain, the Apuan region receives more rain due to Atlantic humid air masses rising Apuan Alps slopes, condensing and triggering intense rainstorms, mainly during autumn and spring (Giannecchini et al., 2012). In fact, this area was hit in the last decades by several intense rainfall events causing victims, destruction of villages and interruption of facilities in 1996, 1998, 2000, 2003, 2009, 2012 and 2014 (Giannecchini et al., 2016).

Cumulative annual precipitation (2004-2019)

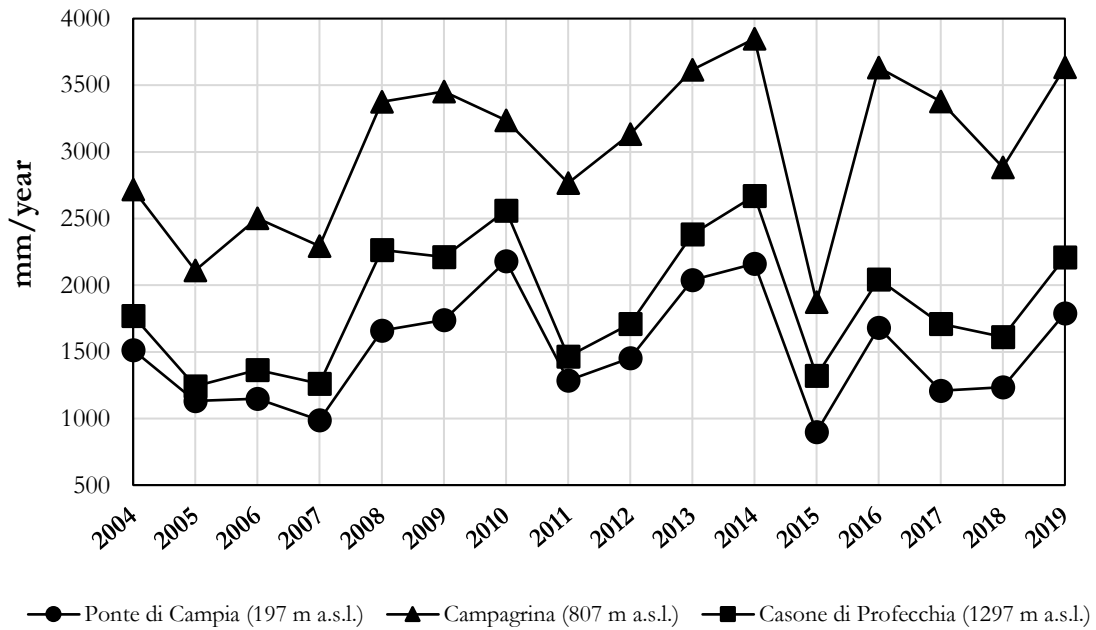


Figure 3-4 Cumulative annual precipitation of three rain gauges in the study area.

Main intense rainfall events (2010-2016)

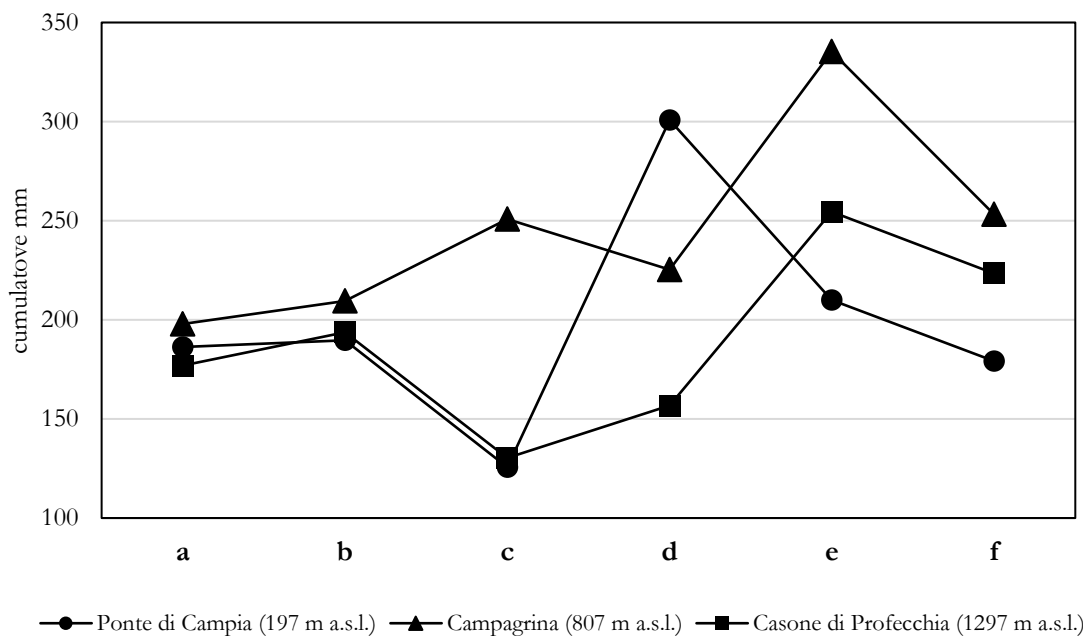


Figure 3-5 Some intense rainfall events occurred in the study area between 2010 and 2016. a- 31/10/2010 - 01/11/2010; b- 25/10/2011; c- 26-27/10/2012; d- 20-21/10/2013; e- 17-19/01/2014; f- 05-06/11/2016.

3.3 GEOLOGICAL OUTLINE

The Serchio valley, known in the literature as Garfagnana graben, is an intramountainous extensional basin forming part of the Northern Apennines orogenic complex (Elter et al., 1975). The Northern Apennines are a fold-thrust belt originated during the Tertiary by the collision between the Apulia (or Adriatic) microplate related to the African plate, and the Briançonnais microplate (Sardinia-Corsica massif), related to the European plate (Carmignani et al., 2004). The collision led to the stacking of the Ligurian and Sub-ligurian Units (Oceanic domain) above the Tuscan Units (Apulian domain), with a top-to-the-East transport direction (Elter et al., 1975), occurred along a regional-scale floor thrust that runs in the “Calcare Cavernoso” formation, a Norian dolomite formation with intercalated evaporite levels (Carmignani et al., 2004). Emplacement of the Tuscan Nappe led to development of greenschists facies metamorphism of the underlying Tuscan Units. Starting Early Miocene (Burdigalian), due to slab retreat, the Apennine compressional front migrates eastward, so the tectonic regime changed from compressive to extensional: the earlier Apenninic orogenic wedge is now affected by widespread exhumation and extensional tectonics which led to the exhumation of the “Alpi Apuane Metamorphic Complex” and the formation of Garfagnana Graben (Carmignani et al., 1994). In Figure 3-6 is represented the tectonic sketch map of the study area and surroundings. Apuan Alps are a tectonic window where Paleozoic basement (Hercynian basement) covered by Mesozoic meta-limestones (“Apuane” and “Massa” units) crop out. Apuan Alps are surrounded and covered by the sedimentary Tuscan nappe, overlaid by ophiolite-bearing Ligurian and Subligurian units (Carmignani et al. 2000). In the study area these units develop towards the East and outcrop in the Garfagnana graben and Northern Apennines. Hercynian basement rocks experienced a pre-Alpine greenschist facies metamorphism and consist mostly on phyllites, schists and quartzites. The “Apuane” and “Massa” Units experienced Alpine greenschists facies metamorphism resulting mainly in marbles with subordinate calcschists, metasandstones and phyllites. Tuscan nappe is made up of Mesozoic carbonates and Mesozoic–Cenozoic pelagic succession and is mainly represented by the arenaceous turbidites of Macigno formation (MAC). Subligurian units is represented by Canetolo unit, a calcareous marly turbiditic sequence, while Ligurian units consists of deep-sea oceanic sediments including Jurassic ophiolites followed by thick sequences of late Cretaceous to middle Eocene calcareous, “Ottone Flysch”. Finally, in the bottom of Serchio valley Villafranchian continental deposits crops out, consisting mainly in weakly cemented fluvial deposits, with gravels, sands and shales.

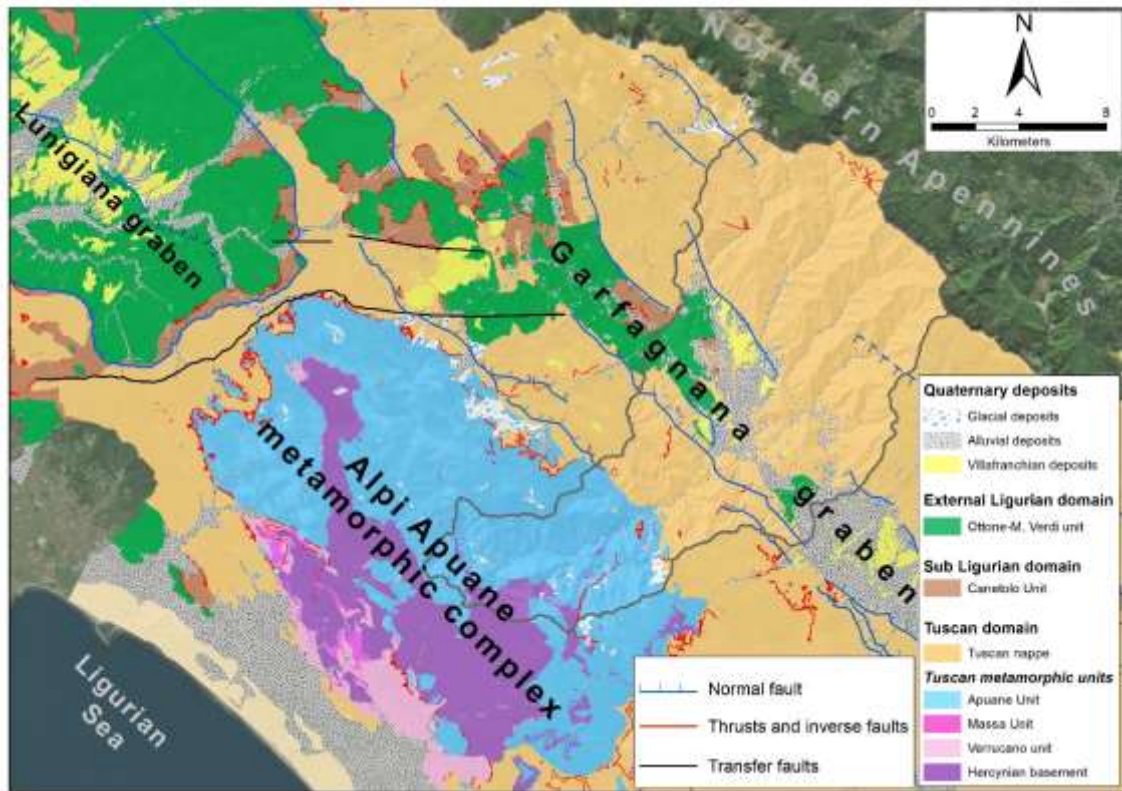


Figure 3-6 Tectonic sketch map of the study area and surroundings (modified from Continuum Geologico della Regione Toscana)

In Figure 3-7 is represented the detailed geological map (scale 1:250.000), a geological cross-section and the histogram of the extension (%) of geological formations. Macigno formation (MAC) is far long the most extended formation in the area, it consists on layered arenites from decimeter to meter scale with subordinate siltstones. In general, these rocks are often covered by sandy-gravel slope deposits and are very prone to landsliding (D’Addario et al. 2018; Disperati et al. 2018). The cross-section highlights the structure of the Garfagnana basin, bordered and dissected by extensional faults. To the SW, marbles of the Apuane Metamorphic Complex are separated from the limestones of Tuscan Nappe by a low-angle normal fault, the latter, the latter, dissected by normal faults merging to the North-East, quickly come in contact with the Macigno Fm. at the bottom of the valley. The North-East sector is characterized by the outcrops of MAC, which is in turn dissected by normal faults merging to the South-West, dividing the formations in four “blocks”, at least. Di Naccio et alii (2013), integrating existing structural geology data with new detailed geomorphic analyses of the fluvial network, established that most of these normal faults are still active with an inferred throw rate ranging from 0.3 to 0.6 mm/year since late Quaternary. Geology is one of the most important conditioning factor controlling the occurrence of landslides, and lithology, which is strictly related to engineering properties of rock itself and the above slope deposits, has a crucial relevance in landslide susceptibility and hazard assessment for each different landslide mechanism (Corominas et al., 2014).

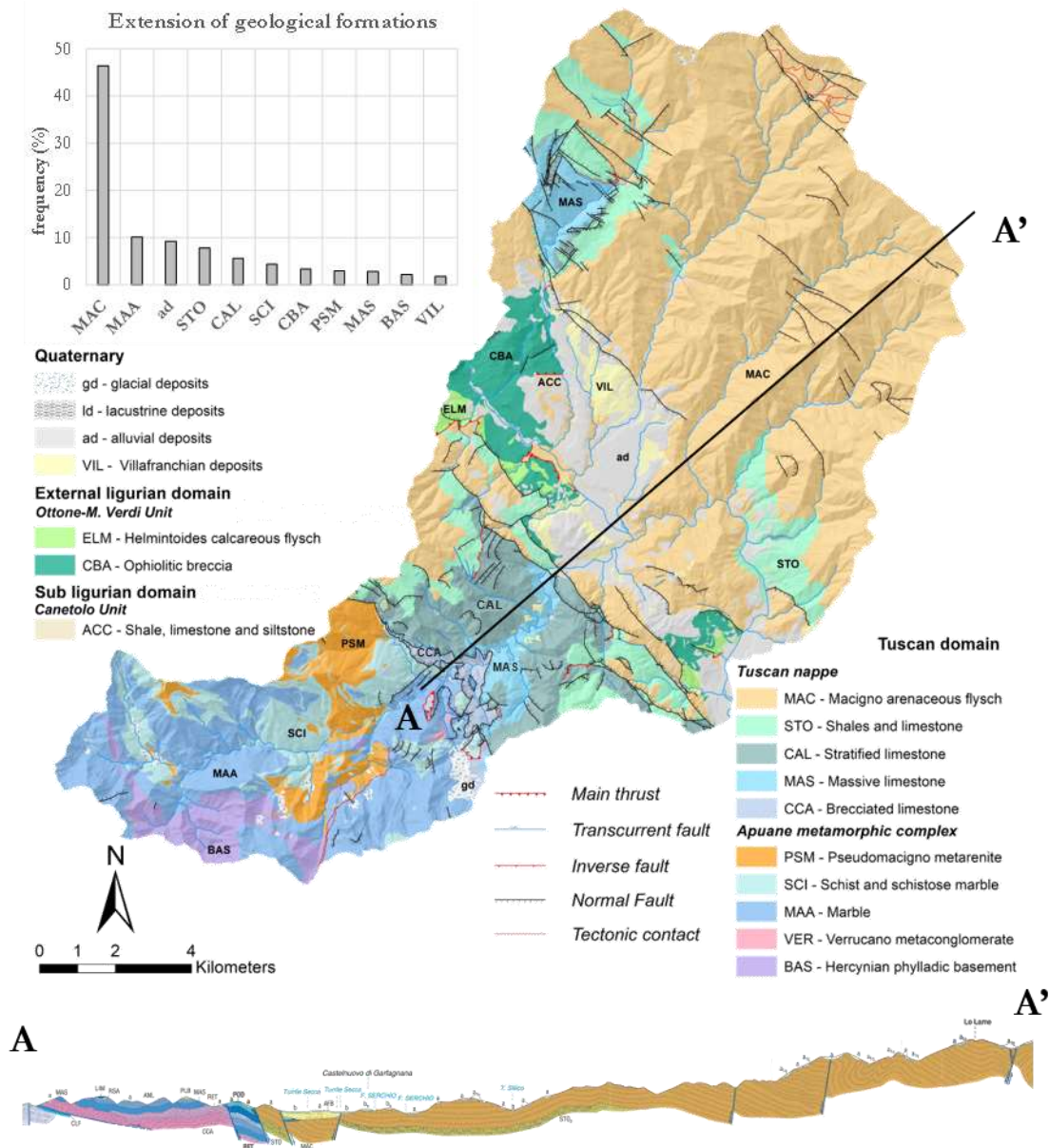


Figure 3-7 Detailed geological map of the study area at the scale 1:250.000 (modified from Continuum Geologico della Regione Toscana), geological cross-section (sample from Progetto CARG Foglio “Castelnuovo Garfagnana”) and frequency distribution of geological formation extension (formation less than 1% are not plotted)

In data-driven landslide susceptibility models, lithology is almost always used as an input conditioning factor (Goetz et al., 2011; Corominas et al., 2014; Zêzere et al., 2017; Reichenbach et al., 2018) while in physically based models may be used to assign to slope deposits a set of parameters which are assumed to depend on the nature of the underlying bedrock (Cervi et al., 2010; Zizioli et al., 2013; Raia et al., 2014; Teixeira et al., 2015; Oliveira et al., 2016; Ciurleo et al., 2017). In this thesis, lithology is an important information which is used as a first order factor for geo-technical parameters, the morphometric analysis and slope deposits depth estimation. For this reason the geological map was the starting dataset to extract the “Bedrock Lithological Units” (BLU), which consist on grouping the formations with similar lithology and stratigraphic relationship, as shown in Figure 3-8. In order to obtain the BLU map, the geological map

of Tuscany Region (Continuum Geologico della Regione Toscana) was used. Figure 3-7 and Figure 3-8 seems very similar to each other, but some formations, as Macigno Fm. (MAC) and Scaglia Toscana Fm. (STO), are composed by several members that may be distinguished at local scale (1:10000). Both these formations have members mainly composed by shales and marls, for this reason, in the BLU map have been separated. Figure 3-9 shows the extension of Bedrock Lithological Units.

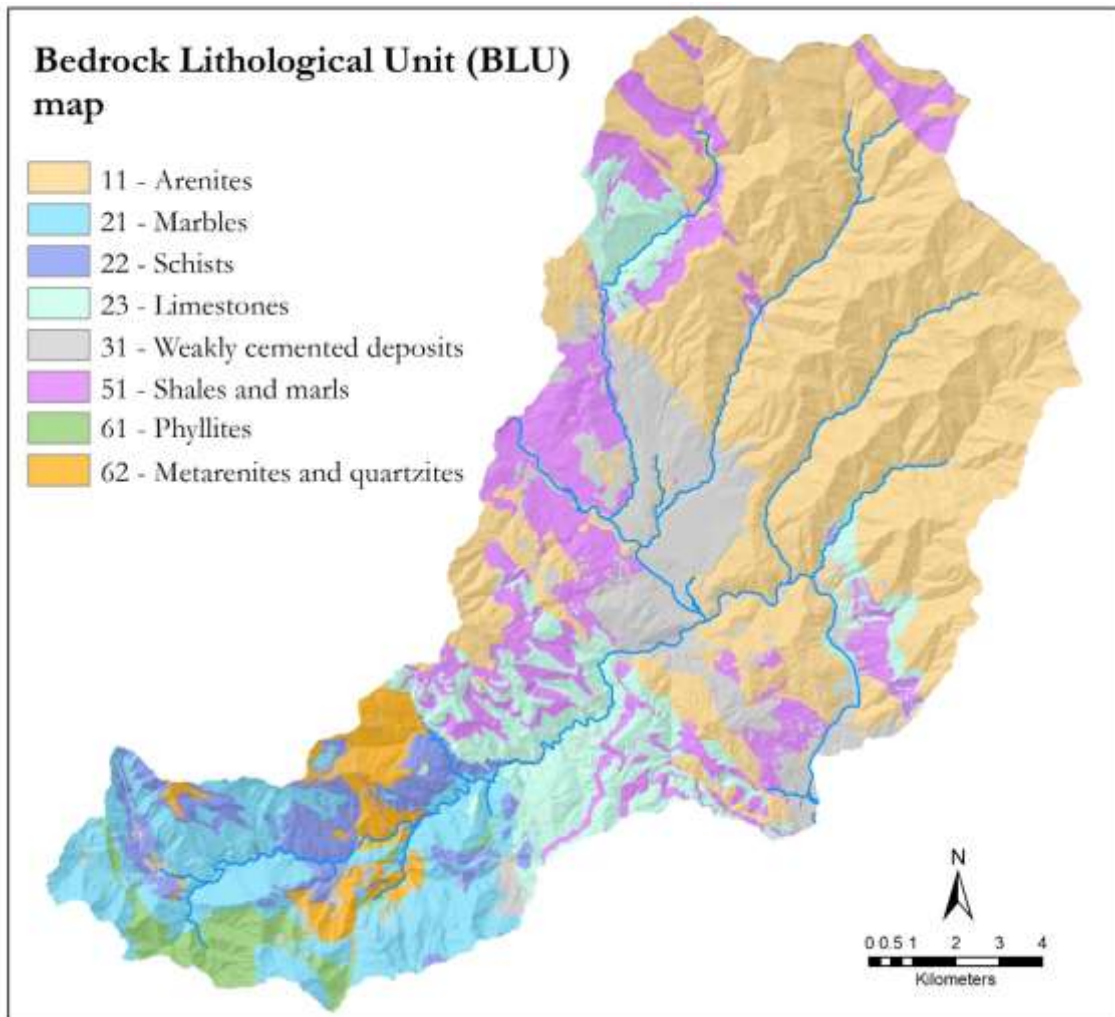


Figure 3-8 Bedrock Lithological Units (BLU) map.

Extent of Bedrock Geological Units

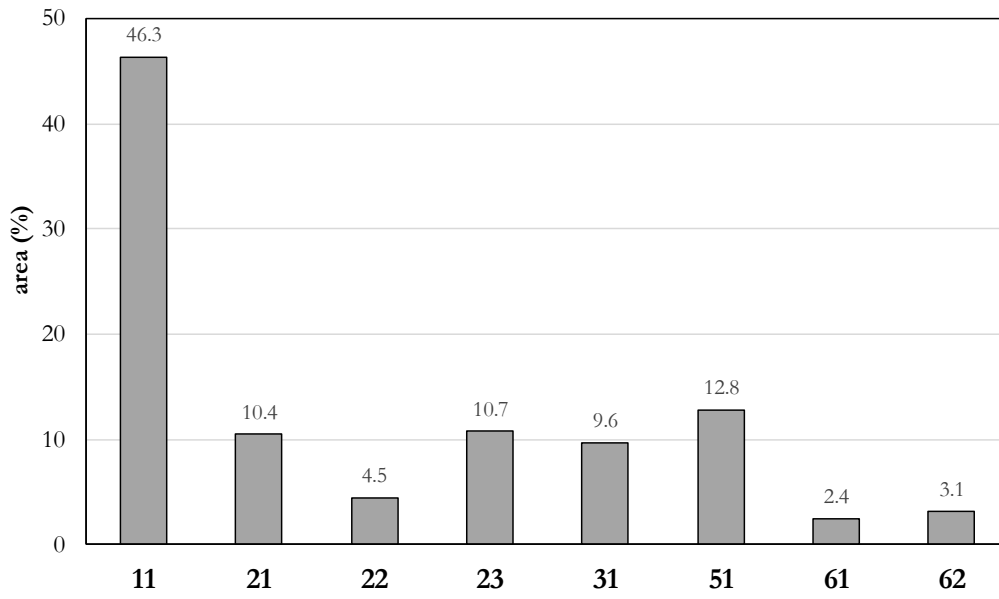


Figure 3-9 Extension of Bedrock Lithological Units (BLU)

4 RESULTS - PROCESSING AND SPATIALIZATION OF DATA

4.1 LANDSLIDE INVENTORY

4.1.1 Landslide inventory accuracy assessment

Once the shallow landslide inventory was prepared, it was necessary to evaluate its accuracy in order to define the quality and reliability of data collected by means visual interpretation. The procedure of accuracy assessment is described in the paragraph 2.7.

In the study area, a total of 249 objects were detected, 196 classified as landslides while 53 classified as stable areas (entities displaying features similar to landslides but classified as stable areas; see paragraph 2.3 for further description). To organize the field validation, objects in the nearby (<1000 meters) of roads and trails were selected; nevertheless, due to reduced accessibility for slope steepness and/or vegetation density, the test dataset consisted of about 56% of visited polygons. Out of a total of 139 visited polygons, 86 were classified as landslides while 53 were classified as stable areas. In addition, further 13 landslides were detected during the field survey (false negatives, FN), mapped within the topographic maps and subsequently stored in the landslide inventory database. In Table 4.1, results of the accuracy assessment are summarized.

Table 4.1 Confusion matrix and statistical measures for accuray assessment

		Field survey				
		Actual positive	Actual negative	Row sum		
Visual interpretation	Labelled positive	68	18	86	TPR	0.84
	Labelled negative	13	53	66	TNR	0.75
	Column sum	81	71	152	PPR	0.79
					ACC	0.80

After the validation step, the final landslide inventory was obtained as a new polygon ESRI Shape File, in which FPs landslides and TNs objects were excluded (Table 4.2).

Table 4.2 Statistics of objects analysed in order to obtain the landslide inventory for this PhD thesis.

Total of delineated objects	249
Delineated landslide	196
Visited landslide objects	86
Visited stable areas objects (FN)	53
Misinterpreted landslides (FP)	18
New detected landslides during fieldwork (IN)	13
Post-validation final number of landslides	191

4.1.2 General statistics of the landslide inventory

In Figure 4-1, the landslide distribution map and general statistics of the landslide inventory are presented. Out of a total of 191 landslides, 81 landslides were visited (blue dots) and most of all are accompanied by the field survey form. Due to the accessibility reasons because of vegetation density and/or morphology, 110 landslides were not visited (red dots).

The top-left graph in Figure 4-1 describes the frequency distribution of landslides for each Bedrock Geological Unit (BLU, see paragraph 3.3), expressed both in terms of absolute frequency and landslide density (Ld, landslide per km²). The absolute number of landslides occurred in each BLU provides a first information about relationships between lithology and landslide distribution, but the landslide density (# / km²) is the right index to quantify this spatial dependence. Considering a total of 191 landslides, the overall landslide density (OLd) is about 0.8 landslide per square kilometer (study area extent 242 km²). The BLU 11 recorded the highest number of landslides but has a Ld value of 0.8, more or less equal to the OLd. In other BLUs, such as BLU 51 and, especially, BLU 23, corresponding to shales/marls and limestones respectively, a higher landslide density is observed. Very few landslides were detected in metamorphic rock areas (BLU 21, 22, 61 and 62). Even if the Ld is quite relevant, the small extent of BLU 61 and 62 (2% and 3% of the study area) could lead to wrong results. Alluvial deposits (BLU 31) with a total of 20 landslides, have a density value equivalent to the OLd value.

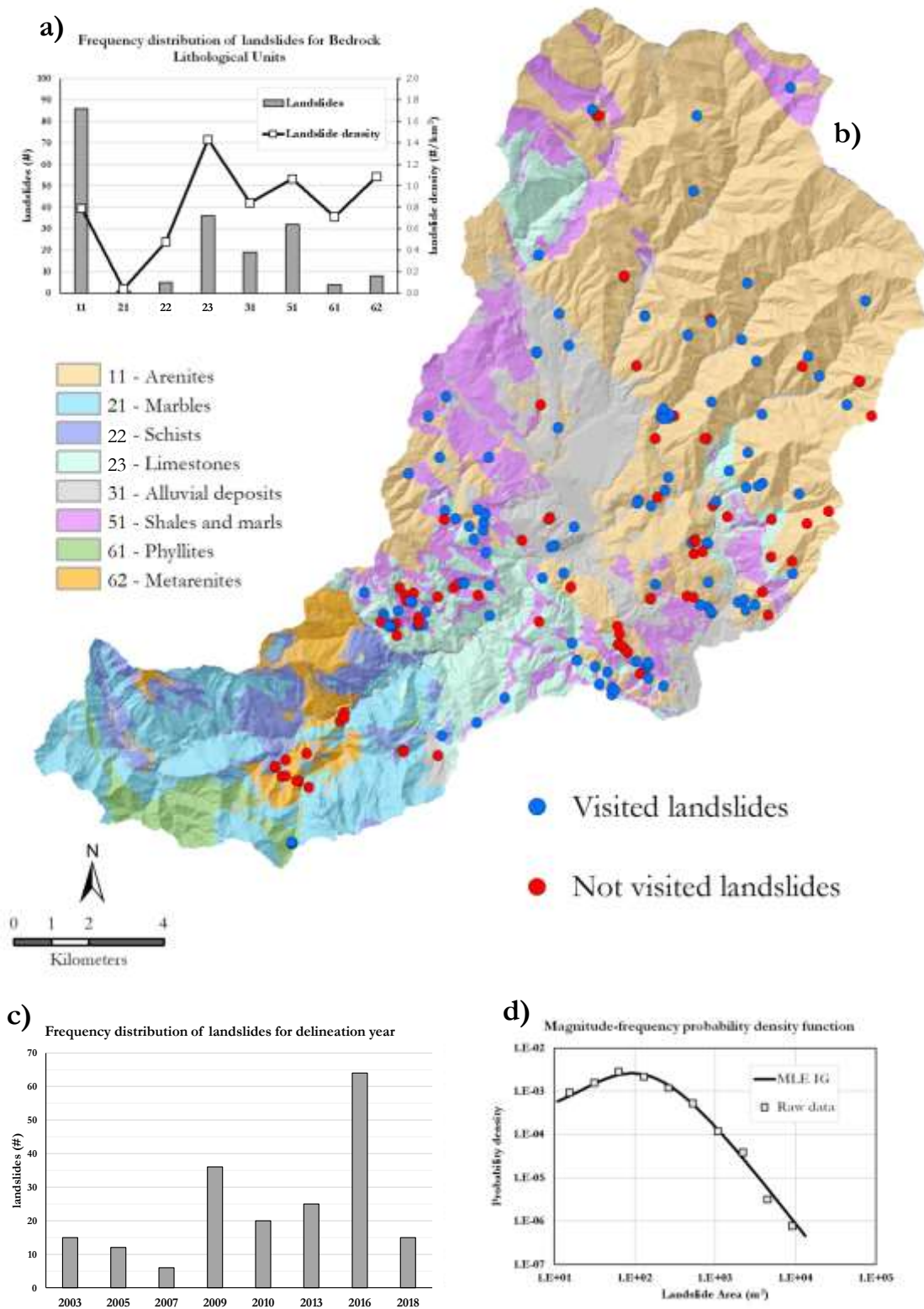


Figure 4-1 Landslide distribution map and general statistics of the landslide inventory. a) frequency distribution of landslides for bedrock lithological units expressed as frequency and density ($\#/km^2$). b) Landslide inventory map distinguishing between visited and not visited landslide. c) Frequency distribution of landslides according to the delineation epoch of orthophoto maps. d) Magnitude-frequency probability density function of the landslide inventory compiled in this PhD thesis.

The highest landslide frequency resulted from orthophoto maps acquired in 2009 and 2016. While the peak of 2016 may be explained with the high quality of the images in respect to the other images, the 2009's peak may be related to the intense rainfall events occurred between 2007 and 2009 (Giannecchini et al., 2016). Landslides detected in 2018 are those detected during field survey (False Negatives, FN), for which the occurrence epoch is unknown. In fact, they can be either landslides occurred after 2016, or they may be occurred earlier even though they are not recognizable in the orthophoto maps.

The magnitude-frequency probability density function of the landslide inventory is provided in Figure 4-1d. The model used to fit raw data is the Inverse Gamma distribution, proposed by Malamud et alii (2004), resulting in an exponent of the inverse power law (α) equal to 1.40 and a rollover occurring at 92 m². Moreover, the median value of landslide area is 268 m², the maximum and the minimum are 13153 and 12 m², respectively.

4.1.3 Characterization of visited landslides

A representative subset of 81 landslides underwent field analysis with collection of information following the standard form provided in the Appendix A. Despite the inventory consists of shallow landslides, the attention was focused about whether the landslide involved either the slope deposits (SD) only, or also the weathered and fractured portion of the underlying bedrock (BR). In order to perform this classification, the SD depth down to the bedrock was compared to the scarp height. When the scarp height is equal or lower than the SD depth, the landslide involved only SD; in this case the slip surface may correspond with the discontinuity between SD and bedrock. In the other cases, the landslide involved also the bedrock (Figure 4-2).

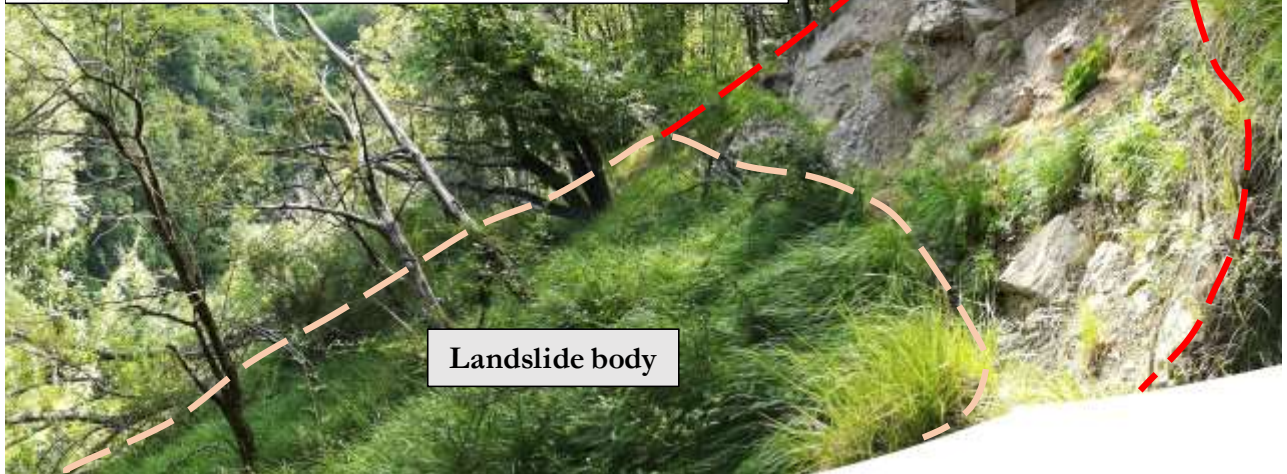
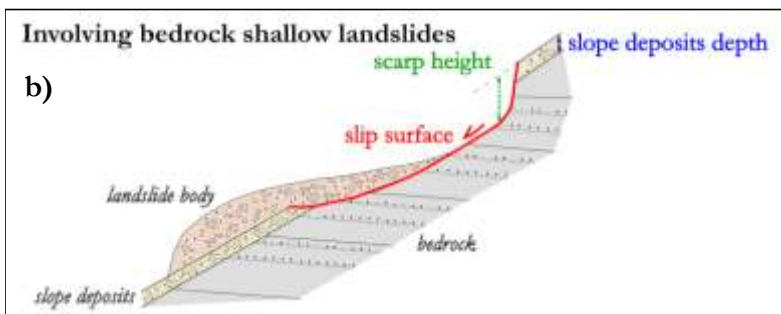
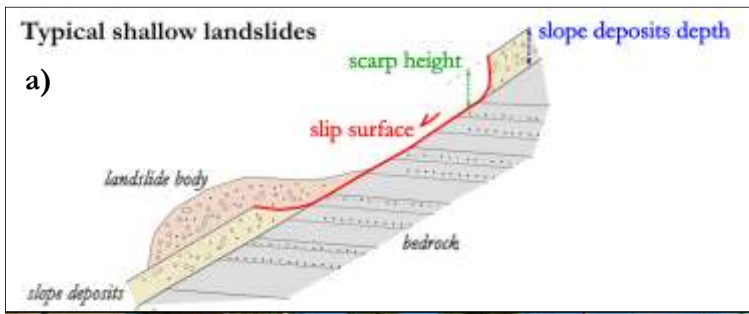


Figure 4-2 Examples of landslides involving either SD only (a, near La Foce) or the underlying bedrock (b, near Rontano).

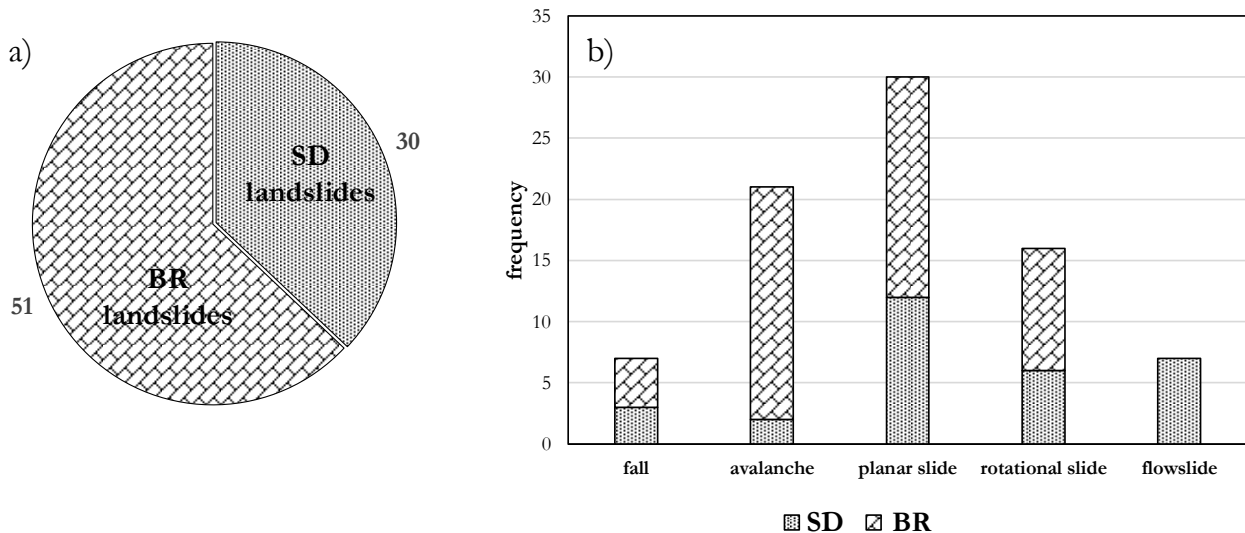


Figure 4-3 Analysis of material and movement types for visited landslides. a) Pie chart of material types. b) Histogram of movement types (Hungr et al., 2014)

In Figure 4-3, according to the classification method described above, visited slope failures were labelled on the basis of both the material and movement types (Hungr et alii, 2014).

Landslides involving bedrock are about the 60% of visited landslides, suggesting that the role of bedrock in shallow landslides development and susceptibility modelling should be explored and taken into account. The frequency distribution of landslide movement types shows that about half of the slope failures are avalanche and planar slide. Nevertheless, separating the movement types on the basis of material types, almost all the avalanches involved bedrock (BR), which is, together with planar slides, the movement type with the highest frequency. Most of SDL are planar slides, and secondly, flowslides and rotational slides, respectively. Some examples of landslides are shown in Figure 4-4. In Figure 4-5 the distribution of slope deposits depth and scarp height is presented. The dashed line in the scatter plot represents the condition in which the SD depth and the scarp height is the same. The dots plotted under the bisector correspond to landslides whose slip surface is shallower than the SD depth, on the contrary, the squares correspond to landslides with a slip surface deeper than SD depth. The boxplots represent the distribution of the scarp height and SD depth measured in the field for SDL and BRL. This graph suggests that BRL have a slip surface usually located between 140 cm to 210 cm, displaying an asymmetric distribution with a median value at 190 cm. These landslides tend to occur where the SD depth is relatively shallow, ranging from 40 cm to 105 cm. A different behaviour can be observed for SDL, whose slip surface is located between 70 cm and 120 cm depth (median 95 cm), and rarely corresponding to the SD-BR discontinuity. In fact, the measured SD depth of landslides involving only SD ranges between 100 cm to 170 cm. These results highlight two very important issues: a) shallow landslides often involve bedrock and, b) the slip surface hardly correspond to the SD/BR discontinuity.



Figure 4-4 Examples of some visited landslides recognized in the study area. a-Avalanche (BR, near Chiozza). b-Fall (BR, near Castelnuovo Garfagnana). c-Planar slide (SD, near Piritano). d-Flowslide (SD, near Eglio)

Another important difference between SDL and BRL is the discard on the area involved in the failure. As shown in Figure 4-6, landslides involving only SD are smaller than landslides involving bedrock. In the scatter plot in Figure 4-6, length vs width of landslides is plotted. Even if the shape is similar, BRL are usually wider and longer. In summary, these results suggest that usually BRL: have a deeper slip surface in respect to SDL, occur where SD depth is less than 1 meter, involve a greater area and are both wider and longer than SDL.

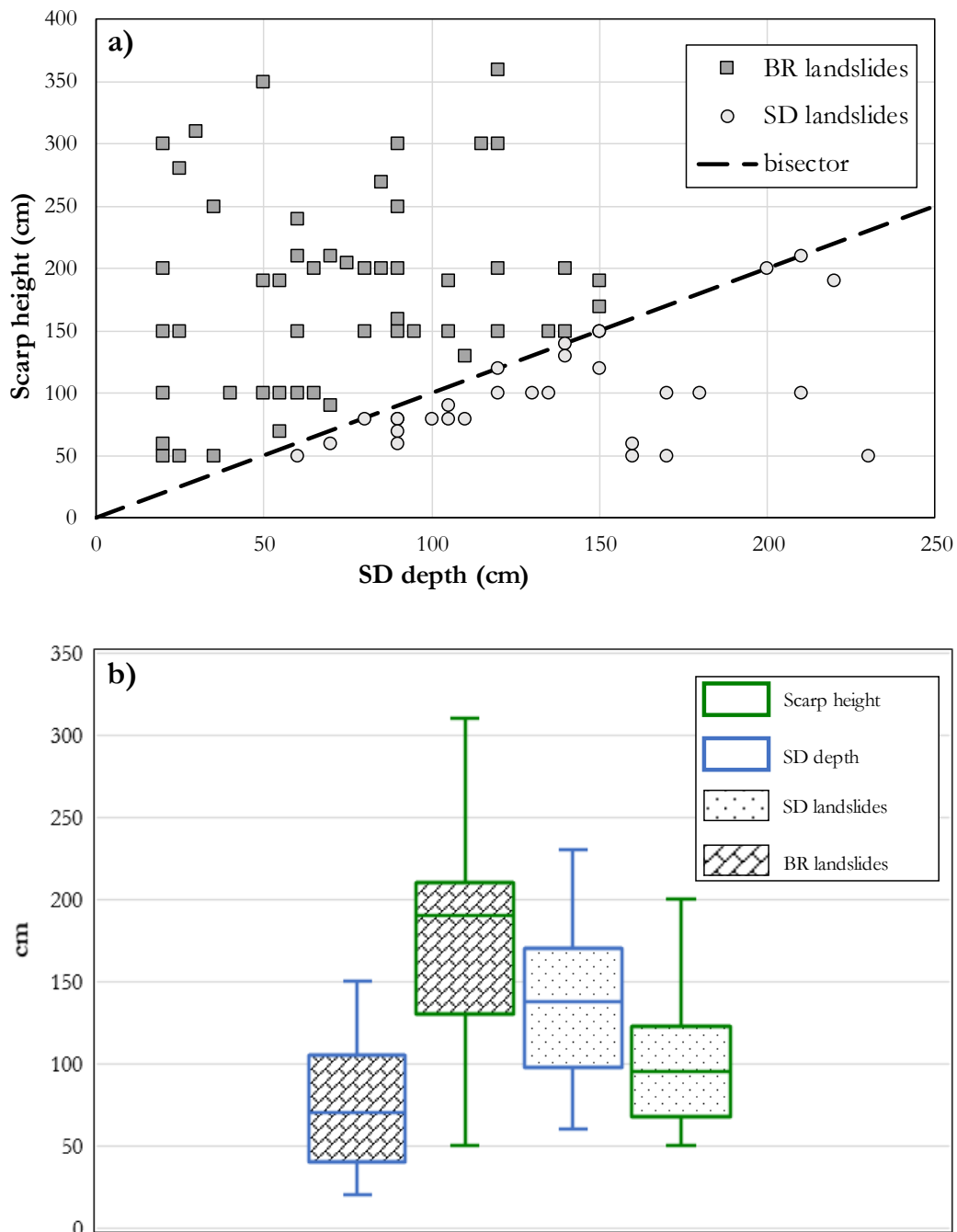


Figure 4-5 Scatter plot of SD depth and scarp height for SDL and BRL (a). Boxplot comparing scarp height and SD depth for SDL and BRL (b).

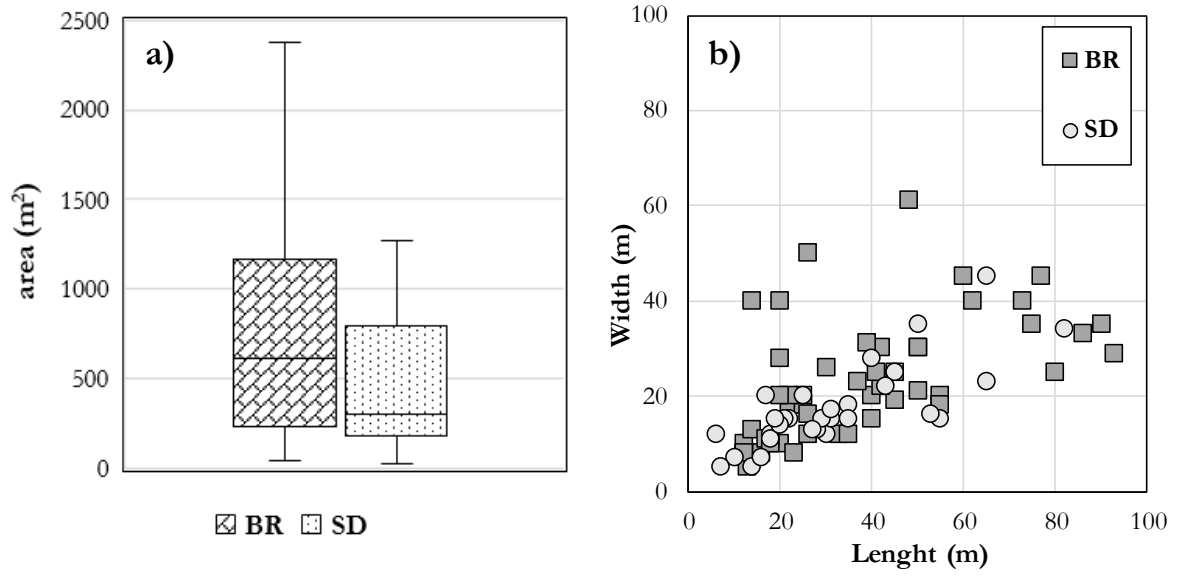


Figure 4-6 Boxplot of landslide area distribution (a) and scatter plot length vs width of landslides (b).

4.2 ENGINEERING GEOLOGICAL CHARACTERIZATION OF SLOPE DEPOSITS

A total of 413 observation sites have been visited during the fieldwork (Figure 4-7). The summary of determinations carried out is detailed in Table 4.3. The distribution of investigations sites for BLU is presented in Figure 4-8. Detailed investigation consisted on the digging using the pickaxe, with measurements of depth as well as collection of data concerning layering, grain size estimation, and texture analysis. Where possible, SD samples were collected. Otherwise, when the SD depth was relatively thin or the discontinuity between SD and BR was naturally exposed (e.g. road cuts), a quick investigation was performed, by measuring the SD depth only. The small number of investigation sites in BLUs 21 (Marbles) and 22 (Schists) is due to the widespread bedrock outcrop that characterizes these lithologies. Instead the small number of investigation sites within the BLU 61 (Phyllites) and 63 (Metarenites) is related to the lack of roads crossing those BLU. Geotechnical parameters of the above mentioned BLUs were obtained by previous investigations recently conducted by Geomatica Lab (DSFTA, University of Siena) in the framework of research projects executed in adjacent areas (Disperati et al., 2018).

Table 4.3 Summary of field investigations for the engineering geological characterization of SD

Observation sites	413
Detailed investigations (digging)	294
Quick investigations	119
Lab grain size test	125
Lab unit weight test	162

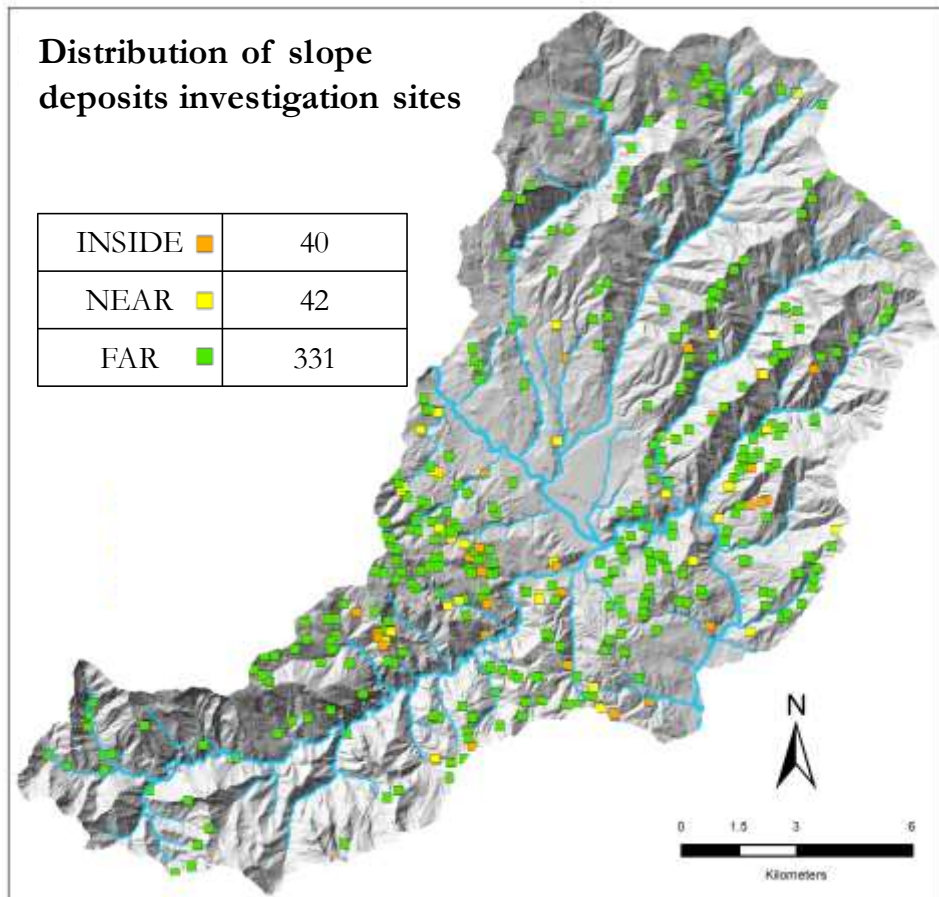


Figure 4-7 Distribution of slope deposits investigation sites. Orange squares are observation conducted inside some visited landslides, yellow conducted near visited landslides and green conducted far from landslides.

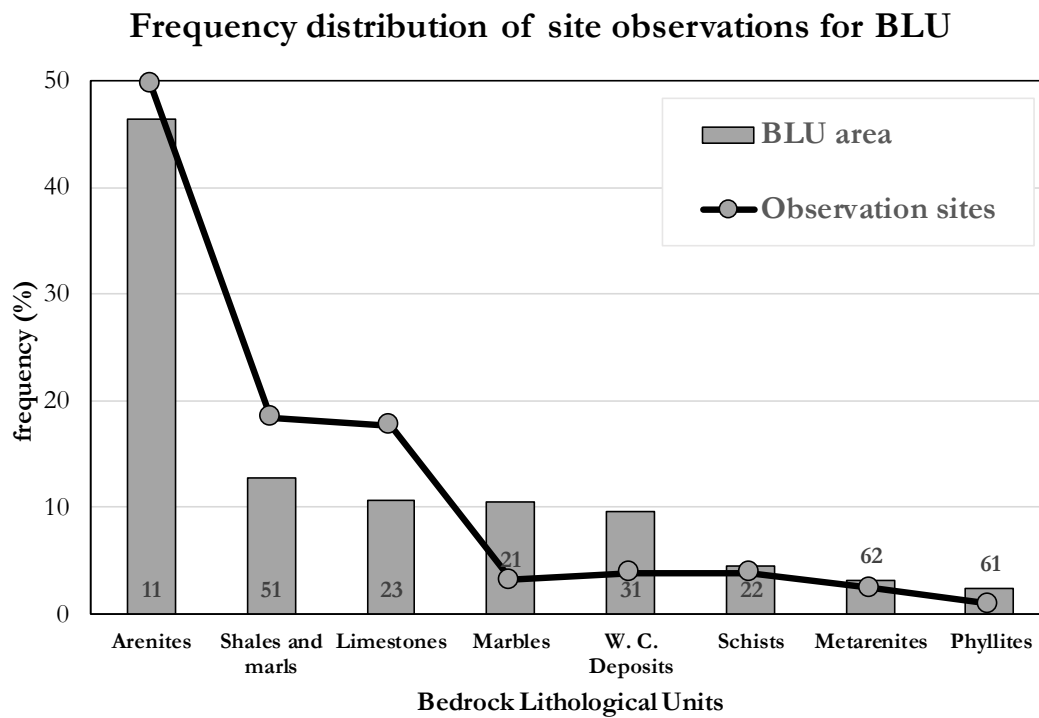


Figure 4-8 Percentage frequency distribution of observation sites chosen for the analysis of slope deposits. The label refers to BLU code.

4.2.1 Extraction of Morphometric units

Morphometric Units were obtained by performing the classification of a set of morphometric variables obtained by the DEM, as described in paragraph 2.4.3. The classification was performed independently for each BLU. As a first step, slope steepness, curvatures (transversal and longitudinal) and contributing area layers were obtained (Figure 4-9) by using different GIS tools like ESRI ARCGis, LandSerf and Whitebox.

The number of morphometric clusters chosen for the classification may vary for different BLUs considering: a sufficient number of observation sites for each BLU, BLU extension and the variability of BLU morphology. As a consequence, for this PhD, the number of clusters ranges between 5 and 15. In Figure 4-10 an example of the Morphometric Units map, obtained by unsupervised classification, is provided. In the example 10 clusters were chosen in order to describe the morphology: the classes 10 and 9 identify channels and impluviums, while the classes 1 and 7 represent ridges, differentiated on the basis of steepness and curvature; the classes 4 and 5 represent more or less straight steep slopes; 6 and 8 correspond to the highest portions of the slope with different degree of concavity and steepness; 2 and 3 clusters are located in the proximity of the drainage network representing low steep areas.

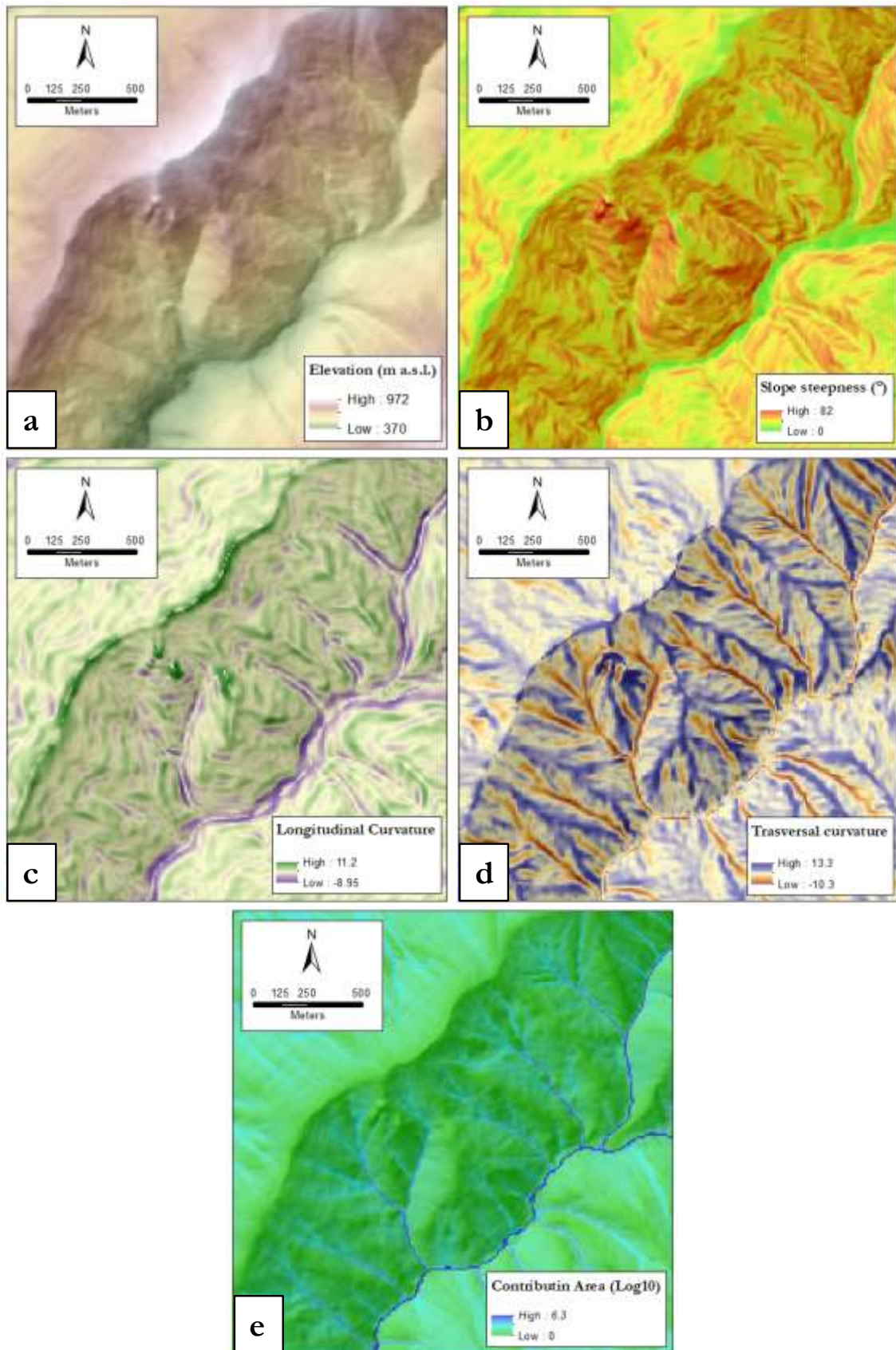


Figure 4-9 Morphometric variables used to perform the ISODATA unsupervised classification aimed at obtaining the Morphometric Unit map for each BLU of the study area.

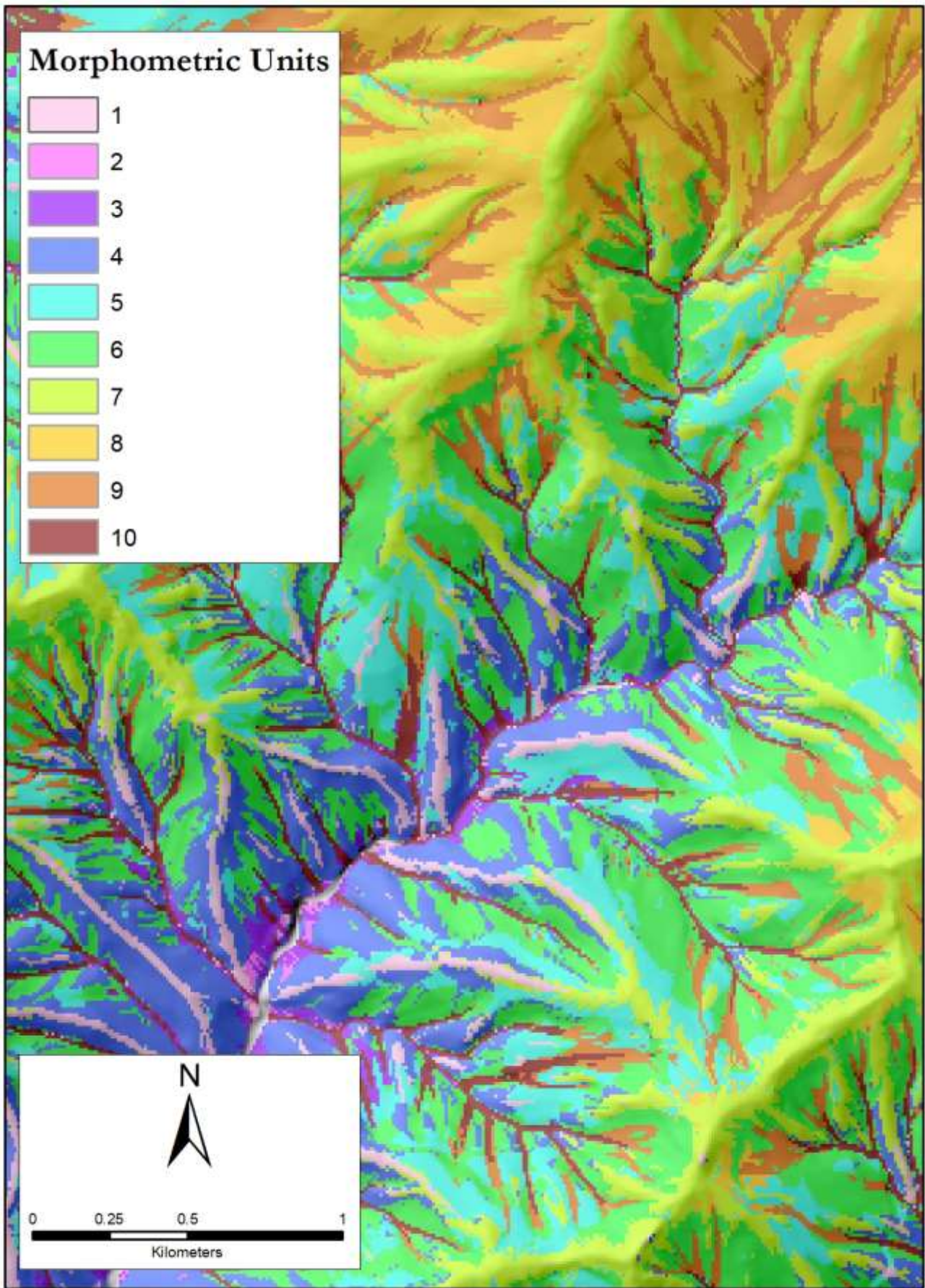


Figure 4-10 Example of the unsupervised classification of morphometric variables.

4.2.2 Depth classes

In order to take into account SD depth uncertainty and variability, each pixel is assigned to a depth categorical class depending on the morphometric features of the pixel itself and surrounding pixels. In order to define the width of depth classes, the cumulative frequency of SD depth measurements of detailed investigations (Figure 4-11) has been calculated. Therefore, analysing the cumulative frequency curve in Figure 4-11, a range of 30 cm wide was suitable to split the SD depth in five classes where the depth value was higher than 30 cm. The low frequency of data below 30 cm is due to the lack of detailed investigations below this threshold, because when the SD depth is thinner than 30 cm it is difficult to conduct a detailed investigation, but only quick investigation. The SD depth classification system adopted in this thesis is a hierarchical system with homogeneous class size, based on quantitative and qualitative classifiers which are: SD depth measure and SD areal frequency (Table 4.4). At level one, two group of SD are identified: “thin” SD (class A) and “thick” SD (class B) which depth threshold is assumed to be 30 cm. The class “A”, depth lower than 30 cm, is split in two classes of second order: the A1, which is mainly characterized by bedrock outcrop, and the A2, in which the SD cover prevails (Figure 4-12).

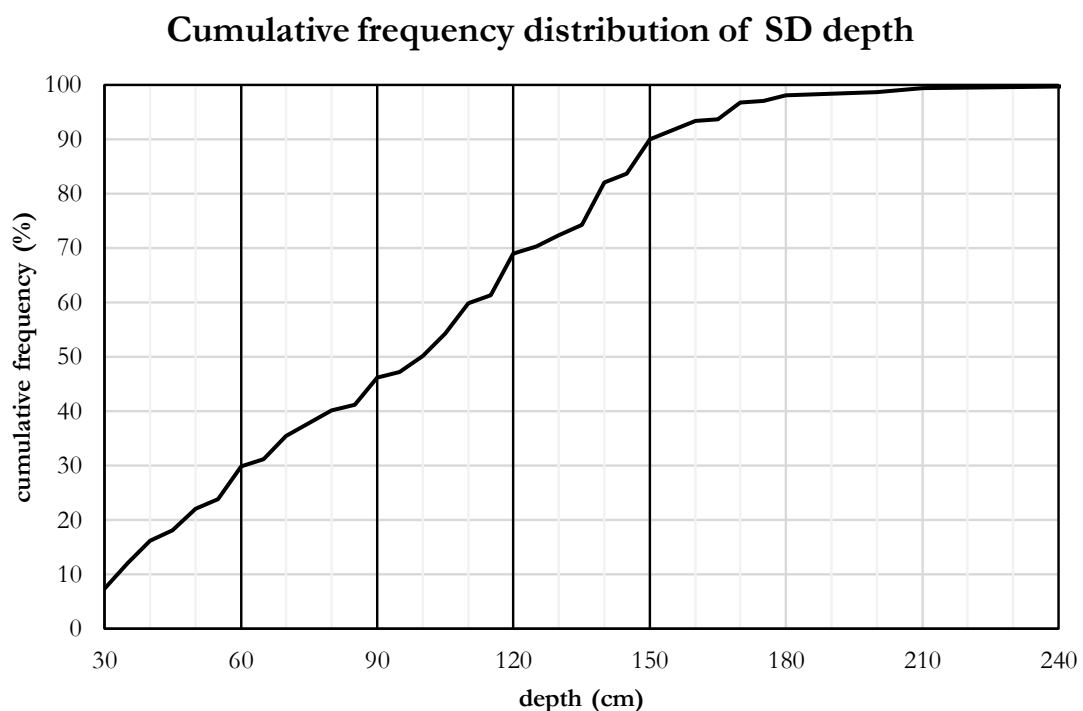


Figure 4-11 Cumulative frequency distribution of SD depth obtained from detailed investigations

As described above, due to environmental factors, the SD depth can vary locally. For this reason, a transition class between class “A” and “B” is introduced (A2B), in order to describe areas generally attributable to A2 depth class, in which non mappable portion of SD with depth bigger than 30 cm occurs (Figure 4-13). Thick SD, belonging to class “B”, are divided into five classes of homogeneous size (30 cm):

B1, B2, B3, B4 and B5 (Figure 4-13, Figure 4-14, Figure 4-15). Fall into class B5 all SD that have a depth bigger than 1.5 meters, because the tools used to open the digs make complex to manually reach higher depths.

Table 4.4 The slope deposits depth classification

First order group	Depth class	Description	Depth range (m)
A ("thin" SD)	A1	Continuous or prevailing outcropping bedrock	0 - 0.1
	A2	Continuous or prevailing SD cover	0.1 - 0.3
	A2B	As A2 with local not-mappable areas with depth >0.3 m	0.1 - 0.6
B ("thick" SD)	B1	Bedrock generally not outcropping, continous SD cover	0.3 - 0.6
	B2	Bedrock generally not outcropping, continous SD cover	0.6 - 0.9
	B3	Bedrock generally not outcropping, continous SD cover	0.9 - 1.2
	B4	Bedrock generally not outcropping, continous SD cover	1.2 - 1.5
	B5	Bedrock generally not outcropping, continous SD cover	>1.5

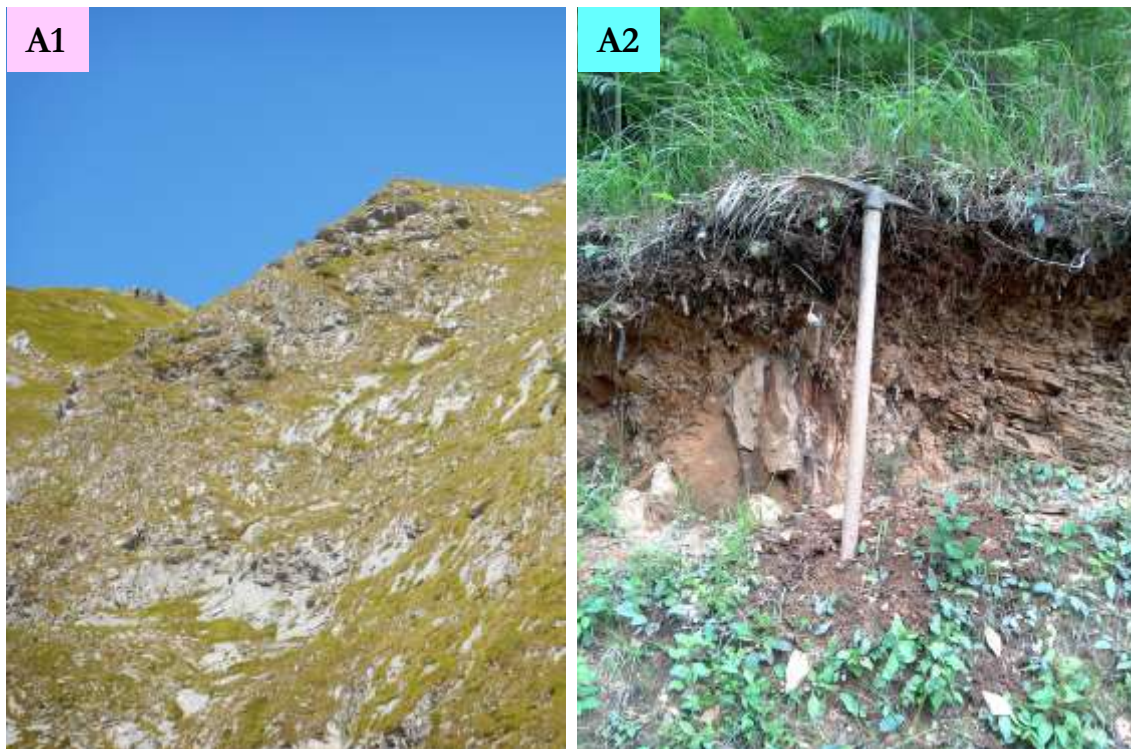


Figure 4-12 SD depth class A1 and A2. Pickaxe length: 90 cm.



Figure 4-13 SD depth class A2B and B1. Pickaxe length: 90 cm.



Figure 4-14 SD depth class B2 and B3



Figure 4-15 SD depth class B4 and B5. Pickaxe length: 90 cm.

4.2.2.1 Slope deposits depth maps

The slope deposits depth map (SDd) is obtained by intersecting the unsupervised classification of morphometric units with field depth measurements, reclassified according to the previous paragraph. Each morphometric unit was assigned to the most frequent depth class resulting by the observations sites falling within the same unit.

This method is applied at BLU scale, and then all the maps are merged into a single raster file. However, as can be seen from Figure 4-8, some BLU are not well-sampled either for logistical reasons or for the low area covered by the BLU itself. SDd map of BLUs 21 and 22 (Marble and Schists respectively) and 31 (Weakly cemented continental deposits) has been obtained coupling field site observations with visual interpretation of orthophoto maps. The land characterizing 21 and 22 BLUs has the greatest relief energy, with the highest erosion rates due to heavy rainfall and, given its carbonatic nature, the development of karst dynamics is widespread, making it predominantly without slope deposit and poor vegetation. BLUs 61 and 62 cover about 5% of the whole study area and are crossed by few roads making it difficult to carry out exhaustive sampling. However, the research activities conducted by the Geomatica Lab of the DSFTA (University of Siena) in previous years in adjacent study areas have been used to build the SDd map in this study area. Below are shown the SD depth class assignation tables and related maps of BLUs 11, 23, 51, 61 and 62. Sites observations were randomly split in training dataset (70%) and test dataset (30%). In the tables are reported the assignation statistics as well as the success rate (Table 4.5, Table 4.6,

Table 4.7, Table 4.8, Table 4.9). The SDd map uncertainty is calculated for steps of SD depth errors of 29 cm (Figure 4-16, Figure 4-20, Figure 4-23, Figure 4-25, Figure 4-27). In Figure 4-17, Figure 4-18, Figure 4-19, Figure 4-21, Figure 4-22, Figure 4-24, Figure 4-26 and Figure 4-28 slope deposits depth map of each BLU are showed.

BLU 11 - Arenites

Table 4.5 Matrix of depth class data for BLU 11

Depth range (m)	Depth classes	Morphometric Units											
		1	2	3	4	5	6	7	8	9	10	11	12
0 - 0.1	A1												
0.1 - 0.3	A2		8				5			8			
0.1 - 0.6	A2B	2	1		1		1	1	2	3			
0.3 - 0.6	B1	1	1	2	14	1	1			2			
0.6 - 0.9	B2			4	2	4	11	2	2		4		
0.9 - 1.2	B3			3		5	4	4	4		4		1
1.2 - 1.5	B4	1		3	2	12	4	2	6		2	2	2
>1.5	B5			1		6	1	2	2		2	4	1
Site observations total		4	10	13	19	28	27	11	16	13	12	6	4
Class A probability		0.5	0.9	0.0	0.1	0.0	0.2	0.1	0.1	0.8	0.0	0.0	0.0
Class B probability		0.5	0.1	1.0	0.9	1.0	0.8	0.9	0.9	0.2	1.0	1.0	1.0
Maximum frequency		2	8	4	14	12	11	4	6	8	4	4	2
Morph. Unit Success Rate		0.5	0.8	0.3	0.7	0.4	0.4	0.4	0.4	0.6	0.3	0.7	0.5
Assigned Depth class		A2B	A2	B2	B1	B4	B2	B3	B4	A2	B3	B5	B4

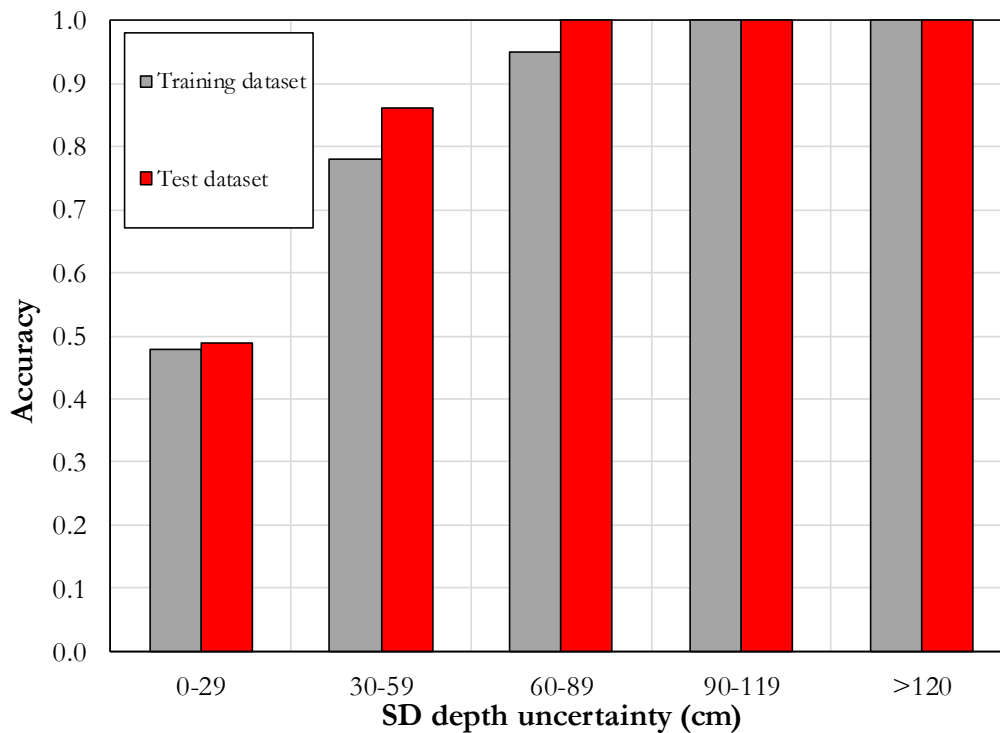


Figure 4-16 Success and prediction rates of SDd map for BLU 11

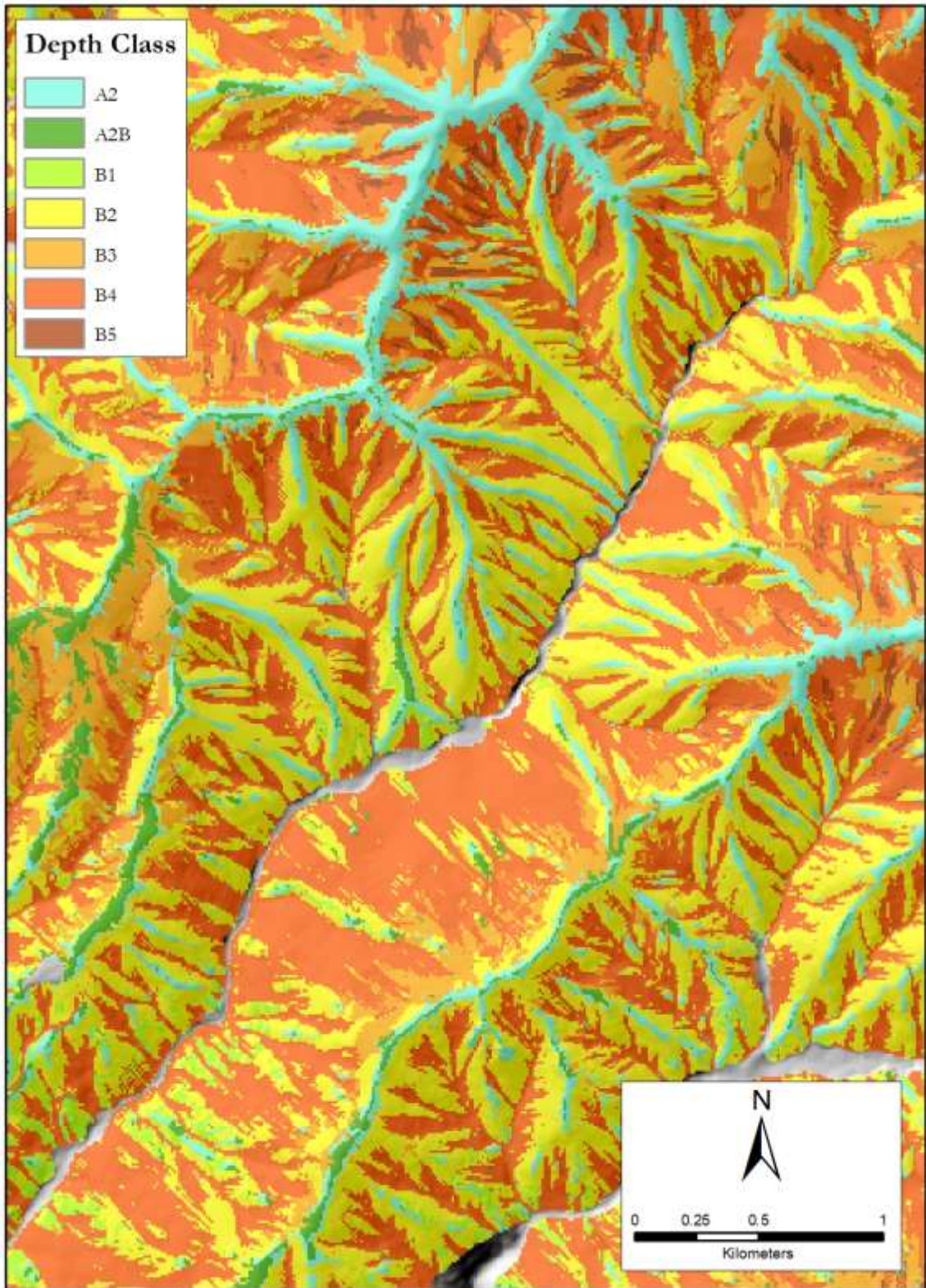


Figure 4-17 BLU11 slope deposits depth map.

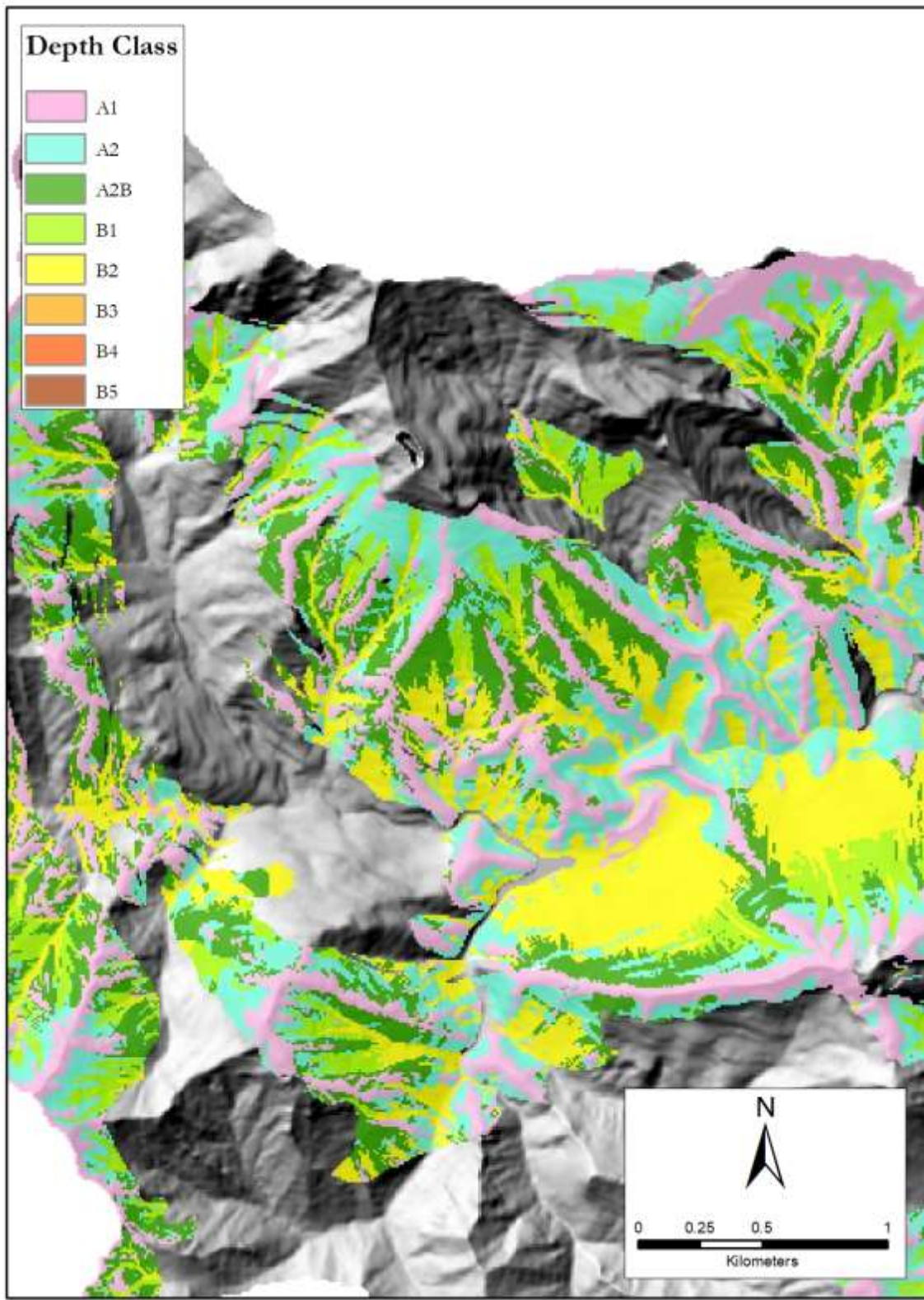


Figure 4-18 BLU21 slope deposits depth map.

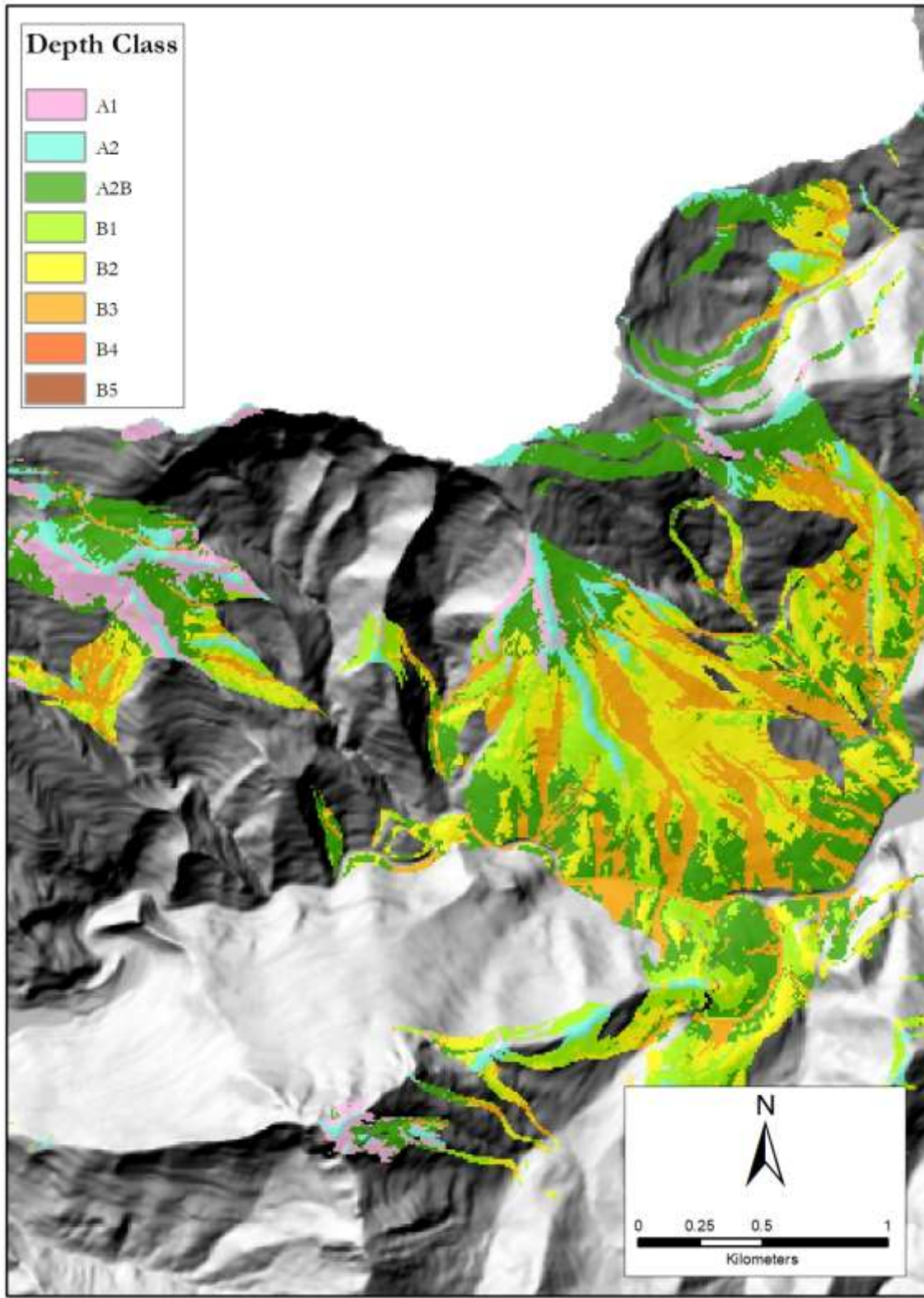


Figure 4-19 BLU22 slope deposits depth map.

BLU 23 – Limestones

Table 4.6 Matrix of depth class data for BLU 23

Depth range (m)	Depth classes	Morphometric Units											
		1	2	3	4	5	6	7	8	9	10	11	12
0 - 0.1	A1					2							
0.1 - 0.3	A2	5	4		1				1				
0.1 - 0.6	A2B	2					1		4	1			1
0.3 - 0.6	B1	1		3			2		1		1		
0.6 - 0.9	B2						6	2			2		
0.9 - 1.2	B3						2	2	1		3	1	
1.2 - 1.5	B4								1			2	2
>1.5	B5								1				1
Site observations total		4	10	13	19	28	27	11	16	13	12	6	4
Class A probability		0.5	0.9	0.0	0.1	0.0	0.2	0.1	0.1	0.8	0.0	0.0	0.0
Class B probability		0.5	0.1	1.0	0.9	1.0	0.8	0.9	0.9	0.2	1.0	1.0	1.0
Maximum frequency		2	8	4	14	12	11	4	6	8	4	4	2
Morph. Unit Success Rate		0.5	0.8	0.3	0.7	0.4	0.4	0.4	0.4	0.6	0.3	0.7	0.5
Assigned Depth class		A2B	A2	B1	A2	A1	B2	B3	A2B	A2B	B3	B4	A2B

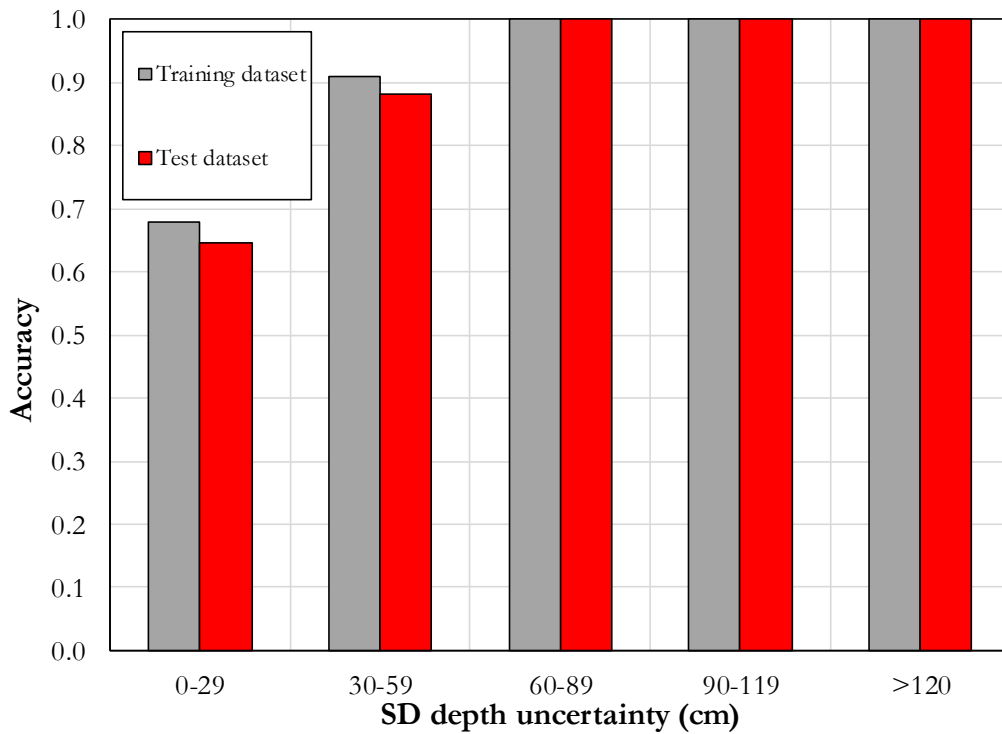


Figure 4-20 Success and prediction rates of SDd map for BLU 23

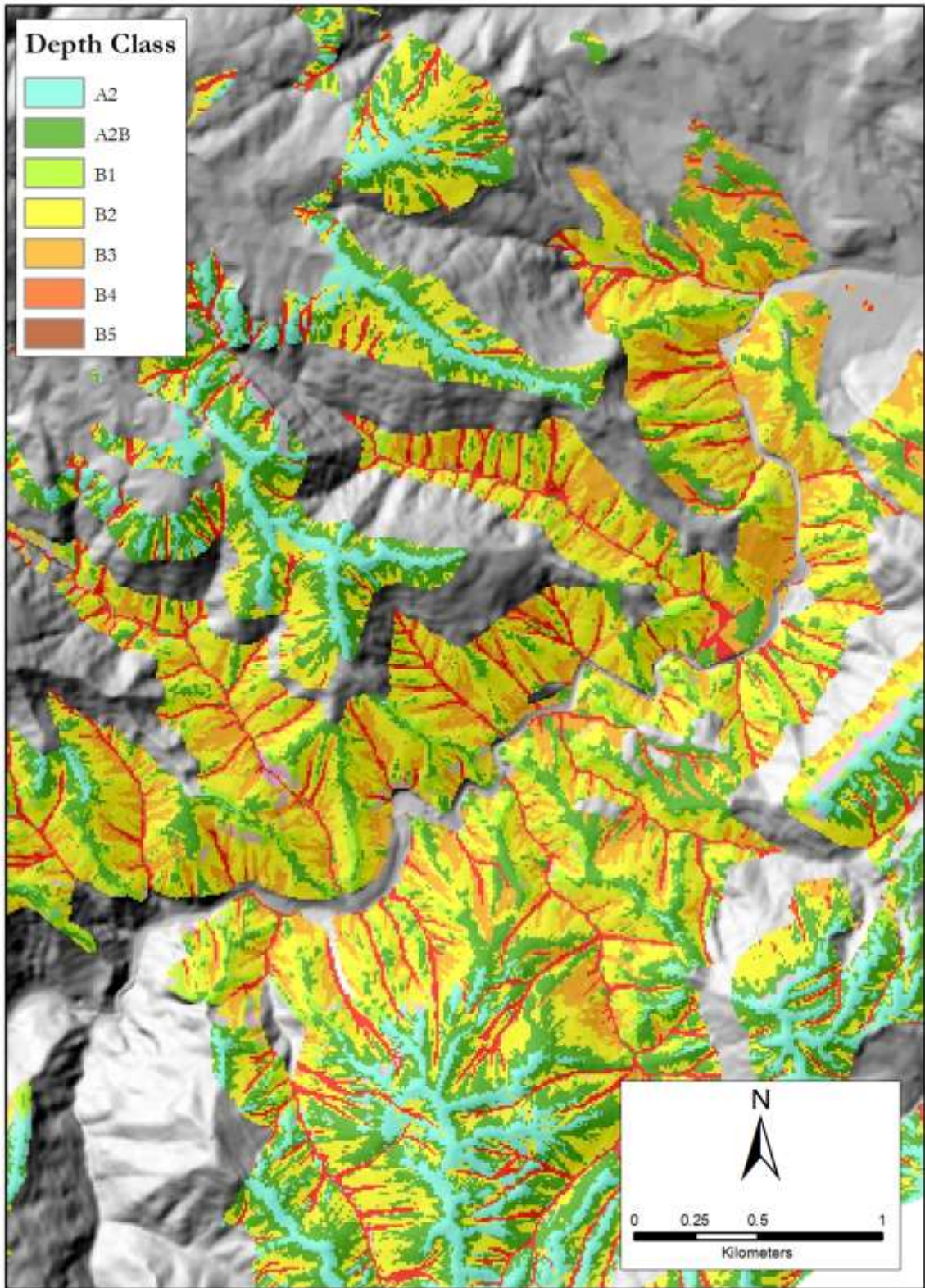


Figure 4-21 BLU23 slope deposits depth map.

BLU 31 – Weakly cemented continental deposits

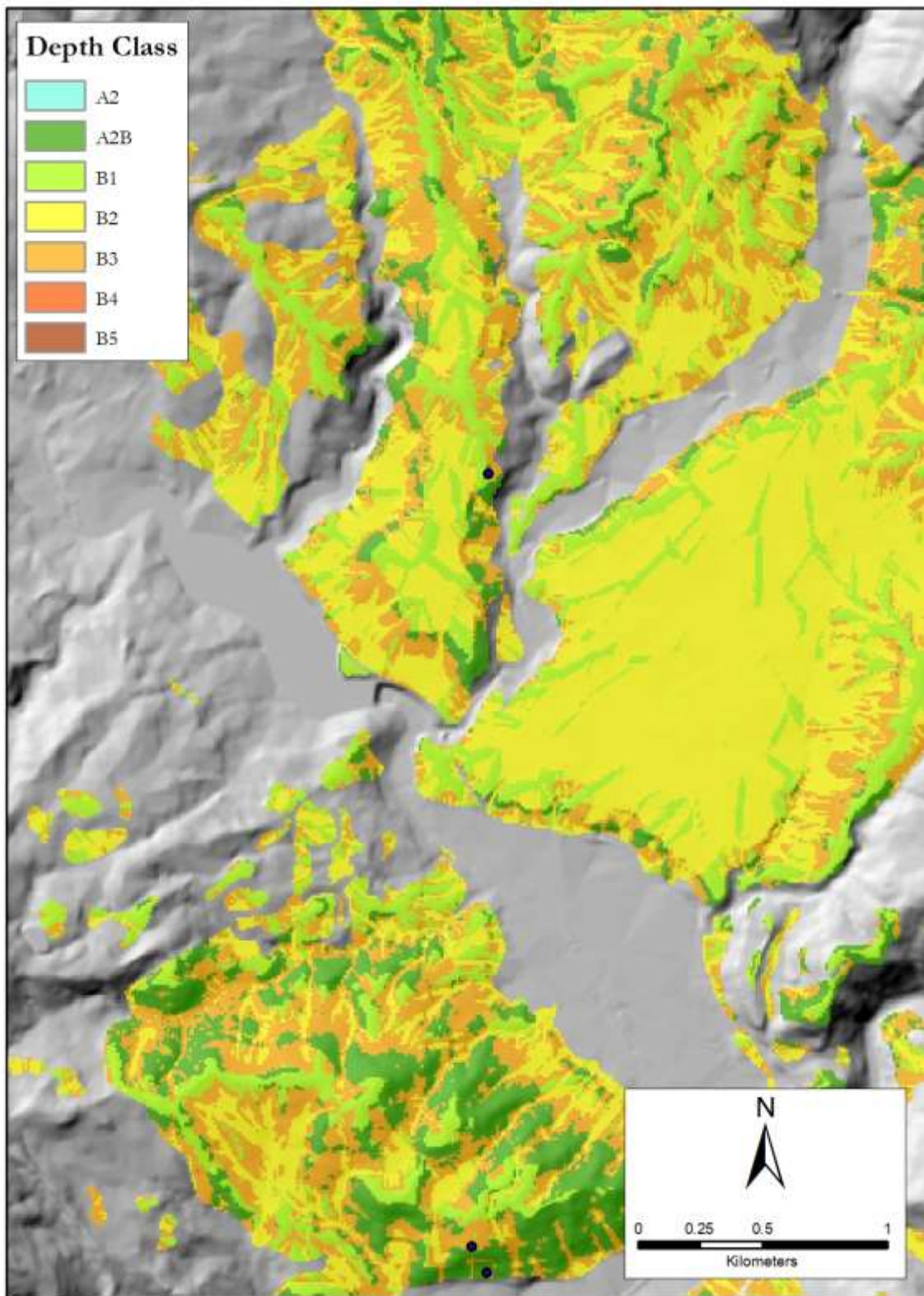


Figure 4-22 BLU31 slope deposits depth map.

BLU 51 – Shales and marls

Table 4.7 Matrix of depth class data for BLU 51

Depth range (m)	Depth classes	Morphometric Units									
		1	2	3	4	5	6	7	8	9	10
0 - 0.1	A1										
0.1 - 0.3	A2			1		1	2				
0.1 - 0.6	A2B	3	1	2		1	1	1			
0.3 - 0.6	B1	1		5		1	5	1		1	
0.6 - 0.9	B2		1	1		4		2		1	
0.9 - 1.2	B3				1	2		3	2		
1.2 - 1.5	B4			1	3	1		1	1		1
>1.5	B5		1		1	1			4		
Site observations total		4	10	13	19	28	27	11	16	13	12
Class A probability		0.5	0.9	0.0	0.1	0.0	0.2	0.1	0.1	0.8	0.0
Class B probability		0.5	0.1	1.0	0.9	1.0	0.8	0.9	0.9	0.2	1.0
Maximum frequency		2	8	4	14	12	11	4	6	8	4
Morph. Unit Success Rate		0.5	0.8	0.3	0.7	0.4	0.4	0.4	0.4	0.6	0.3
Assigned Depth class		A2B	B2	B1	B4	B2	B1	B3	B5	B2	B4

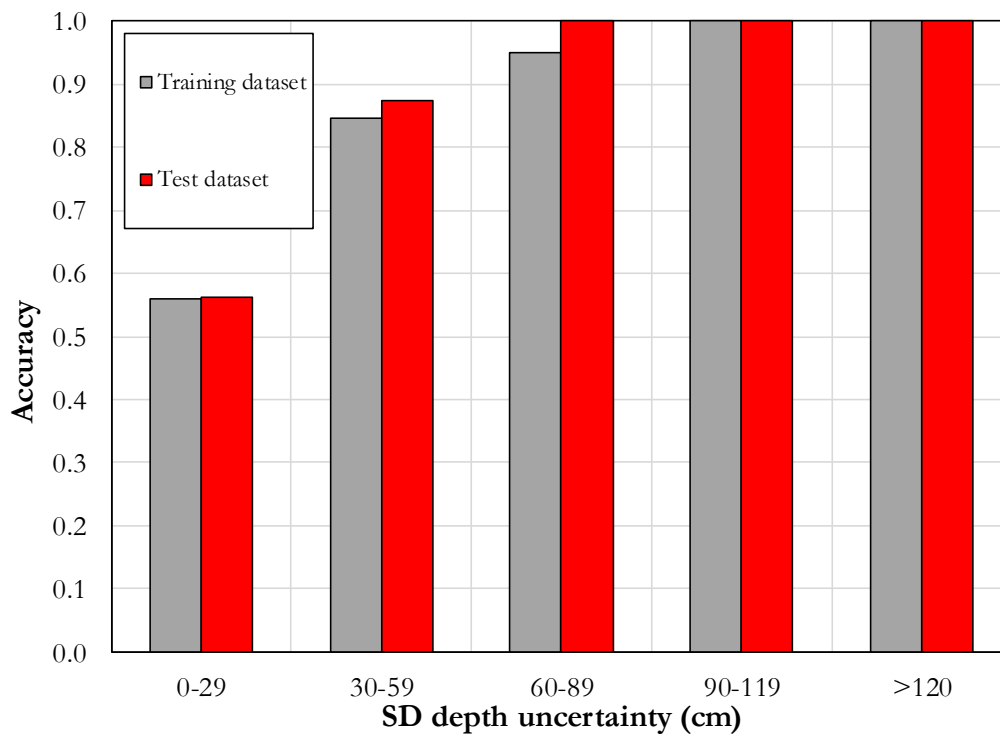


Figure 4-23 Success and prediction rates of SDD map for BLU 51

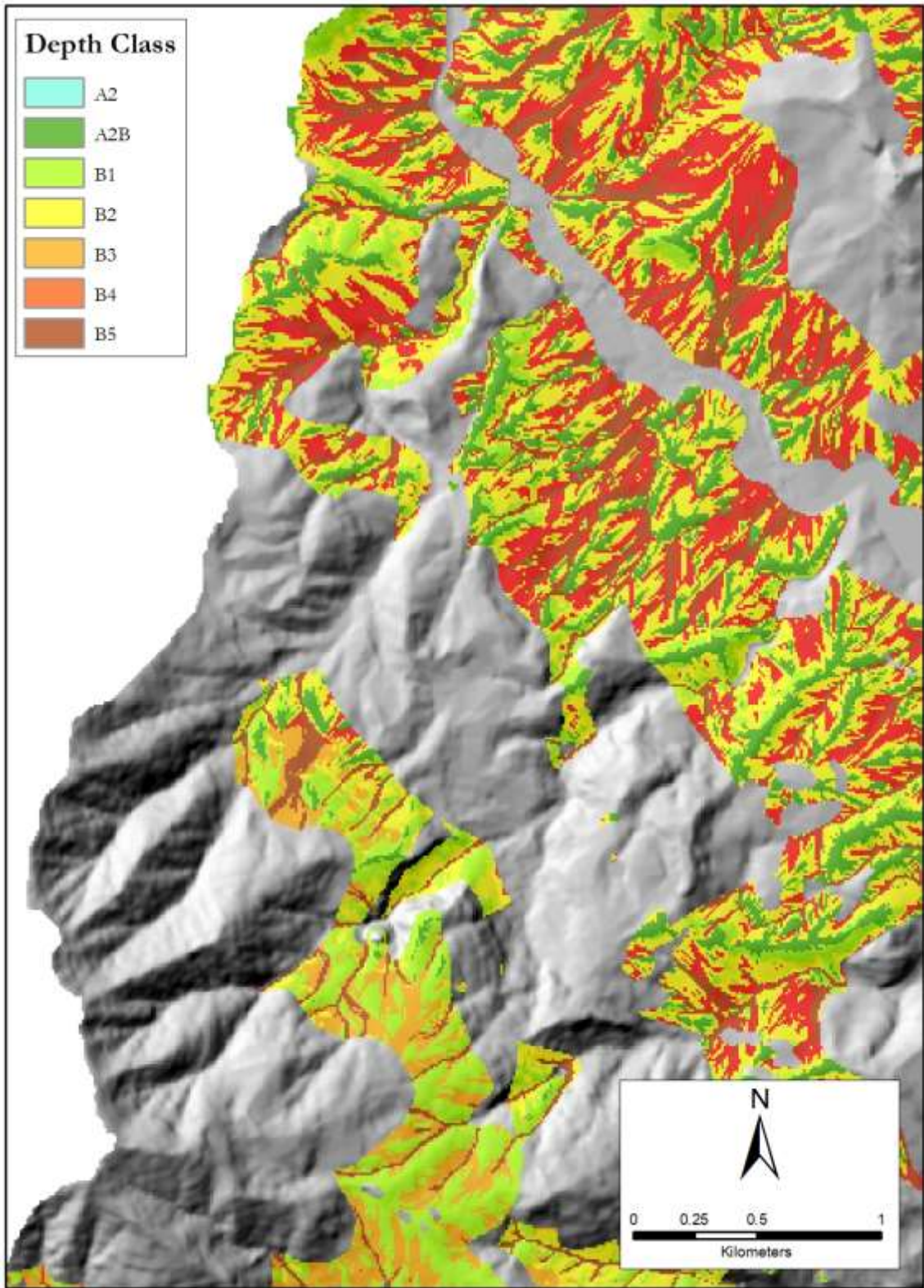


Figure 4-24 BLU51 slope deposits depth map.

BLU 61 – Phyllites

Table 4.8 Matrix of depth class data for BLU 61

Depth range (m)	Depth classes	Morphometric Units													
		1	2	3	4	5	6	7	8	9	10	11	12	13	14
0 - 0.1	A1									1		1	1		5
0.1 - 0.3	A2	1	2				2	3	10	2		7	5	5	
0.3 - 0.6	A2B					1		5	1	6			1	2	1
0.6 - 0.9	B1						3	2	1	10			3		
0.9 - 1.2	B2		9	9		1	2	1	2					1	
1.2 - 1.5	B3			2	1	1	4				5				
>1.5	B4	5				3	2	1							
	B5	2	2	2	4	2									
	Site observations total	8	13	13	5	8	13	12	14	19	5	8	10	8	6
	Class A probability	0.1	0.2	0.0	0.0	0.1	0.2	0.7	0.8	0.5	0.0	1.0	0.7	0.9	1.0
	Class B probability	0.9	0.8	1.0	1.0	0.9	0.8	0.3	0.2	0.5	1.0	0.0	0.3	0.1	0.0
	Maximum frequency	5	9	9	4	3	4	5	10	10	5	7	5	5	5
	Morph. Unit Success Rate	0.6	0.7	0.7	0.8	0.4	0.3	0.4	0.7	0.5	1.0	0.9	0.5	0.6	0.8
	Assigned Depth class	B4	B2	B2	B5	B4	B3	A2B	A2	B1	B3	A2	A2B	A2	A2

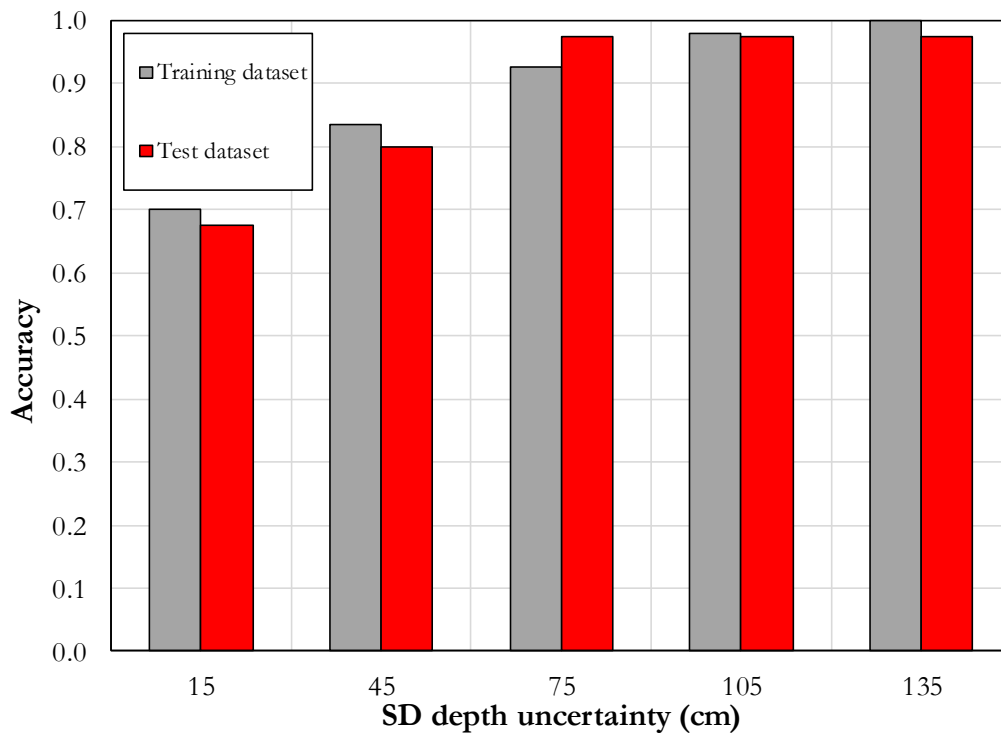


Figure 4-25 Success and prediction rates of SDd map for BLU 61

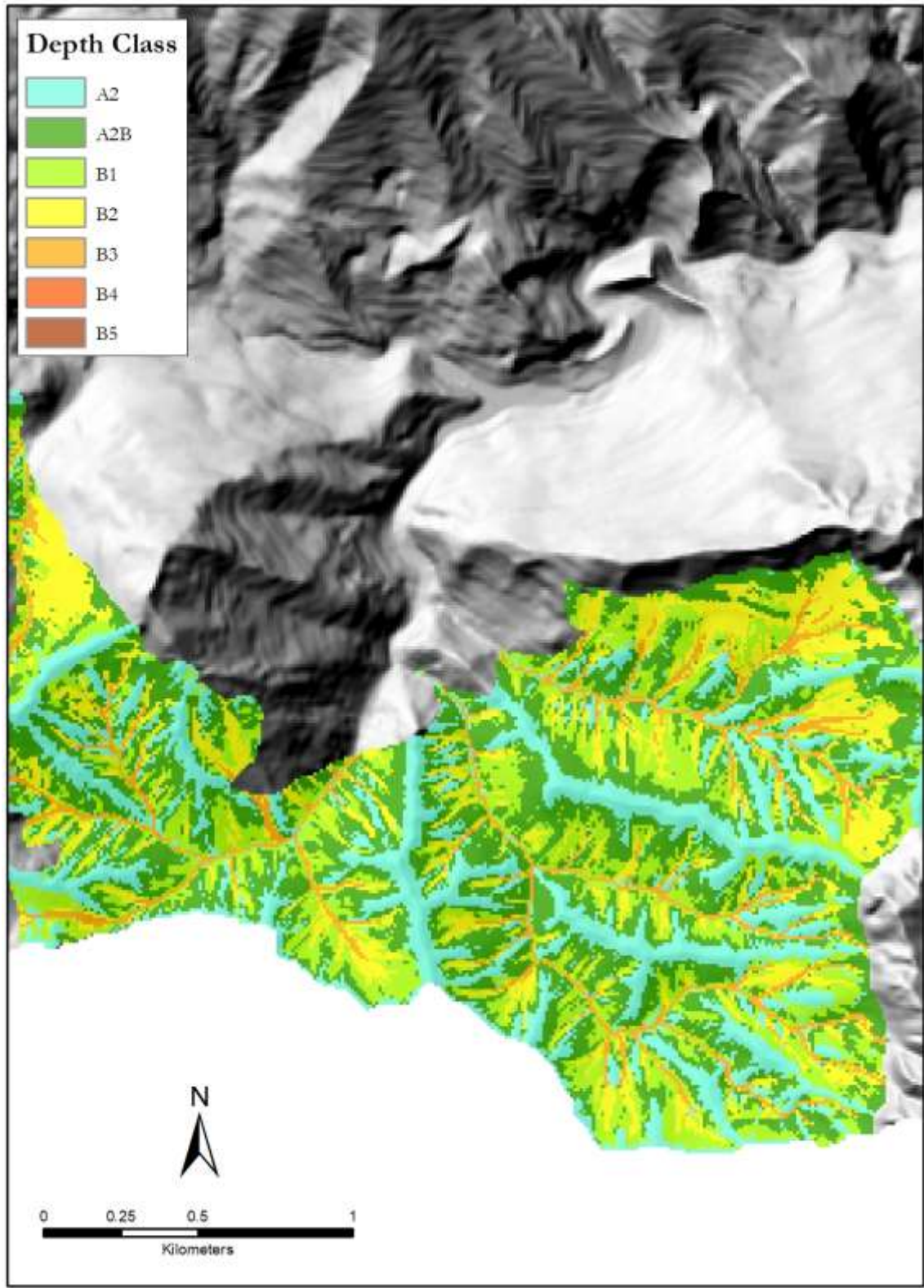


Figure 4-26 BLU61 slope deposits depth map.

BLU 62 – Metarenites and quartzites

Table 4.9 Matrix of depth class data for BLU 62.

Depth range (m)	Depth classes	Morphometric Units									
		1	2	3	4	5	6	7	8	9	10
0 - 0.1	A1										
0.1 - 0.3	A2		1	2	3	26	3	1	5	7	
0.1 - 0.6	A2B	1	1	1		4	4			8	3
0.3 - 0.6	B1	3		2	3		11	3	4	6	1
0.6 - 0.9	B2	5	3	1	7	1	3	1		3	5
0.9 - 1.2	B3	1	10	5	1	1	2				
1.2 - 1.5	B4			5	1						
>1.5	B5		1	1		2		1		3	1
Site observations total		10	16	17	15	34	23	6	9	27	10
Class A probability		0.1	0.1	0.2	0.2	0.9	0.3	0.2	0.6	0.6	0.3
Class B probability		0.9	0.9	0.8	0.8	0.1	0.7	0.8	0.4	0.4	0.7
Maximum frequency		5	10	5	7	26	11	3	5	8	5
Morph. Unit Success Rate		0.5	0.6	0.3	0.5	0.8	0.5	0.5	0.6	0.3	0.5
Assigned Depth class		B2	B3	B4	B2	A2	B1	B1	A2B	A2B	B2

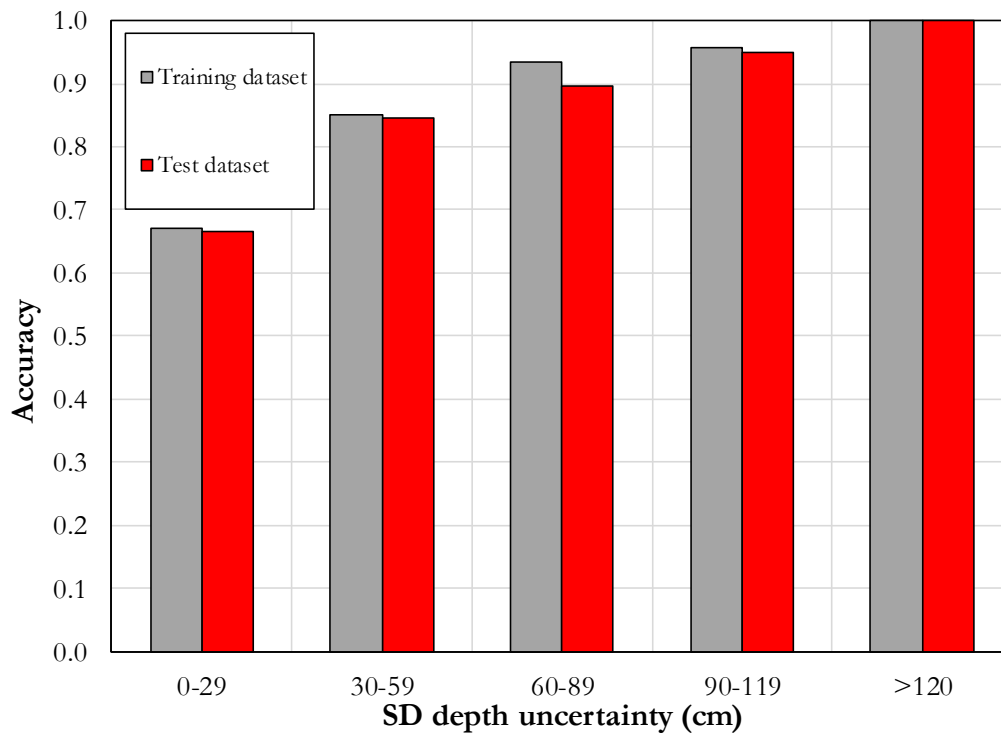


Figure 4-27 Success and prediction rates of SDd map for BLU 62

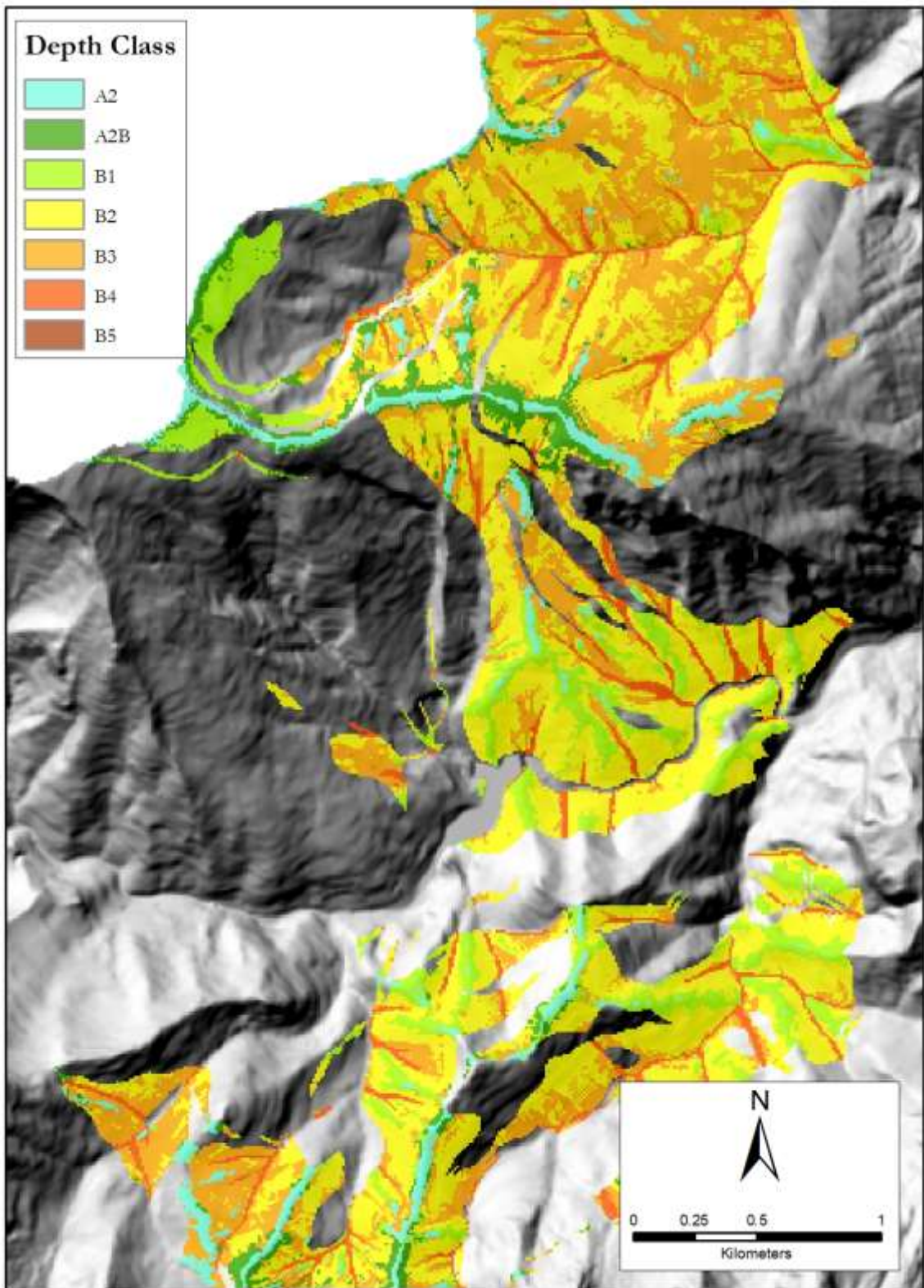


Figure 4-28 BLU62 slope deposits depth map.

4.2.3 Grain size analysis

The results of laboratory analyses and field grain size distribution estimation are presented in the next paragraphs. Then, the comparison of results between the two dataset is described.

4.2.3.1 Laboratory results

For a total of 162 samples, grain size distribution and Atterberg limits were carried out by a private certified geotechnical laboratory. Detailed laboratory results are listed in the Appendix B. In Figure 4-29 results are shown in the plasticity chart based on Atterberg limits. Table 4.10 and Figure 4-30 summarizes the USCS class obtained for samples collected within each BLU.

Table 4.10 USCS class frequency for SD samples collected within each BLU. No samples have been collected in BLU 21.

Bedrock Lithological Unit	USCS class												Total samples
	CL	CL-ML	ML	SC	SC-SM	SM	SP-SM	GC	GC-GM	GM	GP-GM	GW	
11 - Arenites	1	0	2	3	5	34	0	3	2	8	1	0	59
22 - Schists	0	0	0	0	0	1	0	0	1	0	0	0	2
23 - Limestones	1	1	3	4	0	6	0	2	0	4	0	0	21
31 - W.C. Deposits	0	0	1	0	0	2	1	1	0	0	0	0	5
51 - Shales and Marls	0	0	10	7	0	10	0	4	0	2	0	0	33
61 - Phyllites	0	0	5	1	1	6	0	0	0	15	1	1	30
62 - Metarenites	0	0	0	0	0	5	0	2	0	5	0	0	12
	2	1	21	15	6	64	1	12	3	34	2	1	

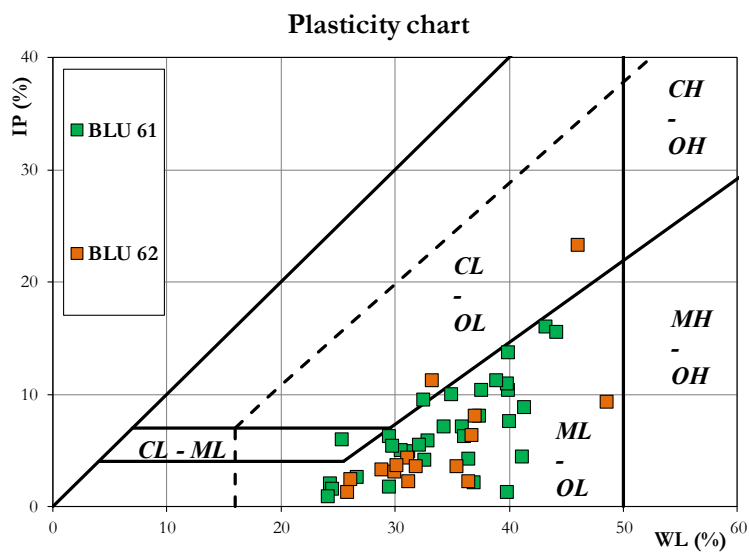
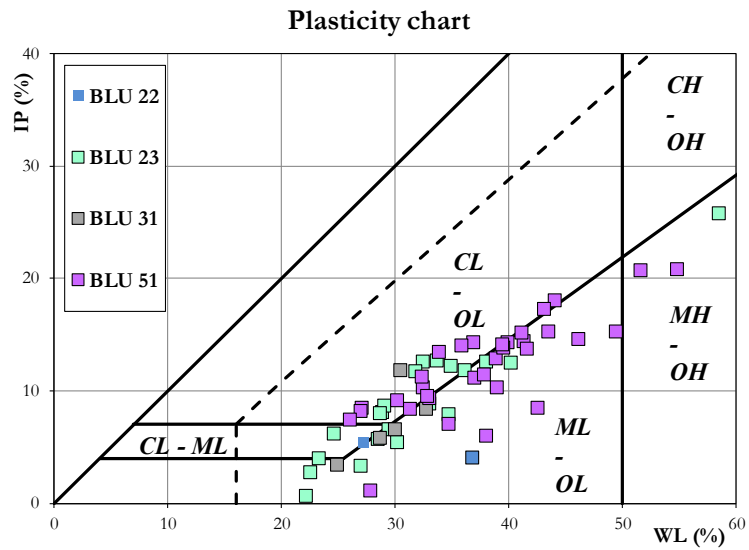
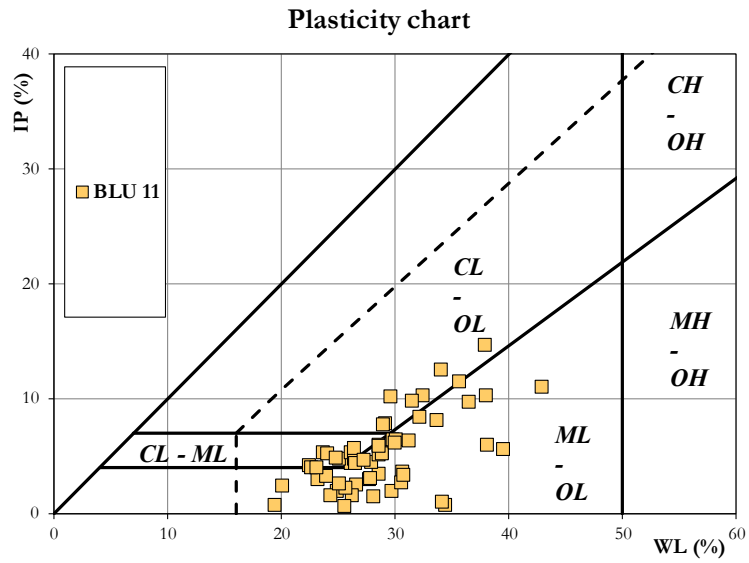


Figure 4-29 Plasticity chart. Note: data for BLU61 and 62 include 42 determinations obtained by a previous research project conducted in an adjacent area (Disperati et al., 2018).

USCS class distribution

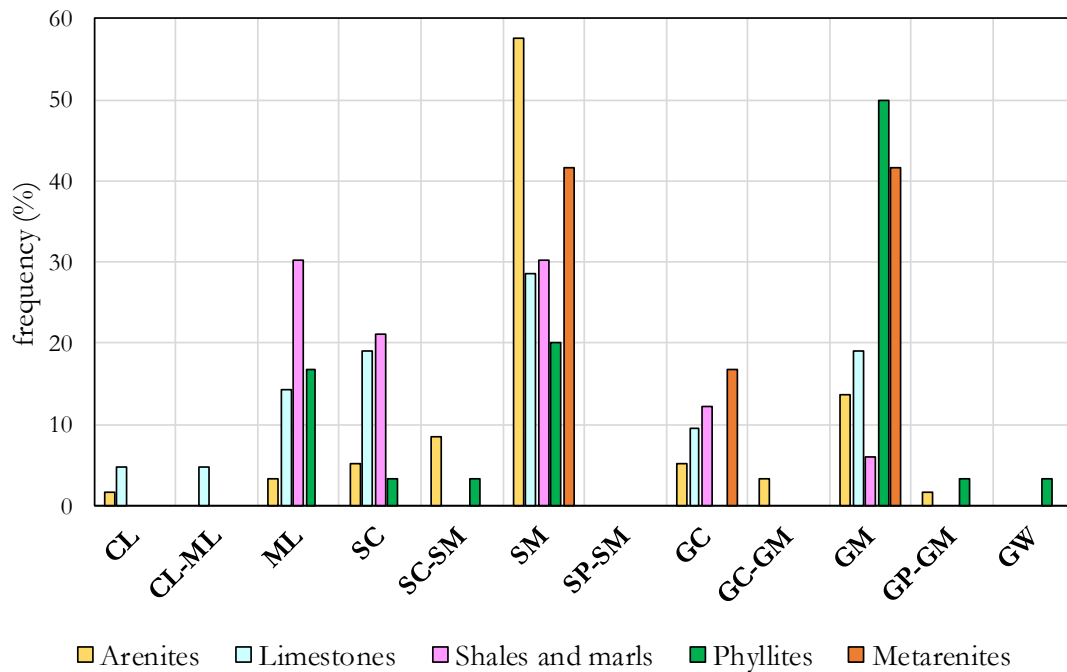


Figure 4-30 USCS class frequency for SD samples collected within each BLU. 11- Arenites, 23-Limestones, 51-Shales and Marls, 61-Phyllites, 62-Metarenites. Note: data for BLU61 and 62 include 42 determinations obtained by a previous research project conducted in an adjacent area (Disperati et al., 2018).

4.2.3.2 Grain size field estimation results

In addition to the analysis of the particle size distribution carried out in the laboratory, the percentages of gravel, sand, silt and clay (fine) were estimated for each observation site, as described in paragraph 2.4. 1. Since the field estimation is semi-quantitative, it is necessary to evaluate the accuracy of the estimation by comparing field estimations with the laboratory results for those observation sites where both data were collected.

In Figure 4-31 the grain size estimation conducted in the field is compared with the laboratory analyses.

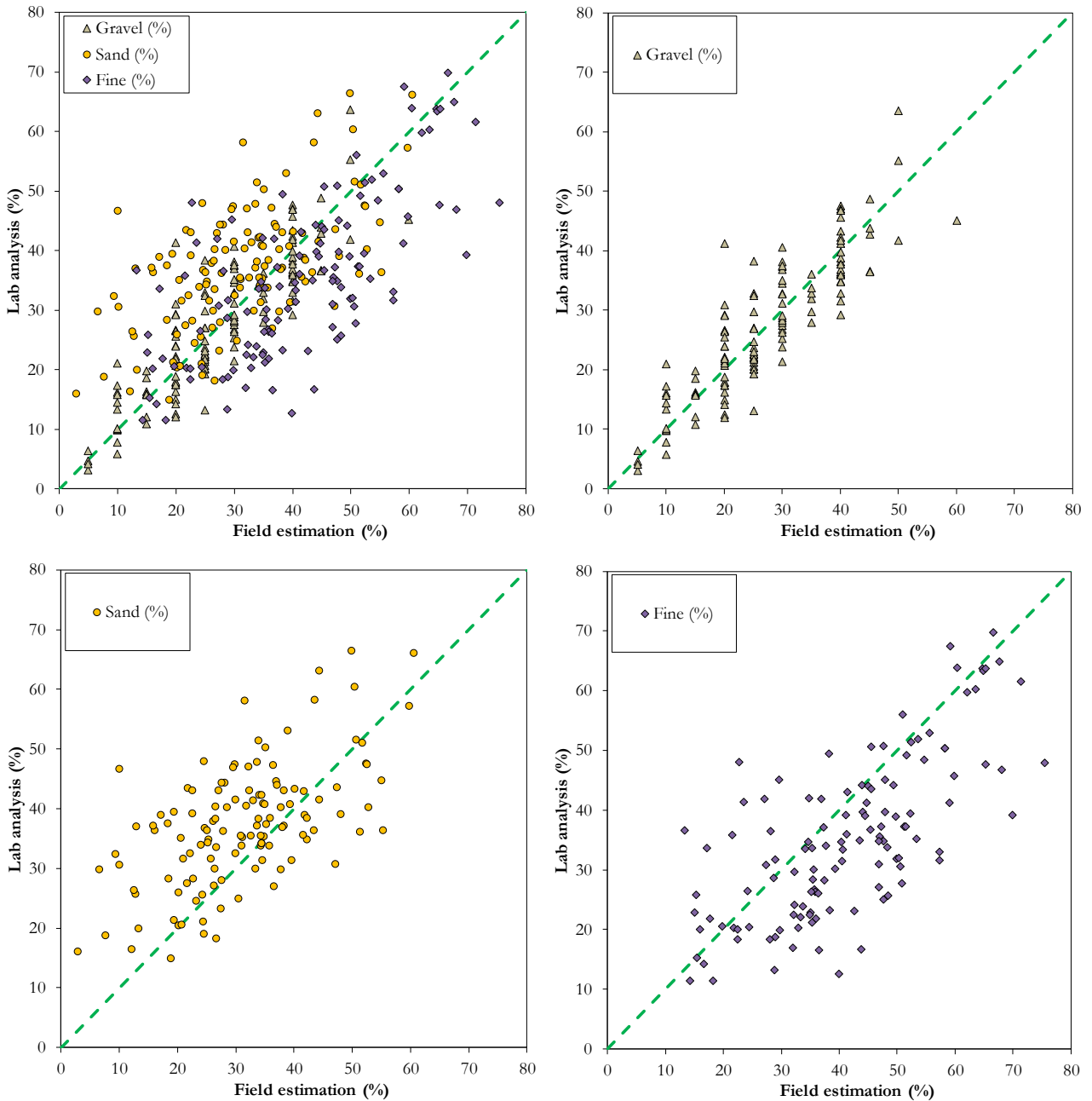


Figure 4-31 Comparison between grain size field estimation and laboratory analysis

The evaluation of the accuracy (Table 4.11) of the field grain size determinations was performed using the Mean Bias Error method (Kato, 2016):

Equation 4-1

$$MBE = \frac{\sum_i^n (field_{gr,sa,fi} - lab_{gr,sa,fi})}{n}$$

Where $camp_{gr,sa,fi}$ is the field estimation of gravel, sand and fines; $lab_{gr,sa,fi}$ is the laboratory analysis according to USCS classification, n is the number of samples.

Table 4.11 Mean Bias Error for grain size distribution

<i>MBE (%)</i>		
Gravel	Sand	Fine
0	-6	6

4.2.4 Unit weight results

Table 4.12 summarizes the statistical results of unit weight determination for each BLU. A complete list of laboratory results is provided in Appendix B.

Table 4.12 Summary of Unit Weight laboratory analysis

BLU	Samples	Dry Unit Weight			
		min	max	average	dev. stand.
11	90	10.5	17.6	13.7	1.8
22	2	12.4	12.7	12.5	0.2
23	20	11.7	16.3	13.3	1.4
31	7	11.3	16.0	14.1	1.8
51	31	11.1	16.7	13.5	1.2
61	9	11.0	15.9	12.7	1.7
62	10	10.5	16.7	12.6	1.9

4.2.5 Engineering Geological Map of Slope Deposits

4.2.5.1 Friction angle of gravelly SD

From the laboratory results the most represented USCS class is the GM among the gravels, which correspond to a silty gravel. This USCS class is not included in the diagram shown in Figure 2-15, since in this diagram the friction angle is obtained for cohesionless materials without plastic fines (NAVFAC, 1986). In order to assess the friction angle of the gravels occurring within the study area, a literature review was performed (Holtz, 1961; Schmertmann, 1978; Bolton, 1986; NAVFAC, 1986; Fragaszy et al., 1992; Fannin et al., 2005; Rollins et al., 2005; Kulhawy and Chen, 2007; Duncan et al., 2014; Ching et al., 2017). The data presented in the above-mentioned studies were plotted in a scatter plot representing the friction angle versus relative density, as this latter parameter is regarded as the most important to control shear strength of gravels (Figure 4-32). Figure 4-33 reports the relative density and friction angle data for a subset of samples from the above literature, having grain size characteristics (such as D50 and D60), dry unit weight and confining stress similar to the slope deposits analysed in this study.

Figure 4-33 shows that the majority of data fall between the Schmertmann and NAVFAC – GP functions and the distribution of points does not appear to depend on the USCS class. The regression functions (black functions) obtained for each USCS class are each other sub-parallel and mostly overlap with the NAVFAC - GW function. Therefore taking into account the results of the literature, it was assumed that the NAVFAC – GW function reasonably can be used to describe the variation of friction angle as a function of the relative density for the gravelly SD under study.

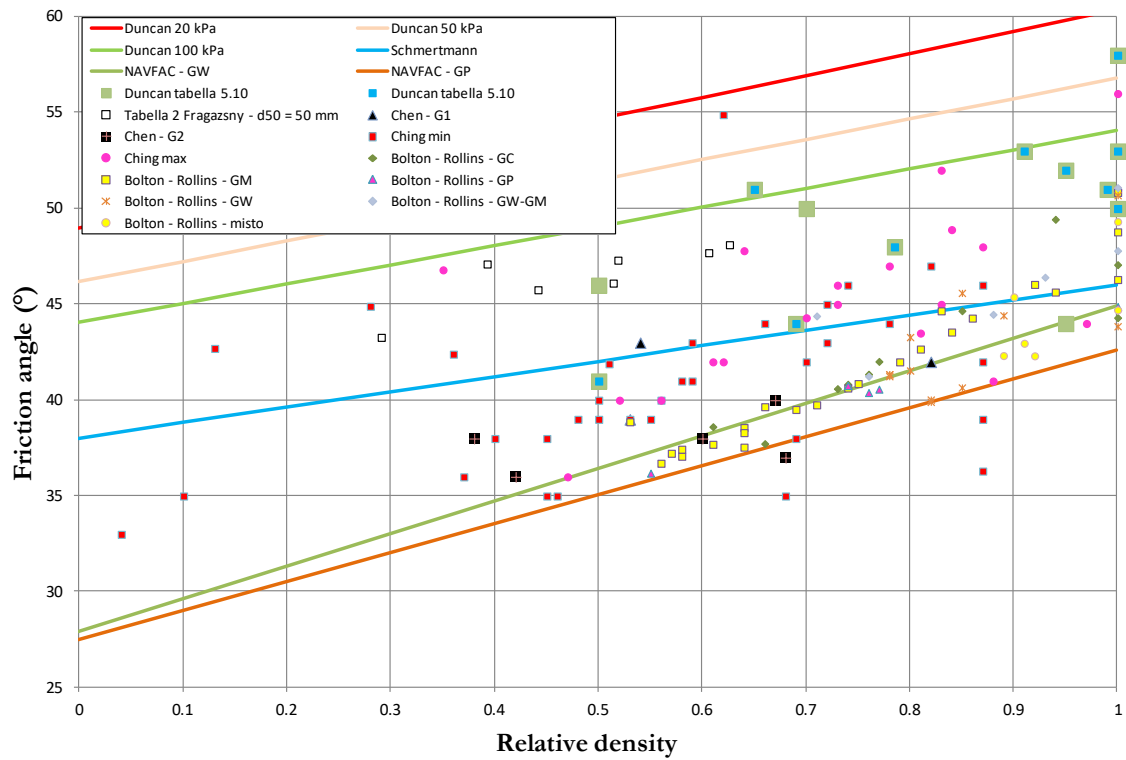


Figure 4-32 Relative density - friction angle diagram resulted from literature review.

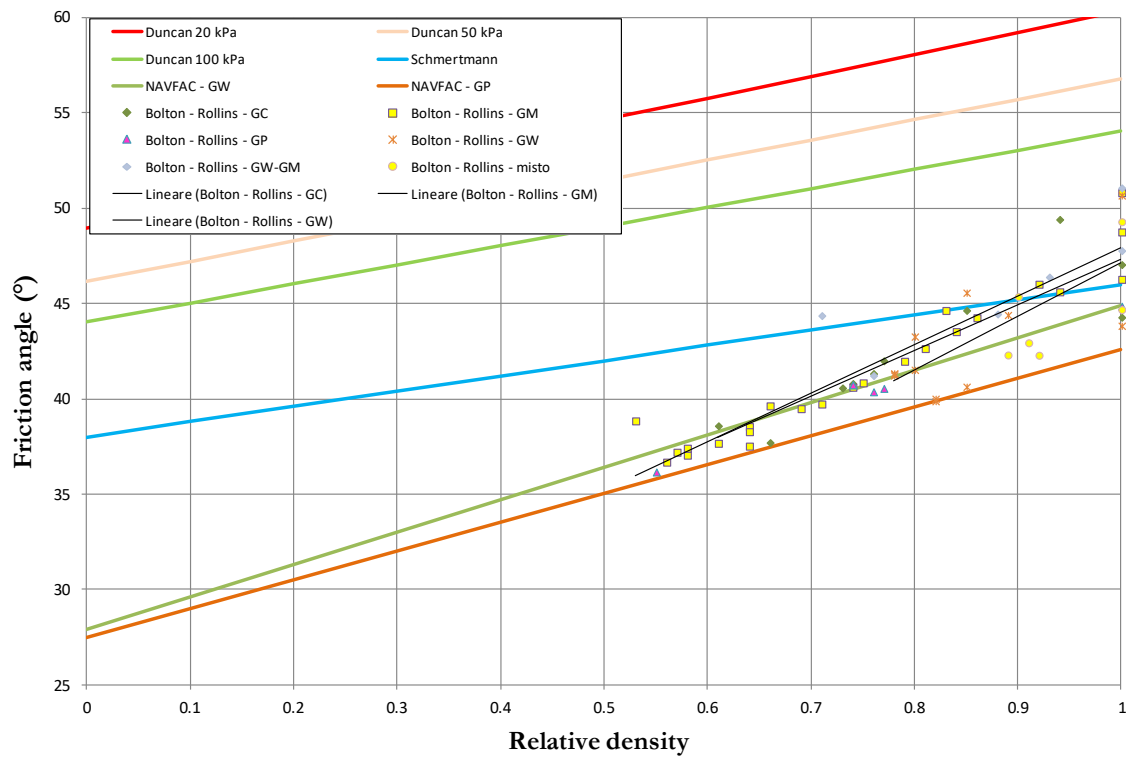


Figure 4-33 Relative density - friction angle diagram taking into account only the data with geotechnical features similar to the SD of this work.

4.2.5.2 Friction angle assessment using NAVFAC diagram

According to the results reported in Table 4.10 and Figure 4-30, the functions of ML and SM were used to estimate friction angle values from the NAVFAC diagram (Figure 2-15), because those are the most frequent USCS classes for slope deposits mainly composed by fine and sand. Instead, for gravelly materials, as mentioned above, the GW function was used. Due to the lack of enough samples, BLU 31 is not reported, while marbles, metacarbonates and limestones data were grouped together as well as for phyllites and metarenites (from Figure 4-34 to Figure 4-37).

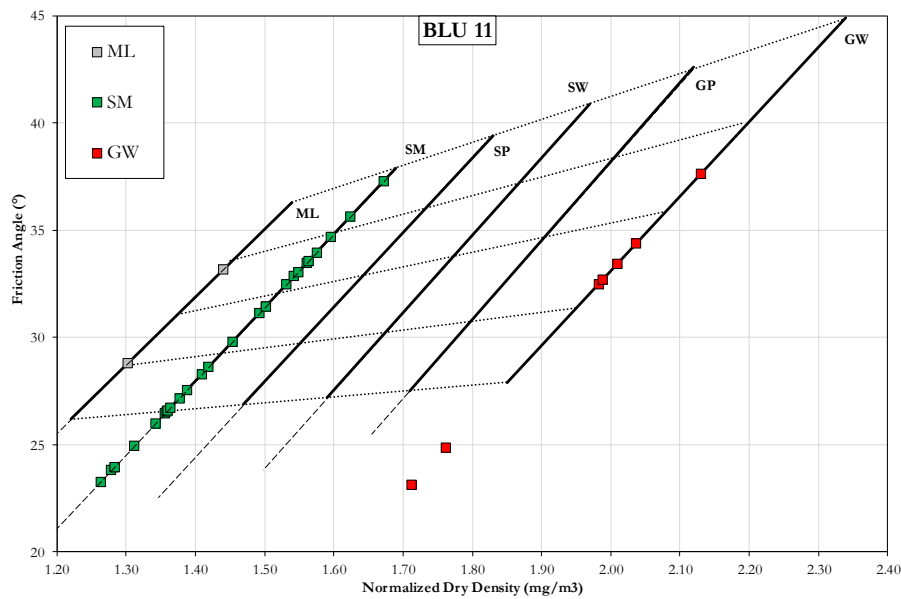


Figure 4-34 NAVFAC diagram for BLU 11

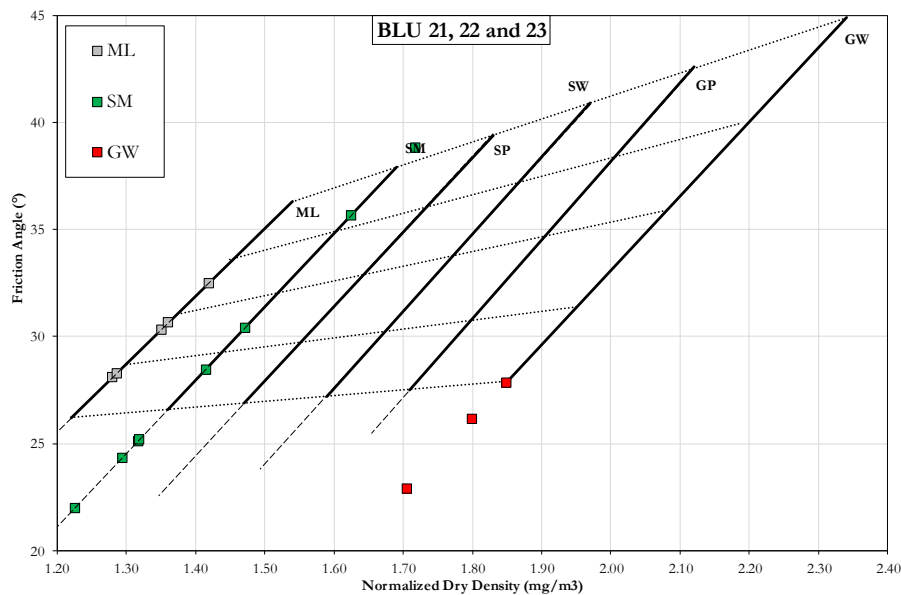


Figure 4-35 NAVFAC diagram for BLU 21,22 and 23

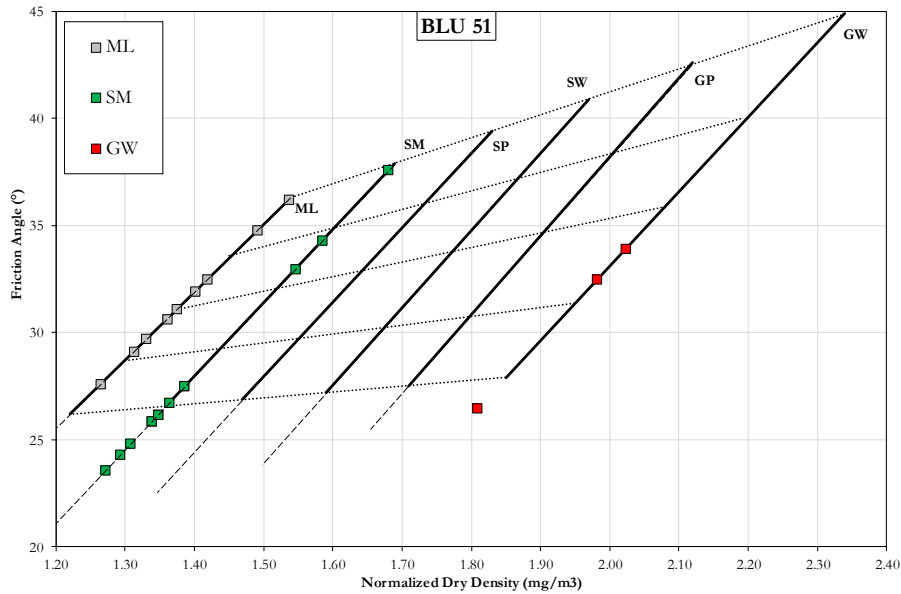


Figure 4-36 NAVFAC diagram for BLU 51

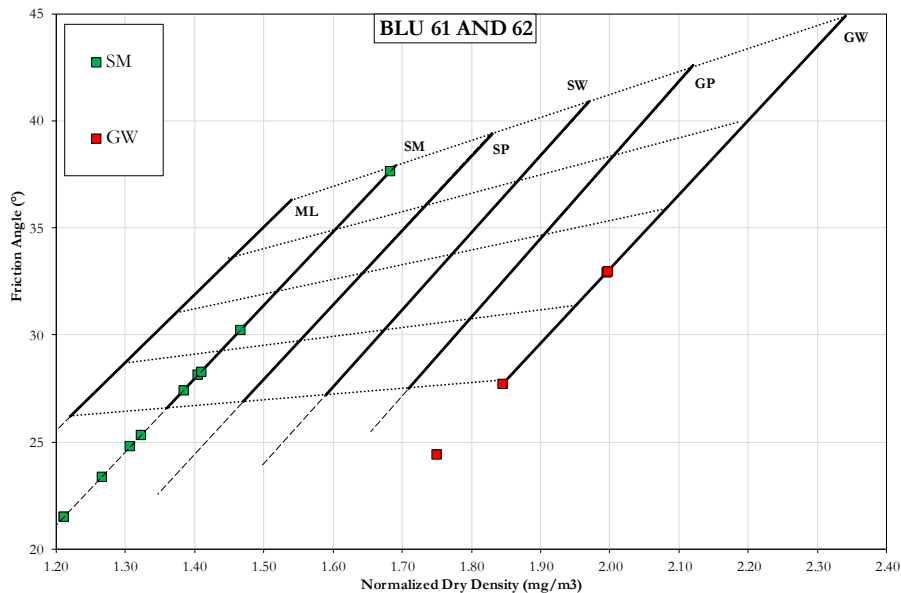


Figure 4-37 NAVFAC diagram for BLU 61 and 62

4.2.5.3 Engineering Geological Units parameters

The SD properties assessed at BLU scale with the procedures described up to now have been obtained exclusively from laboratory data. In order to carry out a regionalized study, it is essential to rely also on field grain size estimations, which being expeditious and cheaper, provide wider dataset. Recent literature studies (Vos et al., 2016) have shown that the deviation between the field estimation and laboratory analysis is in the order of 4 - 16%. The same authors pointed out that there is an intrinsic uncertainty regarding the method by which the grain size fractions in the field are estimated (e.g. USDA Triangle): for the same textural class the range of variability of the corresponding grain size fraction can vary in the

order of 10–45%. Therefore, taking into account these uncertainties, an average bias of 6% (Table 4.11) is considered acceptable, highlighting how the field grain size determinations proved to be quite reliable. Hence, a simplified classification approach was adopted for the field estimations, following the USCS guidelines, which can be described as follows:

- G: gravelly SD (> 50% retained at 0.075 mm sieve), % gravel > % sand;
- S: sandy SD (> 50% at 0.075 mm sieve), % gravel ≤ % sand;
- F: fine grained SD (≤ 50% at 0.075 mm sieve).

Therefore, the association between USCS classes and the classification mentioned above is reported in Table 4.13. In Figure 4-38 is reported the distribution of simplified USCS classes for the SD of each BLU integrating field estimation and laboratory analysis is reported. The prevailing of gravels is due to the fact that sampling gravelly rich SD for unit weight determination and grain size estimation laboratory analysis is impossible with the tools used.

In Table 4.14 are reported the friction angle and dry unit weight resulted from the NAVFAC diagram at BLU scale for each USCS/Simplified USCS class. The saturated soil unit weight has been calculated considering a porosity range about 40%-50%. Then, the saturated density has been carried out adding 5 kN/m³ to the soil dry density. The minimum-maximum ranges were assessed calculating the first and the third quartile of the distributions. These ranges are used to assess the parameters (ϕ and γ_s) at Engineering Geological Unit (EGU) scale calculating the weighted average taking into account the frequency of USCS simplified classes. Note that ML and GW friction angle and dry unit weight values are constant for each BLU. While the ML are not very well represented in the study area, the low number of GW laboratory analysis must be attributed to the difficulty in collecting the samples. In fact, for the unit weight determination, the sampler is not able to penetrate and collect the specimen due to the rich content of gravel, moreover to obtain an accurate grain size estimation in laboratory the minimum sample weight must exceed 6 kg if the largest significant particle size have a diameter of about 75 mm. For the reason listed above, the parameters attributed to fines and gravels are computed using all the samples collected in all the BLUs.

Table 4.13 Association among USCS, simplified classification assumed for deposits which underwent field estimation only, and NAVFAC function used for friction angle estimation.

USCS (simplified)	USCS	NAVFAC
F	MH	ML
	CH	
	ML	
	CL	
S	SC-SM	SM
	SC	
	SM	
	SW-SM	
G	GC-GM	GW
	GC	
	GM	
	GP-GC	
	GP-GM	
	GW	

Distribution of simplified USCS classes for the integrated dataset

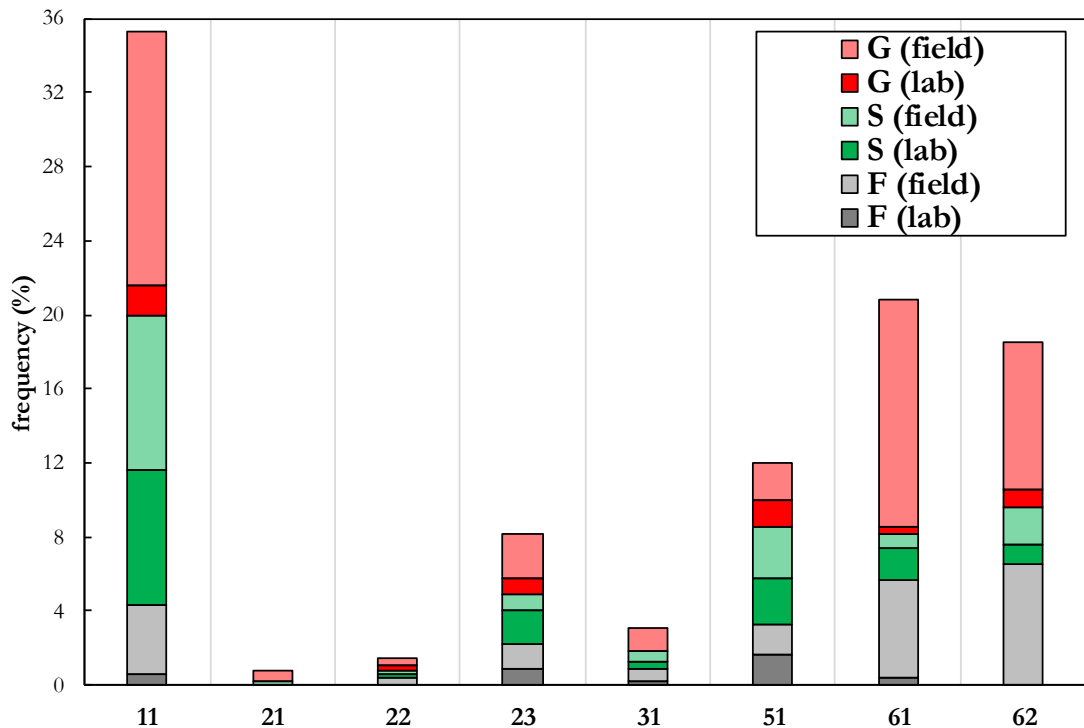


Figure 4-38 Distribution of simplified USCS classes for BLU integrating field estimation and laboratory analysis

Table 4.14 Friction angle and dry unit weight for BLU and relative EGU

Bedrock Lithologica Units and Engineering Geological Units	USCS	Simplified USCS		Friction Angle (°)	Dry Unit Weight (kN/m ³)	Saturated Unit Weight (kN/m ³)
11 EGU: 1101-1112	ML	F	Min	26	12.8	17.8
			Max	33	13.9	18.9
	SM	S	Min	27	13.3	18.3
			Max	33	15.2	20.2
	GW	G	Min	28	12.8	17.8
			Max	33	15.4	20.4
21 EGU: 2101-2110	ML	F	Min	26	12.8	17.8
			Max	33	13.9	18.9
	SM	S	Min	27	12.9	17.9
			Max	33	15.2	20.2
	GW	G	Min	28	12.8	17.8
			Max	33	15.4	20.4
22 EGU: 2201-2210	ML	F	Min	26	12.8	17.8
			Max	33	13.9	18.9
	SM	S	Min	27	12.9	17.9
			Max	33	15.2	20.2
	GW	G	Min	28	12.8	17.8
			Max	33	15.4	20.4
23 EGU: 2301-2312	ML	F	Min	26	12.8	17.8
			Max	33	13.9	18.9
	SM	S	Min	27	12.9	17.9
			Max	33	15.2	20.2
	GW	G	Min	28	12.8	17.8
			Max	33	15.4	20.4
31 EGU: 3101-3105	ML	F	Min	26	12.8	17.8
			Max	33	13.9	18.9
	SM	S	Min	27	12.9	17.9
			Max	33	15.1	20.1
	GW	G	Min	28	12.8	17.8
			Max	33	15.4	20.4
51 EGU: 5101-5110	ML	F	Min	26	12.8	17.8
			Max	33	13.9	18.9
	SM	S	Min	27	13.1	18.1
			Max	28	13.6	18.6
	GW	G	Min	28	12.8	17.8
			Max	33	15.4	20.4
61 EGU: 6101-6114	ML	F	Min	26	12.8	17.8
			Max	33	13.9	18.9
	SM	S	Min	28	12.6	17.6
			Max	29	14.1	19.1
	GW	G	Min	28	12.8	17.8
			Max	33	15.4	20.4
62 EGU: 6201-6210	ML	F	Min	26	12.8	17.8
			Max	33	13.9	18.9
	SM	S	Min	28	12.6	17.6
			Max	29	14.1	19.1
	GW	G	Min	28	12.8	17.8
			Max	33	15.4	20.4

4.3 BEDROCK GEO-MECHANICAL CHARACTERIZATION

The field survey of shallow landslides showed that about 60% of the visited landslides fractured and weathered bedrock underlying the SD. In order to understand the role played by bedrock for shallow landslides development one objective of this PhD research was to analyse and characterize the engineering geological properties of the uppermost bedrock. Due to the wide spatial extent and continuity as well as the high frequency of landslides involving this formation (Figure 3-12), the research focused the attention on the analysis of the rock masses of the Macigno Formation. As described in paragraph 2.2, a field survey was carried out following the same sampling strategy adopted for the slope deposits, that is, bedrock analyses were conducted inside the landslides (INSIDE), near (NEAR) and in the areas not involved by slope failures (FAR). For every 105 investigation sites, Schmidt hammer rebound values were measured, along with orientation and spacing of the main discontinuities, and the "Geological Strength Index" (GSI). In order to explore the distribution of bedrock properties and variability, a descriptive statistical analysis have been performed (Figure 2-1).

In Figure 4-39 the distribution of investigation sites is shown. Orange squares correspond to investigation sites conducted in correspondence of (INSIDE) visited landslides involving bedrock. Yellow squares correspond to observation sites close (less than 250 meters, NEAR) to landslide (both SDL and BRL). Finally, in order to analyse bedrock properties variability in the whole BLU 11, data from investigation sites located at distance higher than 250 meters were conducted (FAR).

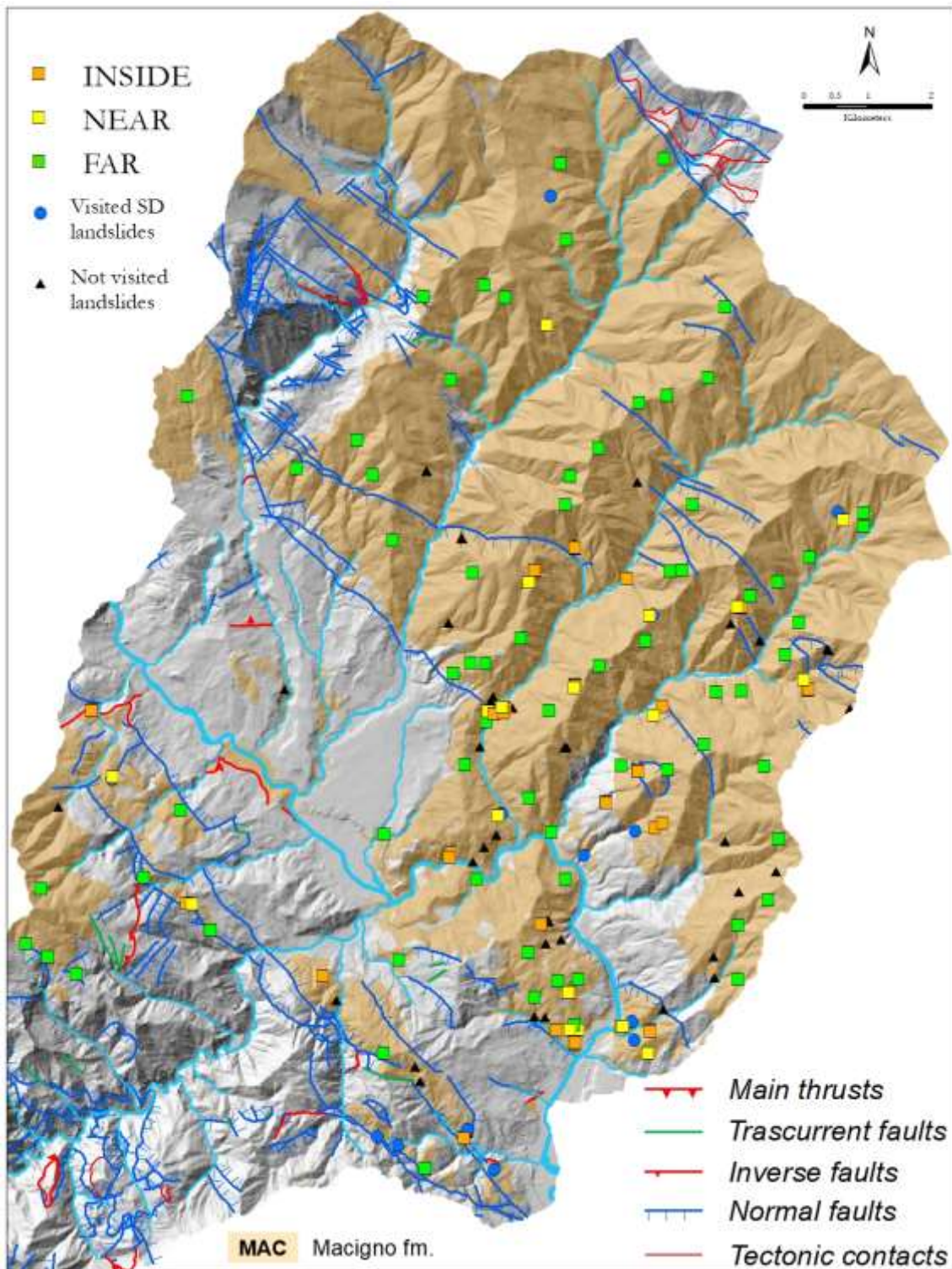


Figure 4-39 Distribution of investigation sites for bedrock geo-mechanical characterization. Orange squares (INSIDE) correspond to visited landslides involving bedrock.

4.3.1 Descriptive statistics of bedrock geo-mechanical properties

One of the aims of the field work was to investigate whether the bedrock geo-mechanical properties change following spatial criteria which may be related to the occurrence of shallow landslides. In Figure 4-40 the boxplot of the distribution of geo-mechanical properties of bedrock, such as Schmidt Hammer (SH) rebound value (Rv, average of 400 measurements), Joint volume density (Jv) and Geological Strength Index (GSI). The diagrams show that geo-mechanical properties inside landslides are worse than NEAR and FAR. The deviation is especially higher for Rv and Jv. These results suggest that bedrock quality may have played a role for slope failures occurrence. The relations among these variables have been investigated (Figure 4-41). Except the scatter plot of Rv vs GSI (Figure 4-41c) which highlights a correlation between the two variables, the other diagrams display a more or less dispersed pattern. Figure 4-41a compares the average and the standard deviation of Schmidt Hammer rebound value. It is worth noting that the graph shows two different patterns, one dispersed, with relatively low values of Rv and high variability of standard deviation, and one clustered, where the standard deviation is included mainly between 4 and 6 with relatively higher Rv values in respect to the dispersed pattern.

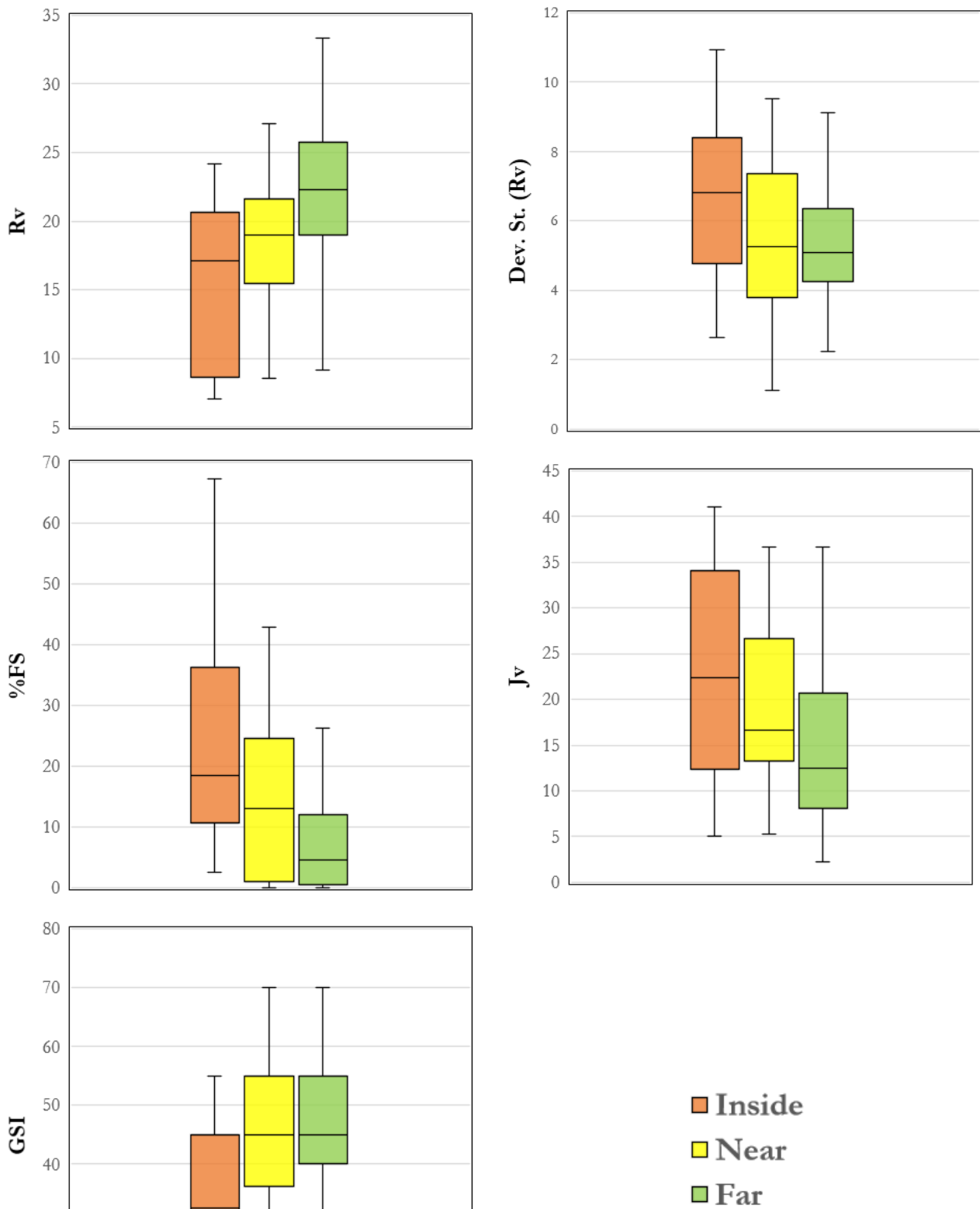


Figure 4-40 Boxplot distribution of geo-mechanical properties of bedrock inside, near and far from landslides.

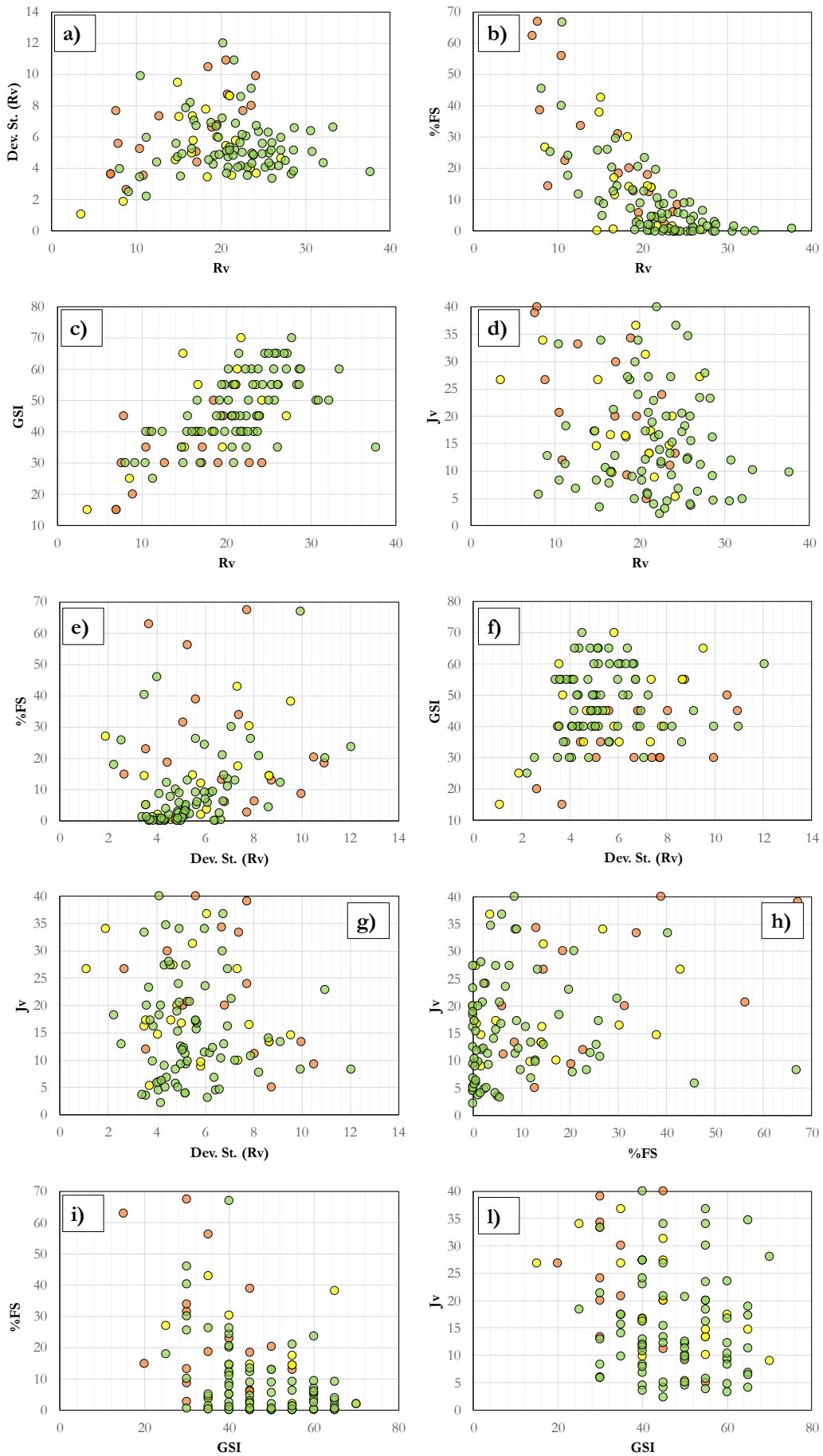


Figure 4-41 Scatter plot among bedrock geo-mechanical properties.

4.3.2 Uni-variate spatial cluster analysis of bedrock properties

In order to evaluate the spatial variability of bedrock geo-mechanical properties, a uni-variate cluster analysis was performed by implementing the Local Moran's Index algorithm, as described in paragraph 2.5.3. This tool allows to verify if the distribution of the analysed variable is spatially dispersed or clustered, identifying two clusters, high values and low values, and the respective outliers. "Not significant" values represent areas in which the variable is randomly distributed. The cluster analysis has been performed for five variables: average SH rebound value (R_v), R_v standard deviation, percentage of low full-scale rebound values, GSI and J_v . For each variable, the incremental spatial autocorrelation analysis has been conducted in order to assess the minimum distance at which the clustering occurs. Observation sites conducted inside landslides (INSIDE) were excluded from the analysis in order to check the regional and local variability of bedrock properties outside the areas affected by slope movements. The results of spatial autocorrelation and uni-variate cluster analysis are presented from Figure 4-42 to Figure 4-47. For each analysis, a box plot is provided describing the distribution of the variable within the clusters.

The uni-variate clustering display good performance when applied for R_v , J_v and GSI. In Figure 4-43, "Not significant" observation sites separate the "High" and "Low" clusters, located in the northern and south-eastern portion of the study area, respectively. The shape of the "Not Significant" data delineate an area which is more or less subparallel to the main normal faults. A similar configuration is displayed by the clustering applied to the GSI. In this case, the "High" cluster is reduced in number, increasing the "Not Significant" data in the eastern portion of the study area (Figure 4-47). A very different configuration is provided by the clustering applied to the J_v (Figure 4-46): the "High" cluster (representing heavy fractured rock masses, hence low quality) has an elongated shape oriented S-NE, more or less perpendicular to the main normal faults, while the "Low" cluster coincides with the "High" cluster of R_v and GSI. The uni-variate cluster analysis applied to low full-scale rebound values (Figure 4-44, %FS) and standard deviation of R_v (Figure 4-45) is characterized by a large amount of "Not Significant" data, meaning that those variables have not a clear clustered pattern.

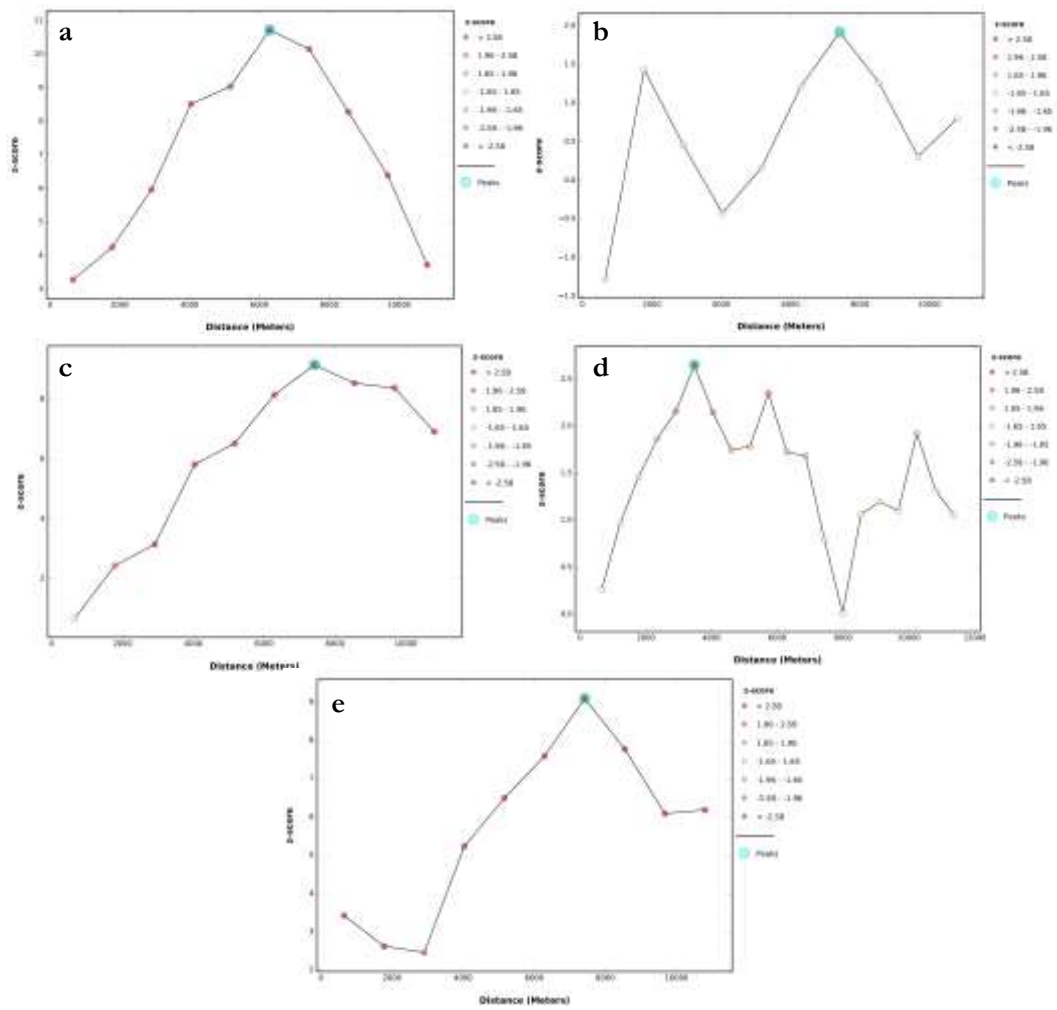


Figure 4-42 Spatial Autocorrelation by Distance plots of the variables used to conduct the Cluster and Outlier Analysis. a- SH rebound value. b- SH rebound value standard deviation. c- SH low full-scale rebound values. d- Joint Volume Density. e- Geological Strength Index.

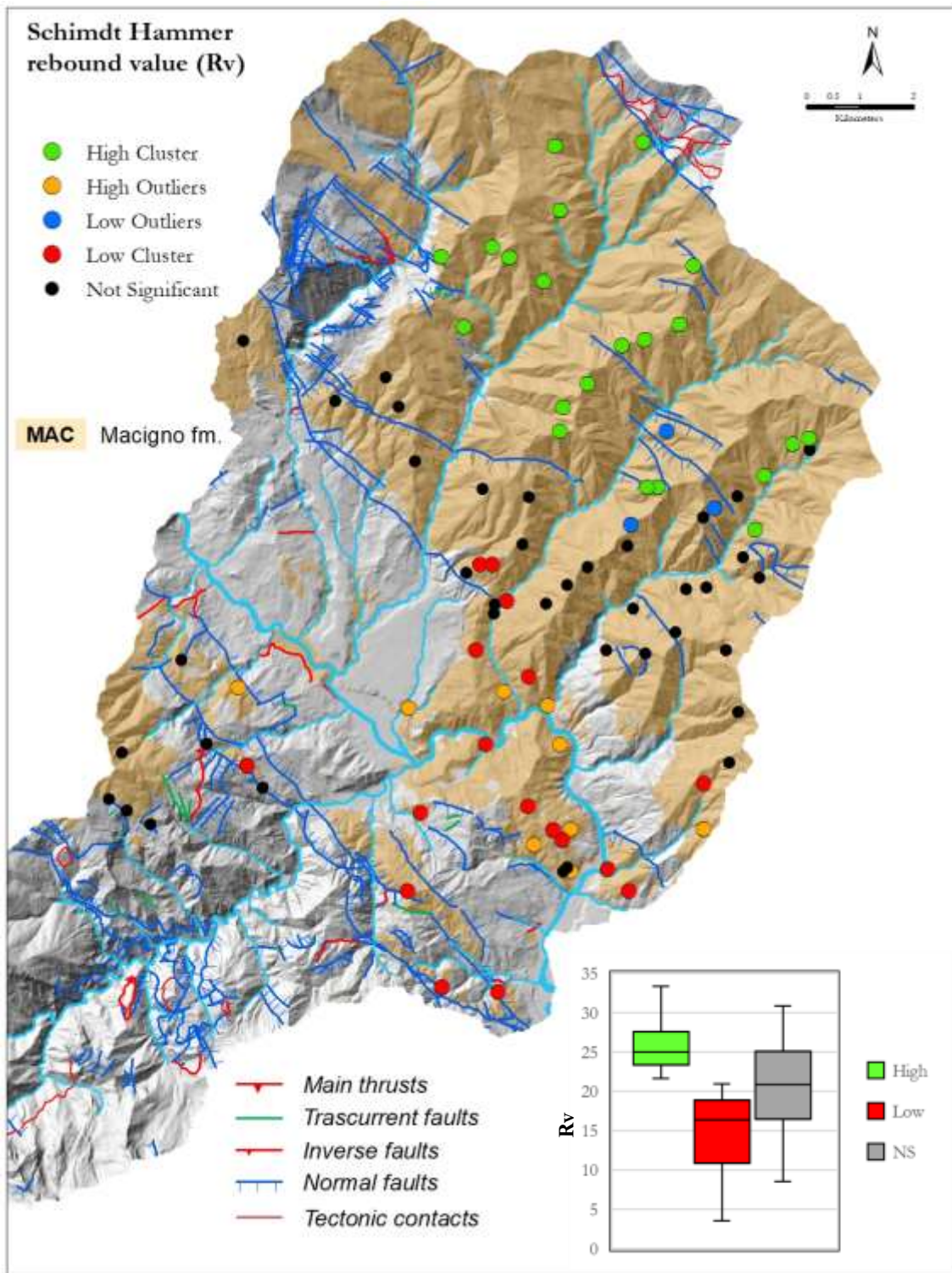


Figure 4-43 Cluster and Outlier Analysis of Schmidt Hammer rebound value Rv

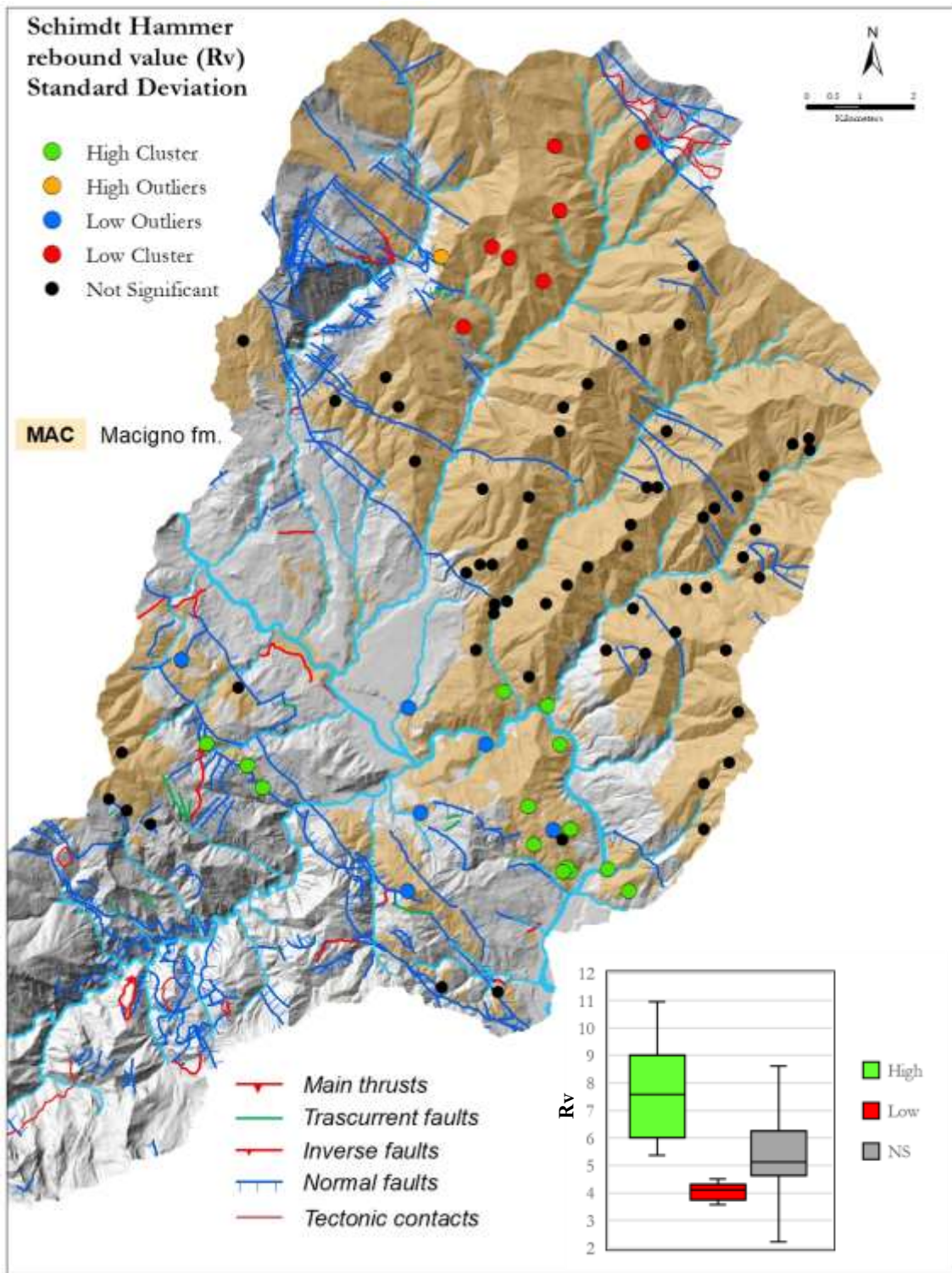


Figure 4-44 Cluster and Outlier Analysis of Rv standard deviation

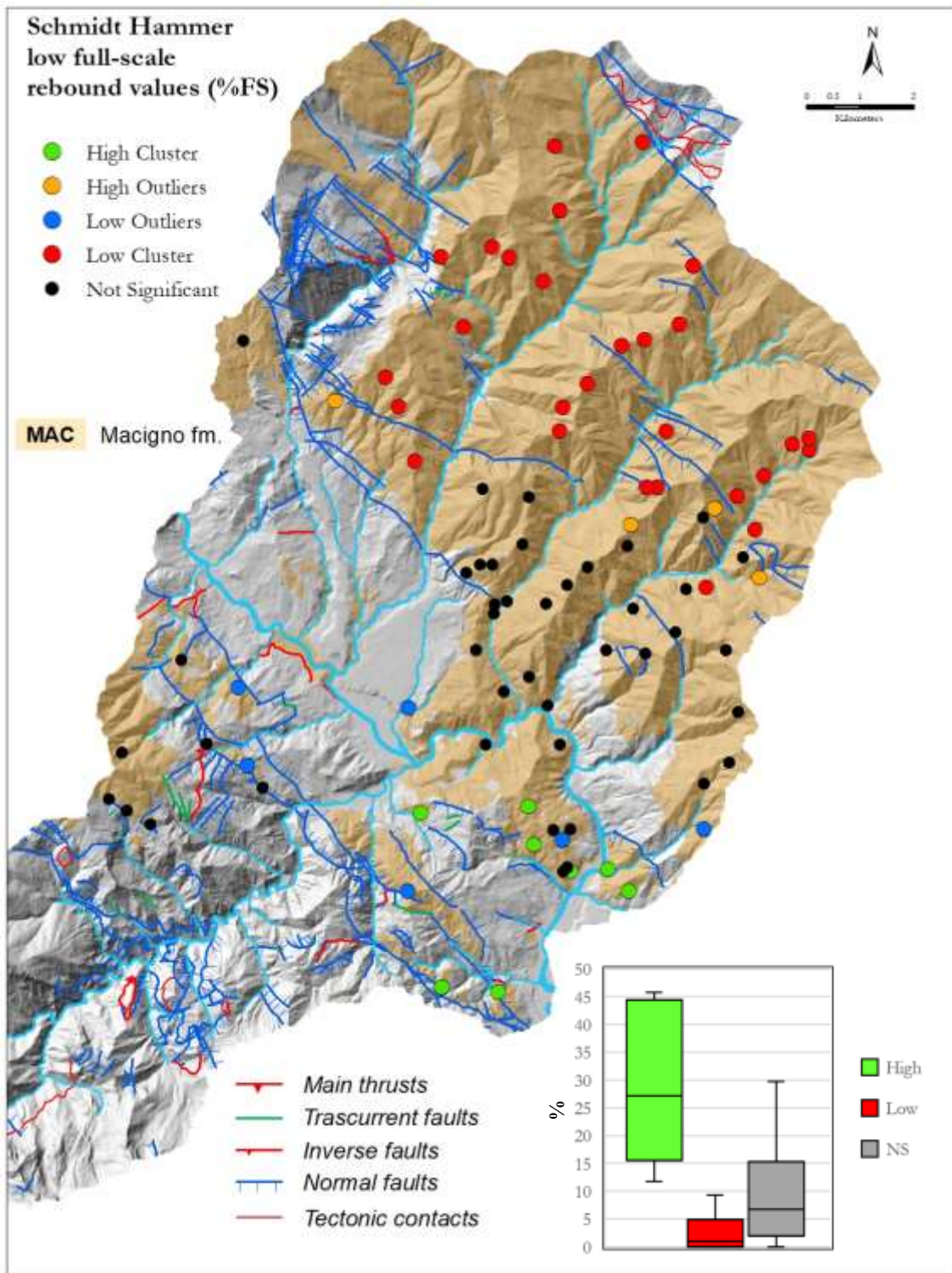


Figure 4-45 Cluster and Outlier Analysis of the percentage of low full-scale rebound values

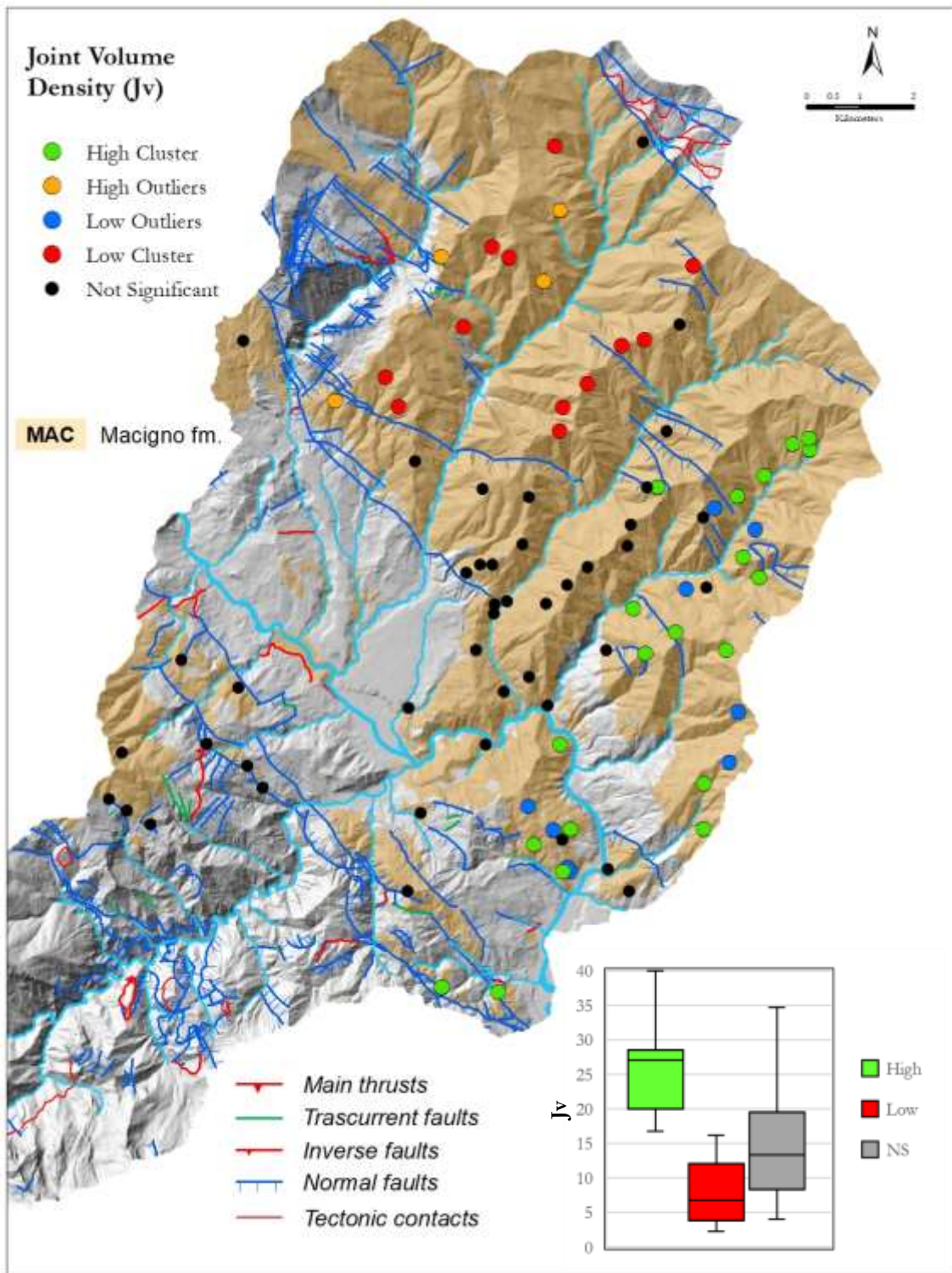


Figure 4-46 Cluster and Outlier Analysis of Joint Volume Density

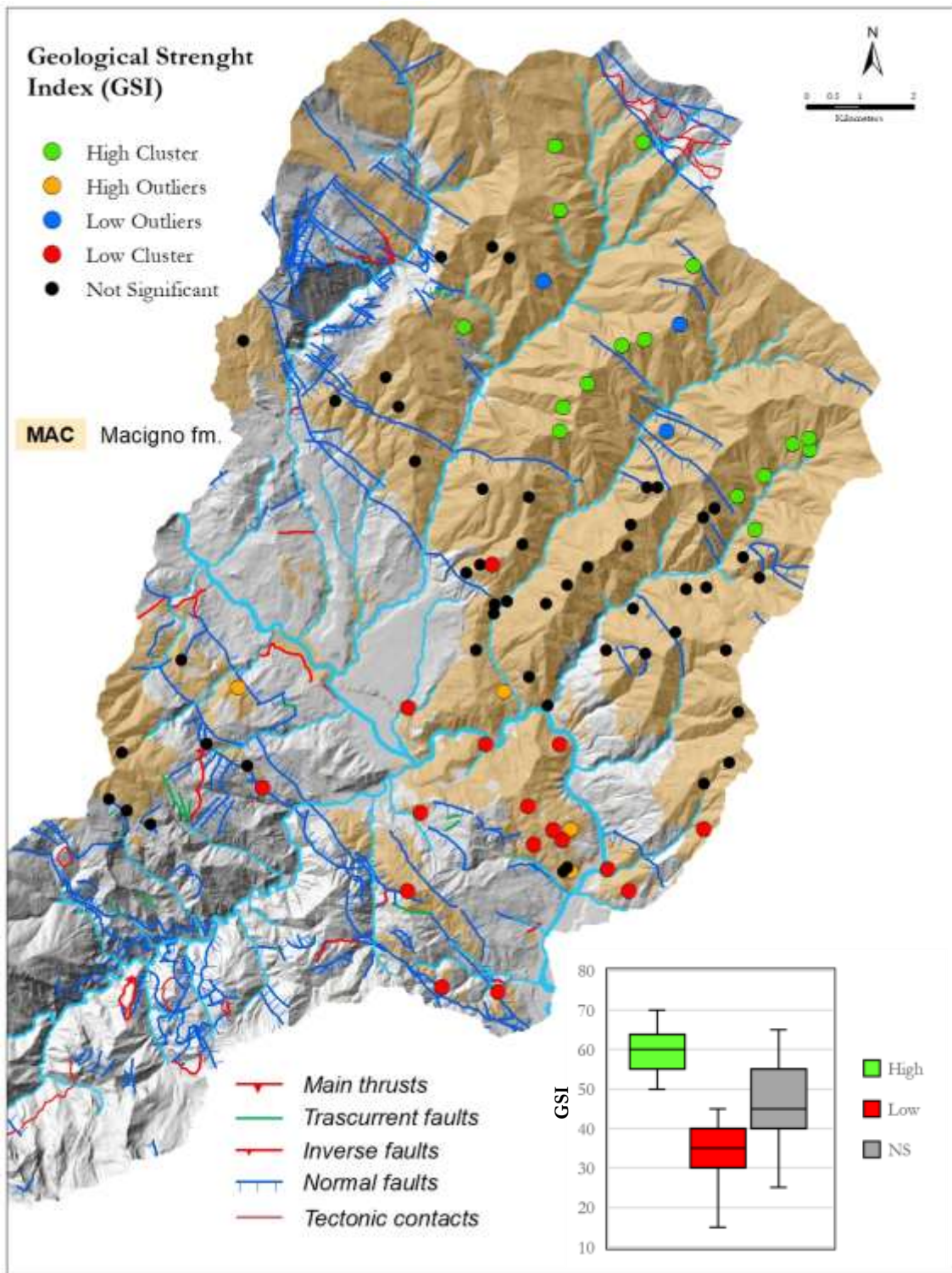


Figure 4-47 Cluster and Outlier Analysis of Geological Strength Index

4.3.3 Multi-variate cluster analysis

Uni-variate clustering has shown that individual variables show a more or less pronounced spatial clustering of the geo-mechanical properties of bedrock. In order to understand how these variables have a dependency with each other and how the datasets of bedrock properties are spatially distributed, it was necessary to perform a multi-variate cluster analysis. In summary, this analysis utilizes unsupervised machine learning methods to determine natural groupings within the data. These classification methods are considered unsupervised as they do not require a set of pre-defined classes to guide or train the grouping of your data. Further description is provided in paragraph 2.5.4.

The analysis was performed for the following variables: Schmidt Hammer rebound value (Rv), Joint volume density (Jv) and Geological Strength Index (GSI). After conducting several tests, the number of neighbours considered in the analysis is 8. The number of output clusters to be obtained was assessed computing the pseudo F-statistic plot (Figure 4-48). This diagram shows a sharp variation of the F-statistic slope when the number of clusters is 4, which is the output of the analysis. The output resulting from the multi-variate cluster analysis is presented in Figure 4-49. The four groups (clusters) resulted to be spatially discriminated, except in the centre of the study area where groups 2,3 and 4 meet at a triple point, enclosed between two normal faults. The group 1 is isolated from the others. This is likely due to the fact that those data resulted to be "Not Significant" in the uni-variate cluster analysis.

Cluster statistics are reported in Figure 4-50 and Figure 4-51. In Figure 4-50 are reported the statistics either for groups and variables. To enhance the reading of the results, the mean, maximum, and minimum values for each group (dot and bars, respectively) of the variables involved (Rv, Jv, GSI) in the analysis are plotted in box plots describing the distribution of those variables. At the bottom of Figure 4-51, the statistics for each variable (Rv, Jv, GSI) are shown and plotted in the box plots (mean, min and max). Figure 4-51 visually summarizes the characteristics of the groups. This parallel box plot shows the average values of the groups for the variables involved. Group 2 appears to have the lowest average Jv, and the highest GSI and Rv values, representing the sites where the rock mass quality is the best. Similar values of GSI and Rv are reached by group 3, which however has the highest Jv, suggesting extensive fracturing of the rock masses. Group 1, in addition to being "isolated" from the other groups, appears to have average values comparable to the total data distribution. Finally, group 4 has a mean Jv similar to the median of the total data distribution, but has very low mean GSI and Rv. This is the cluster with the worst geo-mechanical properties of the rock masses.

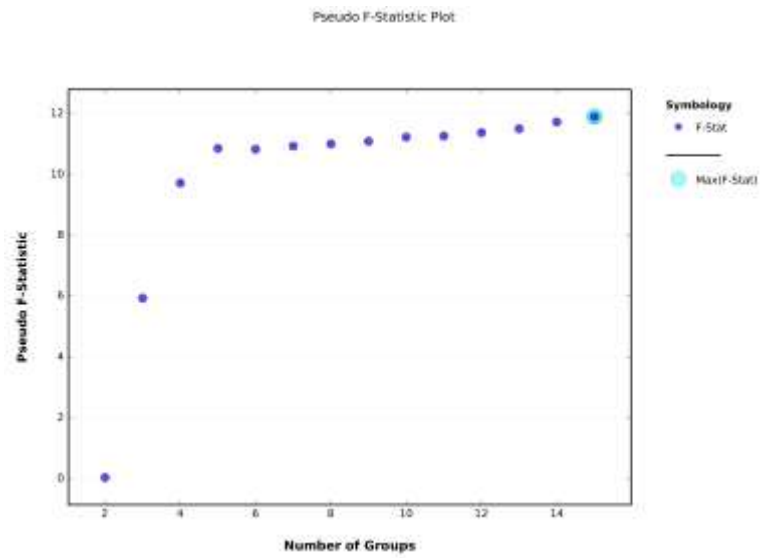


Figure 4-48 Pseudo-F statistic plot used to obtain the number of clusters. Even the peak is located in correspondence of 15 groups, 4 clusters was chosen.

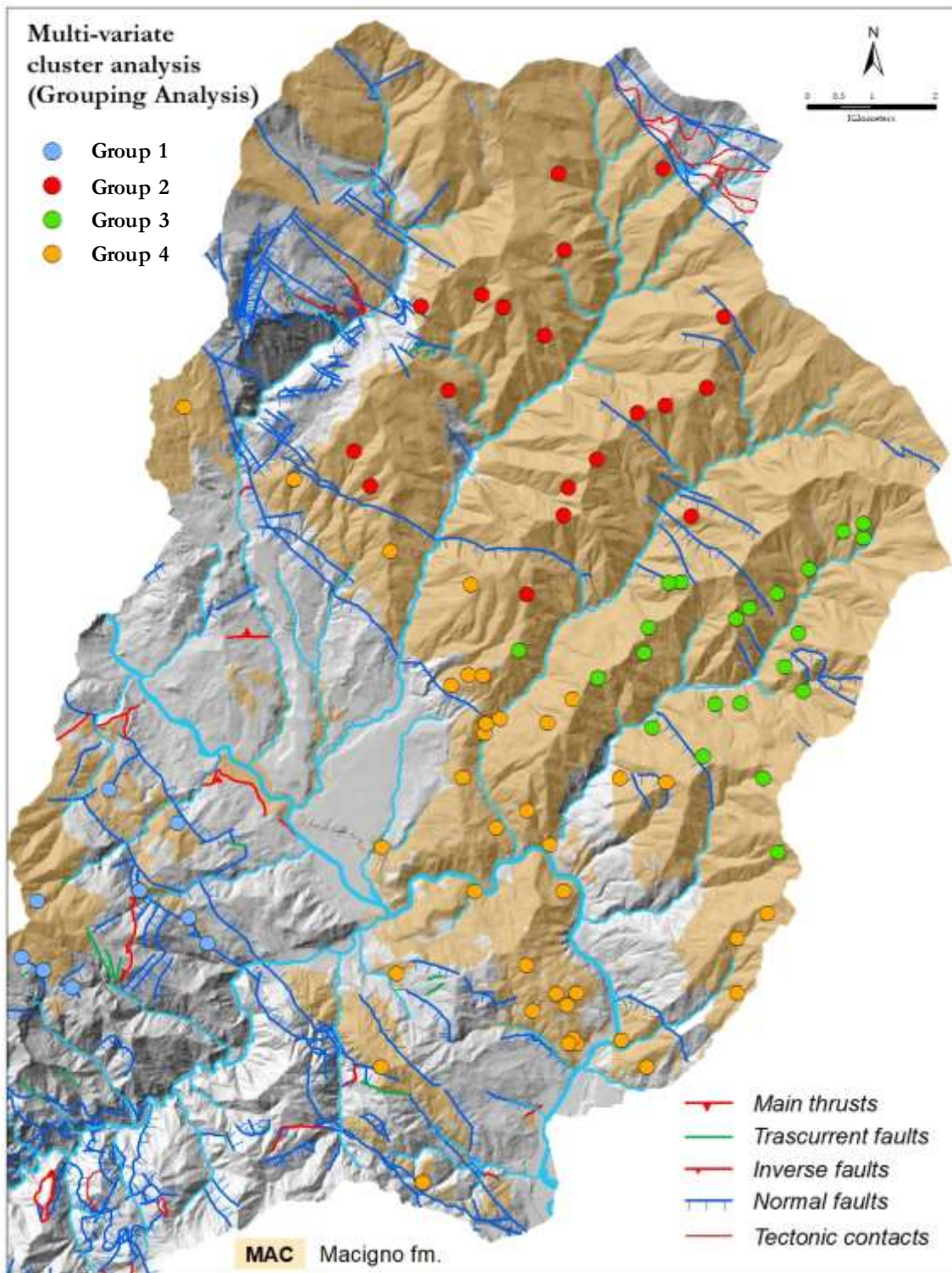
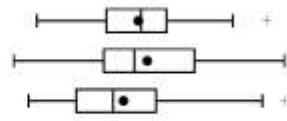


Figure 4-49 Multi-variate cluster analysis.

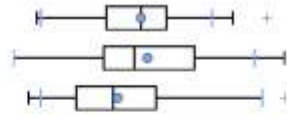
Overall Variable Statistics: Count = 87; Std. Distance = 15.5487; SSD = 193.1590

Variable	Mean	Std. Dev.	Min	Max	R2
RV_MEDIO	21.1060	5.6037	8.0212	37.6575	0.3683
GSI	47.1839	11.1340	25.0000	70.0000	0.2932
JV	16.2138	9.2949	2.2000	40.0000	0.1182



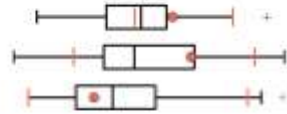
Group 1: Count = 9; Std. Distance = 17.9546; SSD = 38.6339

Variable	Mean	Std. Dev.	Min	Max	Share
RV_MEDIO	21.4355	7.1996	8.5336	30.6324	0.7457
GSI	47.2222	11.8113	25.0000	65.0000	0.8889
JV	15.3667	11.4467	4.0000	36.7000	0.8651



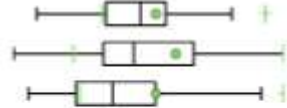
Group 2: Count = 19; Std. Distance = 12.0785; SSD = 31.4224

Variable	Mean	Std. Dev.	Min	Max	Share
RV_MEDIO	25.5154	3.2451	20.6673	33.3120	0.4267
GSI	54.4737	8.4128	35.0000	65.0000	0.6667
JV	11.9211	8.0363	2.2000	34.7000	0.8598



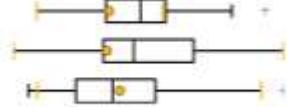
Group 3: Count = 22; Std. Distance = 13.3612; SSD = 47.6162

Variable	Mean	Std. Dev.	Min	Max	Share
RV_MEDIO	23.4420	4.4767	16.5765	37.6575	0.7113
GSI	52.0455	9.3735	35.0000	70.0000	0.7778
JV	21.0909	8.4036	9.8000	40.0000	0.7989



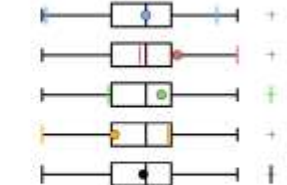
Group 4: Count = 37; Std. Distance = 13.1264; SSD = 75.4866

Variable	Mean	Std. Dev.	Min	Max	Share
RV_MEDIO	17.3726	4.0877	8.0212	24.2601	0.5479
GSI	40.5405	8.1374	25.0000	70.0000	1.0000
JV	15.7243	8.4912	3.5000	36.7000	0.8763



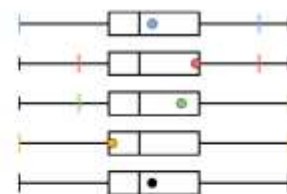
RV_MEDIO: R2 = 0.37

Group	Mean	Std. Dev.	Min	Max	Share
1	21.4355	7.1996	8.5336	30.6324	0.7457
2	25.5154	3.2451	20.6673	33.3120	0.4267
3	23.4420	4.4767	16.5765	37.6575	0.7113
4	17.3726	4.0877	8.0212	24.2601	0.5479
Total	21.1060	5.6037	8.0212	37.6575	1.0000



GSI: R2 = 0.29

Group	Mean	Std. Dev.	Min	Max	Share
1	47.2222	11.8113	25.0000	65.0000	0.8889
2	54.4737	8.4128	35.0000	65.0000	0.6667
3	52.0455	9.3735	35.0000	70.0000	0.7778
4	40.5405	8.1374	25.0000	70.0000	1.0000
Total	47.1839	11.1340	25.0000	70.0000	1.0000



JV: R2 = 0.12

Group	Mean	Std. Dev.	Min	Max	Share
1	15.3667	11.4467	4.0000	36.7000	0.8651
2	11.9211	8.0363	2.2000	34.7000	0.8598
3	21.0909	8.4036	9.8000	40.0000	0.7989
4	15.7243	8.4912	3.5000	36.7000	0.8763
Total	16.2138	9.2949	2.2000	40.0000	1.0000

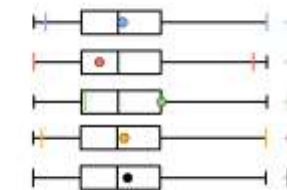


Figure 4-50 Clusters and variables statistics

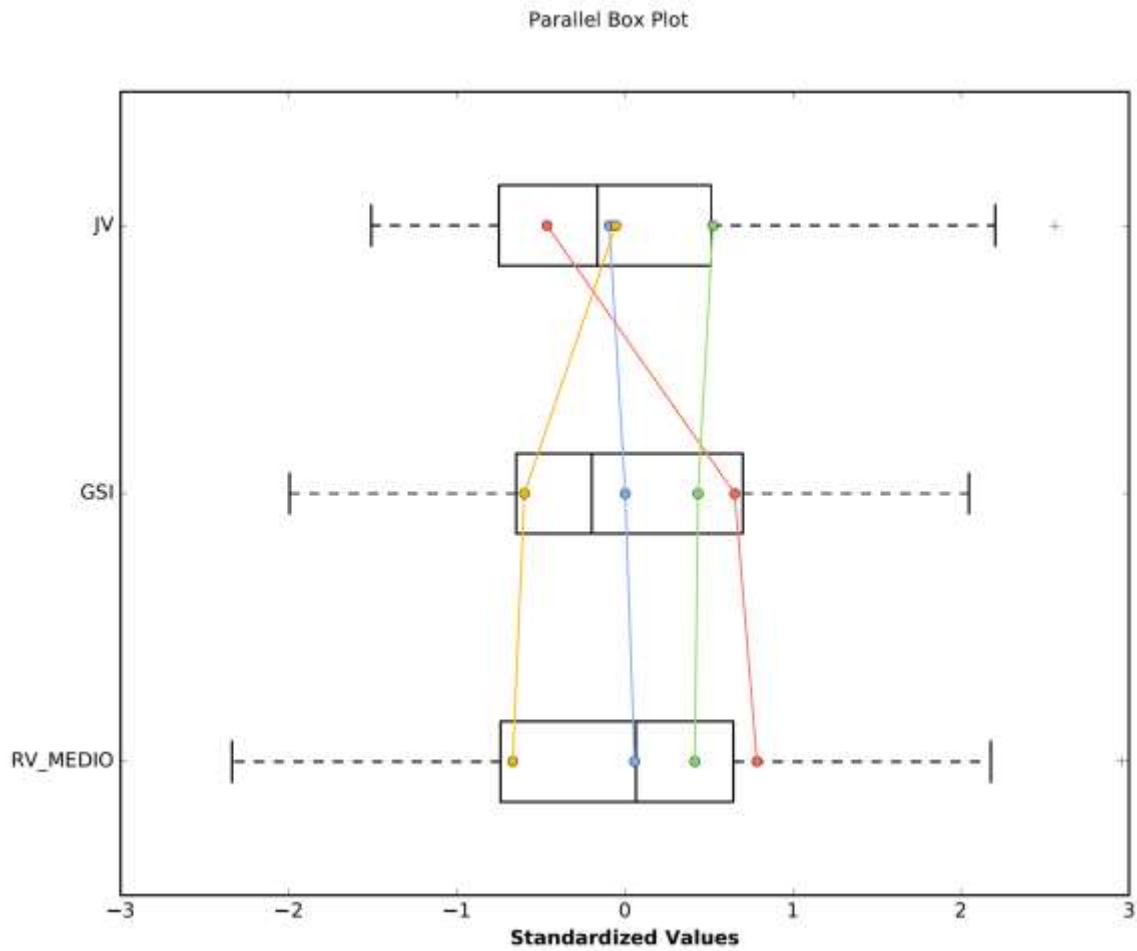


Figure 4-51 Parallel box plot describing cluster statistics of the variables. The dots represent the mean values and the colours represent the groups: blue, group 1; red, group 2; green, group 3; yellow, group 4.

4.3.4 *Bedrock Geo-mechanical Units*

As described in the paragraph 2.5.7., BMUs were obtained from the expert-based delineation following the results of multi-variate clustering taking into consideration tectonic lineaments, morphology and drainage network. Figure 4-52 shows the results for the MAC formation area. The BMU 1 mainly covers the southern region, spreading with a thin flap towards the north-west, where it borders with the BMU 2. As can be seen in the map, the contact between these BLU is marked by the occurrence of a set of NW-SE trending faults steeply dipping towards SW. The literature suggests that these lineaments correspond to the Pliocene-Pleistocene active normal faults of the Garfagnana graben (Di Naccio et al., 2013). Towards SE, this contact separates from the trace of the faults and continues more or less parallel to the direction of the main valley. This section of the contact has been delineated by interpreting both the hillshaded DEM and Google Earth images, which allowed to recognize an alignment of transverse valleys to the main drainage network, all developing at about the same altitude, suggesting the possible occurrence of further normal faults merging towards the southwest. The limit between BMU 2 and BMU 3 in the western part resumes the trace of the system of faults described above and then may be located along the valley following the shape of one of the transversal valleys to the main Serchio river depression. Obviously, this interpretation could be better detailed by increasing observation sites density in this sector of the study area. BMU 4 reflects the portion of isolated Macigno located on the wall of a system of normal faults merging to the northeast and completely develop to the right of the Serchio river.

The picture and data of Figure 4-53 refer to two representative examples of outcrops belonging to BMU 1 and BMU 2, respectively. The first is a very weathered and moderately fractured sandstone with decimetric scale layers of siltstone. The arenaceous portion can be easily fragmented by the hammer, it has an ochre color, which typically develops as the result of the chemical alteration. The other outcrop at the bottom consists almost exclusively of very hard unweathered sandstones with a dark gray colour. The average spacing of the joints is about 50 cm, with rough discontinuity surfaces.

Figure 4-54 shows the boxplots that describe the geo-mechanical properties of the BMUs. BMU 1, developing in the southern and lower in elevation portion of the study area, is characterized by the worse geo-mechanical parameters. The parameters of BMU 2, which covers the northern portion of the area, where both the slope steepness and elevation are higher, constantly above those BMU3. BMU 4 has a wide dispersion than the others. Probably the small number of observations collected in this area does not allow to recognize the clustering phenomena of geo-mechanical parameters. This hypothesis is also suggested by the high frequency of faults.

Finally, in Table 4.15 the equivalent Mohr-Coulomb parameters are summarized (see paragraph 2.5.6 for a detailed description). The first two columns represent the mean and standard deviation of friction angle and effective cohesion for each BMU. Starting from these two values, the maximum - minimum ranges

assigned to the BMUs were calculated. These ranges were used to implement the probabilistic analysis of susceptibility to shallow landslides involving bedrock, by means of a physically based approach. In the Appendix C the input and output parameters for each field observation are listed.

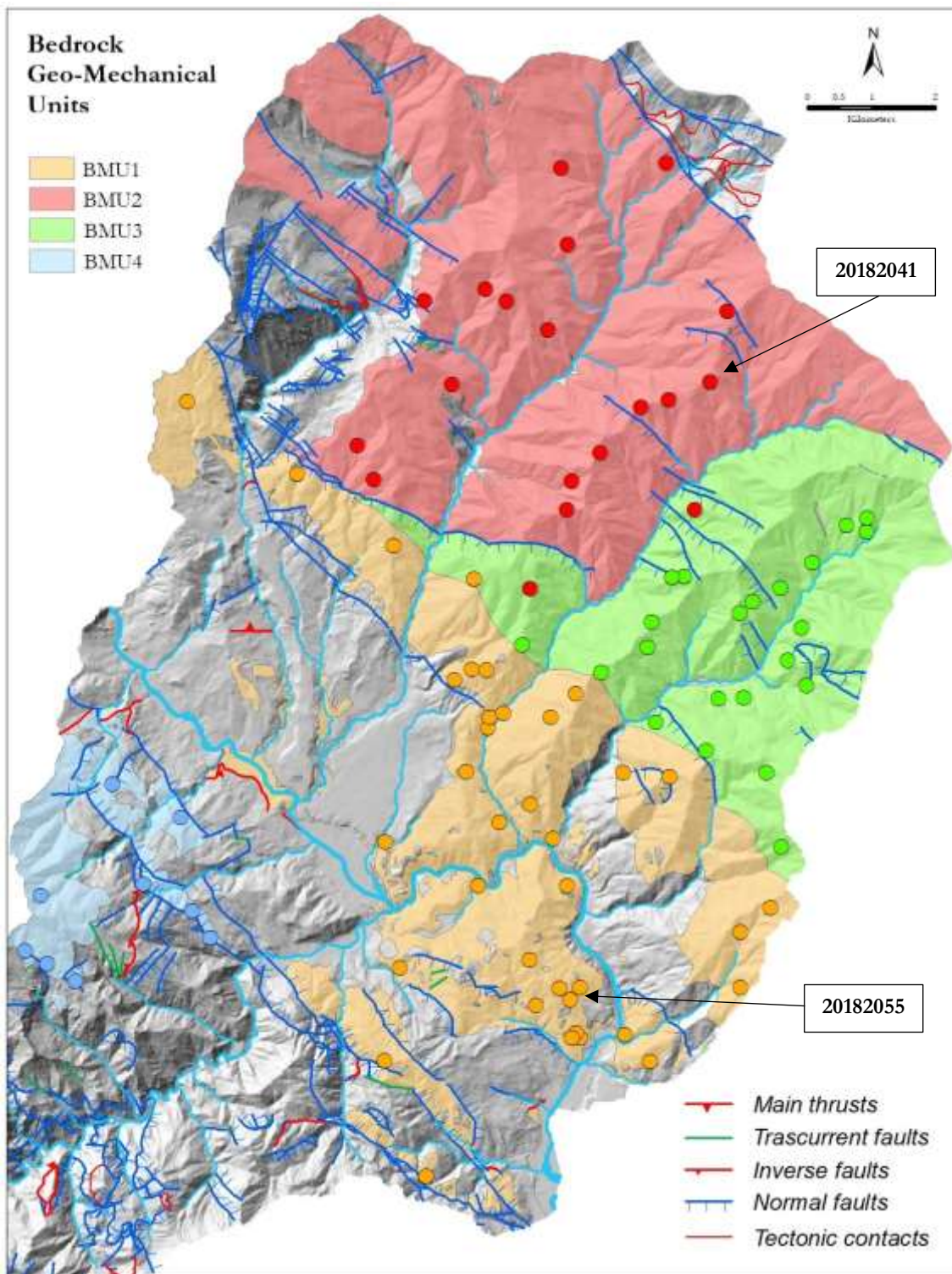


Figure 4-52 Geo-mechanical Bedrock Units (BMU). The colours of BMU reflects the colours resulted from the grouping analysis. The boxes indicate the outcrops shown in Figure 4-53.



BMU	1
ID	20182055
Intact rock str. (MPa)	16
GSI peak	30
ϕ ($^{\circ}$)	20
c' (Kpa)	16
Rockmass str. (MPa)	0.3



BMU	2
ID	20182041
Intact rock str. (MPa)	42
GSI peak	55
ϕ ($^{\circ}$)	31
c' (Kpa)	35
Rockmass str. (MPa)	1.0

Figure 4-53 Representative examples of two outcrops of BMU 1 ad BMU 2 and respective geo-mechanical parameters.

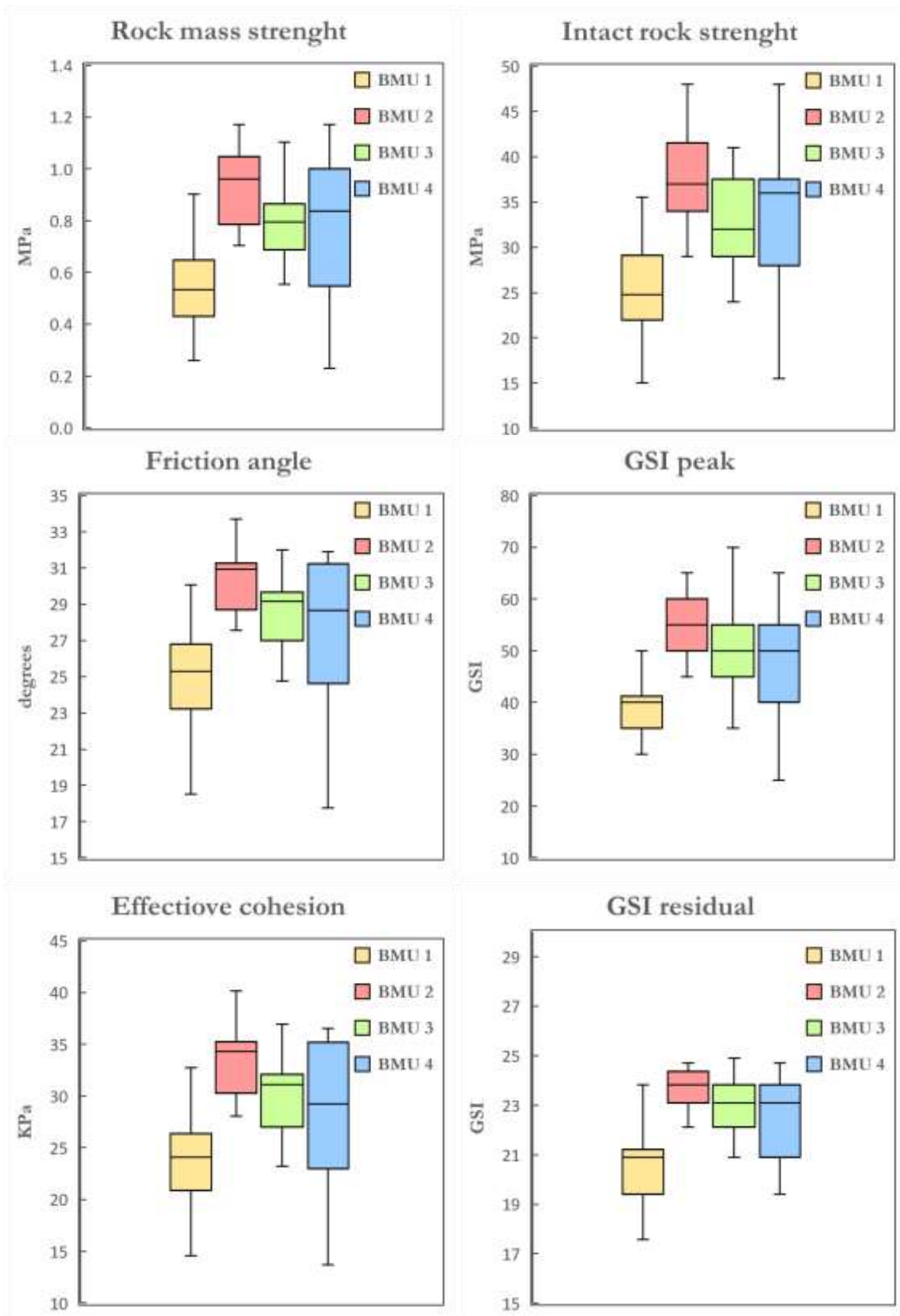


Figure 4-54 Geo-mechanical parameters for Bedrock Geo-Mechanical Units obtained by the method proposed by Hoek & Brown (2002), described in paragraph 2.5.6.

Table 4.15 Mohr Coulomb equivalent parameters of Bedrock Geo-Mechanical Units

		Bedrock Geo-machanical Units			
		1	2	3	4
ϕ (°)	Average	24.9	30.4	28.7	27.5
	Dev. St.	2.8	1.7	1.8	4.7
	Max	26	31	30	30
	Min	23	29	27	25
c' (KPa)	Average	25.9	36.2	32.7	31.0
	Dev. St.	4.7	3.6	3.6	8.2
	Max	28.3	37.9	34.5	34.5
	Min	22.5	33.0	30.8	26.7

5 RESULTS - SHALLOW LANDSLIDE SUSCEPTIBILITY MODELING

5.1 SHALLOW LANDSLIDE SUSCEPTIBILITY ANALYSIS: A COMPARISON BETWEEN PROBSS AND INFORMATION VALUE

One of the aims of this PhD thesis is to compare the results of different modelling approach to assess shallow landslide susceptibility. In this paragraph, the susceptibility results obtained by using a modified version of the SHALSTAB model (Montgomery and Dietrich, 1994), PROBSS, is compared with those obtained by a well-known data-driven method, namely the Information Value (IV, Yin and Yan 1988).

5.1.1 Shallow landslide inventory

In shallow landslide susceptibility models, the landslide inventory is a fundamental tool for different reasons. In physically based methods it is used to evaluate the accuracy of the outputs, while it is necessary for statistical computations where, once split into training and test datasets, it is used as input as well as tool to validate the results of the model. The inventory used in this PhD thesis work is described in paragraph 4.1. Since it was not possible to check in the field the whole shallow landslides dataset, the subdivision of the inventory into training and test datasets was not done randomly but on the basis of visited landslides (VS) and not visited landslides (NVS). The NVS were used as training dataset for the stability analysis conducted with the Information Value model, while VS were used as test datasets for both models, the PROBSS and Information Value (IV).

Since VS are provided with data collected in the field, these landslides allowed to investigate in detail the results of shallow landslides susceptibility modelling.

In Figure 5-1 the shallow landslide inventory is shown as classified into VS and NVS. Out of a total of 191 landslides, 81 landslides were visited and most of all are provided by the field data. Due to the inaccessibility for vegetation density and/or morphology conditions, the remnants 110 landslides were not visited.

Landslide inventory map

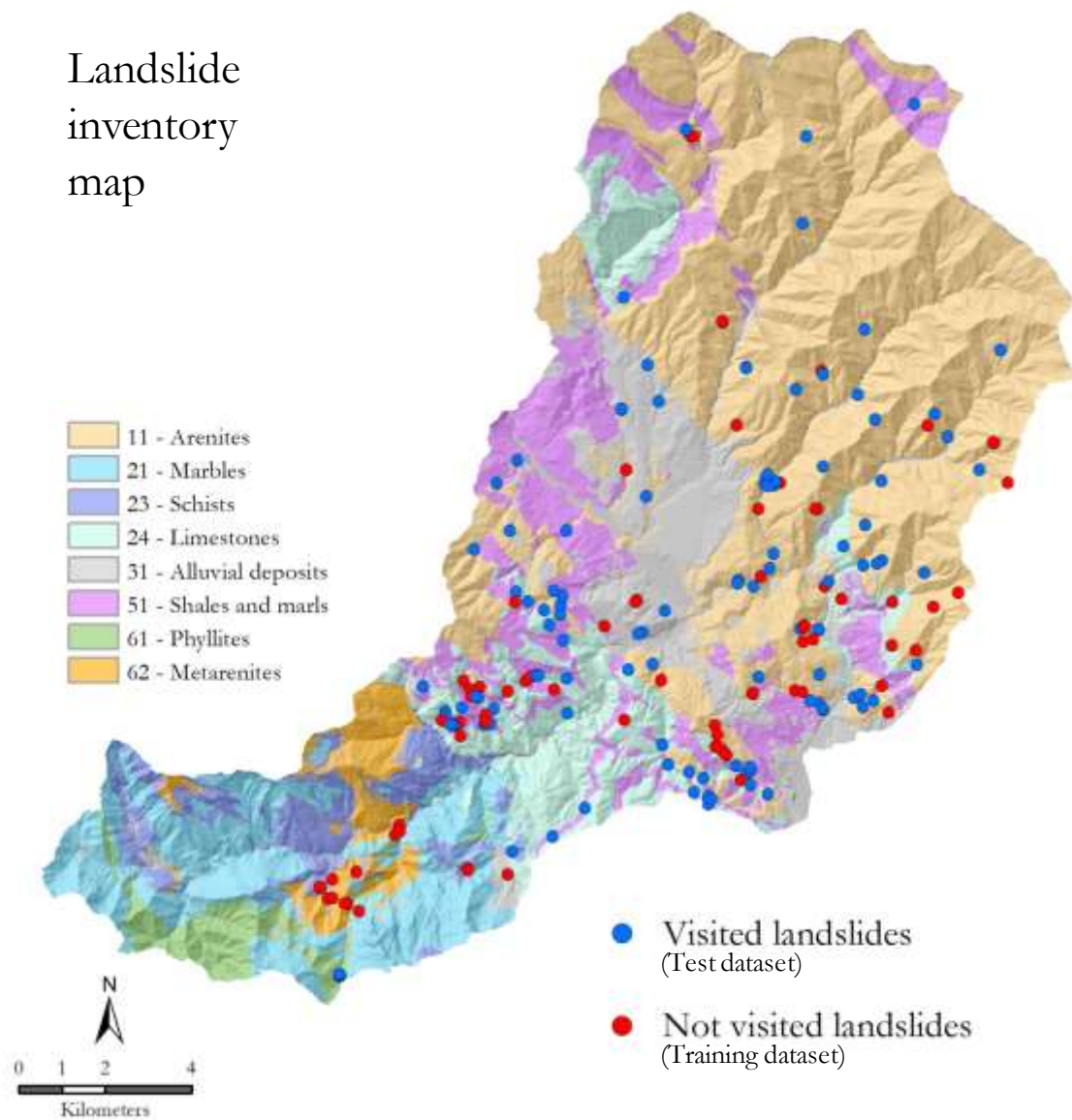


Figure 5-1 Landslide inventory map used to assess shallow landslide susceptibility

5.1.2 *PROBSS input data*

According to the equation and disequations presented in paragraph 2.6.1, PROBSS model requires a set of topographic variables and geo-technical parameters as input data. Topographic variables are provided by two raster files, the slope steepness (degrees) and the contributing area (m^2). As described in paragraph 4.2.5, a set of geo-technical parameters is provided for each EGU (Engineering Geological Unit) and synthesized in the Slope Deposits Engineering Geological Map, in which the ranges of friction angle, effective cohesion, bulk density and slope deposits depth are stored.

5.1.3 *Information value input data*

The selection of the conditioning factors is one of the most important and difficult tasks for data-driven landslide susceptibility analysis. Nevertheless, for each study area a specific set of factors, mostly

depending on geographical and geomorphological contexts, may be recognized (Van Westen et al., 2003). For this reason, determining which and how many conditioning factors are adequate for a specific susceptibility analysis is difficult to assess. Reichenbach et al. (2018) provide an exhaustive review of statistically based methods including the analysis of the most used predisposing factors. Moreover, van Westen et al. (2008) provide an overview of environmental factors, and their relevance for landslide susceptibility assessment considering the scale of analysis.

In this work the selection of predisposing factors was executed coupling expert knowledge and literature review (Table 5.1 and Figure 5-2).

In Figure 5-3 the Information Value weights for each class of the variables are shown, as calculated based on the procedure described in paragraph 2.6.2.

Table 5.1 List of predisposing factors used for IV method

Predisposing factors	Source / software	Description
Bedrock Lithological Units	This thesis	
Elevation	https://www502.regione.toscana.it/geoscopio/cartoteca.html	DEM 10x10m cell size
Topographic Position Index	This thesis , Land Facet Corridor Designer (Jenness, 2006)	
Slope steepness	This thesis , ArcGIS v10.7	Derived from DEM
Slope over Area ratio	This thesis , TauDEM (Tarboton, 1997)	
Slope deposits depth	This thesis	
Profile Curvature	This thesis ,Landserf v2.3	
Transversal Curvature	This thesis ,Landserf v2.3	
Slope Aspect	This thesis ,ArcGIS v10.7	Derived from DEM

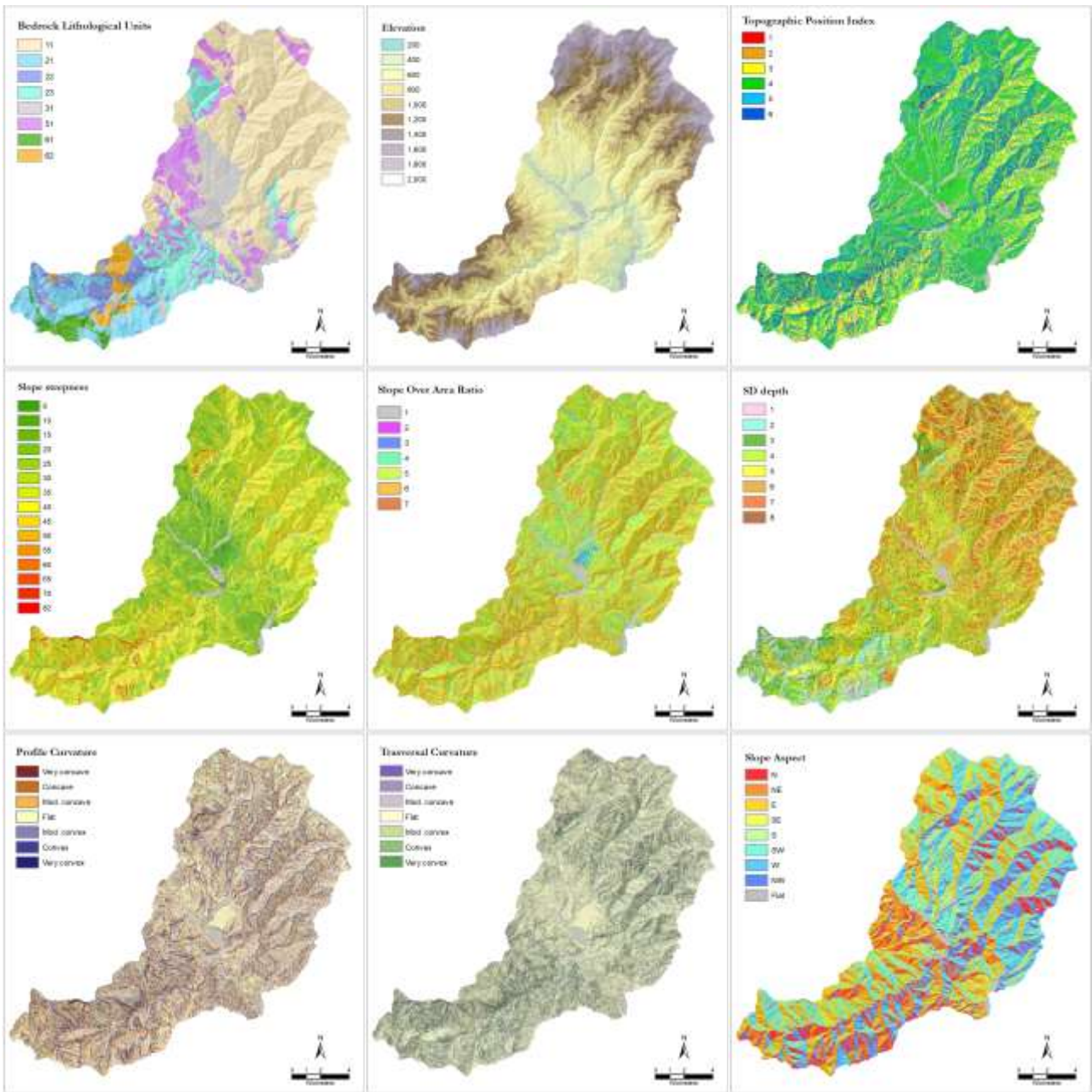


Figure 5-2 Input variables for the Information value model

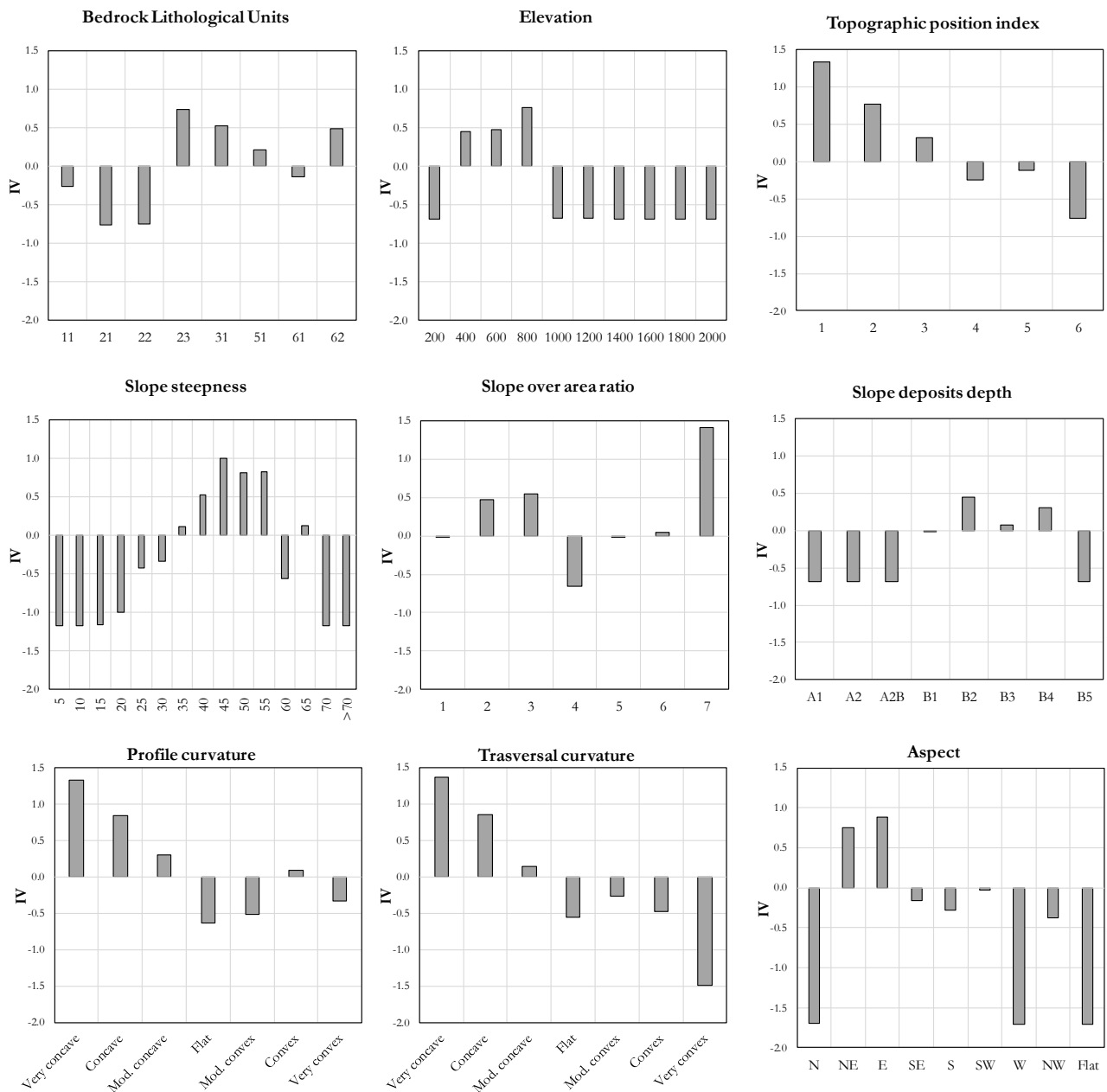


Figure 5-3 Weights for the input variables used to implement the Information value method

5.1.4 Susceptibility maps and accuracy assessment

The output returned by the two slope stability analyses have different meanings. The susceptibility value of the Information Value model is given by the pixel by pixel sum of the weights attributed for each class. As a consequence, the output susceptibility map is described by a range of values, when are negative indicate very low or no susceptibility, while positive values indicate susceptible or very susceptible areas. The physically-based model computes pixel by pixel the probability that in the i_{th} pixel satisfies the stability conditions described by the functions in paragraph 2.6.2. If pixels have a 100% probability of being US or UU, the logarithm of the ratio between the effective rainfall and SD transmissivity ($\log Q_c/T$) is not calculated. Instead, when the probability is lower than 100%, the pixel-by-pixel distribution of the log

Q_c/T values is calculated. Since the model is implemented using a probabilistic approach through Monte Carlo simulation ($n=10000$ runs), as output a $\log Q_c/T$ pixel-by-pixel distribution is provided. The median value of this distribution defines the final pixel-by-pixel $\log Q_c/T$ value.

Given the units used for Q_c (mm/day) and T (m^2/day), it results $Q_c < T$, hence $\log Q_c/T < 0$. The smaller the $\log Q_c/T$, the higher the susceptibility. On the contrary, a $\log Q_c/T$ tending to 0 indicate low susceptibility areas.

In Figure 5-4 and Figure 5-5 the shallow landslides susceptibility maps are shown.

In order to compare the susceptibility maps obtained from the two models, it is necessary to process the raw data by classifying them according to a common criterion. As it is conceived, PROBSS model immediately provides a class, represented by unconditionally stable areas (US). Being known the percentage extension of the US areas in respect with the total extension of the study area, is it possible to define the upper limit of the IV lowest susceptibility class (Stable Areas), by using the US percentage as a percentile of the cumulative frequency distribution of IV values, obtained by ranking the IV data from the lowest to the highest. The rest of the study area, not falling within either the IV susceptibility class 1 (Stable Areas) or the US area, was further split into 4 classes of equal areal extension (%). In this case, the US percentage is 64%, and thus the remaining 36% was divided into 4 classes.

The validation and the accuracy assessment of the two landslide susceptibility models is evaluated by means receiver operating characteristic curve analysis, or simply ROC analysis (Hanley and McNeil, 1982; Beguería, 2006; Fawcett, 2006).

To perform this analysis, the test dataset (Visited Landslides) is intersected with the grid of the susceptibility map, resulting in four possible outcomes. If a computed unstable cell is inside the observed landslide area, it is counted as true positive (TP); if it is outside the observed landslide area, it is counted as false positive (FP). If a computed stable cell corresponds to an observed landslide cell, it is counted as false negative (FN); otherwise, it is classified as true negative (TN). To perform the ROC analysis, two quantities were calculated: sensitivity (True Positive Rate), defined as the ratio between TP and the sum of TP and FN; and specificity (False Positive Rate), defined as the ratio between TN and the sum of TN and FP. In the ROC plot, the sensitivity of the model is plotted against the 1-specificity. These values indicate the ability of the model to correctly discriminate between positive and negative observations in the validation sample. A high sensitivity indicates a high number of correct predictions, whereas a high specificity indicates a low number of false positives. The area under the ROC curve (AUROC) can serve as a global accuracy statistic for the model. This statistic ranges from 0.5 (random prediction, represented by a diagonal straight line) to 1 (perfect prediction) and can be used for model comparisons (Cervi et al., 2010; Zizioli et al., 2013; Oliveira et al., 2016). The ROC curves obtained for the two susceptibility models are shown in Figure 5-6. The frequency distribution of test dataset (Visited Landslides) for each susceptibility class is plotted in Figure 5-7. Note that the extension of susceptibility classes is 64% and 9%,

respectively of Stable Areas (SA) and Low Susceptibility (LS), Medium Susceptibility (MS), High Susceptibility (HS) and Very High Susceptibility (VHS).

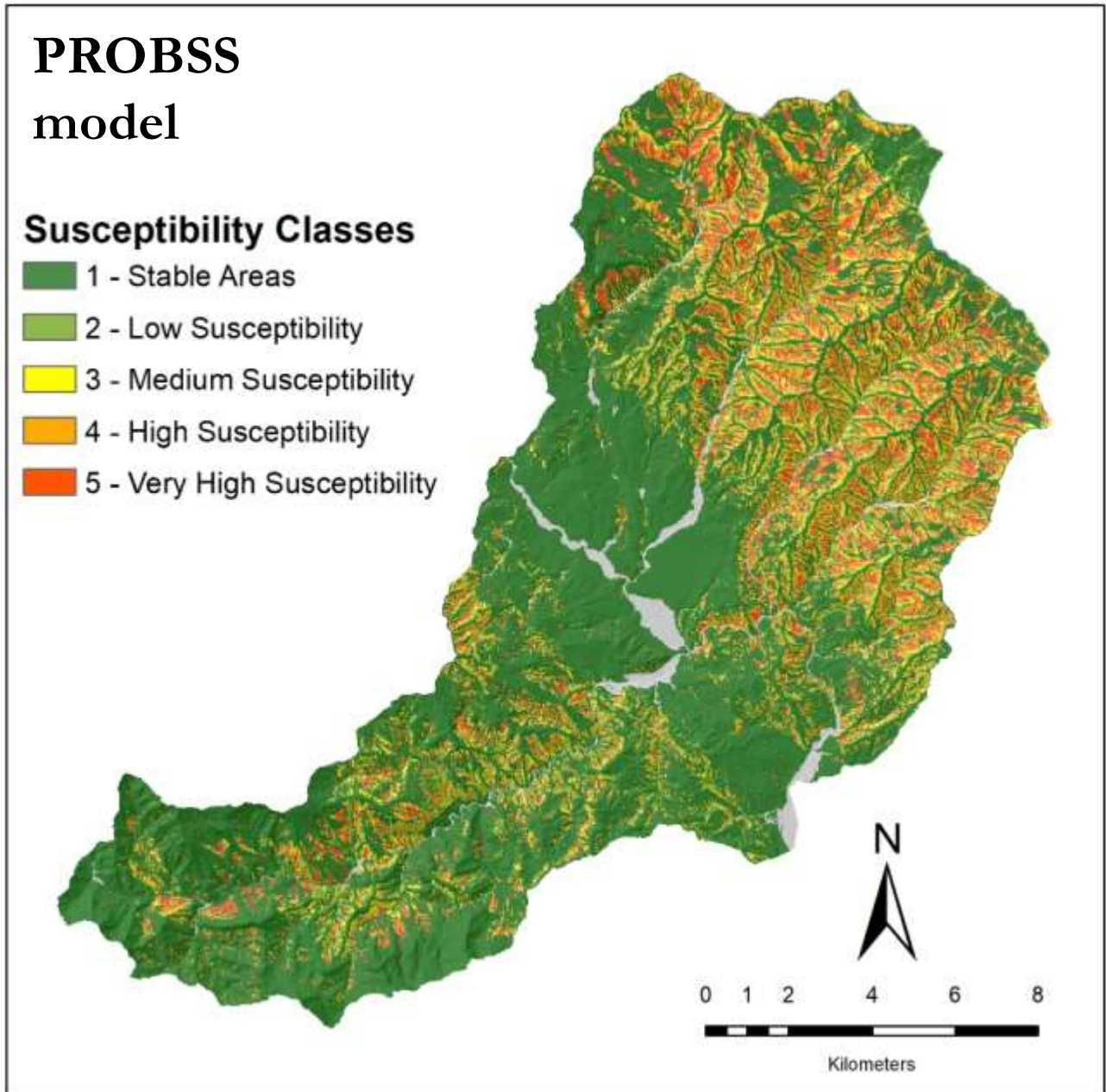


Figure 5-4 Shallow landslide susceptibility map computed by the PROBSS model. The susceptibility classes were obtained by classifying the distribution of the median $\log Q_c/T$.

INFORMATION VALUE model

Susceptibility Classes

-  1 - Stable Areas
-  2 - Low Susceptibility
-  3 - Medium Susceptibility
-  4 - High Susceptibility
-  5 - Very High Susceptibility

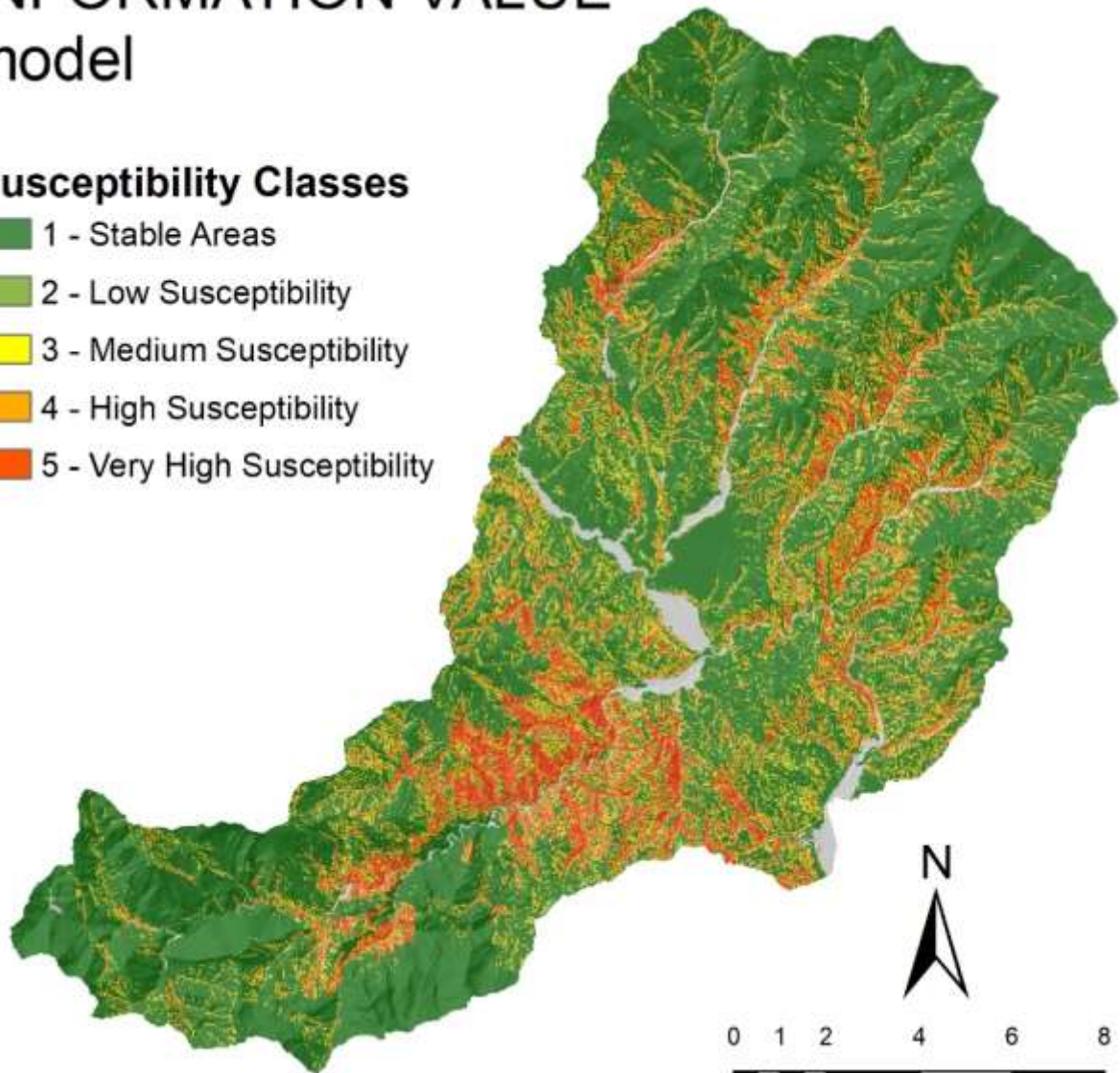


Figure 5-5 Shallow landslide susceptibility map computed by Information Value.

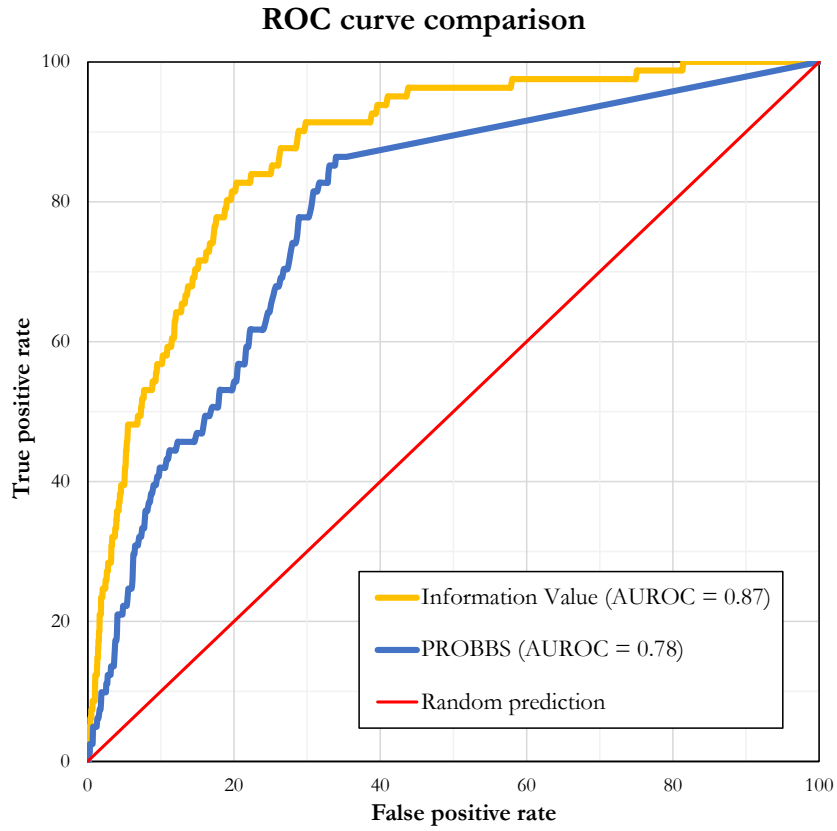


Figure 5-6 ROC plots and respectively AUROC values for the two different susceptibility models.

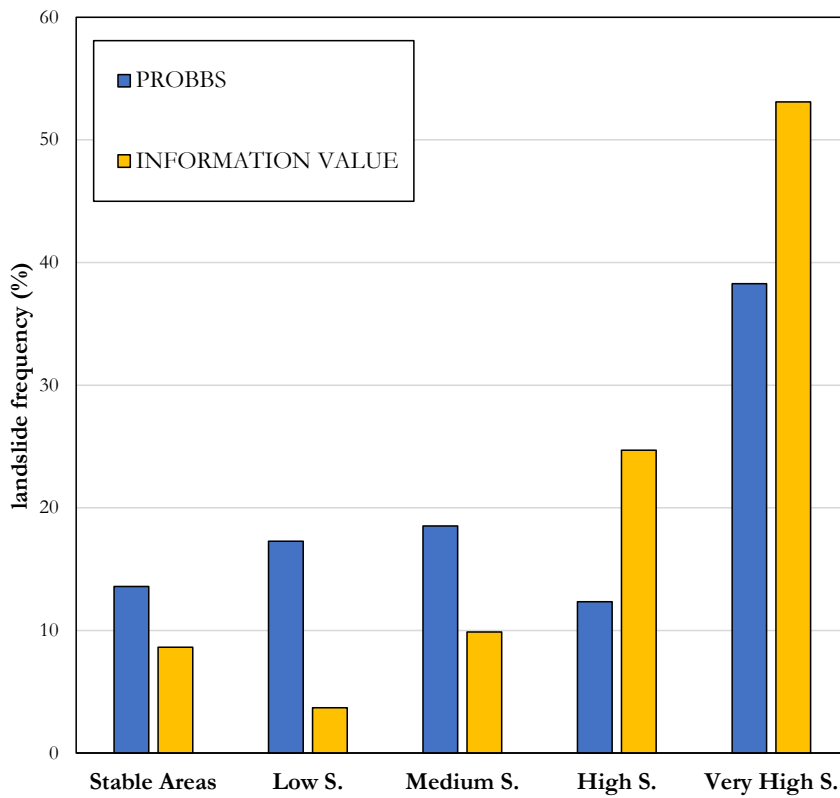


Figure 5-7 Comparison of frequency distribution of VS landslides (test dataset) in susceptibility classes obtained by physically- based and data driven modelling

5.1.5 Discussion

The susceptibility maps shown in Figure 5-4 and Figure 5-5 are considerably different. Obviously, while the map obtained from PROBSS is strictly correlated with topography, SD depth and geotechnical parameters, the distribution of susceptibility classes in the map obtained from Information Value depends mainly on the training dataset landslide distribution. The IV map abruptly discriminates between Stable Areas and High and Very High susceptibility areas. This is reflected in the higher values of the AUROC, which is remarkably high, and it is confirmed in Figure 5-7, where about 80% of slope failures occurred in the classes with the higher probability of landsliding. On the contrary, about 30% of landslides occurred in low susceptibility class and in stable areas of the PROSS model. This may be mainly due to different reasons: geo-technical parameters such as internal friction angle or the cohesion or the dry density but also the depth of the slope deposit, may not reflect the real site-specific conditions. It would therefore be a problem related to the determination and regionalization of these parameters, which hardly may be solved when assessing landslide susceptibility at regional scale. The second reason to consider is that the reference model for evaluating slope stability is the infinite slope model, which is a rough representation of a more complex process as the triggering of shallow landslides. Finally, concerning the space-time distribution of pore pressure, the stability model implemented is a steady state model assuming that rainfall infiltrates until reaching the SD-BR interface, then following topographically determined flow paths (Montgomery et al., 1998). As a matter of fact, it is known that rainfall and infiltration are rarely steady state processes. Moreover, also water leakage occurs through the bedrock, especially as a consequence of rock fracturing.

About input parameters, the probabilistic implementation of PROBSS by the Monte Carlo simulation with a sampling size of 10000 iterations, should have limited uncertainty. Since the landslides used to validate the models have been analysed during fieldwork, their characteristics may be analysed in order to understand whether some specific conditions may imply a stability behaviour with relevant deviations from the assumption of the infinite slope model. As described in the paragraph 4.1.3, for 60% of VS landslides the sliding surface is located below the discontinuity between the slope deposit and the bedrock. By assessing the accuracy of the physically based model results by using as test dataset made up of landslides developed within the slope deposits or involving the bedrock, it is possible to evaluate the model capability to predict one dataset rather than the other. As shown in Figure 5-8, although AUROC values are never high as the case of the Information Value, it is possible to observe that the two different curves provide different results, especially in the most relevant part of the ROC plot: for false positive rate <10%, the deviation between the functions is almost 15% and locally gets to about 20%; for false positive rate of 10-20%, the deviation is still about 10%. While, the lower slope of the final stretch indicates a lower number of landslides in stable areas. This comparison suggests that the single-layer

infinite slope model provides better results when SDL are taken into account as test dataset. At the same time this model is less suitable to describe the spatial variability of susceptibility to shallow landslides involving bedrock.

By analysing the distribution of the VS dataset (Figure 5-9), split into involving Bedrock landslides (BRL) or slope deposits landslides (SDL), it should be noted that:

- The accuracy for SDL (slope deposits landslides, dotted filling) is very good, both for PROBSS and with IV (Information Value) models. In the latter, over 70% of landslides occur within the high and very high susceptibility classes. The PROBSS model perform a bit worse, the 57% of landslides occur in the higher susceptibility classes.
- The distribution of BRL (Bedrock involved landslides, Bricks filling) within the susceptibility classes lead to very different results depending on the model used. About 30% of BRL, occur either in the Stable Areas or the Low susceptibility areas modelled with PROBSS. Instead, the IV performs very well, as a clear strong positive trend between landslide frequency and increasing susceptibility is observed.
- The quite poor results of the physically based model obtained for BRL are not actually negative results. In fact, they confirm that models based on the infinite slope are not well suitable to predict shallow landslide susceptibility if these shallow landslides may develop their rupture surface below the discontinuity between slope deposit and bedrock.

The high performance obtained by the IV model may be explained with its dependance on the training dataset. For the IV model, the training dataset was represented by NVS landslides, therefore no information is available about the materials involved.

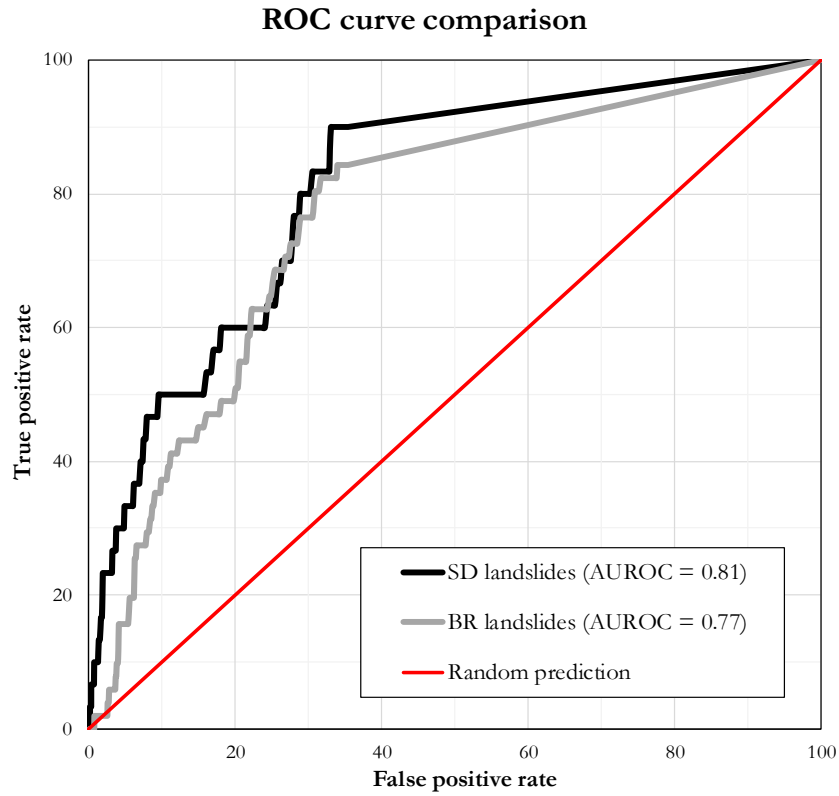


Figure 5-8 ROC plots and AUROC values obtained for the PROBSS model by using landslide test datasets either involving the SD only, or the bedrock also.

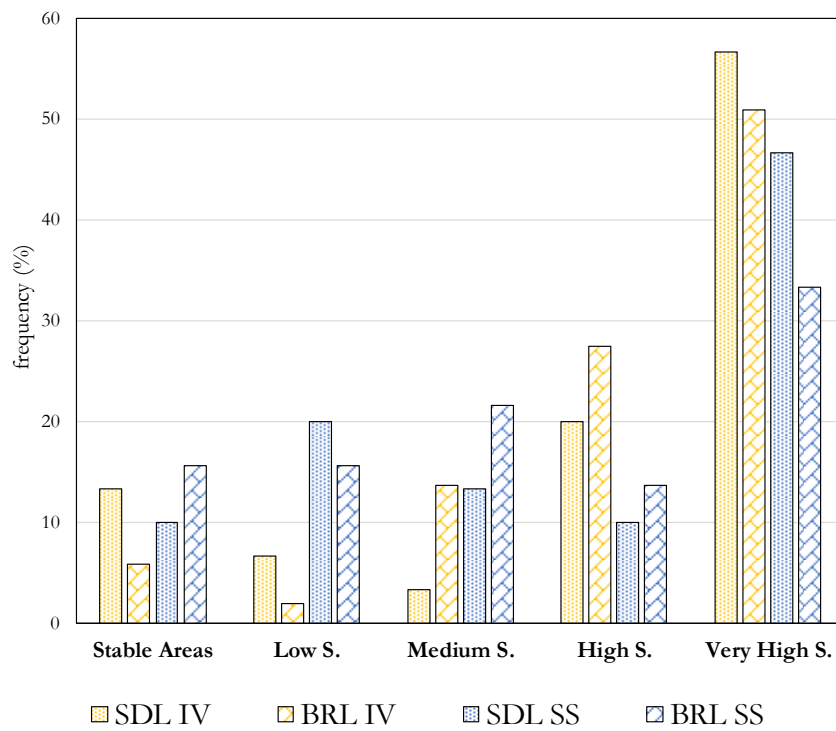


Figure 5-9 Frequency distribution of both SDL and BRL within the susceptibility classes obtained by both modelling approaches.

5.2 EXPLORING DIFFERENCES BETWEEN SHALLOW LANDSLIDES INVOLVING SLOPE DEPOSITS AND/OR BEDROCK BY MEANS OF INFORMATION VALUE METHOD

In the light of the results obtained in the previous section, to understand the differences between SDL and BRL, two susceptibility maps were obtained using SD visited landslides, subsequently validated with BR visited landslides, and vice versa. The aim of adopting this strategy is to verify that SDL and BRL occur under different conditions, providing two susceptibility maps displaying a distinct distribution of slope failures prone areas. To perform the slope stability analysis, the Information Value model is used due to its dependency on the training dataset.

Figure 5-10 shows the landslide inventory map of visited landslides, discerning between slope deposit landslides (SDL) and bedrock involving landslides (BRL).

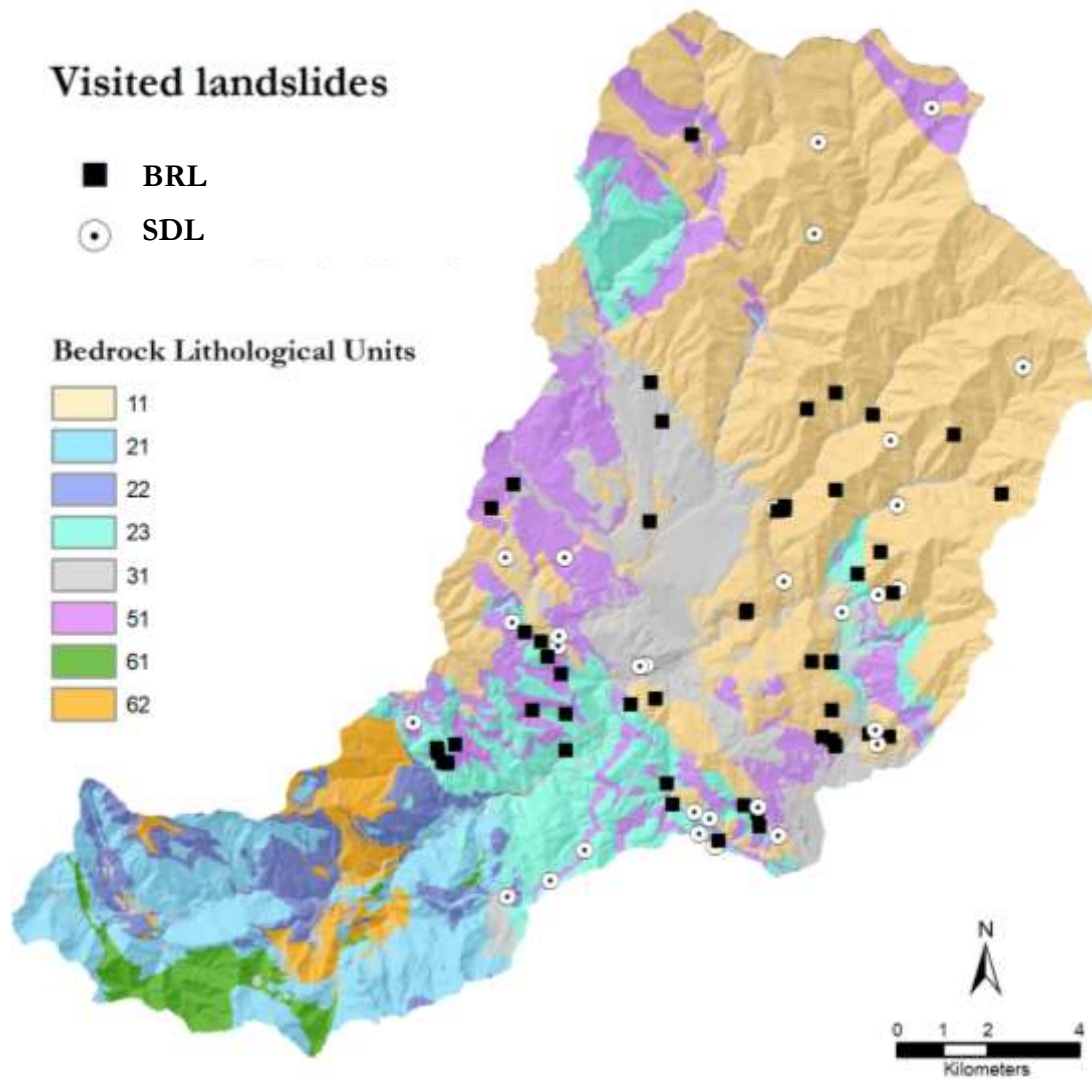


Figure 5-10 Landslide inventory map of visited landslides either involving SD or also the BR

5.2.1 Information value input data and weighs determination

In Table 5.2 the training and test datasets used to implement the Information Value models are described. The same predisposing factors presented in paragraph 5.1.3. (Figure 5-2) were adopted to perform the susceptibility analysis. In Figure 5-11 the weighs of the input variables are shown.

Table 5.2 Training and test datasets used to perform the susceptibility analysis with IV

Model name	Training dataset	Test dataset
M1	SDL	BRL
M2	BRL	SDL

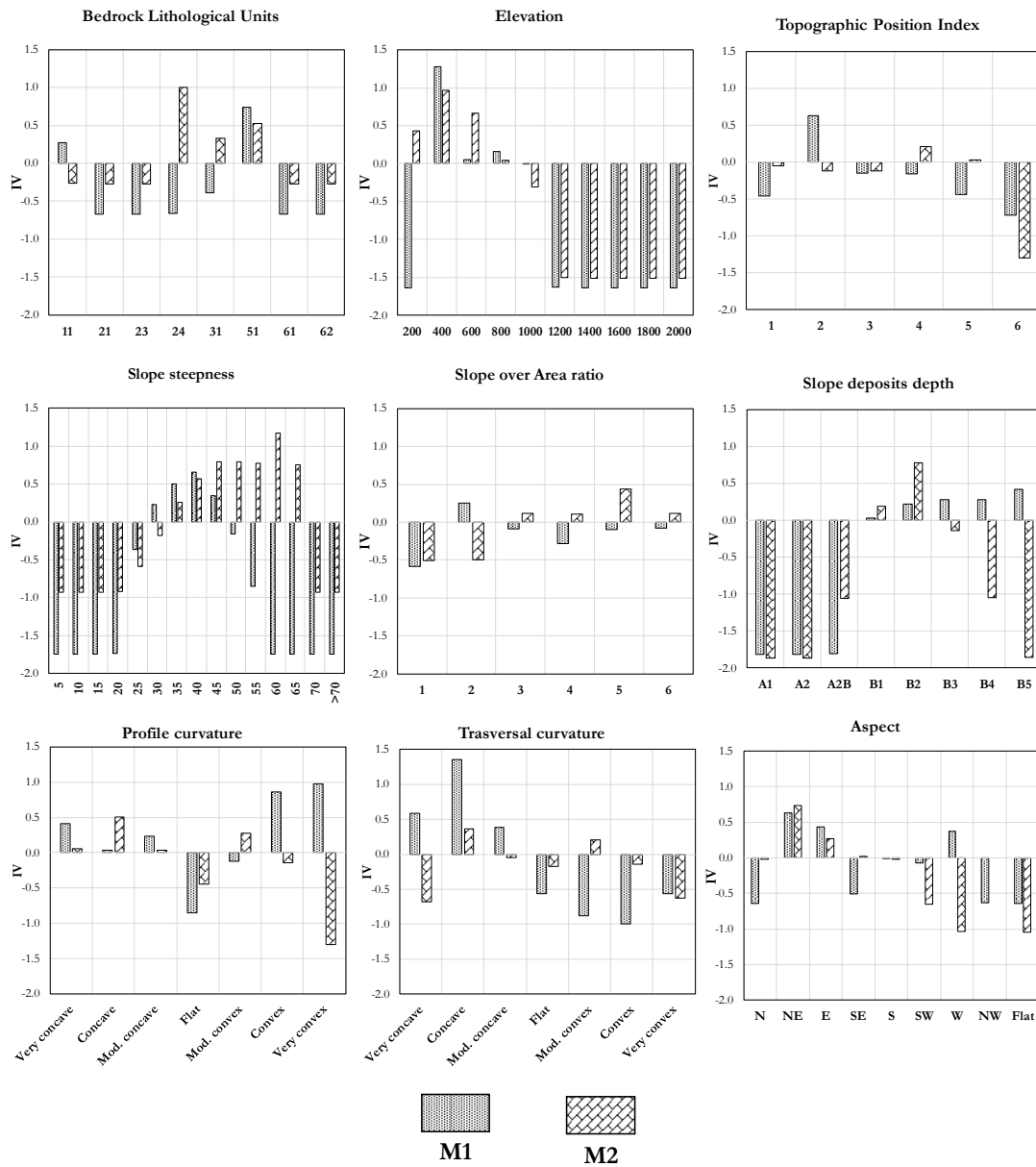


Figure 5-11 Information Value weights for slope deposit landslides and bedrock involving landslides

5.2.2 Susceptibility maps and accuracy assessment

In Figure 5-12 and Figure 5-13 M1 and M2 susceptibility maps are presented. Figure 5-14 shows the ROC curve resulted from the models, while in Figure 5-15 the distribution of landslides in susceptibility classes is reported.

Susceptibility classes were defined according to the method described at paragraph 5.1.4, that is the 64% of the study area is classified as stable, while the remaining is split into 4 classes of equal extension.

INFORMATION VALUE

M1

Susceptibility Classes

-  1 - Stable Areas
-  2 - Low Susceptibility
-  3 - Medium Susceptibility
-  4 - High Susceptibility
-  5 - Very High Susceptibility

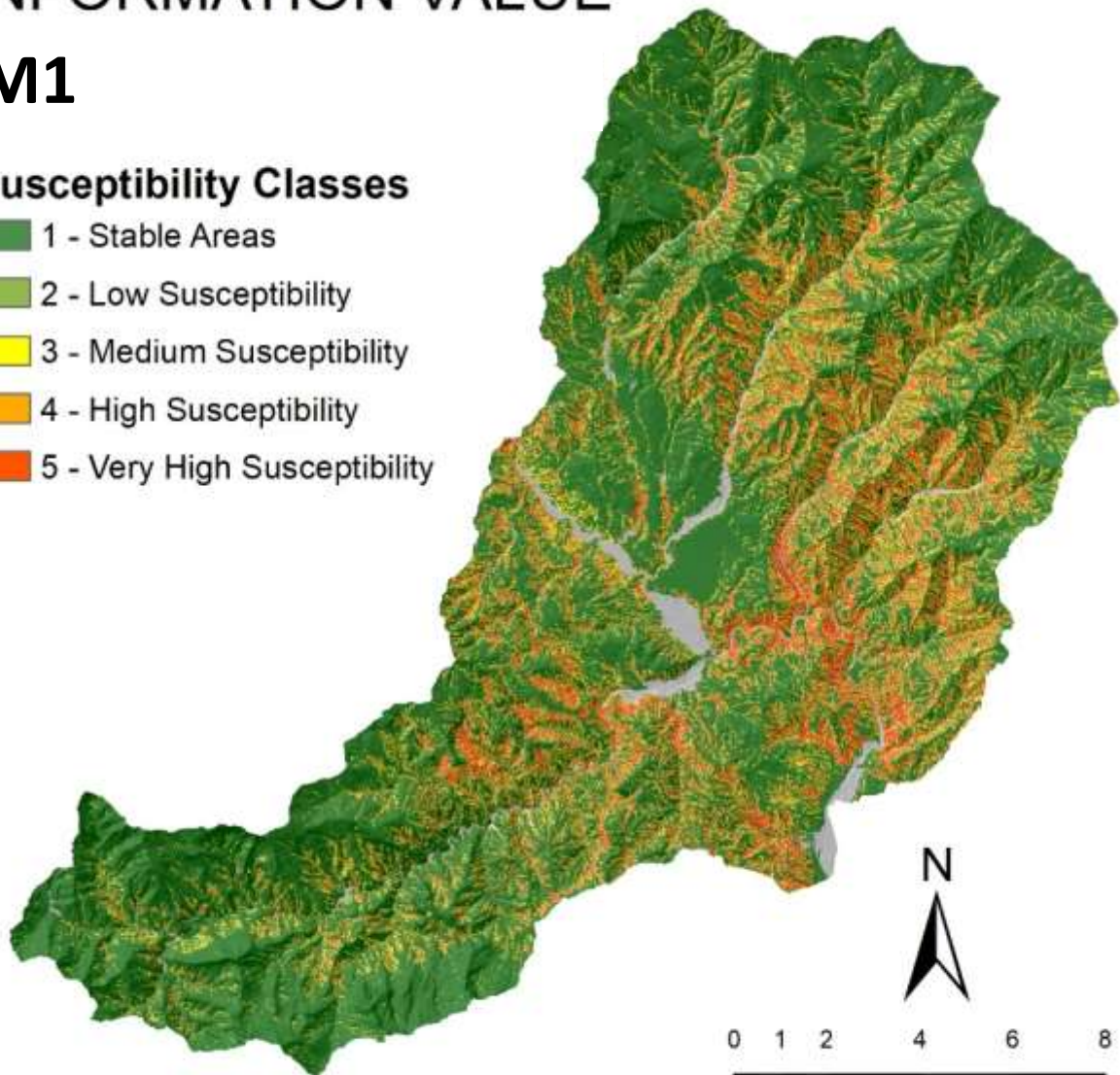


Figure 5-12 Susceptibility map obtained from SDL as training dataset

INFORMATION VALUE

M2

Susceptibility Classes

- 1 - Stable Areas
- 2 - Low Susceptibility
- 3 - Medium Susceptibility
- 4 - High Susceptibility
- 5 - Very High Susceptibility

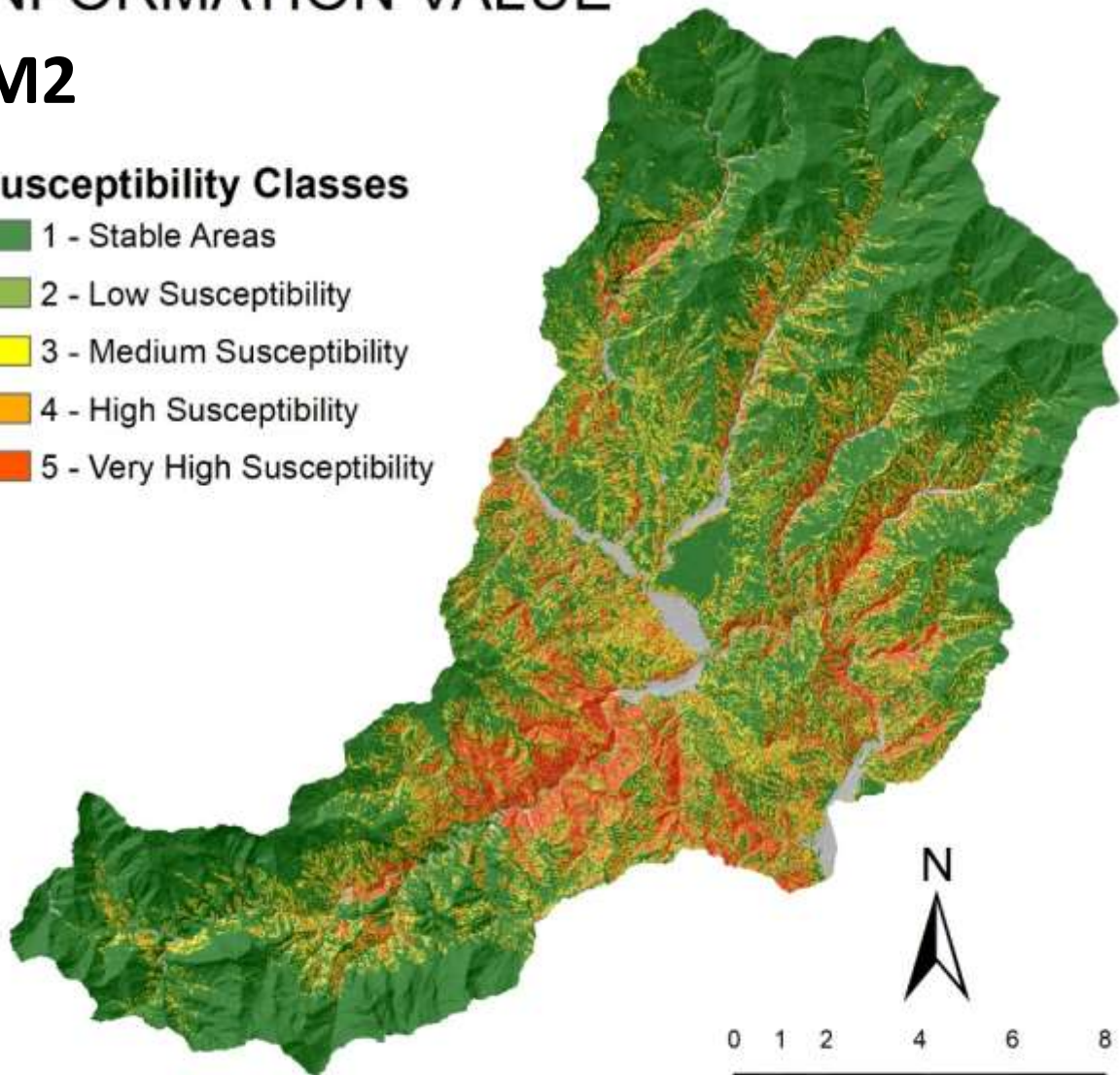


Figure 5-13 Susceptibility map obtained from BRL as training dataset

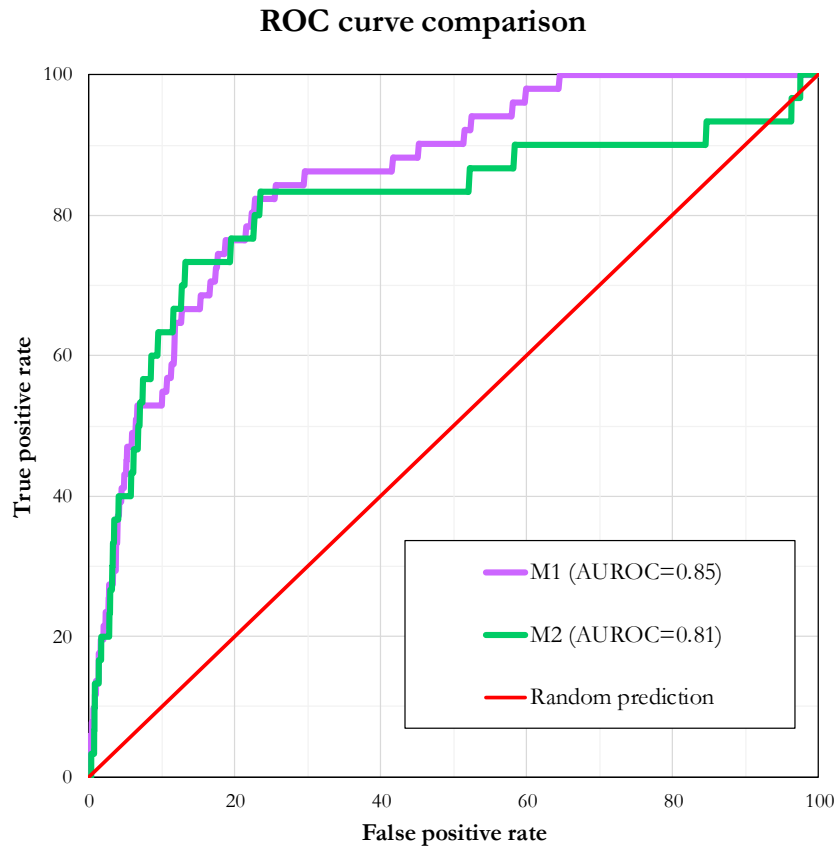


Figure 5-14 ROC curves and AUROC values obtained from M1 and M2 slope stability analysis.

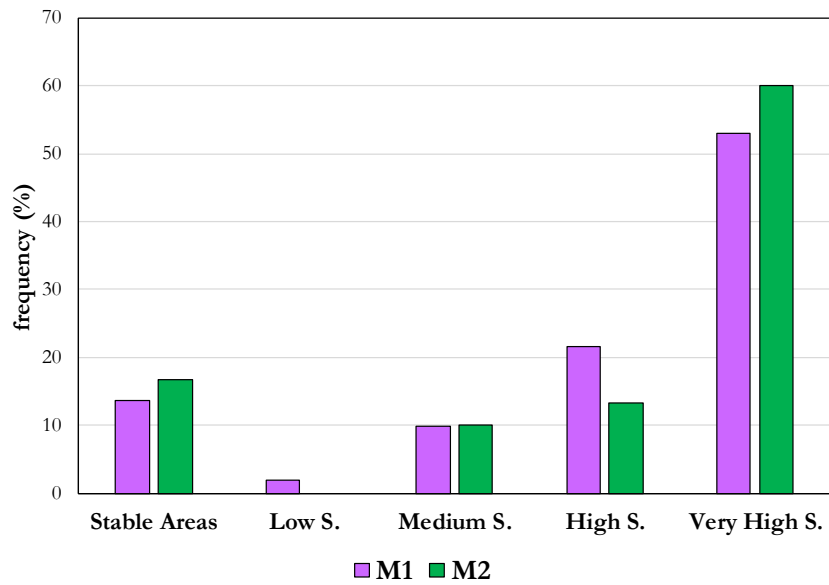


Figure 5-15 Distribution of test landslides in susceptibility classes. The test dataset of M1 is represented by bedrock involving landslides, while M2 test dataset is represented by slope deposit landslides

5.2.3 Discussion

Although the landslides inventory consists of shallow landslides, it is evident both from the graphs showing the weights of each class for each predisposing factors and the related susceptibility maps, that the SDL and BRL tend to occur in different geological, geomorphological and morphometric conditions. However, the AUROC values are high even if the training and test datasets are made up of landslides with different characteristics. By analysing the distribution of landslides of the test dataset into susceptibility classes, it is observed that in general more than 60% are included in the highest susceptibility classes. Only a small amount of these, about 15% is included in the stable areas. It is possible to affirm that the initial intent to discriminate through the data driven model the areas more predisposed to the activation of landslides involving SD only or BR also was not achieved, given the results of accuracy and distribution of landslides of the test dataset in the susceptibility classes. In fact, a lower AUROC values as well as a random distribution of landslides in susceptibility classes was expected. At the cartographic level, however, the maps are different (Figure 5-12 and Figure 5-13), as confirmed also by the different weights assigned to the variables involved for the two different datasets (Figure 5-11).

In order to assess if landslides datasets and relative characteristics are different at cartographic scale, the two susceptibility maps were overlapped. Combining the M1 and M2 susceptibility maps and calculating the deviation among susceptibility classes (Figure 5-16) it is possible detect areas where M1 have higher probability of landslide occurrence, and vice versa. The red coloured scale identifies pixels more prone to activate bedrock involving landslides. On the contrary, blue coloured scale represent pixels where slope deposit landslides tend to occur. The darker the colour tone, the greater the gap between the susceptibility classes. Green areas represent Stable Areas shared between M1 and M2. Grey tones instead are sites which display the same susceptibility class. The pie chart of Figure 5-17 describe the extension of class variability among M1 and M2. The two maps show well-localized and defined differences: the southwest portion involves an increase of susceptibility for BRLs, while in the northeast and east portion appear to be more susceptible to SDL. From a quantitative point of view, the maps are the same for the 51% of the area, of which 5% corresponds to the same susceptibility class while the remaining 46% are the stable areas shared by M1 and M2. In respect to the models presented in paragraph 5.1 where the Stable Areas covered 64% of the study area, the decrease to 46% is probably the most interesting result because almost 20% of the area, is now no longer stable. This highlights the importance to take into consideration the possibility that shallow landslides are complex slope phenomena and not necessarily consisting of loose material that characterizes the debris layer covering the slopes. Moving from one susceptibility class to another with a gap of one or two positions may not significantly affect the general susceptibility description of an area. On the contrary, changes of three or four classes suggest that sites

not prone to develop SDL or BRL instead become high susceptibility areas for one or the other landslide type.

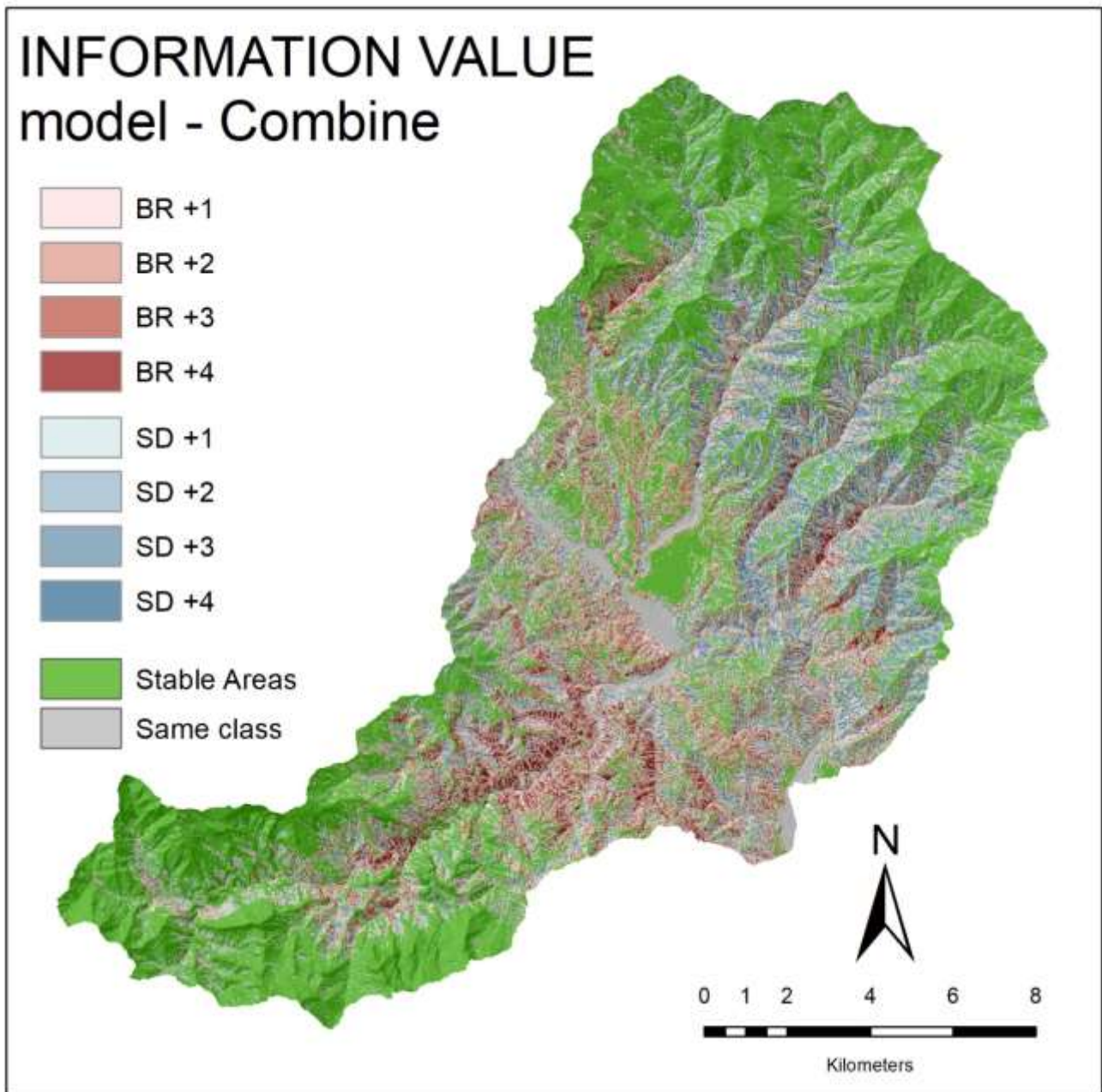


Figure 5-16 Combine between M1 and M2 susceptibility maps. In green the Stable Areas shared by the susceptibility maps reported in Figure 5-12 and Figure 5-13. In grey are represented the areas which display the same susceptibility class. The two-colour scales discriminate between areas susceptible to SDL (blue) or BRL (red) activation. The tone reflects the change in susceptibility class.

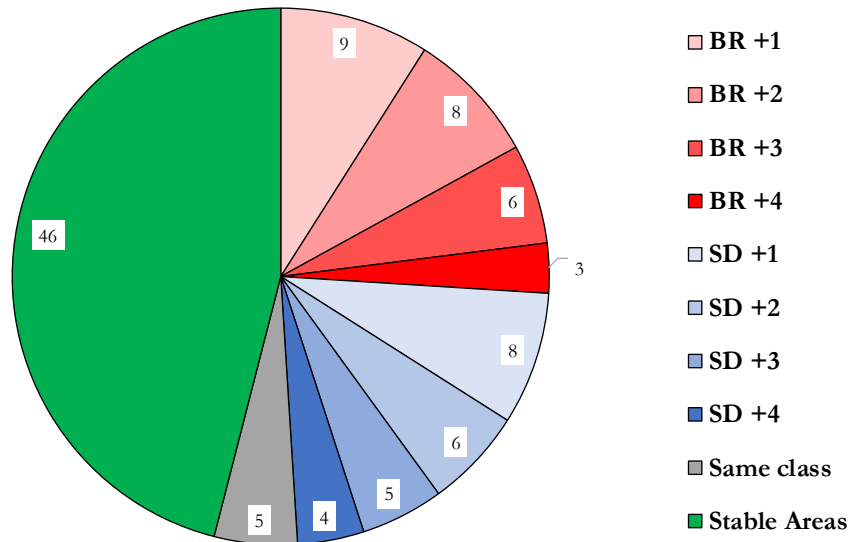


Figure 5-17 Pie chart representing the extent (%) of combined susceptibility classes. The legend description is provided in Figure 5-16.

5.3 PHYSICALLY BASED MODELLING OF SHALLOW LANDSLIDES INVOLVING BEDROCK

In the paragraph 5.2 the differences between shallow landslides either involving only slope deposits or also the bedrock were analysed by means of the IV model. The concept behind the Information Value method, shared with all data-driven methods, is that past landslides are the key to predict the location of future landslides. Hence, these models depend on the training dataset used to compute statistics, giving a fundamental importance to the landslide inventory. Thanks to the information acquired in the field within, close and far from landslides, it was possible to: a) identify landslides involving bedrock (paragraph 4.1.3), and b) to estimate the geotechnical/geo-mechanical properties of both SD and the uppermost bedrock units (paragraphs 4.2 and 4.3). These data allowed to perform a first physically based model of shallow landslide susceptibility where the failure surface is assumed to correspond to the SD-BR interface. This paragraph provides the results of a further physically based model where the failure surface may be located within the bedrock. In this case, one issue to be faced is the rupture surface depth. This kind of discontinuity is almost objectively recognizable in the field. While, different authors (Salciarini et al., 2006; Catani et al., 2007; Zizioli et al., 2013; Kim et al., 2015), including the method proposed in this work, correlate the SD depth with morphometric variables, the weathered and fractured portion of bedrock generally does not define an horizon sharply passing to the underlying fresh bedrock. This condition makes it problematic to define accurate criteria to spatialize the thickness of the uppermost fractured and weathered bedrock.

Some reasons may control the development of this horizon, like the lithological nature (which influences permeability, texture, mineralogy), tectonic evolution, exposure to weathering and climate, and the depth of the surface deposit over the bedrock. The simplest but logical thing that can be done is to measure the rupture surface of bedrock involving shallow landslides, assuming that the failure of the slope occurs where there is the maximum impendency of bedrock properties.

The aim of this paragraph is to compute a slope stability analysis for shallow landslides involving bedrock and compare it with the susceptibility analysis already performed to assess the probability of failure of slope deposits, according to the infinite slope model. Then, in order to evaluate if the slope failure would occur either in the SD or in the BR, the two maps are overlapped and combined. This analysis is applied within the BLU 11, where the Macigno formation crops out, because most of the visited landslides fall within this area (Figure 5-18). The bedrock properties, as well as spatial analysis and calculation of equivalent Mohr-Coulomb parameters were carried out for this lithology. The depth of the rupture surface of involving bedrock landslides was defined adding 2 meters to the SD depth map. This quantity

reflects the median value of the scarp height exposing the bedrock within the visited landslides, as shown in Figure 4-5.

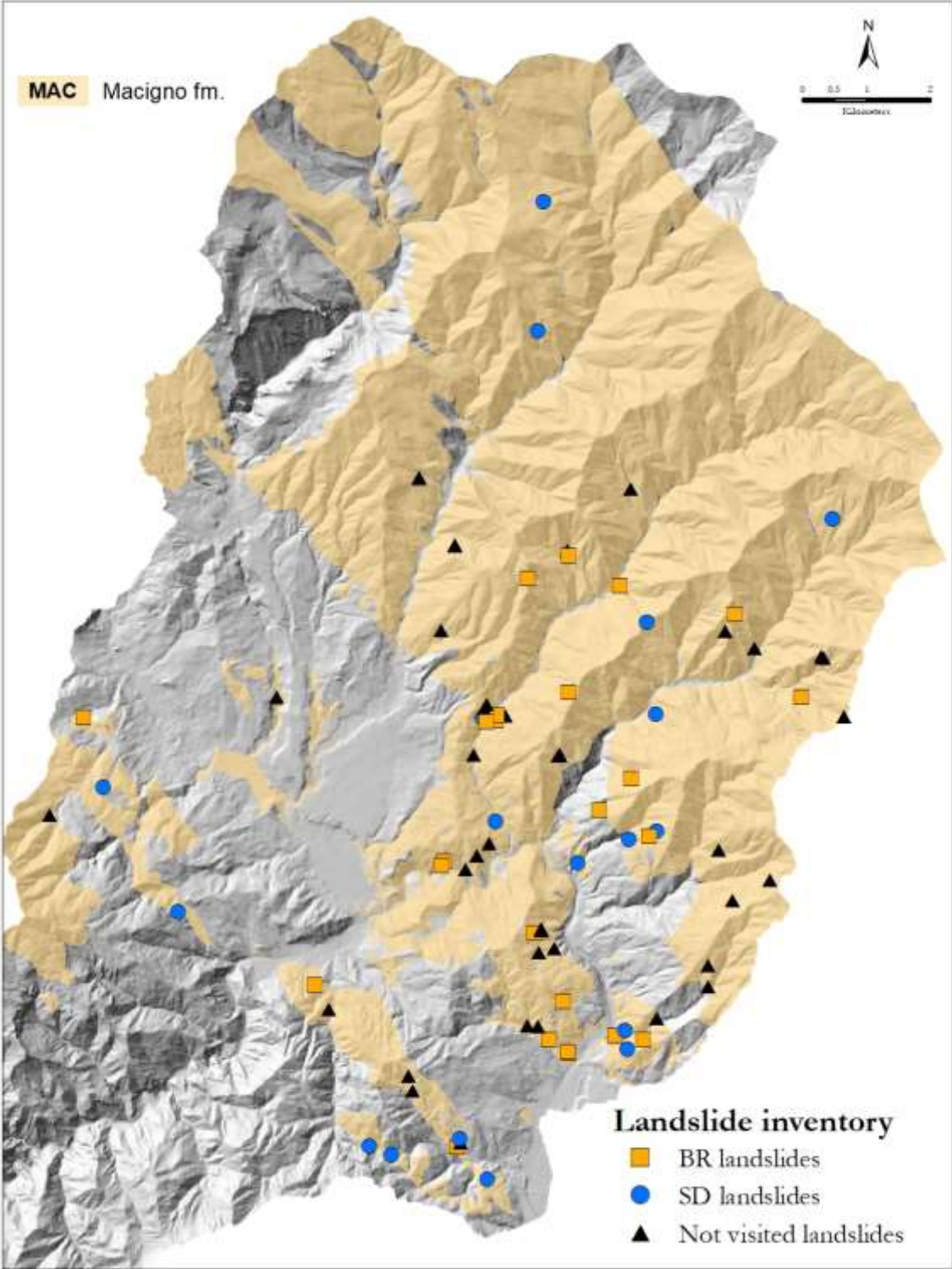


Figure 5-18 Visited landslides (BR and SD) and not visited landslides located within the BLU 11(Macigno Fm.)

5.3.1 PROBSS input data

The implementation of the physically-based model for shallow landslide susceptibility assessment with a sliding surface localized below the discontinuity between bedrock and slope deposits here proposed is simple. As with the other models, PROBSS needs topographical inputs, such as slope and accumulation area, a layer that describes the equivalent Mohr-Coulomb parameters of Geo-mechanical units and finally a layer that identifies the depth at which the sliding can take place. In Figure 5-19 the Bedrock Geo-mechanical Units with corresponding parameters are reported. The depth of the sliding surface was obtained by adding to the depth map of the slope deposits constantly 2 m. This means that, for example, if a given site falls into the depth class B1 (30-60 cm) of the slope deposits, the sliding surface is expected to occur between 230 and 260 cm.

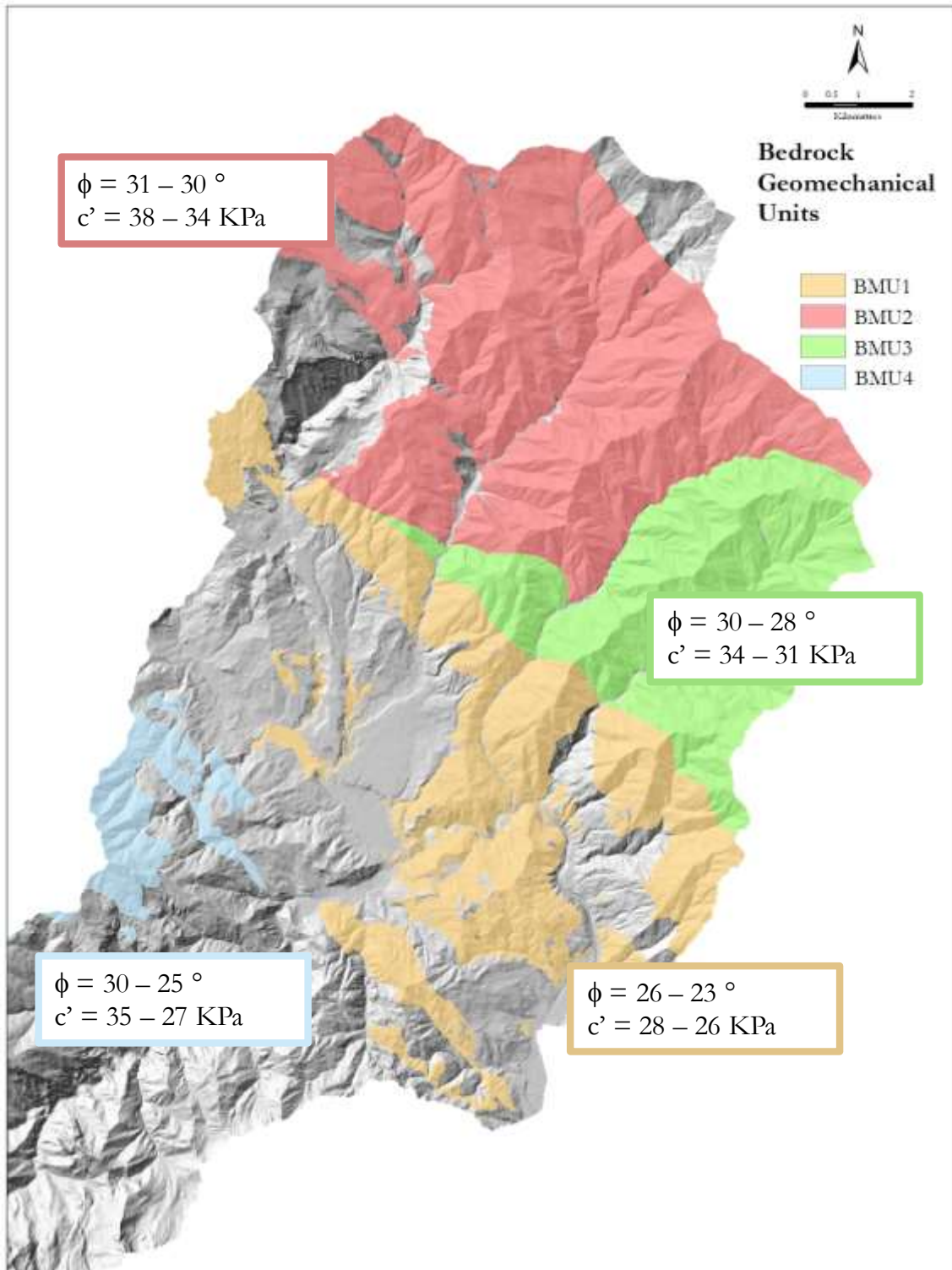


Figure 5-19 Bedrock Geo-mechanical Units map and their corresponding Mohr-Coulomb parameters used for the physically-based modelling.

5.3.2 Susceptibility maps and accuracy assessment

The resulting susceptibility map for bedrock involved shallow landslides is shown in Figure 5-20. The 83% of the study area resulted to be Unconditionally Stable (Stable Areas). The remaining 17%, equally split in 4 susceptibility classes, is mainly confined to the Southern-western portion of the study area where the BMU1 is present. This is strictly related to the input geotechnical parameters which resulted from the processing of field data and the expert-based subdivision in BMU. In order to verify the accuracy of this results, the map is validated using as a test dataset both BR visited landslides and SD visited landslides. As shown in Figure 5-21, the performance of the model is high for BRL (AUROC = 0.86), while it is lower for SDL (AUROC = 0.75).

Bedrock involved shallow landslides susceptibility map

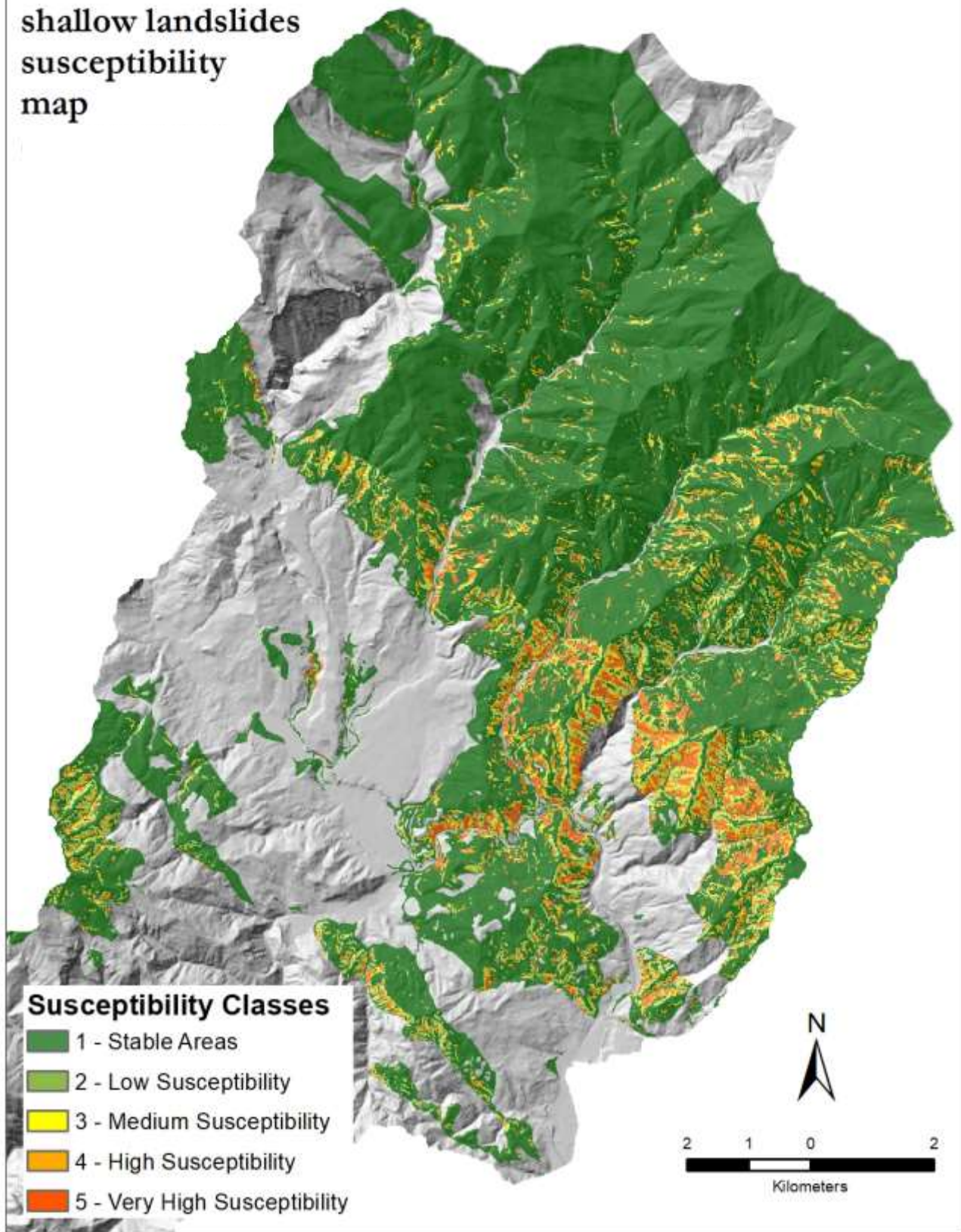


Figure 5-20 Bedrock involved shallow landslides susceptibility map obtained from PROBSS model. The susceptibility classes were obtained by classifying the distribution of the median $\log Q_c/T$.

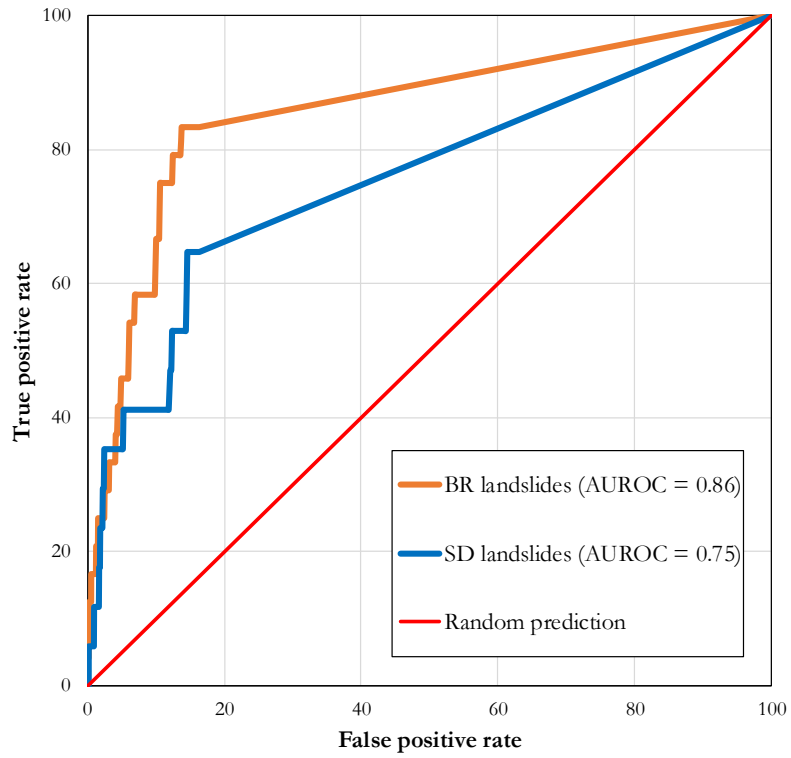


Figure 5-21 ROC curves and AUROC values obtained from the two landslides datasets

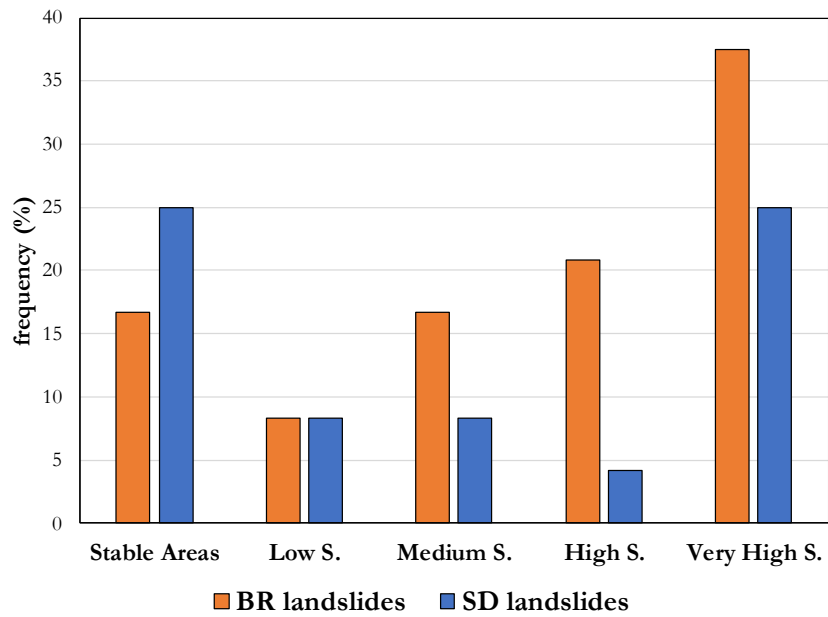


Figure 5-22 Distribution of BR and SDL in susceptibility classes.

5.3.3 Discussion

The susceptibility map presented in Figure 5-20 is the first attempt to predict at regional scale the probability of occurrence of shallow landslides that involve the fractured and weathered portion of rock masses. The distribution of susceptibility is strongly influenced by the setting of Geo-Mechanical Bedrock Units and related geotechnical parameters, which lead to abrupt gaps of susceptibility classes, between the northern and the southern portions of the study area. According to the distribution of BR visited landslides, the model here presented shows very good performance, as demonstrated by both the ROC curve and the AUROC value (Figure 5-21). In Figure 5-22 the distribution of BR and SDL within the different susceptibility classes is shown. The histogram suggests that: 16% of BRL, falling in Stable Areas, are not predicted to fail by the model; nevertheless about 60% of BRL occurred in the highest susceptibility classes (High and Very High). Even though the performance of the model in respect to the SDL is quite weak, about 30% of SDL are located into the highest susceptibility classes. This suggests that SDL and BRL may share some conditioning factors this kind of model is not able to control. Moreover, a similar result is obtained in the paragraph 5.2, where the susceptibility assessment for the two different datasets was performed by using the Information Value.

Figure 5-23 is a scatter plot of the median $\log Q_c/T$ values of BRL and SDL obtained from the two different physically based models. In the x-axis the median $\log Q_c/T$ value resulted by the model in Figure 5-4, computed assuming a sliding surface corresponding to the slope deposit/bedrock discontinuity (SD model) is reported. While, in the y-axis the median $\log Q_c/T$ resulted from the model presented in this paragraph, assuming a sliding surface located beneath the slope deposit/bedrock discontinuity (BR model), is reported. A landslide where the failure occurs in correspondence of the slope deposit/bedrock discontinuity or above should have a higher susceptibility value in the SD model rather than in the BR model, and vice versa. The susceptibility value increase in the bottom left corner, while the top right represents Stable Areas (no $\log Q_c/T$ computed), therefore a dot located in the x or in the y axis correspond to a landslide occurred in an Unconditionally Stable site. The dots located in correspondence of the bisector are landslides which obtain the same susceptibility value (median $\log Q_c/T$) whether the sliding surface corresponds to the SD/BR discontinuity or is below it. The larger the dot distance from the bisector, the greater the $\log Q_c/T$ deviation between the models. It is expected the orange dots should be located under the bisector, while the opposite for the blue dots. Even if the deviation between the two models is not wide for some landslides, the majority of SDL are located over the bisector suggesting that the SD model well predict these slope failures. Moreover, a significant number of SDL are predicted as Stable in the BR model. Despite the BR model performed quite well, testified by orange dots having a significantly higher $\log Q_c/T$ deviation from the bisector than blue dots, there is a significant number of BRL with a lower $\log Q_c/T$ value in the SD model or which are stable according to the BR model. Several

explanations can be given for substrate landslides that fall in stable areas or that are more susceptible according to the SD model. Among all, they may be sites where the depth map is not accurate, or, due to the small extension of these shallow landslides, the DEM may not be enough effective in characterizing the morphology of those locations.

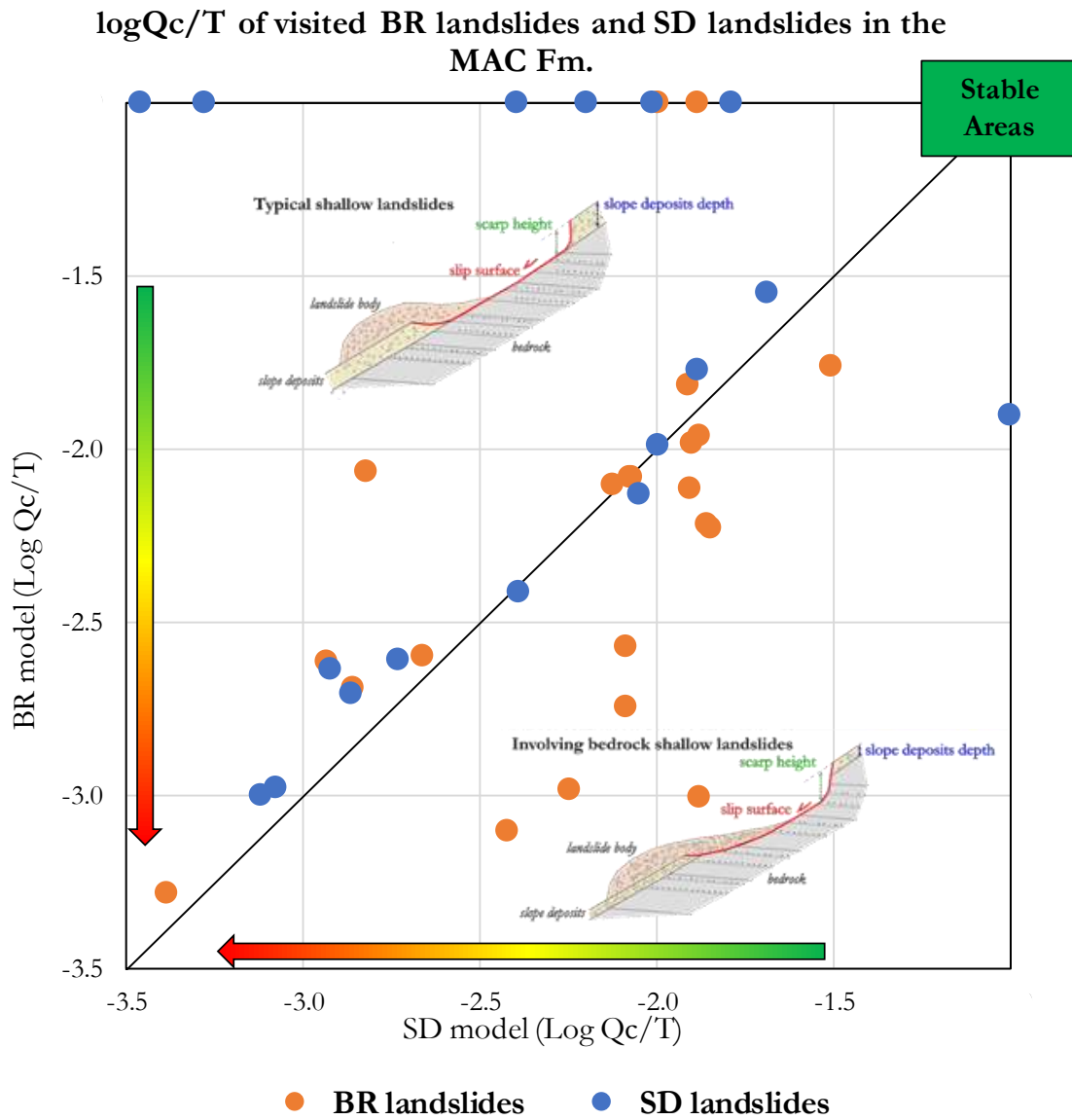


Figure 5-23 Comparison between median Log Qc/T of visited BR and SDL occurred in the Macigno Formation.

Combining, overlapping and comparing both the susceptibility maps allow to spatially discriminate between the areas where either one kind of landslide or the other is more probable to occur. In order to compare and discriminate between areas where the landslides involve SD only or BR also, different approaches can be proposed. Here, two different approaches are presented and discussed.

In the map presented in Figure 5-24, the combination of the two physically based susceptibility models is provided intersecting the susceptibility classes of the two input maps. In this way, it is possible to highlight the areas in which the deviation between the susceptibility classes of the models is present. In example, a pixel classified in the low susceptibility class (2) in the SD model and in the very high susceptibility class (5) in the BR model, is represented by a red tone, corresponding in the legend of Figure 5-24 to “BR +3”. Note that the same result could be obtained if the pixel was classified as “Stable Area” (1) in the SD model and in the high susceptibility class (4) in the BR model. With the green color are represented Stable Areas shared by both models, while the grey describes sites which display the same susceptibility class, regardless of the severity of the input class. Red/orange and blue tones describe the increase of susceptibility class.

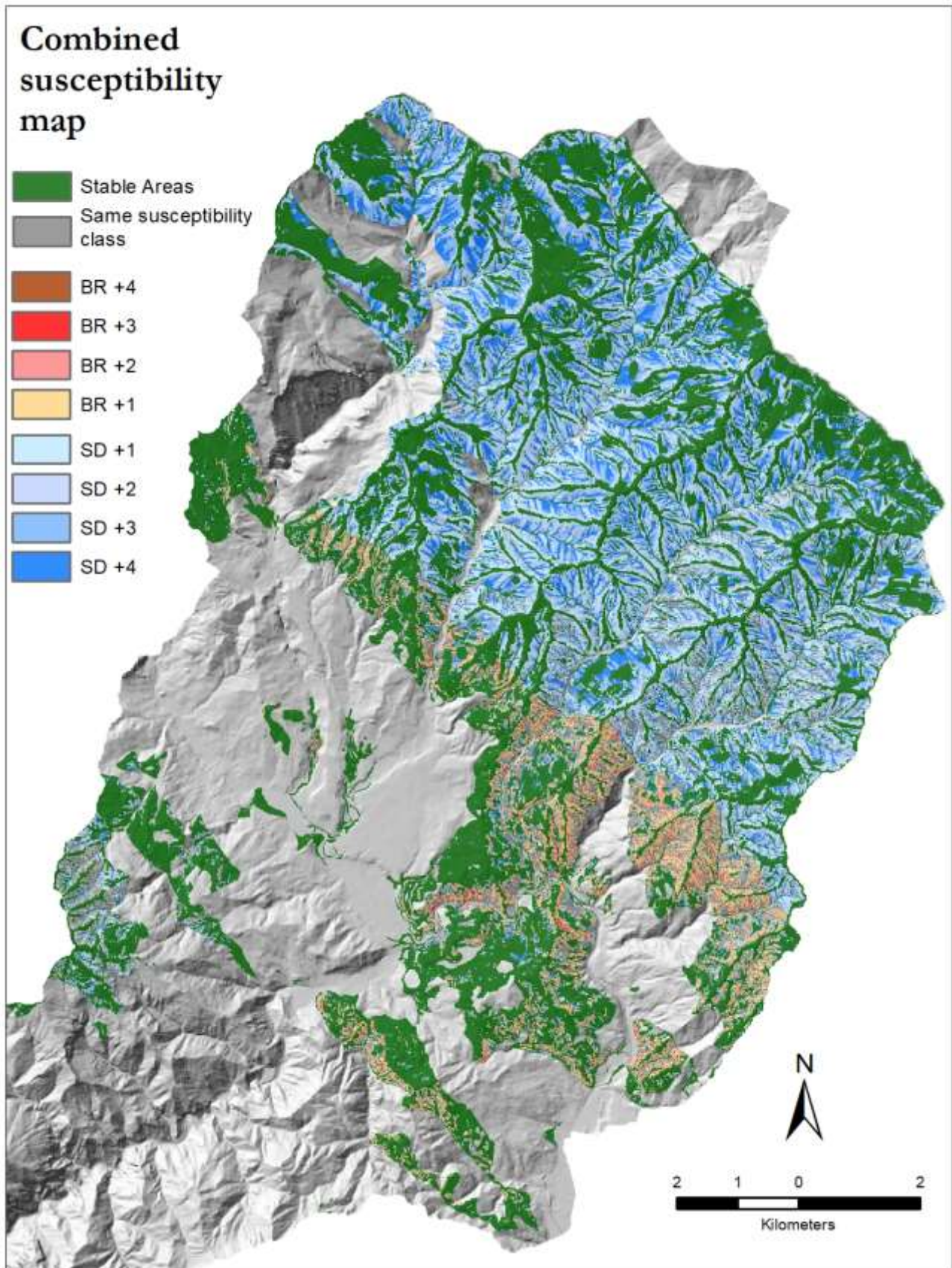


Figure 5-24 Combination of the two susceptibility map. The input maps were classified in susceptibility classes and then intersected. With red tones are represented pixels where the susceptibility class of the BR model map is higher. With blue tones are represented pixels where the susceptibility class of the SD model is higher. Grey pixels represent areas where the two models share the susceptibility class. In green, the stable area are represented.

Another more accurate approach can be followed. As introduced in paragraph 2.6.1, locations characterized by lower $\log Qc/T$ are interpreted as more susceptible to shallow landsliding. Instead, locations with higher values of this indicator are interpreted as more stable, as less frequent rainfall events would be required to cause instability (Montgomery and Dietrich, 1994). Consequently, in order to compare two maps of $(\log Qc/T)_{SD}$ and $(\log Qc/T)_{BR}$ representing the pixel-based susceptibility to SDL and BRL respectively, the following ratio may be used:

Equation 5-1

$$r_{SD/BR} = \frac{\log Qc/T_{SD}}{\log Qc/T_{BR}}$$

The condition $r_{(SD/BR)} > 1$ will indicate pixels with higher susceptibility to SDL than BR, the opposite for the condition $r_{(SD/BR)} < 1$. Nevertheless, the physically based model chosen in this PhD thesis to estimate pixel-by-pixel $\log Qc/T$ was implemented with a probabilistic approach: first, ranges representing the variability of input parameters were defined, then, for a large number n (ex., $n=10,000$) of iterations, sets of parameter values were randomly selected from these ranges to obtain the frequency distribution of $\log Qc/T$, this latter representing the whole set of values which may trigger landsliding.

This output allowed us to perform a more advanced analysis about the type of landslides which are expected to be triggered within the study area. Considering that lower values of $\log Qc/T$ correspond to more frequent rainfall events, the lower percentiles (namely, the percentile 25 – p25) of the $\log Qc/T$ frequency distribution were assumed to be more representative than the higher to perform the comparison between susceptibilities to SDL and BRL. These values were used to calculate $r_{(SD/BR)}^{p25}$ and to select the most probable type of landslides, as above described.

Moreover, in order to obtain a comprehensive new map which describes the susceptibility for both SDL and BRL, the minimum $\log Qc/T$ 25th percentile value of the two distributions was selected pixel-by-pixel and merged in a unique output (Figure 5-25).

Integrated SD and BR susceptibility map

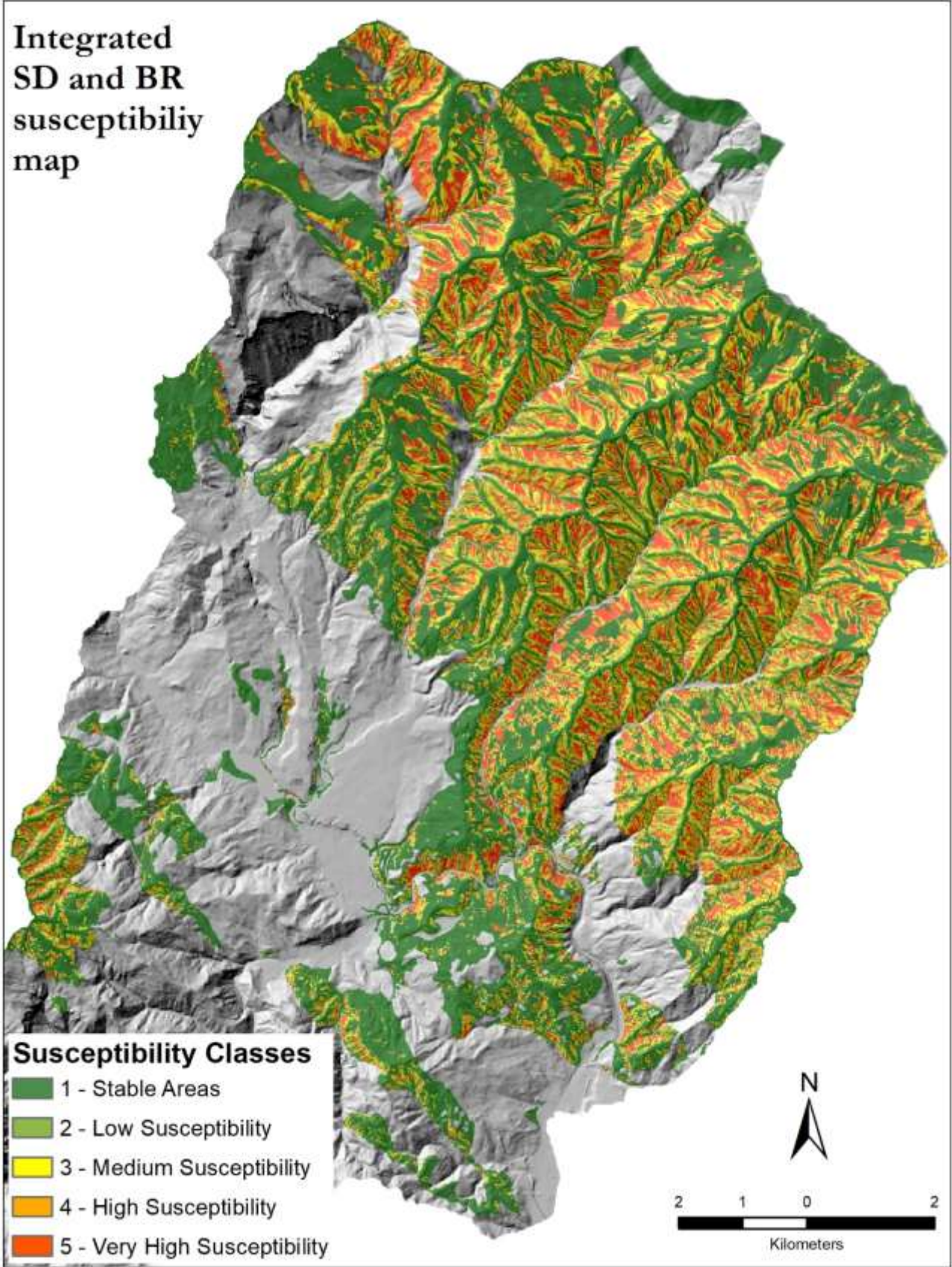


Figure 5-25 Integration of SDL and BRL landslides susceptibility models. The susceptibility is expressed as the 25th percentile of the log Q_c/T distribution.

The distributions of $\log Q_c/T$ of the two susceptibility models were then used to calculate the normalized overlap O_v between the ranges ($p_{95} - p_5$), as defined in the following equation:

Equation 5-2

$$O_v = \frac{R - (d_{p5} + d_{p95})}{R} * 100$$

where d_{p5} and d_{p95} are the absolute deviation between the 5th and 95th percentile values of $\log Q_c/T$ respectively, while R is the range between the minimum 5th percentile and the maximum 95th percentile of the two distributions. An example of $\log Q_c/T$ distributions and percentage of overlapping is provided in Figure 5-26.

This approach has allowed to provide an estimate of the degree of discrimination between the two failure type probabilities. Small values of O_v indicate pixels where the probability of the selected landslide type is “clearly” higher than the other, while high values (up to 100%) indicate that the probabilities of SDL and BRL are each other similar. Both the above information are represented together in Figure 5-27.

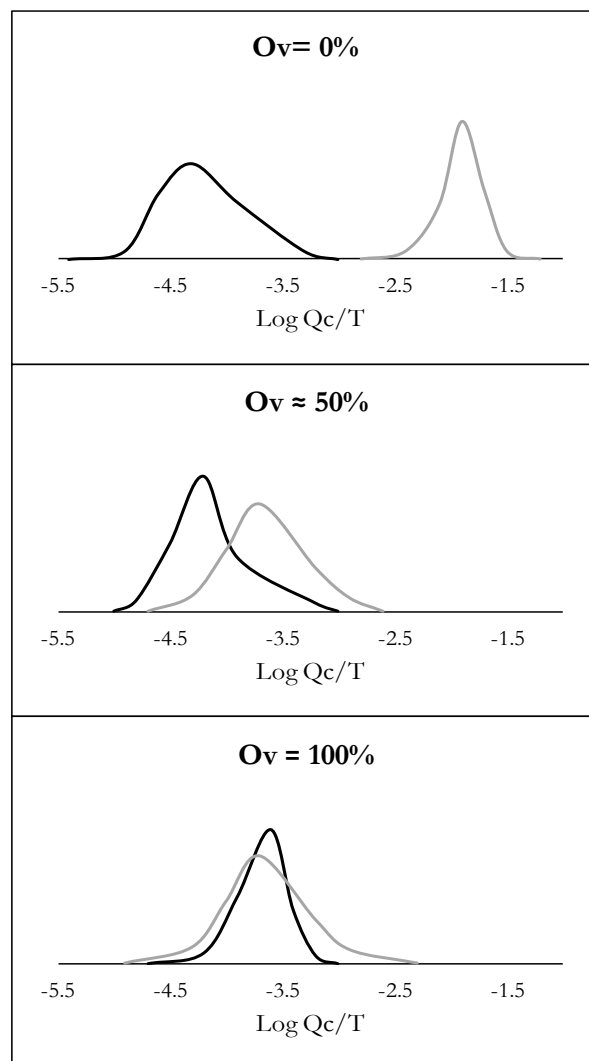


Figure 5-26 Example of percentage of overlapping for $\log Q_c/T$ distributions

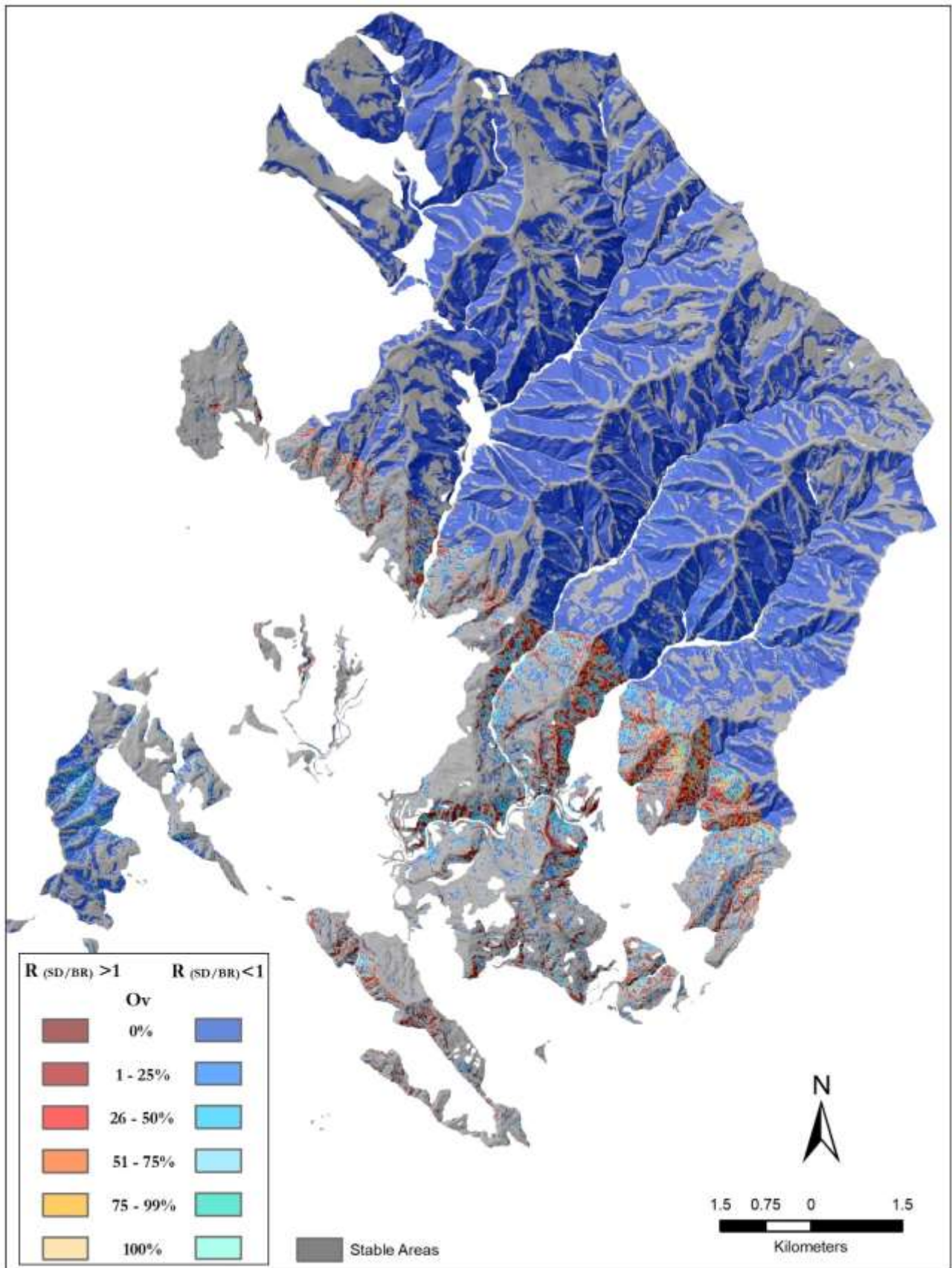


Figure 5-27 Map describing both the $r_{(SD/BR)}$ and Ov (%).

6 GENERAL DISCUSSION

6.1 SHALLOW LANDSLIDE INVENTORY

In order to conduct shallow landslide susceptibility analyses, the availability of a landslide inventory, best if providing accurate information on both the state of activity and the date of occurrence is a fundamental tool for obtaining reliable results. The study area is located in the Tuscany Region which provides a geological and geomorphological database including a landslide inventory, which was compiled by means the regional geomorphological survey and post-event reports provided by local administration and research institutions. The landslide database of the Tuscany Region is also an input for the IFFI project (Figure 6-1, *Inventario Fenomeni Franosi Italiani*), a national scale project aimed at mapping all landslides occurring in Italy. However, the Tuscan regional database of landslides mostly provides information on the date of occurrence of the phenomena, the state of activity and the type of movement.

For this reason, when this PhD program was conceived, the first step was to compile a new multi-temporal inventory of shallow landslides, mostly triggered by intense rainfall events (Figure 3-12) through visual interpretation of orthophotos maps. The Tuscan Region, from the 2000s onwards, regularly acquires (approximately every three years) these remote sensing data for the entire regional territory. Although there are automatic and semi-automatic methods based on the analysis of satellite images or digital terrain models, the multi-temporal visual interpretation of orthophotos was chosen as it is currently to be one of the most widely used and accurate methods (Guzzetti et al., 2012). Furthermore, considering that the aim was to map shallow landslides, this method is very effective especially in densely wooded areas where landslides can be easily recognized thanks to abrupt local-scale variations in texture and tone / color, sharp interruption of vegetation and cultivated fields, disruption of linear patterns, and occurrence of U-shaped elongated features.

Fieldwork tasks in the landslide areas allowed to assess the accuracy of both remote recognition and object delineation, as well as acquiring in situ data for the characterization of landslides and materials involved.

The validation of the inventory led to visit about 56% of the interpreted objects obtaining an overall accuracy of 0.8 with a True Positive Rate of 0.84. Out of 86 mapped polygons, 18 were found to be false positives (objects erroneously mapped as landslides). In general, these misinterpreted entities were found to be man-made excavations along the slopes, recent deforestation areas, and, rarely, outcrops of rock or loose debris. About 13 landslides were recognized in the field only (False Negatives). Two reason may be invoked to explain why these features were not identified from the images: either they were triggered after the acquisition of the most recent orthophoto analyzed (2016), or they were located within shaded areas. All the orthophoto maps analyzed were acquired in the same season and time interval, late spring in the morning. This implies that the slopes exposed towards W-NW may be often not enough illuminated to identify the scar of shallow landslides. Nevertheless, only 3 of the 13 landslides (False

Negatives) are located in W-NW shadowed slopes. This suggests that probably the remaining 10 landslides could be occurred after 2016.

When dealing with shallow landslides, the time factor is important. Being these phenomena of modest size and depth, in mid-latitude climate conditions the regrowth of vegetation can be fast so within few years the landslide scar may be not recognizable neither remotely nor during fieldwork.

Since the orthophotos analyzed were acquired from 2003 onwards and the validation field survey was carried out in 2018, it is interesting to discuss the conditions of vegetation regrowth in the visited landslides. The Table 6.1 shows the frequency percentage of visited landslides classified as a function of the time span between development and image acquisition, as well as the degree of vegetation regrowth. It is interesting to note that about 50% of shallow landslides occurred more than 5 years before the validation field survey are not easily accessible and recognizable. This highlights how important it is for shallow landslides to conduct a multi-temporal interpretation of images acquired in epoch close to failure time (best at 5 years or less) in order to mitigate the issue of obtaining an incomplete landslide inventory. The magnitude-frequency function is often used to investigate the completeness of a landslide inventory, to quantify the amount of slope failures expected after a given event and to estimate the role of landslides in erosion processes (Malamud et al., 2004; Fell et al., 2008; Corominas et al., 2014). Several studies have proposed that the non-cumulative size-frequency distribution of landslides follows a negative power-law relationship for medium to large landslides (Hovius et al., 1997; Pelletier, 1997; C. Stark and Hovius, 2001; Ardizzone et al., 2002; Malamud et al., 2004). The non-cumulative frequency-density of a landslide inventory is given by the number of landslides versus the range of area. The probability density function (pdf) can be estimated normalizing the frequency-density to the total number of landslides of the inventory. In the literature, power-law relationship exponent estimation varies from $\alpha = 1.4$ to $\alpha = 3.3$ (Van Den Eeckhaut et al., 2007). This scaling exponent may vary with underlying geology (Guzzetti et al., 2008; Frattini and Crosta, 2013b; Hurst et al., 2013) or with the failure type (Brunetti et al., 2009; Hurst et al., 2013). The landslide size-distribution exhibits a negative power-law relationship for medium to large events, meanwhile pdf shows a rollover to a positive power-law relationship for smaller landslides. In the literature, there's no agreement about the definition of the rollover. Some authors defined the rollover as the modal value of pdf distribution (Stark and Hovius, 2001; Stark and Guzzetti, 2009b; Li et al., 2016) while other authors consider the rollover approximately as the point of departure of the data from the power-law (Guthrie and Evans, 2004; Guthrie et al., 2008). Regarding the meaning of rollover, three main hypotheses have been proposed. The first is ascribed to the interplay of cohesion and friction, stating that these parameters counteract landsliding for small or large landslides respectively (Pelletier, 1997; Guzzetti et al., 2002; Malamud et al., 2004; Stark and Guzzetti, 2009b). Alternatively, erosion, reworking of deposits and fast vegetation regrowth may be responsible for the concealing of small landslides, resulting in a under sampling of the landslide inventory (Brardinoni and Church, 2004).

Another issue regards the spatial resolution and the scale of the remotely sensed data used to acquire landslides data (Galli et al., 2008; Guzzetti et al., 2012). The landslide dimension at which rollover occurs in historical inventories is located at larger sizes in respect to event-based inventories because small landslide “disappears” faster in respect to larger landslides (Trigila et al., 2010; Guzzetti et al., 2012). For the pdf of the shallow landslide inventory compiled in this work (reported in Figure 6-2), the power-law relationship exponent resulted to be in agreement with the literature ($\alpha = 1.4$) and the rollover was located at ca 92 m². In the Figure 6-2 this pdf is plotted together with the pdf of the Tuscany Region inventory. The latter is shifted to the right as it is most probably depleted for small landslides, thus demonstrating that an adequate inventory is needed to model shallow landslides susceptibility. The roll over in the function of the Tuscany Region is at ca 1025 m² while α is 1.2. Anyway, the inventory here proposed cannot be considered completely representative, as it does not include slow moving and/or deep landslides. Nevertheless, the pdf distribution of the multi-temporal inventory built during this PhD research suggests: a) the rollover is a recurrent phenomenon depending on the scale of analysis, b) shallow large landslides (area > 10⁴ square meters) are lacking.

The distribution and frequency of shallow landslides (Figure 4-1) is closely linked to the lithological nature of the bedrock on which they occur (Bedrock Lithological Unit, BLU), which influence the properties of the involved materials, the morphology of slopes and the hydraulic conditions. For the whole study area, the average density is 0.8 landslides/km². The BLU which appears to have the greatest number of landslides is BLU11 (Sandstones), while the one with the least number is BLU21 (Marbles). By normalizing the frequency for the extension of the BLUs, it appears that the BLU with the highest landslide density are BLU23 (Limestones) and BLU51 (Shales and Marls). BLU 62 (Metarenites) and 61 (Phyllites) show high density values however given both the small number of landslides and the small extent, the data cannot be considered reliable. The meta-carbonates BLUs (21 and 22) show the lowest landslide density. This result is in good agreement with the common lack of slope deposits and the excellent quality of the bedrock. The high density within BLU 23 and BLU 51 may be explained with two different reasons. Most of the landslides that occur in the BLU 23 involved bedrock (out of 15 landslides visited, 13 involve the bedrock). Consequently, as highlighted by the results of physically based modelling applied to bedrock landslides, it is reasonable to assume that the rocks under the contact with the slope deposits have poor quality due to weathering and fracturing. BLU 51 is made up of shales and marls, where an equal distribution of landslides either involving the bedrock or the slope deposit only are observed. In the first case, since this rock mass have low permeability, the overlying slope deposits are quickly saturated during intense rainfall events, triggering shallow landslides. Instead, involving bedrock landslides may have been caused by the low shear strength of clayey and marly materials. BLU 31 consists mainly of weakly cemented continental deposits, that are nowadays incised and eroded by the drainage network, leading to the formation of very steep river embankments. It is reasonable to hypothesize that

these landslides may be caused both by the steep morphology and bank erosion processes. Most of landslides occurred in the BLU 11 (Sandstones) involved the bedrock. Given the large number of landslides visited during fieldwork in this BLU, a modified physically based susceptibility model was implemented for this area also including the topmost bedrock underlying the slope deposits.

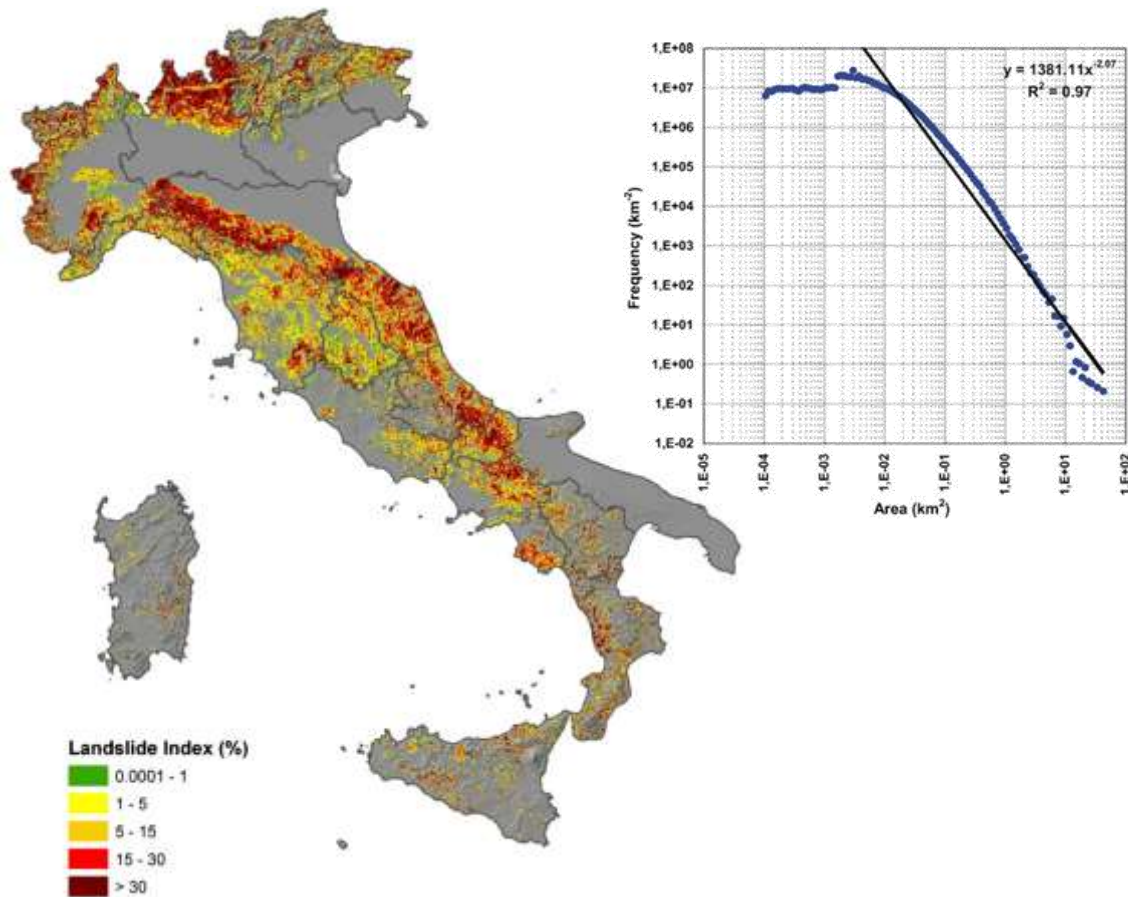


Figure 6-1 Landslides index map and landslide area-frequency distribution of the IFFI project (from Trigila et al. 2010).

Table 6.1 Vegetation regrowth degree in visited landslides according to the period of occurrence

Vegetation degree of regrowth (% frequency)	Time elapsed between landslide occurrence and the fieldwork			
	Over 10 years	Within 10 years	Within 5 years	Within 2 years
No vegetation regrowth, fresh scar	29	14	37	54
Poor vegetation regrowth, all the landslide features easily recognizable	17	36	42	31
Widespread vegetation regrowth, scarp and accumulation body not easily recognizable	38	43	21	15
Completely regrowth of bush and trees, not recognizable in the most recent images	17	7	0	0
Total	100	100	100	100

Magnitude-frequency probability density function

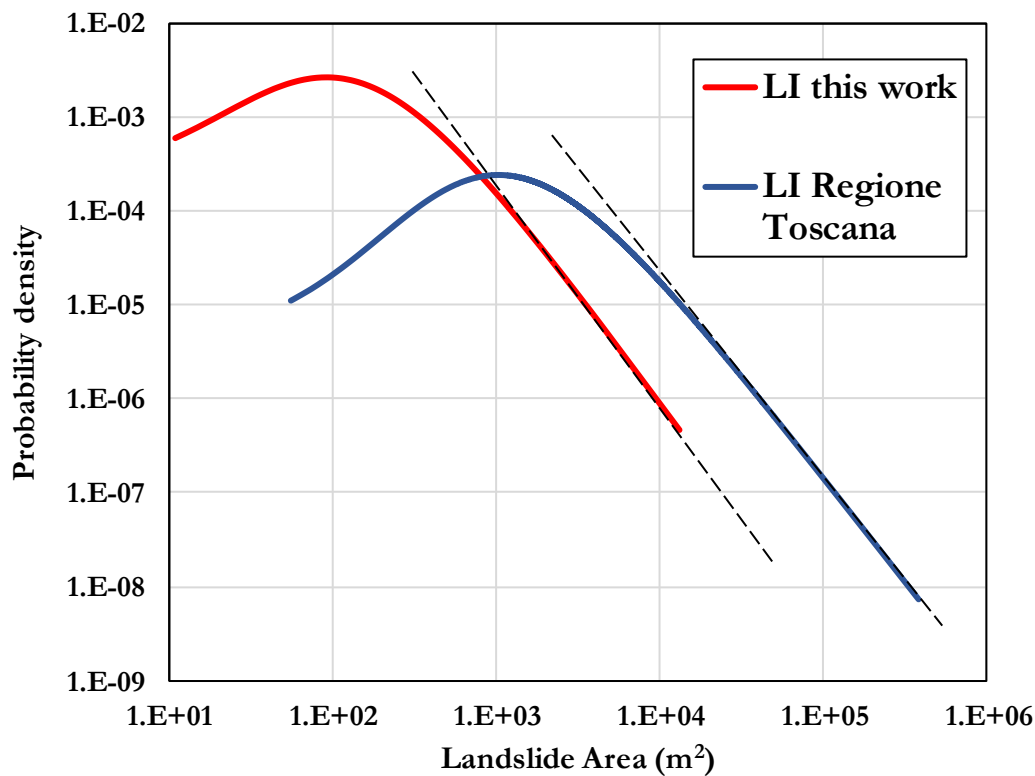


Figure 6-2 Magnitude-frequency relations obtained for the LI compiled in this work and the Tuscan Region database

The field survey allowed to acquire also important information such as material involved, the movement type and geometric features of shallow landslides. A very interesting finding was the high percentage (about 60%) of landslides developing the sliding surface below the discontinuity between the slope deposit and the bedrock. These observations were carried out on the main scarp, as well as on the lateral scarps.

Planar rockslides and avalanches typically characterize involving bedrock landslides. According to the definition of Hungr et alii (2014), rock planar slides consists on the sliding of a mass of rock on a planar rupture surface, with little internal deformation. The slide head may be separating from stable rock along a deep, vertical tension crack. This kind of landslides may evolve in a rock avalanche if the material disintegrates during the run-out. Rock avalanche are phenomena characterized by the interaction among rock fragments and water, which lead to a flow-like motion. For both these failure types bedrock fracturing and weathering is a predisposing factor. Field evidences suggest that in bedrock landslides, sub-vertical joint systems orthogonal to bedding, may play a fundamental role for the failure.

According to the classification proposed by Hungr et al. (2014), the majority of SDL are planar debris slide, where an almost planar rupture surface develops parallel to the ground surface. Sometimes, debris slides become flow-like after a short distance and transform into debris avalanches. Rotational slides are

characterized by scarp height larger than 1.5 m. Granular flow-slide are present in the study area and characterized mainly by gravelly and sandy SD lying above the Macigno formation.

Due to logistical and approaching problems, it was not possible to visit additional landslides and conduct further detailed analyses. It is worth noting that these problems that led to visiting some landslides instead of others could be a source of uncertainty in the data acquired in the field. However, even if the distribution of the landslides visited is not random, the data obtained from the field survey are sufficiently heterogeneous to exclude major errors.

6.2 SLOPE DEPOSITS FEATURES AT REGIONAL SCALE

About 8 months were necessary to develop the Slope Deposits Engineering Geological Units map (SDEG map), 4 months for the collection of data in the field, 2 for laboratory analyzes and 2 for data processing. The method described here allowed to produce a fairly accurate map of the depth of the slope deposits and to estimate their geotechnical parameters, on lithological and morphometric basis. It is fair to note that although there are more advanced methods to estimate the depth (automatic drilling machine, geophysical methods) and shear strength parameters of SD (shear tests), it is unlikely to think of using those tools in a large area that has a mountainous and logistically complex morphology. Furthermore, the costs would be enormous to reach an adequate amount of data to characterize an area such as the one investigated in this work. The proposed method is spatially oriented to regionalize, which can certainly be improved, has a limited cost, while the consumption of time and energy depends on the geological and geomorphological variety of the survey sites. The uncertainty resulting from this procedure is discussed below.

The depth of the slope deposits is a tricky quantity to estimate predict and its spatial variability can be of the order of tens of centimeters moving tens of meters. For this reason, instead of mapping the SD depth as a spatially continuous set of scalar values, a nomenclature of depth classes with constant amplitude was chosen. Having set the width of the classes at 30 cm, the minimum expected uncertainty within each class is ± 15 cm. The accuracy of SD depth map proposed in this work ranges from 0.49 to 0.68, as described in paragraph 4.2.2. If, on the other hand, a greater error is accepted, i.e. that the uncertainty expected for each class is ± 45 cm and therefore the assigned class is the one immediately higher or lower, the accuracy rises from a minimum of 0.77 to a maximum of 0.88. As a general results the SD depth map highlight that depth increases moving from the ridges towards the valley floor, in accordance with the theoretical models that describe the development of the SD along the slopes (Dietrich et al., 1995; Lu and Godt, 2011).

The modelling of SD depth is fundamental task for landslide susceptibility analysis and several authors proposed different approaches in the last decades (Salciarini et al., 2006; Segoni et al., 2012; Zizioli et al., 2013; Kim et al., 2016; Cascini et al., 2017) to predict SD depth at regional scale. With the exception of Kim et alii (2016), where the depth measurements of the slope deposits are interpolated with the kriging method, the other authors model this parameter on a morphometric basis, using variables such as elevation, slope, curvature, and so on. Results by Salciarini et alii (2006) show that errors between predicted and modelled depth is often greater than one meter and may overcome 1.5 m (Figure 6-3). The same deviation (Figure 6-4) is about 0.5 m with maximum values of about 1 m for the model adopted by Zizioli et alii (2013). In two different study areas Segoni et alii (2012) obtained with the GIST model a mean absolute error of 11 cm and 23 cm for the first and the second study area, respectively (Figure 6-5).

The approach developed by Cascini et alii (2017) consists on the assignation of a depth range (with a variable amplitude ranging from 0.5 m to 2 meters) combining thematic maps such as lithology, slope, elevation, curvature and landslide mechanism. The 55% of the test dataset used to validate the depth map resulted to have a deviation between measured and observed values equal or less than 0.3 m (Figure 6-6). Finally, the mean absolute error resulted from the cross-validation of the SD depth map by Kim et alii (2016) is 0.74 meters (Figure 6-7).

Given the results listed above, the method proposed in this work allow to obtain a map of slope deposits depth reasonably accurate, especially considering the study area extension and the involvement of regions characterized by pronounced geological and geomorphological variability. In this regard, for the approach proposed in this PhD thesis, the main assumption is that different lithologies imply different landforms, which in turn affect the distribution of SD depth. Carbonate, metacarbonate and phylladic rocks in fact give rise within the study area to steep landforms characterized by very thin deposit depths, as the classes with a depth of less than 90 cm prevail. Sandstone as well as shale and marl are covered by thicker slope deposits which are often deeper than 120 cm in correspondence of large first order hollows and at the foot of longer hillslopes.

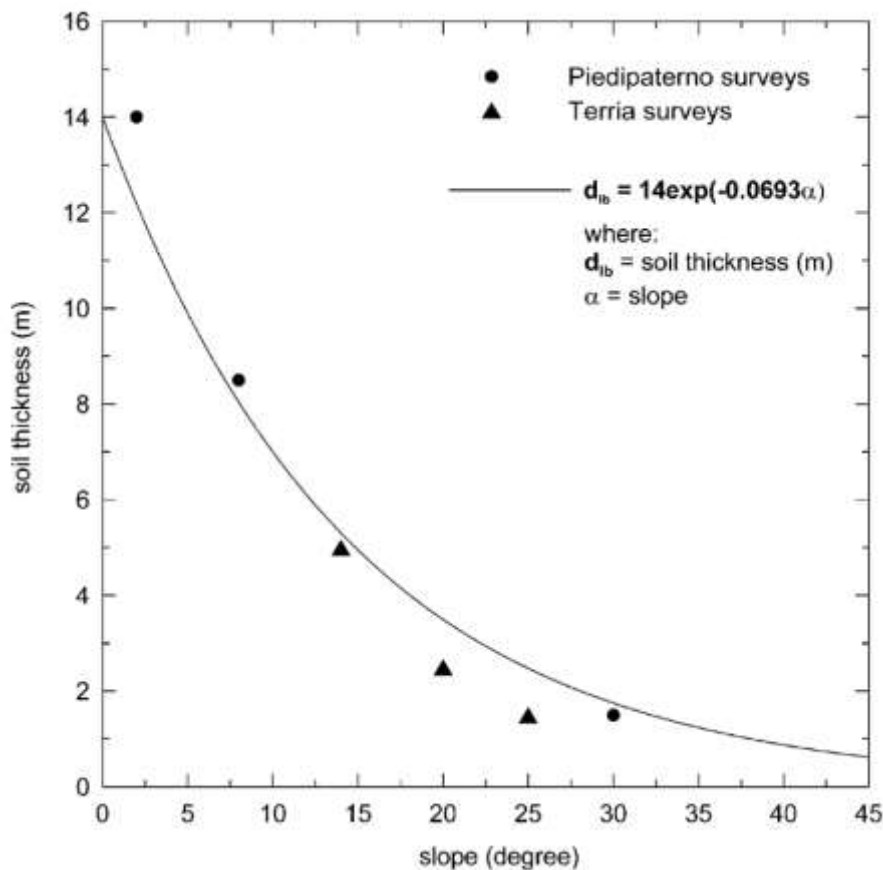


Figure 6-3 Relationships between soil thickness and slope values; data are modelled by using an exponential model (from Salciarini et al. 2006)

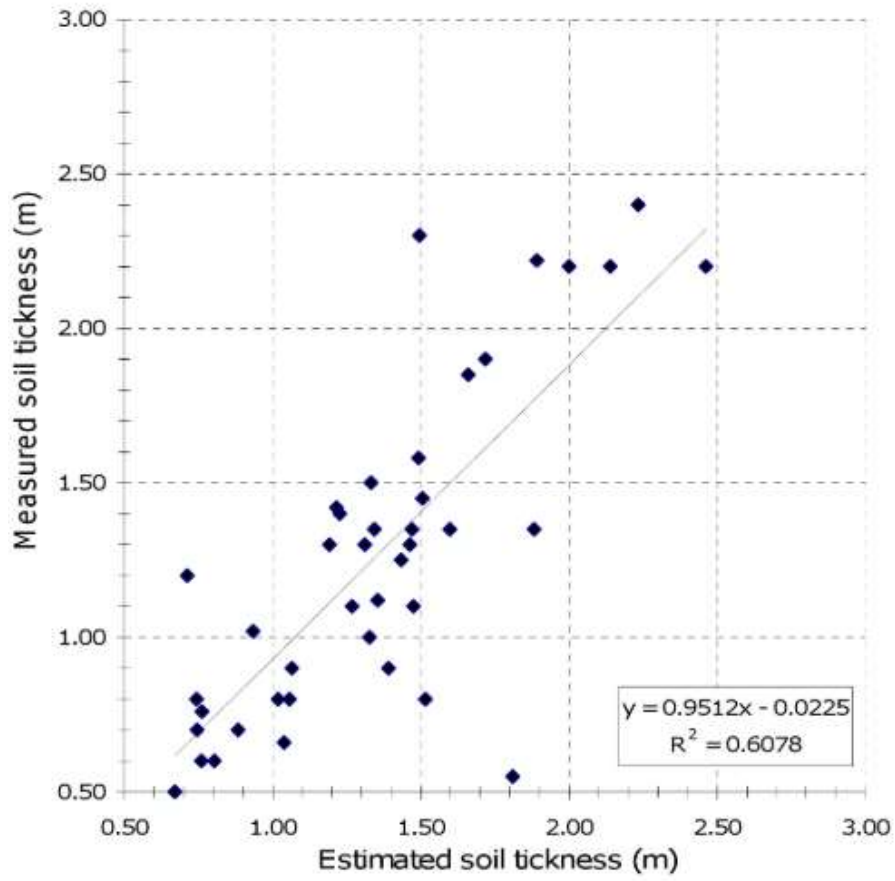


Figure 6-4 Scatter plot of soil thickness calculated by a topographic model and field measurements (from Zizioli et al. 2013)

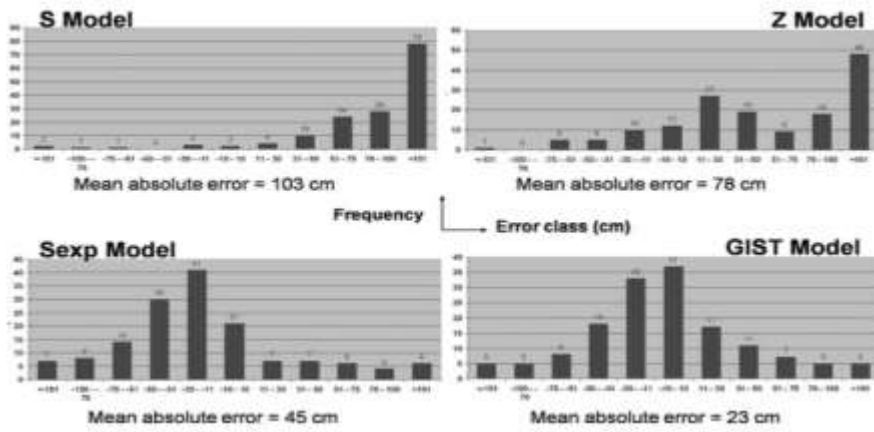
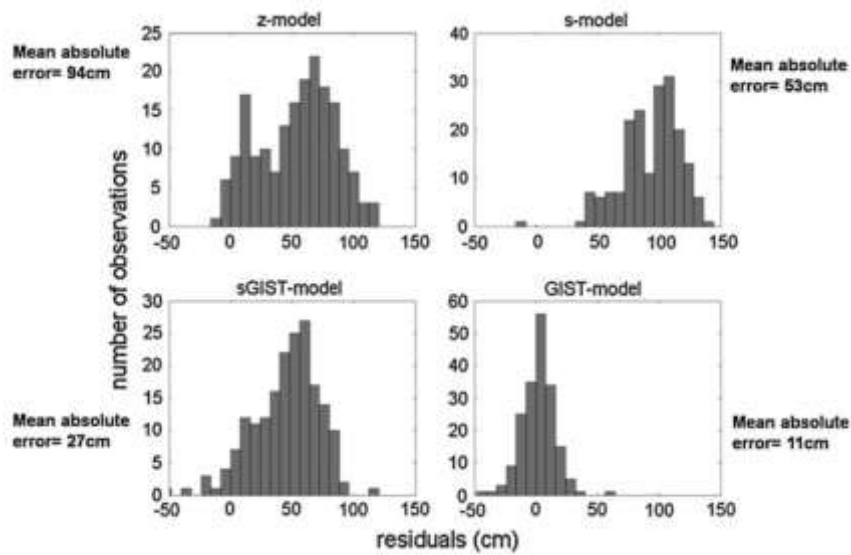


Figure 6-5 Frequency-Error histogram and mean absolute error for the two study area of the model proposed by Segoni et alii (2012)

Table 4 Table of differences necessary to verify the consistency criterion

Mv-Av (m)	# points	%
±0.1	32	13
±0.2	32	13
±0.3	73	29
±0.4	48	19
±0.5	63	25

Figure 6-6 Results of depth discard between measured and observed data (Mv-Av) (from Cascini et alii, 2017)

Classification		Measured WSD	IWSD	MBSD	IBSD
a) Soil depth statistics (unit: m)	Minimum	0	0.013	0	0.013
	Maximum	1.91	1.916	2.40	2.33
	Mean	0.97	0.91	1.14	1.07
	Standard deviation	0.4467	0.4461	0.4941	0.4916
b) Cross validation	MAE	-	0.73	-	0.740
	MSE	-	3.51	-	4.23

MWSD: measured weathered soil depth (m).
IWSD: interpolated weathered soil depth (m).
MBSD: measured surface to bedrock soil depth (m).
IBSD: interpolated surface to bedrock soil depth (m).

Figure 6-7 SD depth statistics and cross validation of the SD map proposed by Kim et alii (2016)

From the laboratory results of the grain size and plasticity properties, a correlation emerges between the USCS class of SD and the lithological nature of the underlying bedrock. The sandstones (BLU11) are almost exclusively characterized by SM deposits (silty sand), shales and marls tend to generate finer deposits belonging to the ML, SM and SC (silt, silty sand and clayey sand, respectively) classes, the metasedimentary rocks (Phyllites and Metarenites, BLU61 and BLU62) have deposits of similar composition (SM and GM, silty sand and silty gravel) although with varying proportions. The deposits lying above the limestones of BLU 23 instead, have a wider variability: the USCS classes show the modal value SM, but SC, GM and ML are also widespread.

Working at regional scale, further data than laboratory results are necessary in order to estimate the variability of geotechnical parameters of slope deposits.

To this purpose, also results of field estimations were used. Figure 4-25 shows the scatter plots comparing the grain size proportions resulting from the two datasets, and in Table 4.9 the Mean Bias Error for each class is reported. As shown by the graphs the average error is the same and is ca 6%.

In the work of Vos et alii (2016) these authors observed that the uncertainty between the field and laboratory estimates due to the operator for sandy, silty and clayey fractions (according to limits USDA), is respectively 4, 12 and 16%. Furthermore, these authors pointed out that an intrinsic uncertainty affects the method used to estimate the grain size fractions in the field: the range of variability for the same textural class in the USDA triangle is generally in the order of 10–45%. Therefore, taking into account these issues, an average difference of $\approx 6\%$ between the field estimates and laboratory tests may be considered a good result.

When integrating field and laboratory analysis datasets of grain size according to a simplified USCS classification (Figure 4-38) a relevant outcome is the marked increase of gravel. When a slope deposit is composed by more than 40% of coarse-grained particles ($d > 2$ mm) both undisturbed and representative sampling are tricky. Considering the simplified USCS classes: SD in the BLU 11 (sandstones) are

essentially composed by gravels and sands (silty sands mainly), BLU 51 (shales and marls) and 23 (limestones) display similar proportion among F-S-G, while BLU 61 and 62 (phyllites and metarenites) are poor in sandy SD in respect to G and F. Finally, BLU 21, 22 and 31 are very little represented.

In order to collect SD parameters used to perform landslide susceptibility analysis a literature review was conducted (Table 6.2) to compare them with the friction angles and saturated unit weights obtained by this research (Table 4.14). About 40% of the papers listed in the table, implement the stability analysis by using both shear strength parameters and unit weight acquired from the literature. Among the works where SD properties were assessed by means of laboratory analysis, only the works of Chen and Zhang (2014) and Cervi et al. (2010) are performed at regional scale, confirming that when working for large areas it is too costly in terms of time and resources to conduct laboratory shear tests on a large amount of representative samples. However, the results of saturated unit weight determinations of this research (17.8-20.4 KN/m³) are in good agreement with those obtained by Zizioli et alii (2013), as well as the friction angles (26.2°-33°). A good degree of agreement there is observed with the data provided by Marin and Mattos (2019), Meisina and Scarabelli (2007) and Salciarini et alii (2006). Since no direct laboratory shear tests were carried out in this work, the effective cohesion values were estimated in back-analysis starting from the input values shown in the Table 6.3. Initial c' data were assigned for each EGU based on particle size distribution and USCS class. The calibration was performed at EGU scale taking into account both the absolute susceptibility results obtained by PROBSS and the new inventory of shallow landslides compiled in this work. The PROBSS model provides three different conditions: the Q_c -dependent (Q_{cd}), the Unconditionally Stable (US) and Unconditionally Unstable (UU). Since PROBSS is a steady-state model, in UU areas slope failure occurs even when the SD is dry ($W = 0$). These areas are probably rock outcrops, where the slope steepness is too high to allow sediment accumulation (Montgomery et al. 1998). Thanks to the SD depth map obtained in this research, bedrock outcrops and/or very thin SD depth (<30cm) areas have a well-constrained distinction, decreasing the probability of misprediction occurring when UU areas are widespread. Consequently, since the UU condition is a paradox, the first calibration to be performed on the effective cohesion is to set its minimum value at BLU scale in order to minimize the UU areas. The US zones are sites where there is no slope failure even when the $W = 1$, i.e. the water table reaches the topographical surface. The maximum effective cohesion value is set at EGU scale in order to minimize the number of landslides falling within the stable areas. By intersecting the levels of US, EGU and landslides, the c' maximum value is decreased in the EGUs in which slope failures have occurred. A similar approach is performed in the Q_c -dependent (Q_{cd}), corresponding to those areas which do not fulfil both the UU and US condition, maximizing the susceptibility value in EGUs where landslides have occurred by decreasing the value of c' . The procedure described above is iterative. To quantify the role of effective cohesion for the estimation of the susceptibility to SD, two scenarios with

constant c' values of 1 kPa and 10 kPa are respectively computed and compared with the output of the model obtained after the calibration of c' (Figure 6-8).

Table 6.2 Literature review of shear strength and saturated unit weight values used as input parameters for regional physically-based susceptibility modeling

Reference	Saturated unit weight (kN/m ³)	Friction Angle (°)		Effective cohesion (kPa)		Source of SD parameters	Study area (km ²)
		min	max	min	max		
Teixeira et al. (2015)	13.7-15.7	31	35	2	2.3	back-analysis	1.2
Marin and Mattos (2019)	19-19.5	22.5	30	7.9	15	lab test on specimens	0.1
Meisina and Scarabelli (2007)	19.5	18	35	0	0.23	lab test on specimens	5
Michel et al. (2014)	14-21	25	37	9	14	lab test on specimens	16
Zizioli et al. (2013)	17.4-19.9	23	32	0	10	lab test on specimens	26
Pradhan and Kim (2016)	16.5	35.6	35.6	2.14	2.14	lab test on specimens	33
Chen and Zhang (2014)	21	31	42	2	6	lab test on specimens	164
Cervi et al. (2010)	20-24	10	35	0	10	lab test on specimens	450
Oliveira et al. (2017)	17.5-21	19	27	1	4	literature	14
Salciarini et al. (2006)	18-19.5	18	34	0	10	literature	100
Carrara et al. (2008)	18	30	40	1	3	literature	300
Weidner et al. (2018)	15	30	35	1	4	literature	375
Wang et al. (2020)	13-21	16.5	40	5	50	literature	2*10 ⁵

Table 6.3 Comparison among results of physically-based susceptibility models implemented with constant effective cohesion values of either 1kPa or 10 kPa, or based on c' calibration

Effective Cohesion			US (%)		QcS (%)		UU (%)	
min	max	median	Total area	Landslides	Total area	Landslides	Total area	Landslides
1			26.3	2.6	62.4	82.7	11.3	14.7
10			97.3	87.4	2.7	12.6	0	0
3.15	6.27	4.75	64.6	13.6	35.3	86.4	0.1	0.0

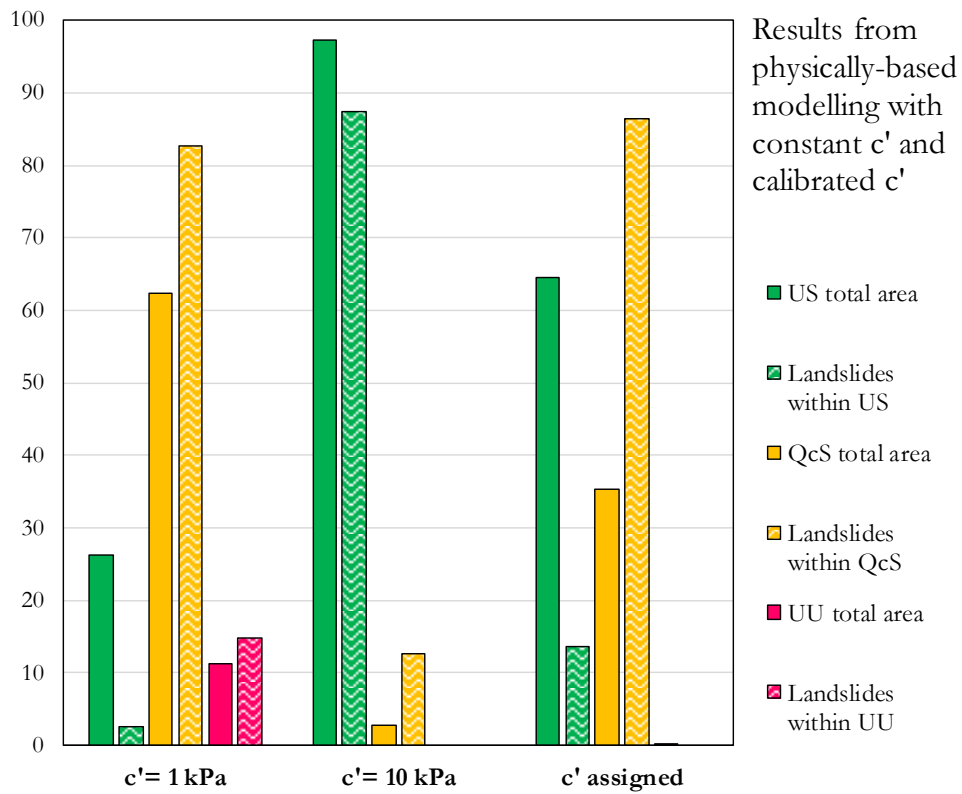


Figure 6-8 Quantification of the role of effective cohesion for the estimation of susceptibility of SD. Effects of constant c' values of 1 kPa and 10 kPa compared with the c' range obtained by model calibration.

6.3 ASSESSMENT OF BEDROCK GEO-MECHANICAL PROPERTIES AND REGIONALIZATION

In the literature different methods for the classification of rock masses have been proposed. Among the most used the Barton's Q (Barton, 1976), RMR (Bieniawski, 1993), RMI (Palmstrøm, 1996) and GSI (Hoek, 1994; Marinos and Hoek, 2000) methods may be selected. All these methods were developed as a response to the need to quantify the quality of rock masses for engineering purposes. Except for the GSI, this is done mainly by integrating a set of "weights" derived from physical and engineering geological characteristics, such as the lithological nature, the uniaxial compressive strength and the frequency, weathering and persistence of discontinuities. Excepting for the GSI, the application of the rock mass classifications listed above is time consuming and not feasible for regional scale rock mass quality assessment. For this reason, in this work the GSI was preferred due to its fastness and versatility in characterizing natural outcrops. This method was integrated with the analysis of the joints and the in-situ acquisition of Schmidt hammer rebound (R_v) applied over the whole extension of the outcrops, by using a regular grid consisting of twenty nodes where twenty rebounds are acquired. This approach allowed to calculate an outcrop average rebound value R_v that was then used to empirically estimate the uniaxial compressive strength (UCS) by means the empirical correlation proposed by Deere and Miller (1966), chosen because reach the highest correlation index (0.94) and include the dry unit weight. The Deere & Miller formula was obtained by measuring mainly hard rocks, for this reason the minimum R value measured by the authors in their specimens is 23. The rebound values obtained in this work are sometimes lower than this value, opening up the issue of the reliability of the empirical relationship to calculate low UCS values. Among other empirical correlations available in the literature (Table 2.5), validity ranges that are suitable for the purpose of this work are proposed by: Aufmuth (1973), Torabi et al. (2011), Karaman and Kesimal (2015), Selçuk and Yabalak (2015) and Hebib et al. (2017). The empirical correlation proposed by Aufmuth is the only one based on a linear equation and tends to overestimate the value of UCS compared to other works. Hebib et al. (2017) conduct the analysis only in sedimentary rocks. In the functions proposed by Torabi et al. (2011), Karaman and Kesimal (2015) and Selçuk and Yabalak (2015) the dry unit weight is not considered. Regarding this issue, Aydin and Basu (2005) discuss the usefulness of implementing in empirical correlations the dry unit weight affirming that where reliable density measurements are available, they will likely correlate as well with the mechanical properties as the Schmidt hammer test. The use of dry unit weight may help reducing the influence of surface deterioration and/or small-scale variations (of asperities, minerals, cracks, etc), which could dominate Schmidt hammer results of certain specimens. Since one of the objectives of this PhD thesis is to characterize the properties of sub-surface rock masses at regional scale, the dry unit weight is useful for discriminating among rock

masses of the same or different BLU but affected by different processes of micro-fracturing and weathering.

In the literature, few works have been found aiming at spatialization of rock masses quality at regional scale and they are based on geostatistical methods. Shokri et alii (2020) provide a review about spatial correlation of measurements in rock mass. The authors report a summarizing table of semi-variogram parameters (nugget, sill, range) of several case studies aiming to spatialize geotechnical properties such as GSI, Schmidt Hammer rebound, UCS, RMR and so on. Mammoliti (2020) proposed an expeditious method based on the systematic collection of fieldwork hardness measurements to describe the variability of subsurface rock masses quality at the map scale. The spatialization of field data was performed by using Bayesian Networks and morphometric variables. Nevertheless, in this thesis, the aim was to recognize the existence of spatial domains (BMU) characterized by different geo-mechanical properties. Hence, uni-variate and multi-variate clustering were used to highlight that, within the same geological formation (the Macigno flysch, MAC), a clustered variability of rock mass properties occurs influencing the distribution of shallow landslides. The expert-based delineation of BMUs is based on the assumption that the geological evolution of the study area, together with meteoric weathering and erosion, played a fundamental role in shaping the landscape and diversifying the geo-mechanical evolution of rock masses. The biggest limitation of this approach is that the boundaries of the BMUs are abrupt and not always defined by indisputable geological evidence.

The distribution of bedrock properties in the Macigno formation is characterized by the occurrence of a low-quality cluster, located in the southern portion of the study area, in which R_v and GSI have the lowest values. Higher R_v and GSI occur in the western and eastern portion (BMU3 and 4) displaying also an increase of J_v , suggesting that while the BMU1 is the most weathered, BMU3 and BMU4 are more fractured. Finally, BMU2, located in the northern portion, has the lowest J_v and the highest R_v and GSI. This clustering may be related to the structural setting of the study area. The Garfagnana valley is a tectonically active narrow post-collisional basin (Carmignani et al., 2001) with a Late Quaternary throw rates ranging from 0.4 to 0.6 mm/year (Di Naccio et al., 2013) bounded by two main sub-parallel ridges less than 20 km far to each other. Both the ridges reach about 2000 m a.s.l. In the southwest mainly consisted in green schists facies metamorphic rocks while in the north-east sedimentary flysch (Macigno fm.) crops out from the bottom of the valley to the watershed (Figure 3-7). This morpho-structural setting is due to regional systems of normal faults dissecting the Apennine's chain. The geo-mechanical clusters, recognized by integrating field surveys and spatial processing of measurements during this PhD research, coupled with the tectonic information above-mentioned, allow to depict an interesting novel framework: quality of the rock masses increases in correspondence of the footwall of major normal faults, while are worst at the hanging wall, which today correspond to the bottom of the Garfagnana valley. This area

corresponds more or less to the BMU1. These characters may be explained with both a slow erosion rate and lower topographic elevation, which in turn imply faster weathering as well as slower bedrock erosion. The Macigno sandstones is a rock used as building material and dimension stone since prehistoric times and is still quarried in some areas of the northern Apennines. In Lezzerini et alii (2008), rock specimens were sampled into two quarries located about 50 km away from the study area of this PhD thesis, to uniaxial compression test. The UCS resulted to be 140 MPa. The UCS results obtained here by means empirical correlations, provided maximum values of 70 MPa and minimum values of 15 MPa. Although these data cannot be directly compared, it is worth to note that the geomechanical properties of the subsurface units of this formation are spatially heterogeneous as a combined effect of regional tectonics and weathering. As a consequence, the same formation may result as a source for dimension stone or either the location for one of the most landslide prone areas in northern Apennines (Avanzi et al. 2010 and references there in; D'Addario et al. 2018).

As for the procedure here implemented to estimate the shear strength parameters of the bedrock, the method proposed by Hoek and Brown (1997) to calculate Mohr-Coulomb equivalent parameters is widely accepted and used in the literature (Sjöberg, 1997; Marinou and Hoek, 2001; Cai et al., 2004, 2007; Priest, 2005; Tüdeş and Ceryan, 2011; Shen et al., 2012; Berti et al., 2017; Vásárhelyi and Kovács, 2017; Wei et al., 2019). The method allows to estimate the internal friction angle and effective cohesion of rock masses by using the uniaxial compressive strength (UCS), a frictional parameter (m_i) and the GSI. In general, rock masses exhibit post-peak strain-softening behaviour where the post-peak strength depends on the resistance developed on the failure plane against further straining (Cai et al., 2007). In jointed rock masses the failure occurs mainly depending on fractures orientation, degree of interlocking and surface roughness. The current GSI system guidelines were developed for the estimation of the peak strength. Cai et alii (2007) proposed a new method for the estimation of residual strength of rock masses reducing the peak GSI to the residual GSI, based on in-situ block shear test data from three large scale cavern construction sites and data from a back-analysis of rock slopes (Figure 6-9). Since the aim of this work is to evaluate shear strength parameters of jointed rock masses affected by deformation due to slope failures, the equivalent Mohr-Coulomb parameters were calculated using the residual GSI. In Table 6.4 the shear strength parameters obtained with the Mohr-Coulomb failure criterion during this PhD research are compared with other datasets from the literature. Except the work of Tüdeş and Ceryan (2011), in the other papers the parameters were calculated for slope analysis purposes.

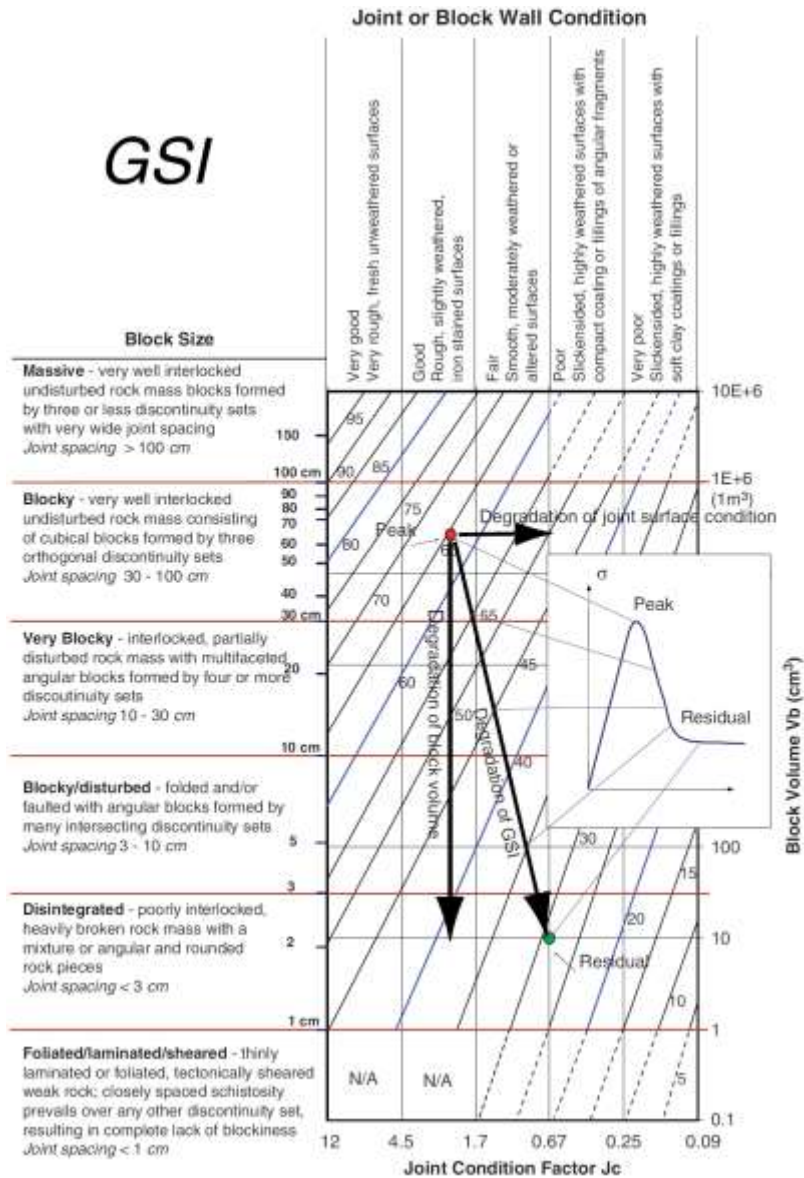


Figure 6-9 Degradation of the block volume and joint surface condition of a rock mass from peak to residual state (from Cai et alii, 2007)

Table 6.4 Shear strength parameters using Hoek-Brown criterion obtained in the literature

Reference	UCS (MPa)	GSI	GSI _r	ϕ (°)	ϕ_r (°)	c' (KPa)	c'_r (KPa)	Lithology	Purpose
Berti et al. (2017)	20	35		28-30	-	20-40	-	Arenaceous Flysch	Slope stability
Shen et al. (2012)	30	15	-	21-27	-	151-212	-	Schist	Slope stability
<i>This work</i>	12-70	25-70	13-27	24-57	18-34	17-240	14-40	Sandstone	Slope stability
Tüdeş and Ceryan (2011)	12-132	7-33	5-16	11-24	10-16	290- 3360	124-1896	Intrusive	Road cut
Wei et al. (2019)	30	5	-	24-38	-	12-41	-	Sandstone	Slope stability

The residual shear strength parameters calculated in this thesis are quite similar to those used in the works of Berti et al. (2017) and Wei et al. (2019). These authors once the friction angle and effective cohesion were determined, computed a slope stability analysis using Finite Elements Method. Ca' Mengoni landslide modelled by Berti et alii (2017) is a deep-seated landslides more than 1 km long with a main scarp of 70 meters and a sliding plane located in general 30 meters below the topographic surface. The best accuracy was obtained with a combination of $\phi = 29^\circ$ and $c' = 40$ KPa.

Even if the landslide inventory of this work consists of shallow landslides with a main scarp located always shallower than 4 meters, the shear strength parameters assigned to BMUs are reasonable and in accordance with the literature.

6.4 SHALLOW LANDSLIDES SUSCEPTIBILITY MODELLING

The aims of the susceptibility modelling were:

- To perform a physically-based regional susceptibility analysis for shallow landslide and calibrate the input parameters in order to obtain accurate results in respect to the landslide inventory
- To compare the susceptibility distribution between the physically-based and the data-driven method
- To compare the results of modelling SDL and BRL by using the Information Value
- To assess the susceptibility of involving bedrock landslides by means the physically based method

All the key objectives listed above are already discussed separately in chapter 5. Here, the discussion will mainly concern the limits and merits of the models used, evidences and questions the models have highlighted and hypothesis beyond landslides affecting the bedrock.

In respect to a data-driven approach, the complexity of physically-based models rely on parameterisation that can be a tricky task because of the uncertainty of critical parameters such as the distribution of SD depth, geotechnical and hydraulic properties. Further drawbacks of the physically based method are the degree of simplification involved and the need for large amounts of reliable input data. Nevertheless, being based on slope stability models, they follow a white-box approach where the involved physical processes are recognized and modelled (Corominas et al., 2014).

The comparison between PROBSS and Information Value (IV) has the aim to highlight the differences between two different approaches. In order to obtain satisfying results, the physically-based approach required an extensive field data acquisition task and calibration of input geotechnical parameters. Instead, a detailed landslide inventory and the spatial analysis of predisposing factors were necessary to perform data driven susceptibility analysis.

A result that the physically based model showed, was to confirm that the method here proposed, even if based on the simplified approach of both the infinite slope and the steady state hypothesis for the evaluation of pore pressure, may provide accurate results if the input parameters are obtained by integrating fieldwork observation and measurements, as well as, lab determinations. The approach here presented for the realization of the slope deposits depth map, integrating the morphometric analysis with field measurements, was found to be effective and is expected it could be in other contexts, also. The engineering geological parameterization of materials, both the slope deposits and the rock masses, provided results in line with the literature data where the strength parameters were mainly assessed from direct laboratory tests. Obviously, apart the accuracy assessment performed for the susceptibility results (chapter 5), a task for undisturbed samples collection and lab determinations of physical-mechanical

parameters would allow to test also the reliability of the input parameter ranges mainly obtained by semi-quantitative field estimations.

Using the IV model allowed to explore and analyse the role of predisposing factors for the development shallow landslides either involving the slope deposits, or also the underlying bedrock. Because the data driven models are sensitive to the input landslide dataset used to calculate the weights, it was possible to compare and combine the susceptibility maps obtained using SDL and BRL (Figure 5-16). In order to discriminate sites where SDL and BRL tend to occur, the frequency distribution of some morphometric variables and SD depth was analyzed in high susceptibility classes (Figure 6-10). From the histograms below, it is evident that there are some predisposing factors that rule the location of sliding surfaces: the slope failure with a rupture surface located below the SD/BR discontinuity (red bars) occur in steeper slopes, in thinner SD and in convex curvatures.

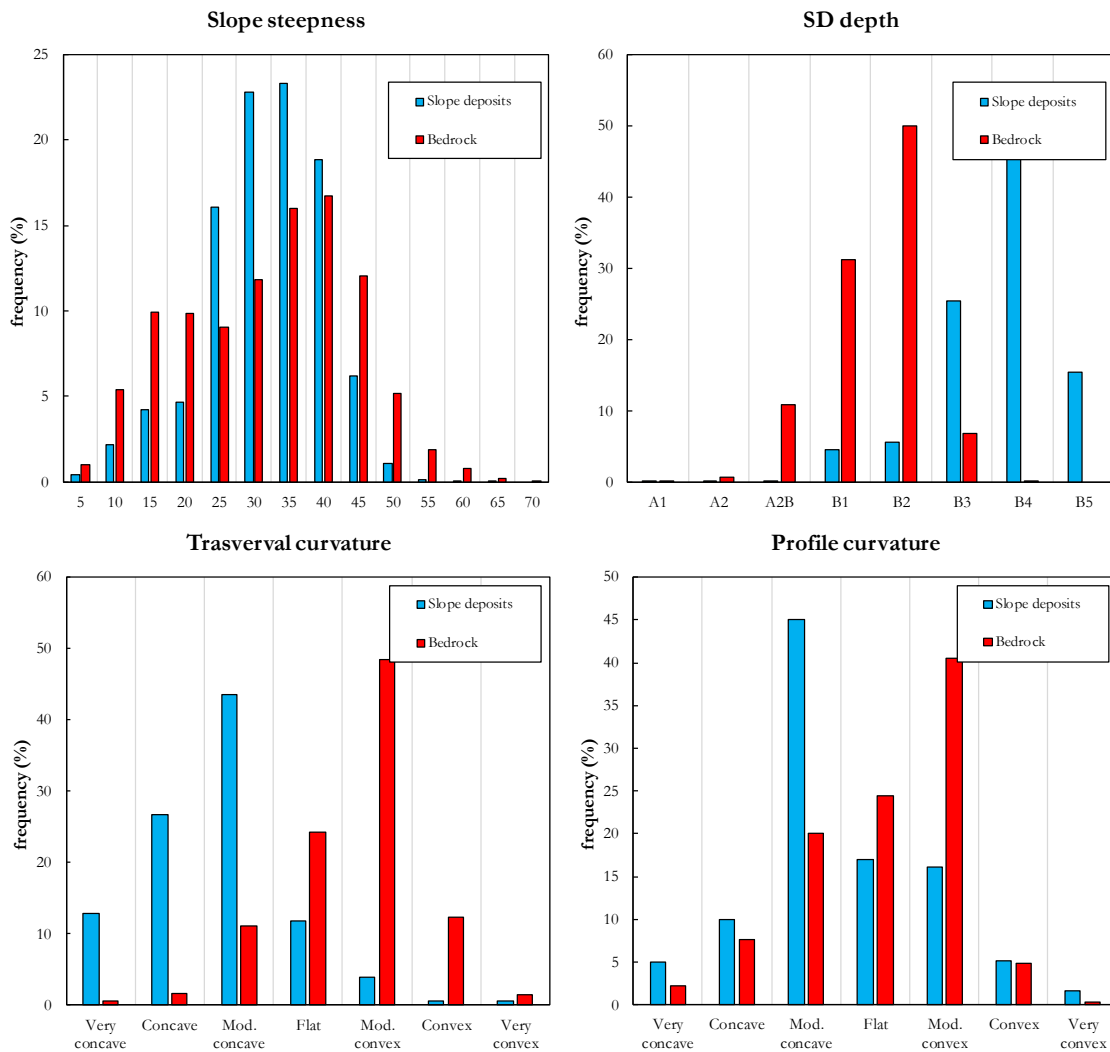


Figure 6-10 Frequency distribution of some morphometric variables and SD depth in high susceptibility classes. The red bars refer to bedrock landslides, blue bars to slope deposits landslides.

The median measured scarp height of SD visited landslides is about 1 meter and is 2 meters for BRL (Figure 4-5). The simplification of the infinite slope, where a failure surface parallel to the ground surface develops at the bedrock-slope deposits discontinuity, quite often does not agree with the field observation within the study area of this PhD thesis. In fact, the rupture surface frequently occurs within the slope deposits, at least 0.2-0.5 meters above the bedrock interface. Moreover, a large percentage (about 60%) of the visited landslides developed a sliding surface located below the discontinuity between the slope deposit and the bedrock. From the field observations (Figure 4-5), most of the BRL occurred mainly where the SD depth is below 1 meters, while the rupture surface is usually located at 2 meters depth, suggesting that the fractured and weathered bedrock layer extended in depth for more than 1-1.2 meters under the slope deposits/bedrock interface.

In his PhD thesis, Papasidero (2019) characterized the hydrological properties of the SD, focusing mainly on field determinations of hydraulic conductivity (K) and its spatialization on regional scale. To reach this objective, several (more than 700) hydraulic conductivity in situ tests (K tests) were carried out in Northern Tuscany, some of them located in the study area of this thesis.

For each borehole, different tests were performed at increasing depth, generally involving horizons 20-30 cm thick. This method allowed to investigate the variation of K with depth within the slope deposits (Figure 6-11).

A high negative correlation was observed between $\log K$ and the depth ($R - \text{Pearson} = -0.79$). Moreover, when selecting only the K tests performed downhole, that is in the deepest horizons, the decrease of $\log K$ was observed with increasing SD depth (Figure 6-12).

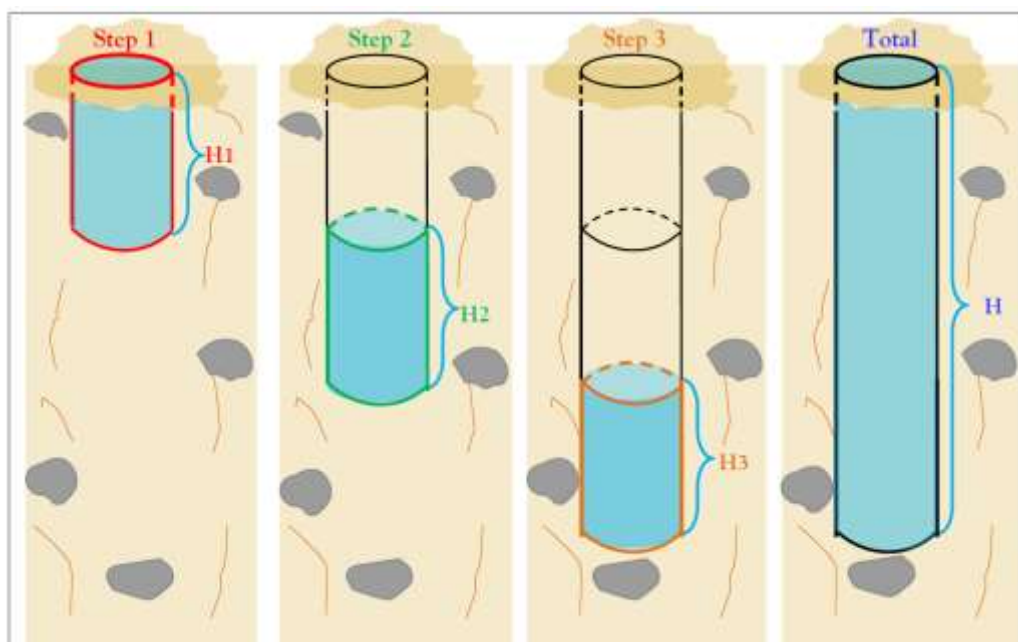


Figure 6-11 Hydraulic conductivity in situ test scheme (from Papasidero 2019)

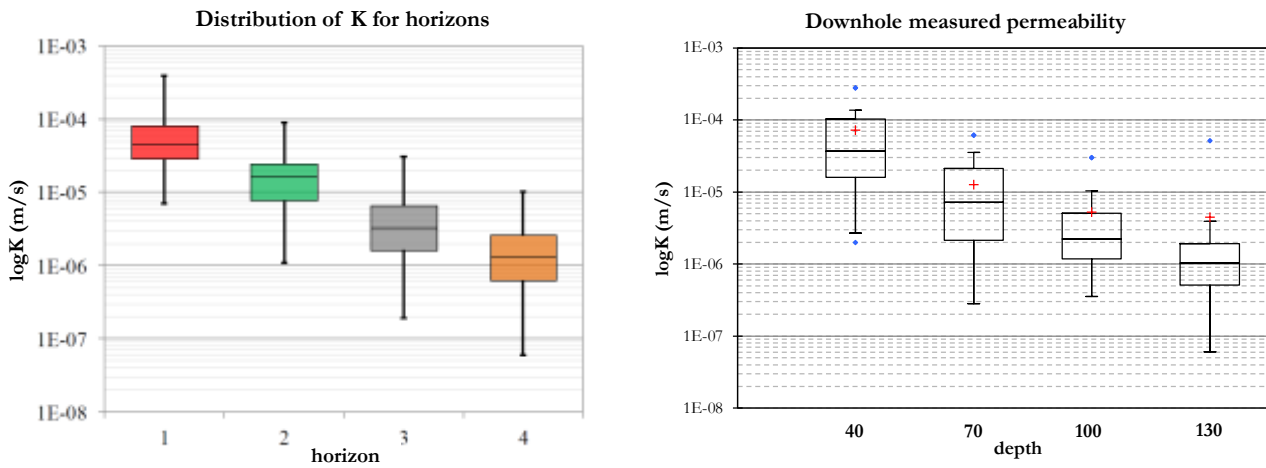


Figure 6-12 Measured K distribution for each horizon at site scale (left). Distribution of K measured at the bottom of the boreholes (right, deepest horizons)

In summary, the conclusion that can be drawn is that the deepest SD horizons has the lowest permeability, and since the depth of the deepest horizon varies with the depth of the slope deposits, it can be stated that, as a general condition, a thin SD has a bottom permeability greater than a deep SD, and the deviation of K is almost of two orders of magnitude.

According to what has been said so far, it is possible to hypothesize the scenarios that ruled the development of shallow landslides that involve the bedrock or not (Figure 6-13). Where there is a thin slope deposit, and the quality of bedrock is good, shallow landslides should develop with a rupture surface parallel to the topographic surface and coinciding with the discontinuity between slope deposits and bedrock. On the other hand, if the quality of the bedrock is low, the water infiltration proceeds vertically until a hydraulic discontinuity is found which in this case should be localized in the bedrock, between the weathered and fractured shallower portion and the underneath more intact portion. In this scenario the failure surface is localized in the low-quality bedrock. Where there are thick (> 90 cm) slope deposits, the quality of the bedrock plays a secondary role since the hydraulic discontinuity can be located in the deepest portion of the SD. In this scenario, the landslide will have a rupture surface localized above the discontinuity between slope deposits and bedrock. According to this hypothesis, the conditions that should trigger landslides involving bedrock are less frequent, however in accordance with the modalities of genesis and development of the slope deposits, where these are thicker the slope steepness may not be enough to overcome the resistant forces to trigger landsliding.

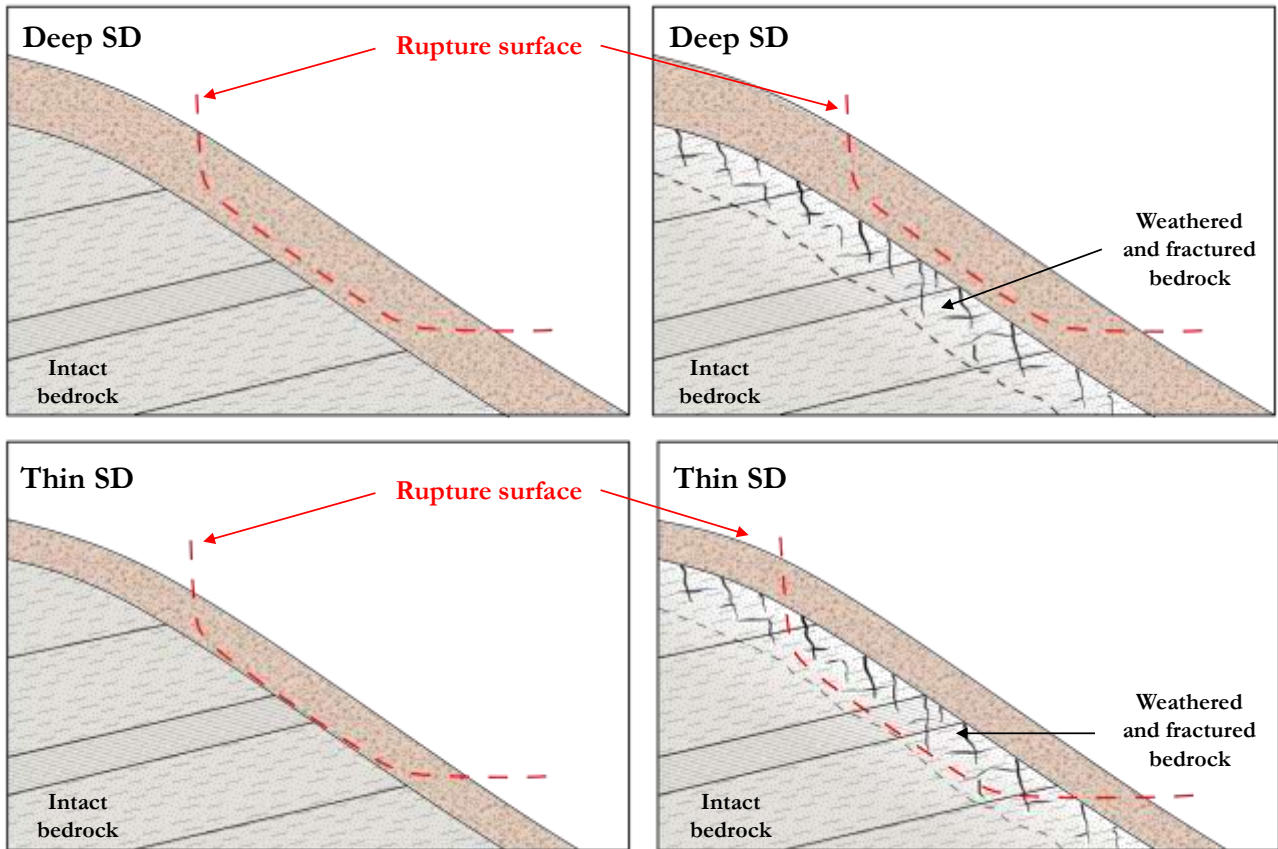


Figure 6-13 Landsliding scenarios according to SD depth and bedrock quality

7 CONCLUSIONS

In the field of landslide susceptibility assessment different modelling approaches can be implemented with different degrees of detail. Landsliding is a complex phenomenon and its modelling aimed at predicting where these phenomena are most likely to occur is a tricky issue to perform. Moreover, for both data-driven and physically-based models, paying adequate attention to the predisposing factors, triggering factors, and input parameters is no less important. For these reasons these latter tasks represent the focus of this PhD thesis which was organized in the following main topics: realization of a multitemporal shallow landslide inventory, acquisition of new field and lab data about slope deposits and sub-surface bedrock susceptible to shallow instability and regionalization of their engineering geological parameters, comparison between data-driven and physically-based methods for landslide susceptibility assessment and analysis of the role of bedrock for the development of shallow landslides.

The new multitemporal landslide inventory compiled by means of visual interpretation of orthophoto maps allowed to detect recent (2003-2016) slope failures occurred in a portion of the Garfagnana basin. The inventory represented the starting point to plan and implement a method based on integration of field survey and laboratory analyses, aimed at investigating and constraining the materials involved in landsliding from an engineering geological point of view. Field observations allowed us to highlight that shallow landsliding processes depend on the depth of the slope deposits, as well as they involve the upper portion of the underlying weathered and fractured bedrock.

For these reasons, fieldwork and laboratory analyses focused on the spatial distribution of depth of slope deposits and weathered bedrock depth, as well as the characterization of their engineering geological properties (namely, shear strength parameters and unit weight).

Shallow landslides inventory

- The overall accuracy of the multitemporal landslide inventory evaluated by means of field checks resulted to be 0.80, while the true positive rate was 0.86.
- During the fieldwork, 81/191 landslides occurring within different Bedrock Lithological Units (BLU) were visited and analyzed. The 40% of these slope failures involves the slope deposits only (SDL), while the 60% involves also the weathered and fractured upper portion of the bedrock (BRL).
- The two groups of landslides show further different characteristics: BRL are larger (median area ca. 600 m² instead of 350 m²), have a deeper scarp height (about 2 m instead of 1 m) and generally occur where slope deposits are thinner.

- Apart the above differences, all the landslides recognized can be considered as “shallow”, according to the size and the shallow rupture surface.

Slope deposits

- The results of this PhD research allowed to highlight that different bedrock lithology and morphometric conditions represent the main parameters to predict the spatial variation of both their depth and engineering geological parameters.
- For each Bedrock Lithological Unit, a multivariate analysis of derivatives of the DEM, such as slope steepness, flow accumulation, curvatures and elevation was performed in order to extract sets of 5 - 15 morphometric units, or landforms.
- Data about slope deposits were collected for a total of 413 field observation sites located inside, near and far from landslides. Field investigation often consisted in the vertical hand digging by the pickaxe, with measurement of soil depth as well as collection of data concerning layering, grain size and texture. Slope deposits samples were collected in order to conduct lab test for the estimation of unit weight and grain size distribution. When the slope deposits depth was relatively thin, quick investigation was performed by measuring the SD depth.
- The integrated analysis of field data, lab results and the morphometric units allowed us to obtain the Engineering Geological map of the Slope Deposits, where a set of parameters, such as slope deposit depth, friction angle, effective cohesion and unit weight are assigned to each Engineering Geological Slope Deposits unit.
- The hierarchical nomenclature adopted to describe the spatial distribution of slope deposits depth consists of 2 first order classes and 8 second order classes. Thin slope deposits belong to the first order group "A", while thick deposits belong to the group "B". The group “A” is made up of three second order classes where the depth ranges between 0 cm and 30 cm. The group “B” is made up of five second order classes, each one characterized by a constant depth interval of 30 cm. For each observation site the depth class was defined according to the field measurements. Then, the most frequent depth class was assigned to each morphometric unit. The accuracy of the SD depth map ranges from 0.49 to 0.68, with an expected uncertainty of ± 15 cm. With an expected uncertainty of ± 45 cm, the accuracy rises from a minimum of 0.77 to a maximum of 0.88. The accuracy and the uncertainty resulted by the method proposed in this PhD thesis are similar or better to other methods proposed in the literature.
- From lab tests of grain size distribution, plasticity and unit weight, integrated by field grain size estimations, slope deposit samples were classified following the USCS nomenclature. Then, by using literature empirical correlations integrating unit weight, relative density and USCS class, the ranges for friction angle were estimated. These results are in good agreement with those obtained

by direct shear tests reported in the literature. Instead, the effective cohesion was evaluated in back analysis by calibrating the results of physically based modelling with the landslide inventory.

Bedrock

- In order to characterize bedrock geo-mechanical properties, the same sampling strategy adopted for the slope deposits was carried during field survey, that is, bedrock information was acquired inside and near the landslides, as well as in the areas not affected by slope failures. For each one of the 105 investigation sites, ca. 400 Schmidt hammer rebound values were acquired, along with orientation and spacing of the main discontinuity sets, and the Geological Strength Index (GSI).
- The descriptive statistics of the above data highlighted that the quality of the sub-surface bedrock is different when comparing among locations inside, near and far from landslides. In addition, the uni-variate and multi-variate spatial analysis enabled to recognize that this heterogeneity defines different spatial clusters. In general terms, this is an important outcome which is useful to improve regionalized landslide assessment studies, because it shows that geo-mechanical characters spatially vary identifying different Bedrock Geo-mechanical Units correlated with geology, structural setting and the DEM.
- According to the spatial clustering of field observations, the study area was split in 4 Bedrock Geo-mechanical Units. To estimate the corresponding Mohr-Coulomb equivalent shear strength parameters, the Hoek & Brown failure criterion integrated with the GSI was used. The output parameters resulted to be in good agreement with the literature.

Shallow landslide susceptibility modelling

- Regionalized susceptibility was estimated by both data-driven and physically based methods and the results were compared.
- The results of the data-driven susceptibility analysis, described in terms of both AUROC and distribution of landslides within the susceptibility classes, showed that BRL and SDL should be investigated and analysed separately. In order to accurately distinguish between these shallow landslide types, remote sensing and morphometric analysis is generally not adequate, hence field work continues to represent a fundamental task to obtain reliable regionalized susceptibility analyses.
- Even though detailed landslide inventories are in principle not mandatory to perform regionalized susceptibility analyses by using physically based methods, these represent a fundamental tool in order to validate and critically analyse the modelling results. The first modelling tasks of this PhD were performed assuming a rupture surface located in correspondence of the slope deposits/bedrock interface, that is the typical infinite slope approach. The validation was

performed by using all the visited landslides as a test dataset, hence without discriminating between BRL and SDL. The AUROC value obtained from the physically based model compared to the data driven model would have led to the first conclusion that black box models may be preferred when applying numerical modelling at the regional scale, especially if no information of the materials involved in the slope failure were available. Instead, by separately modelling BRL and SDL, i.e. by performing numerical analyses based on either the slope deposits or the subsurface bedrock parametrization, the accuracy of the output susceptibility maps are significantly improved and result to be almost similar to those obtained by data driven methods.

- The results of this PhD thesis highlight the importance of the probabilistic approach when performing stability analysis by using physically based methods. Both the natural variability and the determination uncertainty of the input parameters, such as slope deposits depth and shear strength may be reasonably represented by this approach. Namely, having available a distribution of critical effective rainfall Q_c values, enabled us to produce different scenarios of susceptibility, e.g. different maps corresponding to different percentiles, and to infer various issues like: estimating how relevant are uncertainties for the definition of the final susceptibility classes, identifying the recurring characters of those areas where the uncertainty of the Q_c estimations are larger. In this PhD thesis, the probabilistic approach also allowed us for a smooth assessment of the potential for the occurrence of either bedrock or deposit landslides (BRL or SDL). Furthermore, as a further step, the frequency distribution of Q_c could be integrated with the rainfall intensity probability distribution at regional scale in order to obtain a landslide hazard instead of susceptibility map. In this context, also the return period of rainfall events should be taken into account, as well as the deviation between total and effective rainfall resulting from the integrated effects of evapotranspiration, runoff and ground-soil storage processes.

In conclusion, this thesis represents a contribution toward the definition of general robust criteria and methods for field data acquisition and processing, aimed at performing regional-scale susceptibility analyses for shallow landslides, where the rupture surface may be located either in correspondence of the slope deposit-bedrock discontinuity or within the weathered and fractured upper portion of underlying rock masses.

APPENDIX A

DATA:	ID FRANA:	RILEVATORE:
PRESENTE IN DB GIS <input type="checkbox"/> si <input type="checkbox"/> no	ID DS:	ID LITEC:
LOCALITA':	NUM_SEZ:	RIF_COORD:
QUOTA:	NORD:	EST:

FRANA		
Material type	Movement type (Hungri et al., 2014)	
<input type="checkbox"/> ROCK <input type="checkbox"/> SOIL / DEPOSIT / COLLUVIUM	<input type="checkbox"/> FALL <input type="checkbox"/> TOPPLE <input type="checkbox"/> SPREAD	<input type="checkbox"/> SLIDE <input type="checkbox"/> PLANAR <input type="checkbox"/> ROTATIONAL <input type="checkbox"/> FLOW <input type="checkbox"/> FLOWSLIDE <input type="checkbox"/> DEBRIS FLOW <input type="checkbox"/> EARTH FLOW <input type="checkbox"/> AVALANCHE
Substrato	Coinvolgimento <input type="checkbox"/> SI <input type="checkbox"/> NO	<small>(Compilare se non eseguibile OSSUTEK)</small>
Bedding:	Descrizione:	
Joints:	_____	
GSI:	_____	
morfometria scar.	morfologia scarp.	Morfometria
altezza (m) _____ larghezza (m) _____	<input type="checkbox"/> rettilinea <input type="checkbox"/> curva <input type="checkbox"/> multipla <input type="checkbox"/> irregolare	Disliv corona-piede (m): _____ Lunghezza corona-piede (m): _____ Larghezza (m): _____ Angolo sup. scivolamento (°): _____
EROSIONE IN ATTO	CAUSE	
	predisponenti	scatenanti
<input type="checkbox"/> ruscellam. diffuso <input type="checkbox"/> fosso di erosione concentrata <input type="checkbox"/> calanchi <input type="checkbox"/> erosione di sponda <input type="checkbox"/> approfondimento in alveo <input type="checkbox"/> soliflusso <input type="checkbox"/> reptazione	<input type="checkbox"/> litologia <input type="checkbox"/> morfologia <input type="checkbox"/> assetto strutturale <input type="checkbox"/> faglie e fratturazione <input type="checkbox"/> alterazione <input type="checkbox"/> uso del suolo	<input type="checkbox"/> eventi sismici <input type="checkbox"/> erosione al piede <input type="checkbox"/> eventi meteorici <input type="checkbox"/> estremi <input type="checkbox"/> stagionali <input type="checkbox"/> antropiche <input type="checkbox"/> carico a monte <input type="checkbox"/> drenaggio impedito <input type="checkbox"/> disboscamento <input type="checkbox"/> sbancamento <input type="checkbox"/>

zone limitrofe alla frana			
<input type="checkbox"/> seminato <input type="checkbox"/> frumento <input type="checkbox"/> foraggio <input type="checkbox"/> altro <input type="checkbox"/> frutteto <input type="checkbox"/> bosco	<input type="checkbox"/> pascolo <input type="checkbox"/> vigna <input type="checkbox"/> arbustivo <input type="checkbox"/> aree incolte <input type="checkbox"/> urbanizzato	tipologia bosco: <input type="checkbox"/> faggio <input type="checkbox"/> cerro / quercia <input type="checkbox"/> castagni <input type="checkbox"/> acacia / <input type="checkbox"/> conifere <input type="checkbox"/> misto _____	stato vegetativo: <input type="checkbox"/> naturale <input type="checkbox"/> antropico diametro fusto (cm): distanza media tra fusti (m):
area in frana	NOTE		
Grado rivegetazione: <input type="checkbox"/> totalmente riveg. <input type="checkbox"/> abbastanza riveg. <input type="checkbox"/> parzialm. riveg. <input type="checkbox"/> assente	Tipologia rivegetazione: <input type="checkbox"/> erbacea <input type="checkbox"/> arbustiva <input type="checkbox"/> arborea diametro fusto (cm): _____		

APPENDIX B

Slope deposits grain size field estimation

ID Site	ID sample	Formation	BLU	Gravel	Sand	Fine	USCS (simplified)
D41006	D41006GA	MAC	11	25	51	24	S
D41010	D41010GA	MAC	11	25	50	25	S
E41003	E41003GA	MAC	11	25	34	41	S
E41009	E41009GA	MAC	11	25	51	24	S
E41015	E41015GA	MAC	11	30	32	38	S
E41019	E41019GA	MAC	11	40	19	41	G
E41023	E41023GA	MAC	11	30	34	36	S
E41024	E41024GA	MAC	11	45	38	17	G
E41026	E41026GA	MAC	11	15	55	30	S
E41033	E41033GA	MAC	11	25	52	23	S
E41052	E41052GA	MAC	11	35	43	22	S
E41086	E41086GA	MAC	11	40	40	20	S
E41087	E41087GA	MAC	11	50	34	16	G
E41089	E41089GA	MAC	11	35	17	48	G
E41091	E41091GA	MAC	11	45	25	30	G
E41092	E41092GA	MAC	11	20	32	48	S
E41097	E41097GA	MAC	11	40	16	44	G
E41106	E41106GA	MAC	11	20	26	54	F
E41111	E41111GA	MAC	11	15	37	48	S
E41124	E41124GA	MAC	11	40	42	18	S
E41127	E41127GA	MAC	11	40	42	18	S
E41145	E41145GA	MAC	11	15	39	46	S
E41159	E41159GA	MAC	11	20	42	38	S
E41169	E41169GA	MAC	11	20	27	53	F
E41174	E41174GA	MAC	11	25	32	43	S
E41190	E41190GA	MAC	11	35	30	35	G
E41195	E41195GA	MAC	11	40	27	33	G
E41210	E41210GA	MAC	11	20	52	28	S
P41005	P41005GA	MAC	11	25	34	41	S
P41005	P41005GB	MAC	11	30	34	36	S
P41015	P41015GA	MAC	11	5	30	65	F
P41018	P41018GA	MAC	11	15	35	50	S
P41018	P41018GB	MAC	11	40	26	34	G
P41023	P41023GA	MAC	11	20	36	44	S
P41023	P41023GB	MAC	11	20	35	45	S
P41025	P41025GA	MAC	11	20	28	52	F
P41036	P41036GA	MAC	11	35	30	35	G
P41040	P41040GA	MAC	11	10	38	52	F

P41040	P41040GB	MAC	11	25	33	42	S
P41061	P41061GA	MAC	11	10	55	35	S
P41062	P41062GA	MAC	11	5	44	51	F
P41062	P41062GB	MAC	11	5	44	51	F
P41069	P41069GA	MAC	11	45	40	15	G
P41088	P41088GA	MAC	11	40	26	34	G
P41098	P41098GA	MAC	11	30	48	22	S
P41098	P41098GB	MAC	11	30	47	23	S
P41101	P41101GA	MAC	11	20	30	50	S
P41101	P41101GB	MAC	11	25	28	47	S
P41106	P41106GA	MAC	11	20	35	45	S
P41106	P41106GB	MAC	11	20	36	44	S
P41107	P41107GA	MAC	11	40	31	29	G
P41126	P41126GA	MAC	11	25	24	51	F
P41127	P41127GA	MAC	11	25	39	36	S
P41127	P41127GB	MAC	11	25	37	38	S
P41129	P41129GA	MAC	11	25	60	15	S
V41011	V41011GA	MAC	11	20	23	57	F
V41016	V41016GA	MAC	11	20	10	70	F
V41018	V41018GA	MAC	11	40	28	32	G
V41028	V41028GA	MAC	11	30	35	35	S
E41185	E41185GA	SSR	22	20	33	47	S
I41045	I41045GA	MCP	22	40	8	52	F
E41044	E41044GA	STO3	23	25	35	40	S
E41069	E41069GA	MAI	23	30	47	23	S
E41070	E41070GA	MAI	23	45	38	17	G
E41072	E41072GA	LIM	23	40	31	29	G
E41083	E41083GA	LIM	23	30	33	37	S
E41084	E41084GA	LIM	23	25	37	38	S
E41108	E41108GA	STO3	23	30	10	60	F
E41113	E41113GA	STO3	23	40	28	32	G
E41139	E41139GA	MAI	23	20	36	44	S
I41006	I41006GA	MAI	23	10	23	67	F
I41008	I41008GA	LIM	23	15	20	65	F
I41014	I41014GA	MAI	23	40	31	29	G
I41057	I41057GA	LIM	23	20	22	58	F
I41061	I41061GA	CCA	23	50	13	37	G
I41061	I41061GB	CCA	23	50	21	29	G
P41011	P41011GA	MAI	23	10	42	48	S
P41011	P41011GB	MAI	23	10	42	48	S

P41124	P41124GA	CCA	23	45	7	48	G
P41124	P41124GB	CCA	23	15	23	62	F
V41006	V41006GA	STO3	23	30	35	35	S
V41007	V41007GA	STO3	23	30	38	32	S
E41078	E41078GA	bnb	31	60	27	13	G
E41162	E41162GA	VILc	31	20	53	27	S
E41163	E41163GA	VILc	31	20	53	27	S
P41038	P41038GA	VILa	31	15	27	58	F
P41066	P41066GA	bna	31	25	61	14	S
E41042	E41042GA	STO	51	30	25	45	G
E41046	E41046GA	STO	51	10	22	68	F
E41071	E41071GA	POD	51	25	38	37	S
E41077	E41077GA	pv	51	40	44	16	S
E41098	E41098GA	POD	51	20	25	55	F
E41099	E41099GA	POD	51	30	19	51	F
E41100	E41100GA	POD	51	20	21	59	F
E41101	E41101GA	POD	51	10	25	65	F
E41102	E41102GA	POD	51	20	20	60	F
E41103	E41103GA	POD	51	20	24	56	F
E41105	E41105GA	OMT	51	30	24	46	G
E41109	E41109GA	STO	51	25	16	59	F
E41114	E41114GA	STO	51	40	13	47	G
E41129	E41129GA	POD	51	30	22	48	G
E41130	E41130GA	POD	51	35	20	45	G
E41137	E41137GA	POD	51	10	19	71	F
E41138	E41138GA	POD	51	20	12	68	F
E41155	E41155GA	MMA	51	40	27	33	G
E41156	E41156GA	MMA	51	30	35	35	S
E41164	E41164GA	bv	51	40	28	32	G
E41168	E41168GA	bv	51	30	35	35	S
I41004	I41004GA	POD	51	25	34	41	S
I41025	I41025GA	POD	51	5	3	92	F
P41039	P41039GA	STO	51	40	21	39	G
P41043	P41043GA	POD	51	20	31	49	S
P41046	P41046GA	POD	51	10	26	64	F
P41072	P41072GA	STO	51	10	50	40	S
P41082	P41082GA	STO	51	35	29	36	G
P41112	P41112GA	POD	51	30	34	36	S
P41112	P41112GB	POD	51	30	35	35	S
P41122	P41122GA	POD	51	10	25	65	F

P41123	P41123GA	POD	51	30	18	52	F
V41001	V41001GA	STO	51	25	25	50	F
E41136	E41136GA	PSM	62	40	32	28	G
I41030	I41030GA	PSM	62	20	23	57	F
I41036	I41036GA	PSM	62	40	13	47	G
I41036	I41036GB	PSM	62	40	13	47	G
I41038	I41038GA	PSM	62	15	9	76	F

Slope deposits grain size laboratory analysis

ID Site	ID sample	Formation	BLU	Gravel	Sand	Fine	Silt (0,074 - 0,002 mm)	Clay (<0,002 mm)	USCS simplified	USCS
D41006	D41006GA	MAC	11	22	51	26	22	5	S	SC-SM
D41010	D41010GA	MAC	11	19	60	20	17	4	S	SM
E41003	E41003GA	MAC	11	27	37	36	30	6	S	SM
E41009	E41009GA	MAC	11	23	36	41	33	8	S	SC
E41015	E41015GA	MAC	11	29	43	28	24	4	S	SC-SM
E41019	E41019GA	MAC	11	29	39	31	24	8	S	SC-SM
E41023	E41023GA	MAC	11	31	42	27	21	6	S	SM
E41024	E41024GA	MAC	11	49	37	14	11	3	G	GM
E41026	E41026GA	MAC	11	19	36	45	36	9	S	SC
E41033	E41033GA	MAC	11	32	47	20	17	3	S	SM
E41052	E41052GA	MAC	11	28	36	36	28	8	S	SM
E41086	E41086GA	MAC	11	36	43	21	18	2	S	SM
E41087	E41087GA	MAC	11	42	38	20	17	3	G	GC-GM
E41089	E41089GA	MAC	11	36	39	25	21	4	S	SM
E41091	E41091GA	MAC	11	44	36	20	17	3	G	GM
E41092	E41092GA	MAC	11	16	58	26	22	3	S	SM
E41097	E41097GA	MAC	11	47	36	17	14	3	G	GM
E41106	E41106GA	MAC	11	21	27	52	39	13	F	ML
E41111	E41111GA	MAC	11	16	44	40	33	6	S	SM
E41124	E41124GA	MAC	11	40	38	22	19	3	G	GM
E41127	E41127GA	MAC	11	46	43	11	10	1	G	GP-GM
E41145	E41145GA	MAC	11	16	41	44	37	7	S	SM
E41159	E41159GA	MAC	11	41	35	23	18	5	G	GM
E41169	E41169GA	MAC	11	26	38	35	29	6	S	SM
E41174	E41174GA	MAC	11	30	47	23	21	2	S	SM
E41190	E41190GA	MAC	11	32	47	21	18	3	S	SM
E41195	E41195GA	MAC	11	37	43	20	17	3	S	SM
E41210	E41210GA	MAC	11	13	51	37	31	6	S	SM
P41005	P41005GA	MAC	11	33	34	33	24	9	S	SC
P41005	P41005GB	MAC	11	27	51	22	17	5	S	SM
P41015	P41015GA	MAC	11	4	32	63	50	14	F	ML
P41018	P41018GA	MAC	11	11	50	39	32	7	S	SM
P41018	P41018GB	MAC	11	38	38	24	20	4	G	GC
P41023	P41023GA	MAC	11	17	38	44	33	11	S	SM
P41023	P41023GB	MAC	11	29	34	37	26	11	S	SM
P41025	P41025GA	MAC	11	26	23	51	33	18	F	CL

P41036	P41036GA	MAC	11	30	47	23	20	3	S	SM
P41040	P41040GA	MAC	11	8	43	49	43	7	S	SM
P41040	P41040GB	MAC	11	27	30	43	37	6	S	SM
P41061	P41061GA	MAC	11	13	45	42	33	9	S	SM
P41062	P41062GA	MAC	11	6	63	31	27	3	S	SM
P41062	P41062GB	MAC	11	5	58	37	30	8	S	SM
P41069	P41069GA	MAC	11	43	31	26	22	4	G	GM
P41088	P41088GA	MAC	11	35	32	34	27	6	G	GM
P41098	P41098GA	MAC	11	41	39	20	19	2	G	GM
P41098	P41098GB	MAC	11	38	43	18	17	2	S	SM
P41101	P41101GA	MAC	11	27	41	32	27	5	S	SM
P41101	P41101GB	MAC	11	25	44	31	26	5	S	SM
P41106	P41106GA	MAC	11	21	35	44	35	9	S	SM
P41106	P41106GB	MAC	11	27	34	40	32	7	S	SM
P41107	P41107GA	MAC	11	48	34	19	16	3	G	GC
P41126	P41126GA	MAC	11	38	34	28	19	8	G	GC
P41127	P41127GA	MAC	11	21	53	26	20	6	S	SC-SM
P41127	P41127GB	MAC	11	22	44	34	28	6	S	SC-SM
P41129	P41129GA	MAC	11	20	57	23	18	5	S	SM
V41011	V41011GA	MAC	11	24	43	33	25	8	S	SM
V41016	V41016GA	MAC	11	14	47	39	31	8	S	SM
V41018	V41018GA	MAC	11	32	44	24	21	3	S	SM
V41028	V41028GA	MAC	11	38	34	28	22	6	G	GC-GM
E41185	E41185GA	SSR	22	24	41	35	30	5	S	SM
I41045	I41045GA	MCP	22	42	19	39	34	5	G	GC-GM
E41044	E41044GA	STO3	23	23	42	35	24	11	S	SC
E41069	E41069GA	MAI	23	21	31	48	33	15	S	SC
E41070	E41070GA	MAI	23	37	30	34	22	11	G	GC
E41072	E41072GA	LIM	23	36	35	29	19	9	G	GM
E41083	E41083GA	LIM	23	27	35	37	26	11	S	SM
E41084	E41084GA	LIM	23	24	27	49	36	14	S	SM
E41108	E41108GA	STO3	23	24	30	46	25	21	S	SM
E41113	E41113GA	STO3	23	42	28	30	21	8	G	GC
E41139	E41139GA	MAI	23	18	47	35	32	3	S	SM
I41006	I41006GA	MAI	23	6	24	70	57	13	F	ML
I41008	I41008GA	LIM	23	16	20	64	51	12	F	ML
I41014	I41014GA	MAI	23	33	35	32	24	8	S	SC
I41057	I41057GA	LIM	23	22	27	50	43	7	F	ML
I41061	I41061GA	CCA	23	64	20	17	14	3	G	GM
I41061	I41061GB	CCA	23	55	32	13	12	2	G	GM

P41011	P41011GA	MAI	23	16	39	45	33	13	S	SC
P41011	P41011GB	MAI	23	14	35	51	37	14	F	CL
P41124	P41124GA	CCA	23	37	30	34	27	7	G	GM
P41124	P41124GB	CCA	23	12	28	60	42	18	F	CL-ML
V41006	V41006GA	STO3	23	28	37	35	26	9	S	SM
V41007	V41007GA	STO3	23	37	40	22	15	7	S	SM
E41078	E41078GA	bnb	31	45	18	37	28	9	G	GC
E41162	E41162GA	VILc	31	18	40	42	36	6	S	SM
E41163	E41163GA	VILc	31	22	47	31	27	4	S	SM
P41038	P41038GA	VILa	31	16	33	50	42	8	F	ML
P41066	P41066GA	bna	31	23	66	11	9	2	S	SP-SM
E41042	E41042GA	STO	51	26	35	39	23	16	S	SC
E41046	E41046GA	STO	51	10	43	47	33	14	S	SC
E41071	E41071GA	POD	51	21	37	42	27	15	S	SC
E41077	E41077GA	pv	51	43	41	15	11	4	G	GC
E41098	E41098GA	POD	51	17	34	48	36	12	S	SM
E41099	E41099GA	POD	51	29	15	56	41	15	F	ML
E41100	E41100GA	POD	51	12	21	68	41	27	F	ML
E41101	E41101GA	POD	51	17	19	64	42	22	F	ML
E41102	E41102GA	POD	51	15	21	64	44	19	F	ML
E41103	E41103GA	POD	51	22	25	53	35	18	F	ML
E41105	E41105GA	OMT	51	28	21	51	37	14	F	ML
E41109	E41109GA	STO	51	22	37	41	24	17	S	SM
E41114	E41114GA	STO	51	36	37	27	21	6	S	SM
E41129	E41129GA	POD	51	33	32	35	27	7	G	GC
E41130	E41130GA	POD	51	33	26	41	32	9	G	GM
E41137	E41137GA	POD	51	10	28	62	46	15	F	ML
E41138	E41138GA	POD	51	19	16	65	48	17	F	ML
E41155	E41155GA	MMA	51	38	40	22	14	8	S	SC
E41156	E41156GA	MMA	51	37	41	22	18	4	S	SM
E41164	E41164GA	bv	51	47	36	17	13	3	G	GM
E41168	E41168GA	bv	51	33	41	26	21	6	S	SM
I41004	I41004GA	POD	51	13	48	39	32	7	S	SC
I41025	I41025GA	POD	51	3	16	81	58	23	F	ML
P41039	P41039GA	STO	51	35	35	30	22	9	S	SC
P41043	P41043GA	POD	51	31	25	44	31	13	G	GC
P41046	P41046GA	POD	51	10	30	60	44	16	F	ML
P41072	P41072GA	STO	51	21	66	13	11	2	S	SM
P41082	P41082GA	STO	51	34	40	26	22	4	S	SM
P41112	P41112GA	POD	51	35	35	30	23	7	S	SM

P41112	P41112GB	POD	51	35	31	34	24	10	G	GC
P41122	P41122GA	POD	51	16	37	48	33	15	S	SM
P41123	P41123GA	POD	51	25	37	37	28	9	S	SC
V41001	V41001GA	STO	51	20	48	32	18	14	S	SM
E41136	E41136GA	PSM	62	41	40	18	16	2	G	GM
I41030	I41030GA	PSM	62	29	39	32	23	8	S	SM
I41036	I41036GA	PSM	62	39	26	36	26	10	G	GC
I41036	I41036GB	PSM	62	36	26	37	25	12	G	GC
I41038	I41038GA	PSM	62	20	32	48	36	12	S	SM

ID Site	ID sample	Formation	BLU	Laboratory analysis							
				D10	D17	D20	D30	D50	D60	Cu*	Cc**
D41006	D41006GA	MAC	11	0.009	0.026	0.032	0.092	0.248	0.511	57	1.835
D41010	D41010GA	MAC	11	0.009	0.038	0.071	0.141	0.295	0.402	42	5.246
E41003	E41003GA	MAC	11	0.005	0.022	0.021	0.040	0.201	0.628	124	0.498
E41009	E41009GA	MAC	11	0.003	0.007	0.009	0.025	0.102	0.220	81	1.017
E41015	E41015GA	MAC	11	0.010	0.025	0.032	0.083	0.324	1.294	133	0.543
E41019	E41019GA	MAC	11	0.005	0.020	0.025	0.061	0.305	1.663	314	0.419
E41023	E41023GA	MAC	11	0.006	0.022	0.032	0.092	0.740	2.521	404	0.539
E41024	E41024GA	MAC	11	0.027	0.096	0.136	0.307	3.744	12.179	448	0.284
E41026	E41026GA	MAC	11	0.002	0.007	0.012	0.026	0.097	0.197	82	1.470
E41033	E41033GA	MAC	11	0.021	0.046	0.074	0.192	0.716	2.177	102	0.792
E41052	E41052GA	MAC	11	0.003	0.009	0.015	0.028	0.195	0.407	121	0.588
E41086	E41086GA	MAC	11	0.020	0.054	0.069	0.172	1.368	3.679	182	0.399
E41087	E41087GA	MAC	11	0.022	0.048	0.074	0.194	1.608	5.727	260	0.297
E41089	E41089GA	MAC	11	0.009	0.024	0.040	0.127	0.794	3.089	348	0.585
E41091	E41091GA	MAC	11	0.021	0.049	0.076	0.187	1.878	7.560	360	0.221
E41092	E41092GA	MAC	11	0.012	0.037	0.059	0.095	0.243	0.382	33	2.032
E41097	E41097GA	MAC	11	0.021	0.078	0.103	0.232	2.959	12.845	600	0.196
E41106	E41106GA	MAC	11	0.001	0.004	0.005	0.016	0.061	0.140	120	1.510
E41111	E41111GA	MAC	11	0.004	0.014	0.023	0.033	0.147	0.243	67	1.251
E41124	E41124GA	MAC	11	0.022	0.035	0.057	0.172	1.794	4.700	217	0.290
E41127	E41127GA	MAC	11	0.057	0.123	0.157	0.298	2.684	9.258	161	0.167
E41145	E41145GA	MAC	11	0.003	0.008	0.009	0.021	0.112	0.237	69	0.564
E41159	E41159GA	MAC	11	0.007	0.024	0.040	0.340	3.061	5.100	764	3.387
E41169	E41169GA	MAC	11	0.005	0.013	0.024	0.049	0.214	0.472	103	1.098
E41174	E41174GA	MAC	11	0.023	0.034	0.059	0.127	0.417	1.098	48	0.637
E41190	E41190GA	MAC	11	0.022	0.040	0.069	0.133	0.401	1.687	77	0.479
E41195	E41195GA	MAC	11	0.016	0.046	0.072	0.168	0.718	3.139	191	0.548
E41210	E41210GA	MAC	11	0.005	0.018	0.023	0.037	0.134	0.185	38	1.497
P41005	P41005GA	MAC	11	0.003	0.009	0.020	0.047	0.465	1.799	521	0.351
P41005	P41005GB	MAC	11	0.017	0.035	0.058	0.147	0.567	1.407	84	0.918
P41015	P41015GA	MAC	11	0.001	0.004	0.005	0.009	0.028	0.057	57	1.337
P41018	P41018GA	MAC	11	0.005	0.018	0.023	0.037	0.131	0.227	43	1.158
P41018	P41018GB	MAC	11	0.011	0.026	0.040	0.128	0.647	3.184	289	0.467
P41023	P41023GA	MAC	11	0.001	0.008	0.010	0.025	0.096	0.231	172	2.062
P41023	P41023GB	MAC	11	0.001	0.008	0.010	0.032	0.236	0.402	301	1.945
P41025	P41025GA	MAC	11	0.001	0.001	0.004	0.010	0.065	0.260	260	0.355
P41036	P41036GA	MAC	11	0.010	0.031	0.047	0.132	0.378	0.784	78	2.223
P41040	P41040GA	MAC	11	0.004	0.009	0.010	0.027	0.078	0.170	40	1.030

P41040	P41040GB	MAC	11	0.004	0.008	0.012	0.028	0.210	0.795	177	0.212
P41061	P41061GA	MAC	11	0.003	0.007	0.009	0.027	0.122	0.283	92	0.848
P41062	P41062GA	MAC	11	0.022	0.028	0.032	0.072	0.176	0.269	12	0.877
P41062	P41062GB	MAC	11	0.004	0.009	0.014	0.025	0.137	0.228	62	0.754
P41069	P41069GA	MAC	11	0.007	0.025	0.024	0.117	2.692	7.050	946	0.259
P41088	P41088GA	MAC	11	0.005	0.024	0.022	0.050	0.291	1.756	352	0.286
P41098	P41098GA	MAC	11	0.025	0.049	0.073	0.213	1.684	5.099	204	0.356
P41098	P41098GB	MAC	11	0.027	0.067	0.087	0.220	1.590	4.171	155	0.432
P41101	P41101GA	MAC	11	0.008	0.020	0.023	0.057	0.350	1.078	129	0.359
P41101	P41101GB	MAC	11	0.006	0.019	0.022	0.063	0.340	0.848	147	0.803
P41106	P41106GA	MAC	11	0.003	0.007	0.012	0.028	0.141	0.379	143	0.753
P41106	P41106GB	MAC	11	0.004	0.009	0.019	0.031	0.243	0.850	190	0.253
P41107	P41107GA	MAC	11	0.021	0.059	0.087	0.319	4.181	7.063	343	0.701
P41126	P41126GA	MAC	11	0.003	0.011	0.025	0.113	1.557	4.212	1404	1.007
P41127	P41127GA	MAC	11	0.006	0.024	0.029	0.097	0.329	0.707	124	2.312
P41127	P41127GB	MAC	11	0.006	0.023	0.021	0.054	0.222	0.481	81	1.033
P41129	P41129GA	MAC	11	0.007	0.022	0.038	0.123	0.365	0.796	109	2.590
V41011	V41011GA	MAC	11	0.003	0.008	0.011	0.042	0.249	0.755	226	0.697
V41016	V41016GA	MAC	11	0.003	0.008	0.010	0.023	0.146	0.229	80	0.818
V41018	V41018GA	MAC	11	0.021	0.048	0.063	0.116	0.436	1.494	72	0.436
V41028	V41028GA	MAC	11	0.005	0.024	0.026	0.088	0.592	3.338	668	0.460
E41185	E41185GA	SSR	22	0.005	0.008	0.011	0.037	0.653	1.674	314	0.155
I41045	I41045GA	MCP	22	0.008	0.022	0.021	0.031	1.219	6.042	723	0.019
E41044	E41044GA	STO3	23	0.002	0.006	0.008	0.043	0.318	0.923	517	1.145
E41069	E41069GA	MAI	23	0.001	0.003	0.005	0.012	0.100	0.462	462	0.306
E41070	E41070GA	MAI	23	0.002	0.007	0.008	0.038	1.114	3.487	2238	0.263
E41072	E41072GA	LIM	23	0.003	0.010	0.023	0.101	1.570	3.740	1391	1.009
E41083	E41083GA	LIM	23	0.002	0.006	0.008	0.021	0.224	0.573	324	0.421
E41084	E41084GA	LIM	23	0.001	0.003	0.006	0.009	0.087	0.664	497	0.100
E41108	E41108GA	STO3	23	0.001	0.001	0.002	0.006	0.218	0.789	789	0.039
E41113	E41113GA	STO3	23	0.004	0.009	0.025	0.079	1.660	6.642	1878	0.265
E41139	E41139GA	MAI	23	0.010	0.020	0.023	0.041	0.332	0.728	76	0.238
I41006	I41006GA	MAI	23	0.001	0.003	0.004	0.008	0.021	0.028	25	2.291
I41008	I41008GA	LIM	23	0.002	0.004	0.005	0.010	0.022	0.035	23	2.057
I41014	I41014GA	MAI	23	0.004	0.008	0.013	0.054	1.259	3.001	722	0.235
I41057	I41057GA	LIM	23	0.004	0.009	0.014	0.020	0.072	0.538	143	0.200
I41061	I41061GA	CCA	23	0.025	0.084	0.198	0.791	9.358	14.149	571	1.783
I41061	I41061GB	CCA	23	0.030	0.213	0.394	1.780	6.341	9.400	318	11.400
P41011	P41011GA	MAI	23	0.001	0.004	0.006	0.022	0.120	0.315	284	1.397
P41011	P41011GB	MAI	23	0.001	0.004	0.005	0.011	0.061	0.229	229	0.542

P41124	P41124GA	CCA	23	0.005	0.009	0.013	0.033	0.782	3.354	704	0.070
P41124	P41124GB	CCA	23	0.001	0.002	0.003	0.008	0.021	0.077	77	0.837
V41006	V41006GA	STO3	23	0.003	0.007	0.008	0.039	0.211	0.458	136	0.971
V41007	V41007GA	STO3	23	0.006	0.025	0.037	0.156	0.830	3.616	612	1.144
E41078	E41078GA	bnb	31	0.003	0.009	0.014	0.036	2.387	27.143	9077	0.016
E41162	E41162GA	VILc	31	0.005	0.012	0.023	0.028	0.102	0.177	36	0.919
E41163	E41163GA	VILc	31	0.009	0.023	0.027	0.070	0.192	0.318	34	1.660
P41038	P41038GA	VILa	31	0.003	0.006	0.008	0.020	0.072	0.183	53	0.659
P41066	P41066GA	bna	31	0.038	0.167	0.224	0.427	0.882	1.423	37	3.327
E41042	E41042GA	STO	51	0.001	0.003	0.004	0.011	0.326	0.785	785	0.168
E41046	E41046GA	STO	51	0.001	0.004	0.006	0.025	0.096	0.227	199	2.396
E41071	E41071GA	POD	51	0.001	0.003	0.005	0.022	0.356	1.020	1020	0.470
E41077	E41077GA	pv	51	0.026	0.107	0.187	0.618	3.276	6.446	252	2.310
E41098	E41098GA	POD	51	0.002	0.004	0.005	0.008	0.120	0.631	407	0.060
E41099	E41099GA	POD	51	0.001	0.002	0.003	0.006	0.020	0.418	418	0.096
E41100	E41100GA	POD	51	0.001	0.001	0.001	0.003	0.010	0.022	22	0.473
E41101	E41101GA	POD	51	0.001	0.002	0.002	0.005	0.015	0.046	46	0.495
E41102	E41102GA	POD	51	0.001	0.002	0.002	0.006	0.023	0.051	51	0.623
E41103	E41103GA	POD	51	0.001	0.002	0.003	0.007	0.030	0.556	556	0.090
E41105	E41105GA	OMT	51	0.001	0.004	0.005	0.009	0.072	0.227	189	0.309
E41109	E41109GA	STO	51	0.001	0.002	0.003	0.008	0.530	1.330	1330	0.054
E41114	E41114GA	STO	51	0.005	0.011	0.025	0.119	1.174	3.297	716	0.940
E41129	E41129GA	POD	51	0.003	0.006	0.008	0.032	1.110	2.662	823	0.117
E41130	E41130GA	POD	51	0.003	0.005	0.007	0.022	0.619	2.327	847	0.077
E41137	E41137GA	POD	51	0.001	0.002	0.003	0.006	0.021	0.055	55	0.760
E41138	E41138GA	POD	51	0.001	0.002	0.003	0.006	0.019	0.026	26	1.230
E41155	E41155GA	MMA	51	0.005	0.024	0.037	0.246	1.793	4.161	764	2.664
E41156	E41156GA	MMA	51	0.006	0.026	0.048	0.229	1.729	3.951	625	2.092
E41164	E41164GA	bv	51	0.018	0.076	0.143	0.610	4.051	7.580	429	2.776
E41168	E41168GA	bv	51	0.006	0.024	0.026	0.144	1.280	2.836	508	1.319
I41004	I41004GA	POD	51	0.003	0.008	0.010	0.027	0.144	0.305	105	0.821
I41025	I41025GA	POD	51	0.001	0.001	0.002	0.004	0.010	0.024	24	0.651
P41039	P41039GA	STO	51	0.003	0.014	0.020	0.073	0.502	1.991	667	0.892
P41043	P41043GA	POD	51	0.001	0.004	0.006	0.021	0.222	1.278	1061	0.299
P41046	P41046GA	POD	51	0.001	0.002	0.004	0.008	0.026	0.073	73	0.806
P41072	P41072GA	STO	51	0.032	0.159	0.225	0.510	1.507	2.177	68	3.727
P41082	P41082GA	STO	51	0.010	0.025	0.034	0.103	0.431	1.623	167	0.674
P41112	P41112GA	POD	51	0.006	0.022	0.020	0.074	1.429	3.337	603	0.300
P41112	P41112GB	POD	51	0.002	0.009	0.021	0.047	1.477	3.546	1620	0.282
P41122	P41122GA	POD	51	0.002	0.003	0.005	0.008	0.099	0.465	303	0.101

P41123	P41123GA	POD	51	0.003	0.006	0.008	0.021	0.403	1.231	469	0.136
V41001	V41001GA	STO	51	0.001	0.004	0.007	0.034	0.823	1.516	1211	0.626
E41136	E41136GA	PSM	62	0.020	0.057	0.101	0.412	2.829	5.344	263	1.563
I41030	I41030GA	PSM	62	0.004	0.009	0.019	0.053	0.972	1.987	444	0.313
I41036	I41036GA	PSM	62	0.002	0.008	0.010	0.028	1.195	4.261	2084	0.092
I41036	I41036GB	PSM	62	0.001	0.006	0.009	0.031	1.232	3.599	2819	0.209
I41038	I41038GA	PSM	62	0.001	0.005	0.006	0.021	0.094	0.376	291	0.870

ID Site	ID Sample	Formation	BLU	Laboratory analysis					
				IP (%)	WL (%)	WP (%)	A	\bar{d} (mm)	Gs
D41006	D41006GA	MAC	11	6	27	21	1.22	1.37	2.74
D41010	D41010GA	MAC	11	2	26	24	0.57	0.00	2.87
E41003	E41003GA	MAC	11	4	28	24	0.74	1.02	2.63
E41009	E41009GA	MAC	11	10	33	22	1.24	0.66	2.65
E41015	E41015GA	MAC	11	5	24	19	1.31	1.59	2.60
E41019	E41019GA	MAC	11	5	24	19	0.68	1.25	2.78
E41023	E41023GA	MAC	11	5	29	24	0.89	1.71	2.85
E41024	E41024GA	MAC	11	1	20	19	0.20	5.42	2.63
E41026	E41026GA	MAC	11	12	34	22	1.31	0.48	2.73
E41033	E41033GA	MAC	11	4	27	22	1.47	2.58	2.68
E41052	E41052GA	MAC	11	6	30	24	0.75	0.00	2.59
E41086	E41086GA	MAC	11	3	28	25	1.28	2.91	2.76
E41087	E41087GA	MAC	11	5	25	21	1.66	3.46	2.72
E41089	E41089GA	MAC	11	5	27	23	1.23	0.00	2.74
E41091	E41091GA	MAC	11	4	23	19	1.16	3.65	2.71
E41092	E41092GA	MAC	11	3	28	25	0.89	1.23	2.71
E41097	E41097GA	MAC	11	3	25	23	0.84	0.00	2.82
E41106	E41106GA	MAC	11	6	30	24	0.50	0.35	2.78
E41111	E41111GA	MAC	11	6	29	23	0.92	0.61	2.77
E41124	E41124GA	MAC	11	5	29	24	1.67	3.01	2.68
E41127	E41127GA	MAC	11	8	34	26	5.56	0.00	2.73
E41145	E41145GA	MAC	11	8	32	24	1.25	0.52	2.68
E41159	E41159GA	MAC	11	11	43	32	2.20	2.77	2.86
E41169	E41169GA	MAC	11	6	31	25	1.03	1.03	2.70
E41174	E41174GA	MAC	11	5	40	34	2.34	0.00	2.74
E41190	E41190GA	MAC	11	4	23	19	1.41	2.44	2.75
E41195	E41195GA	MAC	11	3	31	28	1.13	2.94	2.83
E41210	E41210GA	MAC	11	6	29	23	1.00	0.64	2.77
P41005	P41005GA	MAC	11	10	32	22	1.09	1.24	2.69
P41005	P41005GB	MAC	11	10	37	27	1.96	1.88	2.71
P41015	P41015GA	MAC	11	11	36	24	0.84	0.13	2.68
P41018	P41018GA	MAC	11	6	30	24	0.91	0.53	2.64
P41018	P41018GB	MAC	11	10	30	20	2.51	2.53	2.70
P41023	P41023GA	MAC	11	3	29	25	0.29	0.45	2.40
P41023	P41023GB	MAC	11	10	38	28	0.93	0.90	2.63
P41025	P41025GA	MAC	11	15	38	23	0.82	0.00	2.75
P41036	P41036GA	MAC	11	3	23	20	0.92	2.10	2.59
P41040	P41040GA	MAC	11	2	27	24	0.36	0.32	2.85

P41040	P41040GB	MAC	11	2	26	25	0.23	0.75	2.71
P41061	P41061GA	MAC	11	2	25	23	0.21	0.48	2.66
P41062	P41062GA	MAC	11	1	26	25	0.15	0.74	2.58
P41062	P41062GB	MAC	11	1	24	23	0.19	0.46	2.58
P41069	P41069GA	MAC	11	2	30	28	0.48	2.70	2.57
P41088	P41088GA	MAC	11	4	26	22	0.67	1.42	2.54
P41098	P41098GA	MAC	11	1	35	34	0.37	3.44	2.65
P41098	P41098GB	MAC	11	1	34	33	0.48	3.43	2.80
P41101	P41101GA	MAC	11	3	31	28	0.55	1.24	2.62
P41101	P41101GB	MAC	11	1	28	27	0.28	1.22	2.72
P41106	P41106GA	MAC	11	6	38	32	0.67	0.55	2.77
P41106	P41106GB	MAC	11	3	31	27	0.48	0.82	2.82
P41107	P41107GA	MAC	11	8	29	21	2.77	4.37	2.68
P41126	P41126GA	MAC	11	8	29	21	0.92	1.87	2.80
P41127	P41127GA	MAC	11	4	23	18	0.65	1.24	2.72
P41127	P41127GB	MAC	11	5	26	21	0.90	0.96	2.64
P41129	P41129GA	MAC	11	3	24	21	0.64	1.47	2.64
V41011	V41011GA	MAC	11	5	29	24	0.64	0.98	2.72
V41016	V41016GA	MAC	11	5	26	22	0.58	0.56	2.72
V41018	V41018GA	MAC	11	2	20	18	0.77	2.12	2.48
V41028	V41028GA	MAC	11	5	25	20	0.77	0.00	2.77
E41185	E41185GA	SSR	22	4	37	33	0.88	0.00	2.83
I41045	I41045GA	MCP	22	5	27	22	1.02	1.43	2.79
E41044	E41044GA	STO3	23	12	32	20	1.09	0.00	2.88
E41069	E41069GA	MAI	23	13	34	21	0.81	0.38	2.75
E41070	E41070GA	MAI	23	12	33	20	1.09	1.26	2.76
E41072	E41072GA	LIM	23	12	36	25	1.24	1.63	2.87
E41083	E41083GA	LIM	23	12	38	26	1.15	0.84	2.72
E41084	E41084GA	LIM	23	12	40	28	0.91	0.41	2.79
E41108	E41108GA	STO3	23	26	59	33	1.24	0.00	2.89
E41113	E41113GA	STO3	23	8	29	21	0.96	1.96	2.69
E41139	E41139GA	MAI	23	8	35	27	2.51	0.89	2.72
I41006	I41006GA	MAI	23	9	33	24	0.67	0.10	2.65
I41008	I41008GA	LIM	23	3	27	24	0.26	0.19	2.61
I41014	I41014GA	MAI	23	12	35	23	1.59	0.00	2.76
I41057	I41057GA	LIM	23	1	22	22	0.07	0.47	2.70
I41061	I41061GA	CCA	23	6	29	23	1.98	7.81	2.80
I41061	I41061GB	CCA	23	7	30	23	3.96	7.21	2.80
P41011	P41011GA	MAI	23	9	29	21	0.68	0.40	2.68
P41011	P41011GB	MAI	23	8	29	21	0.56	0.29	2.79

P41124	P41124GA	CCA	23	5	30	25	0.75	1.44	2.73
P41124	P41124GB	CCA	23	6	25	19	0.34	0.16	2.84
V41006	V41006GA	STO3	23	4	23	19	0.43	1.00	2.59
V41007	V41007GA	STO3	23	3	23	20	0.37	2.37	2.73
E41078	E41078GA	bnb	31	12	31	19	1.32	1.57	2.82
E41162	E41162GA	VILc	31	6	29	23	1.03	0.61	2.77
E41163	E41163GA	VILc	31	3	25	22	0.82	1.16	2.74
P41038	P41038GA	VILa	31	8	33	25	1.00	0.37	2.73
P41066	P41066GA	bnb	31	7	30	24	2.74	2.77	2.82
E41042	E41042GA	STO	51	18	44	26	1.12	0.00	2.57
E41046	E41046GA	STO	51	8	27	19	0.59	0.29	2.74
E41071	E41071GA	POD	51	14	36	22	0.91	0.49	2.80
E41077	E41077GA	pv	51	13	34	21	3.21	4.24	2.68
E41098	E41098GA	POD	51	15	41	26	1.25	0.00	2.68
E41099	E41099GA	POD	51	15	50	34	0.99	0.00	2.82
E41100	E41100GA	POD	51	14	42	28	0.51	0.00	2.86
E41101	E41101GA	POD	51	15	46	32	0.67	0.00	2.78
E41102	E41102GA	POD	51	15	44	28	0.78	0.14	2.82
E41103	E41103GA	POD	51	14	41	27	0.81	0.29	2.85
E41105	E41105GA	OMT	51	9	33	24	0.68	0.45	2.60
E41109	E41109GA	STO	51	21	52	31	1.20	0.00	2.75
E41114	E41114GA	STO	51	11	37	26	1.70	0.00	2.77
E41129	E41129GA	POD	51	17	43	26	2.33	0.00	2.81
E41130	E41130GA	POD	51	21	55	34	2.30	0.00	2.66
E41137	E41137GA	POD	51	14	40	26	0.91	0.00	2.74
E41138	E41138GA	POD	51	14	39	26	0.83	0.00	2.76
E41155	E41155GA	MMA	51	11	32	21	1.45	0.00	2.77
E41156	E41156GA	MMA	51	8	43	34	1.98	0.00	2.82
E41164	E41164GA	bv	51	11	38	27	3.26	0.00	2.77
E41168	E41168GA	bv	51	6	38	32	1.03	1.84	2.76
I41004	I41004GA	POD	51	7	26	19	1.00	0.56	2.76
I41025	I41025GA	POD	51	13	39	26	0.56	0.04	2.80
P41039	P41039GA	STO	51	8	27	19	0.93	1.50	2.71
P41043	P41043GA	POD	51	14	37	23	1.09	0.65	2.80
P41046	P41046GA	POD	51	9	33	24	0.58	0.16	2.75
P41072	P41072GA	STO	51	7	35	28	3.37	2.55	2.71
P41082	P41082GA	STO	51	1	28	27	0.26	0.00	2.79
P41112	P41112GA	POD	51	8	31	23	1.19	1.60	2.77
P41112	P41112GB	POD	51	10	33	22	1.02	1.26	2.74
P41122	P41122GA	POD	51	10	39	29	0.68	0.33	2.65

P41123	P41123GA	POD	51	9	30	21	0.98	0.82	2.62
V41001	V41001GA	STO	51	14	40	26	1.05	0.75	2.65
E41136	E41136GA	PSM	62	4	31	27	1.80	3.71	2.80
I41030	I41030GA	PSM	62	8	37	29	0.97	1.20	2.68
I41036	I41036GA	PSM	62	23	46	23	2.34	1.31	2.68
I41036	I41036GB	PSM	62	11	33	22	0.94	1.06	2.79
I41038	I41038GA	PSM	62	6	37	30	0.51	0.40	2.74

Slope deposits unit weight laboratory analysis

ID Site	Sample ID	BLU	Natural density (g/cm ³)	Natural Unit Weight (kN/m ³)	Dry density (g/cm ³)	Dry Unit Weight (kN/m ³)
D41006	D41006WA	11	1.45	14.24	1.39	13.60
D41010	D41010WA	11	1.55	15.16	1.37	13.47
D41013	D41013WA	11	1.62	15.86	1.43	13.98
E41000	E41000WA	11	1.83	18.00	1.54	15.14
E41001	E41001WA	11	1.56	15.32	1.25	12.23
E41003	E41003WA	11	1.81	17.73	1.48	14.48
E41006	E41006WA	11	1.93	18.97	1.62	15.86
E41009	E41009WA	11	1.78	17.45	1.48	14.48
E41010	E41010WA	11	2.07	20.29	1.80	17.65
E41011	E41011WA	11	1.56	15.26	1.27	12.48
E41015	E41015WA	11	1.85	18.15	1.58	15.46
E41017	E41017WA	11	1.88	18.47	1.64	16.09
E41019	E41019WA	11	1.84	18.06	1.56	15.27
E41023	E41023WA	11	1.58	15.48	1.28	12.53
E41024	E41024WA	11	1.86	18.25	1.65	16.21
E41026	E41026WA	11	1.94	19.00	1.63	15.96
E41029	E41029WA	11	2.01	19.73	1.66	16.32
E41031	E41031WA	11	1.96	19.24	1.58	15.48
E41032	E41032WA	11	1.73	16.97	1.52	14.92
E41033	E41033WA	11	1.79	17.53	1.57	15.36
E41040	E41040WA	11	1.97	19.33	1.69	16.55
E41050	E41050WA	11	1.91	18.76	1.65	16.19
E41052	E41052WA	11	1.65	16.19	1.32	12.94
E41056	E41056WA	11	1.65	16.22	1.41	13.82
E41059	E41059WA	11	1.48	14.49	1.27	12.41
E41061	E41061WA	11	1.75	17.15	1.58	15.54
E41062	E41062WA	11	1.97	19.30	1.68	16.50
E41067	E41067WA	11	1.73	16.94	1.52	14.89
E41086	E41086WA	11	1.61	15.77	1.50	14.69
E41089	E41089WA	11	1.54	15.11	1.44	14.14
E41090	E41090WA	11	1.91	18.71	1.59	15.63
E41091	E41091WA	11	1.72	16.83	1.59	15.61
E41092	E41092WA	11	1.71	16.77	1.58	15.49
E41106	E41106WA	11	1.47	14.37	1.35	13.24
E41110	E41110WA	11	1.57	15.44	1.45	14.19
E41111	E41111WA	11	1.41	13.80	1.26	12.32
E41119	E41119WA	11	1.37	13.40	1.19	11.63
E41124	E41124WA	11	1.78	17.47	1.59	15.61
E41145	E41145WA	11	1.43	13.99	1.20	11.81
E41159	E41159WA	11	1.23	12.02	0.95	9.32
E41179	E41179WA	11	1.12	10.99	0.87	8.50
E41186	E41186WA	11	1.12	10.96	0.97	9.53

E41190	E41190WA	11	1.45	14.19	1.39	13.67
E41195	E41195WA	11	1.28	12.53	1.11	10.93
E41210	E41210WA	11	1.43	14.03	1.32	12.94
I41015	I41015WA	11	1.48	14.47	1.21	11.88
I41040	I41040WA	11	1.29	12.63	1.10	10.74
P41001	P41001WA	11	1.58	15.54	1.20	11.77
P41002	P41002WA	11	1.65	16.16	1.33	13.05
P41005	P41005WB	11	1.39	13.62	1.07	10.54
P41005	P41005WA	11	1.66	16.28	1.32	12.92
P41012	P41012WA	11	1.73	17.01	1.40	13.72
P41015	P41015WA	11	1.51	14.79	1.15	11.24
P41016	P41016WA	11	1.52	14.87	1.15	11.23
P41018	P41018WB	11	1.79	17.56	1.58	15.46
P41018	P41018WA	11	1.83	17.92	1.52	14.94
P41019	P41019WA	11	1.65	16.17	1.31	12.82
P41019	P41019WB	11	1.66	16.26	1.31	12.85
P41020	P41020WA	11	1.67	16.40	1.37	13.47
P41021	P41021WA	11	1.77	17.37	1.39	13.61
P41021	P41021WB	11	1.85	18.12	1.48	14.53
P41022	P41022WA	11	1.34	13.16	1.09	10.70
P41023	P41023WB	11	1.50	14.68	1.13	11.04
P41023	P41023WA	11	1.55	15.25	1.24	12.21
P41025	P41025WA	11	1.82	17.87	1.48	14.50
P41032	P41032WA	11	1.47	14.38	1.15	11.32
P41036	P41036WA	11	1.75	17.13	1.52	14.92
P41040	P41040WA	11	1.39	13.65	1.14	11.22
P41040	P41040WB	11	1.58	15.48	1.28	12.51
P41057	P41057WA	11	1.51	14.85	1.30	12.71
P41061	P41061WA	11	1.67	16.38	1.37	13.43
P41061	P41061WB	11	1.98	19.44	1.66	16.31
P41062	P41062WB	11	1.69	16.58	1.37	13.40
P41062	P41062WA	11	1.75	17.18	1.49	14.57
P41069	P41069WA	11	1.63	15.95	1.34	13.10
P41088	P41088WA	11	1.55	15.17	1.28	12.60
P41098	P41098WA	11	1.21	11.82	0.96	9.42
P41098	P41098WB	11	1.40	13.76	1.23	12.02
P41101	P41101WB	11	1.49	14.64	1.20	11.75
P41101	P41101WA	11	1.51	14.84	1.19	11.70
P41106	P41106WA	11	1.42	13.97	1.12	10.97
P41106	P41106WB	11	1.43	14.03	1.19	11.66
P41107	P41107WA	11	1.35	13.20	1.16	11.40
P41126	P41126WA	11	1.52	14.93	1.36	13.32
P41127	P41127WB	11	1.44	14.09	1.32	12.96
P41127	P41127WA	11	1.46	14.36	1.38	13.49
P41129	P41129WA	11	1.57	15.42	1.51	14.78

V41000	V41000WA	11	1.79	17.52	1.56	15.32
V41011	V41011WA	11	1.43	14.05	1.11	10.87
V41016	V41016WA	11	1.48	14.48	1.23	12.03
V41018	V41018WA	11	1.78	17.43	1.55	15.19
V41026	V41026WA	11	1.77	17.36	1.55	15.21
V41027	V41027WA	11	1.85	18.17	1.55	15.21
V41028	V41028WA	11	1.91	18.71	1.66	16.31
E41180	E41180WA	22	1.33	13.03	1.27	12.41
E41185	E41185WA	22	1.18	11.62	1.11	10.86
I41045	I41045WA	22	1.54	15.08	1.29	12.66
E41044	E41044WA	23	1.81	17.76	1.58	15.53
E41069	E41069WA	23	1.40	13.74	1.26	12.33
E41072	E41072WA	23	1.69	16.59	1.44	14.14
E41083	E41083WA	23	1.53	15.01	1.34	13.14
E41084	E41084WA	23	1.41	13.87	1.27	12.45
E41108	E41108WA	23	1.76	17.30	1.42	13.92
E41113	E41113WA	23	1.49	14.57	1.31	12.87
E41139	E41139WA	23	1.57	15.42	1.31	12.87
I41006	I41006WA	23	1.63	16.03	1.33	13.07
I41008	I41008WA	23	1.54	15.08	1.25	12.29
I41014	I41014WA	23	1.34	13.19	1.19	11.70
I41057	I41057WA	23	1.55	15.20	1.29	12.66
I41061	I41061WA	23	1.37	13.44	1.25	12.30
P41011	P41011WA	23	1.73	16.99	1.41	13.88
P41030	P41030WA	23	1.48	14.55	1.21	11.87
P41031	P41031WA	23	1.59	15.60	1.29	12.62
P41124	P41124WA	23	1.41	13.83	1.21	11.89
P41124	P41124WB	23	1.74	17.10	1.51	14.77
V41006	V41006WA	23	1.86	18.26	1.66	16.28
V41007	V41007WA	23	1.91	18.74	1.65	16.21
E41038	E41038WA	31	1.94	19.05	1.63	16.02
E41043	E41043WA	31	1.75	17.13	1.58	15.51
E41079	E41079WA	31	1.65	16.20	1.43	14.01
E41162	E41162WA	31	1.52	14.90	1.49	14.65
E41199	E41199WA	31	1.33	13.08	1.26	12.33
P41038	P41038WA	31	1.43	14.03	1.15	11.26
P41066	P41066WA	31	1.82	17.88	1.55	15.23
D41003	D41003WA	51	1.54	15.10	1.28	12.51
D41005	D41005WA	51	1.53	15.04	1.38	13.52
E41042	E41042WA	51	1.88	18.49	1.48	14.52
E41046	E41046WA	51	1.87	18.36	1.62	15.89
E41071	E41071WA	51	1.64	16.13	1.41	13.81
E41098	E41098WA	51	1.50	14.70	1.36	13.38
E41099	E41099WA	51	1.49	14.66	1.33	13.04
E41101	E41101WA	51	1.68	16.45	1.41	13.82

E41102	E41102WA	51	1.59	15.60	1.38	13.53
E41103	E41103WA	51	1.76	17.29	1.49	14.61
E41105	E41105WA	51	1.71	16.74	1.49	14.62
E41109	E41109WA	51	1.56	15.33	1.30	12.80
E41129	E41129WA	51	1.40	13.75	1.28	12.52
E41137	E41137WA	51	1.87	18.34	1.53	14.97
E41138	E41138WA	51	1.89	18.50	1.42	13.90
E41156	E41156WA	51	1.49	14.60	1.13	11.11
E41164	E41164WA	51	1.80	17.63	1.52	14.93
E41168	E41168WA	51	1.14	11.18	1.00	9.83
I41004	I41004WA	51	1.69	16.54	1.43	14.01
I41021	I41021WA	51	1.64	16.07	1.36	13.31
I41025	I41025WA	51	1.77	17.35	1.39	13.63
P41039	P41039WA	51	1.92	18.86	1.70	16.68
P41043	P41043WA	51	1.75	17.16	1.50	14.75
P41046	P41046WA	51	1.78	17.42	1.46	14.29
P41072	P41072WA	51	1.53	15.00	1.32	12.99
P41082	P41082WA	51	1.42	13.91	1.15	11.28
P41112	P41112WA	51	1.43	14.07	1.25	12.27
P41112	P41112WB	51	1.57	15.36	1.34	13.18
P41122	P41122WA	51	1.36	13.37	1.19	11.70
P41123	P41123WA	51	1.44	14.11	1.31	12.82
V41001	V41001WA	51	1.50	14.72	1.28	12.55
V41003	V41003WA	51	1.55	15.17	1.31	12.87
C7001	C7001WA	61	1.60	15.65	1.23	12.06
C7008	C7008WA	61	1.54	15.12	1.12	10.97
U7446	U7446WA	61	1.20	11.80	1.05	10.30
U7466	U7466WA	61	1.38	13.51	1.32	12.96
V4050	V4050WA	61	1.61	15.78	1.37	13.39
V4058	V4058WA	61	1.51	14.86	1.14	11.20
V4060	V4060WA	61	1.44	14.12	1.12	10.95
V4122	V4122WA	61	1.87	18.32	1.62	15.87
V4149	V4149WA	61	1.20	11.81	1.02	10.02
V4155	V4155WA	61	1.68	16.52	1.47	14.45
V4385	V4385WA	61	1.21	11.88	1.03	10.08
V4386	V4386WA	61	1.41	13.79	1.25	12.30
V4387	V4387WA	61	1.19	11.66	1.03	10.12
V4388	V4388WA	61	1.20	11.74	1.09	10.66
E41132	E41132WA	62	1.11	10.85	0.90	8.79
E41136	E41136WA	62	1.57	15.43	1.40	13.77
I41030	I41030WA	62	1.50	14.71	1.16	11.42
I41036	I41036WA	62	1.70	16.70	1.45	14.25
I41038	I41038WA	62	1.39	13.67	1.07	10.48
U7505	U7505WA	62	1.27	12.42	1.24	12.12
V4004	V4004WA	62	2.00	19.60	1.70	16.70

V4013	V4013WA	62	1.66	16.24	1.31	12.82
V4015	V4015WA	62	1.42	13.92	1.09	10.73
V4017	V4017WA	62	1.64	16.11	1.29	12.62
V4282	V4282WA	62	1.34	13.12	1.11	10.86

APPENDIX C

ID Site	Rv	GSI peak	GSI residual		Intact rock strenght (MPa)		m _i	
			min	max	min	max	max	min
20120102	25	55	26	21	29	43	16.8	10.4
20120103	20	50	26	21	19	39	16.8	10.4
20120104	29	60	27	22	32	54	16.8	10.4
20120105	21	30	20	15	23	35	16.8	10.4
20120108	31	50	26	21	33	63	16.8	10.4
20120112	11	40	23	18	10	28	16.8	10.4
20120117	23	40	23	18	26	39	16.8	10.4
20120146	15	40	23	18	18	26	16.8	10.4
20120147	31	50	26	21	36	60	16.8	10.4
20120153	22	45	25	20	25	37	16.8	10.4
20120154	22	45	25	20	23	38	16.8	10.4
20120156	26	55	26	21	31	43	16.8	10.4
20120356	11	40	23	18	13	24	16.8	10.4
20120357	38	35	22	17	54	79	16.8	10.4
20170319	8	30	20	15	12	18	16.8	10.4
20170320	22	40	23	18	17	51	16.8	10.4
20170321	21	55	26	21	22	36	16.8	10.4
20170322	12	40	23	18	15	23	16.8	10.4
20170328	24	60	27	22	25	42	16.8	10.4
20170329	33	60	27	22	38	73	16.8	10.4
20170330	25	65	27	22	25	47	16.8	10.4
20170332	29	60	27	22	30	58	16.8	10.4
20170333	24	50	26	21	28	40	16.8	10.4
20170334	16	40	23	18	15	34	16.8	10.4
20170335	15	30	20	15	17	27	16.8	10.4
20170336	24	45	25	20	21	51	16.8	10.4
20170337	26	65	27	22	28	47	16.8	10.4
20182006	17	55	26	21	16	33	16.8	10.4
20182036	21	55	26	21	19	44	16.8	10.4
20182039	22	70	27	22	22	40	16.8	10.4
20182040	24	45	25	20	26	42	16.8	10.4
20182041	28	55	26	21	34	49	16.8	10.4
20182042	29	55	26	21	34	50	16.8	10.4
20182043	27	45	25	20	31	49	16.8	10.4
20182044	26	55	26	21	30	45	16.8	10.4

20182045	21	35	22	17	23	34	16.8	10.4
20182046	9	25	18	13	14	17	16.8	10.4
20182047	20	35	22	17	20	36	16.8	10.4
20182048	10	30	20	15	14	20	16.8	10.4
20182050	16	40	23	18	15	33	16.8	10.4
20182051	24	55	26	21	24	47	16.8	10.4
20182052	15	35	22	17	16	26	16.8	10.4
20182055	9	30	20	15	14	18	16.8	10.4
20182056	19	45	25	20	21	33	16.8	10.4
20182057	21	45	25	20	22	37	16.8	10.4
20182058	15	45	25	20	17	28	16.8	10.4
20182059	20	40	23	18	21	34	16.8	10.4
20182060	15	65	27	22	13	34	16.8	10.4
20182064	18	40	23	18	21	30	16.8	10.4
20182065	17	40	23	18	18	29	16.8	10.4
20182066	24	40	23	18	26	40	16.8	10.4
20182067	19	45	25	20	18	36	16.8	10.4
20182068	21	45	25	20	22	36	16.8	10.4
20182069	19	50	26	21	21	32	16.8	10.4
20182070	22	35	22	17	20	47	16.8	10.4
20182071	21	60	27	22	24	35	16.8	10.4
20182072	26	35	22	17	28	49	16.8	10.4
20182073	22	40	23	18	24	37	16.8	10.4
20182075	21	45	25	20	21	37	16.8	10.4
20182076	23	50	26	21	23	42	16.8	10.4
20182077	20	55	26	21	20	36	16.8	10.4
20182078	17	30	20	15	16	33	16.8	10.4
20182079	21	65	27	22	23	37	16.8	10.4
20182081	17	40	23	18	17	31	16.8	10.4
20182082	21	40	23	18	22	37	16.8	10.4
20182083	19	40	23	18	20	32	16.8	10.4
20182084	17	40	23	18	17	33	16.8	10.4
20182085	27	65	27	22	30	50	16.8	10.4
20182086	25	50	26	21	27	44	16.8	10.4
20182087	22	40	23	18	21	42	16.8	10.4
20182088	17	50	26	21	18	30	16.8	10.4
20182089	27	60	27	22	29	52	16.8	10.4

20182090	22	60	27	22	23	40	16.8	10.4
20182091	28	70	27	22	32	50	16.8	10.4
20182092	23	55	26	21	26	38	16.8	10.4
20182093	24	55	26	21	26	39	16.8	10.4
20182094	18	40	23	18	17	37	16.8	10.4
20182096	15	35	22	17	15	30	16.8	10.4
20182097	11	25	18	13	16	20	16.8	10.4
20182098	19	55	26	21	19	37	16.8	10.4
20182099	23	40	23	18	24	40	16.8	10.4
20182100	26	60	27	22	26	49	16.8	10.4
20182101	24	45	25	20	26	42	16.8	10.4
20182102	26	65	27	22	29	45	16.8	10.4
20182103	27	65	27	22	31	47	16.8	10.4
20182104	25	65	27	22	26	46	16.8	10.4
20182105	15	35	22	17	16	28	16.8	10.4

ID Site	Rockmass strenght (MPa)			Friction angle (degrees)			Effective cohesion (KPa)			BMU
	25th perc	median	75th perc	25th perc	median	75th perc	25th perc	median	75th perc	
20120102	0.8	0.9	1.0	28.8	30.2	31.5	35.6	33.1	38.3	1
20120103	0.6	0.7	0.8	26.4	28.0	29.6	31.4	28.7	34.2	1
20120104	1.0	1.1	1.3	30.4	31.9	33.3	39.4	36.5	42.5	1
20120105	0.4	0.5	0.6	21.8	23.2	24.5	22.6	20.7	24.7	4
20120108	1.0	1.2	1.4	29.9	31.5	33.1	38.6	35.4	41.7	1
20120112	0.3	0.4	0.5	21.7	23.5	25.1	23.4	20.8	26.1	1
20120117	0.6	0.7	0.8	25.5	26.9	28.3	29.1	26.8	31.5	4
20120146	0.4	0.5	0.5	23.1	24.4	25.7	24.8	23.0	27.0	4
20120147	1.0	1.2	1.3	30.0	31.5	33.0	38.6	35.7	41.6	2
20120153	0.6	0.7	0.8	26.3	27.7	29.0	30.6	28.3	33.1	2
20120154	0.6	0.7	0.8	26.2	27.6	28.9	30.4	28.1	32.9	2
20120156	0.8	0.9	1.0	29.0	30.4	31.7	36.0	33.5	38.7	2
20120356	0.3	0.4	0.5	21.9	23.3	24.7	23.2	21.3	25.3	4
20120357	1.1	1.3	1.4	28.8	30.3	31.8	35.5	32.6	38.6	3
20170319	0.2	0.3	0.3	18.1	19.4	20.6	17.3	15.8	19.0	4
20170320	0.6	0.7	0.9	25.1	27.2	29.0	29.7	26.3	33.0	4
20170321	0.6	0.7	0.8	27.2	28.7	30.1	32.6	30.3	35.2	2
20170322	0.4	0.4	0.5	22.2	23.5	24.7	23.4	21.6	25.4	4
20170328	0.8	0.9	1.0	28.7	30.1	31.6	35.6	33.0	38.3	2
20170329	1.2	1.5	1.7	32.1	33.7	35.2	43.7	40.2	47.4	2
20170330	0.8	1.0	1.1	29.4	30.9	32.4	37.3	34.3	40.3	2
20170332	1.0	1.2	1.3	30.4	32.0	33.6	39.7	36.5	43.1	2
20170333	0.7	0.8	0.9	27.8	29.2	30.5	33.4	31.1	36.0	3
20170334	0.4	0.5	0.6	23.4	25.0	26.7	25.9	23.4	28.6	4
20170335	0.3	0.4	0.4	20.2	21.5	22.8	20.2	18.5	22.2	4
20170336	0.7	0.8	1.0	26.8	28.7	30.3	32.5	29.2	35.7	1
20170337	0.9	1.0	1.1	29.7	31.2	32.6	37.9	35.2	40.9	1
20182006	0.5	0.6	0.7	25.9	27.5	29.0	30.4	27.8	33.2	3
20182036	0.7	0.8	1.0	27.4	29.2	30.9	33.7	30.5	36.9	4
20182039	0.7	0.8	1.0	28.5	30.0	31.5	35.4	32.7	38.3	4
20182040	0.7	0.8	0.9	26.9	28.3	29.7	31.8	29.4	34.4	2
20182041	0.9	1.0	1.2	29.8	31.2	32.5	37.7	35.0	40.6	2
20182042	0.9	1.1	1.2	29.8	31.3	32.6	37.9	35.2	40.8	2
20182043	0.8	0.9	1.0	27.9	29.4	30.8	34.0	31.3	36.7	3
20182044	0.8	0.9	1.1	29.1	30.5	31.8	36.2	33.6	39.0	3

20182045	0.5	0.6	0.6	23.4	24.7	26.1	25.2	23.2	27.5	3
20182046	0.2	0.2	0.3	16.6	17.7	18.9	15.1	13.7	16.7	1
20182047	0.5	0.5	0.6	23.1	24.6	26.0	25.1	23.0	27.4	1
20182048	0.3	0.3	0.3	18.8	20.1	21.3	18.2	16.6	20.0	4
20182050	0.4	0.5	0.6	23.3	24.9	26.5	25.7	23.3	28.3	4
20182051	0.8	0.9	1.0	28.4	30.1	31.6	35.4	32.5	38.5	4
20182052	0.4	0.4	0.5	21.5	22.8	24.1	22.3	20.5	24.4	4
20182055	0.2	0.3	0.3	18.5	19.7	21.0	17.9	16.3	19.5	4
20182056	0.5	0.6	0.7	25.4	26.7	28.1	29.0	26.8	31.3	4
20182057	0.6	0.7	0.8	25.9	27.4	28.7	30.0	27.7	32.5	4
20182058	0.5	0.5	0.6	24.2	25.6	26.9	26.9	24.8	29.2	4
20182059	0.5	0.6	0.7	24.4	25.8	27.2	27.3	25.1	29.6	4
20182060	0.5	0.6	0.8	26.1	28.0	29.7	31.4	28.1	34.6	4
20182064	0.5	0.5	0.6	24.0	25.4	26.7	26.4	24.4	28.6	4
20182065	0.4	0.5	0.6	23.4	24.8	26.1	25.6	23.5	27.8	4
20182066	0.6	0.7	0.8	25.6	27.0	28.4	29.3	27.0	31.8	3
20182067	0.5	0.6	0.7	25.2	26.7	28.2	29.0	26.5	31.6	3
20182068	0.6	0.7	0.8	25.8	27.2	28.6	29.8	27.5	32.2	4
20182069	0.6	0.6	0.7	26.1	27.4	28.7	30.2	28.0	32.7	4
20182070	0.5	0.7	0.8	24.0	25.7	27.4	26.9	24.2	29.7	4
20182071	0.7	0.8	0.9	27.9	29.3	30.5	33.7	31.4	36.3	3
20182072	0.6	0.8	0.9	25.2	26.6	28.1	28.5	26.1	31.1	3
20182073	0.6	0.7	0.7	25.1	26.5	27.8	28.4	26.2	30.8	3
20182075	0.6	0.7	0.8	25.8	27.3	28.7	29.8	27.5	32.3	3
20182076	0.7	0.8	0.9	27.3	28.8	30.3	32.9	30.3	35.6	3
20182077	0.6	0.7	0.8	27.0	28.4	29.9	32.2	29.7	34.8	3
20182078	0.4	0.4	0.5	20.6	22.1	23.6	21.2	19.2	23.3	4
20182079	0.7	0.8	0.9	28.2	29.7	31.0	34.6	32.2	37.3	3
20182081	0.4	0.5	0.6	23.5	25.0	26.4	25.8	23.7	28.1	4
20182082	0.5	0.6	0.7	24.9	26.3	27.6	28.0	25.8	30.4	4
20182083	0.5	0.6	0.6	24.1	25.5	26.8	26.6	24.5	28.9	4
20182084	0.4	0.5	0.6	23.7	25.2	26.7	26.2	24.0	28.6	4
20182085	0.9	1.1	1.2	30.2	31.7	33.1	38.9	36.1	42.0	3
20182086	0.8	0.9	1.0	28.0	29.4	30.8	34.1	31.6	36.8	3
20182087	0.6	0.7	0.8	25.1	26.7	28.2	28.8	26.3	31.4	4
20182088	0.5	0.6	0.7	25.4	26.8	28.1	29.1	26.9	31.5	3
20182089	0.9	1.1	1.2	29.9	31.5	32.9	38.5	35.5	41.5	3

20182090	0.7	0.8	0.9	28.2	29.7	31.1	34.7	32.1	37.4	3
20182091	1.0	1.1	1.2	30.6	32.0	33.4	39.7	36.9	42.7	3
20182092	0.7	0.8	0.9	28.0	29.4	30.7	33.9	31.5	36.5	3
20182093	0.7	0.8	0.9	28.1	29.5	30.8	34.1	31.7	36.8	3
20182094	0.5	0.6	0.7	24.0	25.7	27.3	27.0	24.5	29.6	4
20182096	0.4	0.4	0.5	21.7	23.2	24.7	23.0	20.9	25.1	4
20182097	0.2	0.3	0.3	17.3	18.5	19.8	16.0	14.6	17.7	4
20182098	0.6	0.7	0.8	26.9	28.4	29.9	32.2	29.5	34.9	3
20182099	0.6	0.7	0.8	25.4	26.8	28.2	29.0	26.7	31.4	3
20182100	0.8	1.0	1.1	29.4	30.9	32.4	37.3	34.3	40.3	2
20182101	0.7	0.8	0.9	26.9	28.3	29.7	31.8	29.4	34.4	2
20182102	0.9	1.0	1.1	29.7	31.1	32.5	37.7	35.0	40.5	2
20182103	0.9	1.0	1.2	30.1	31.5	32.8	38.5	35.8	41.4	2
20182104	0.8	1.0	1.1	29.4	30.9	32.4	37.3	34.5	40.2	2
20182105	0.4	0.4	0.5	21.7	23.1	24.4	22.8	20.9	24.8	4

REFERENCES

- Abburu, S., & Babu Golla, S. (2015) - Satellite Image Classification Methods and Techniques: A Review. *International Journal of Computer Applications*, 119(8), 20–25. doi: 10.5120/21088-3779.
- Adediran, A. O., Parcharidis, I., Poscolieri, M., & Pavlopoulos, K. (2004) - Computer-assisted discrimination of morphological units on north-central Crete (Greece) by applying multivariate statistics to local relief gradients. *Geomorphology*, 58(1–4), 357–370. doi: 10.1016/j.geomorph.2003.07.024.
- Akgun, A. (2012) - A comparison of landslide susceptibility maps produced by logistic regression, multi-criteria decision, and likelihood ratio methods: A case study at İzmir, Turkey. *Landslides*, 9(1), 93–106. doi: 10.1007/s10346-011-0283-7.
- Allen, G. H., Barnes, J. B., Pavelsky, T. M., & Kirby, E. (2013) - Lithologic and tectonic controls on bedrock channel form at the northwest Himalayan front. *Journal of Geophysical Research: Earth Surface*, 118(3), 1806–1825. doi: 10.1002/jgrf.20113.
- Ameratunga, J., Sivakugan, N., & Das, B. M. (2016) - Correlations of Soil and Rock Properties in Geotechnical Engineering, 1–228. Available at: <http://www.springer.com/series/13410>.
- Anselin, L. (1995) - Local Indicators of Spatial Association—LISA. *Geographical Analysis*, 27(2), 93–115. doi: 10.1111/j.1538-4632.1995.tb00338.x.
- Ardizzone, F., Cardinali, M., Carrara, A., Guzzetti, F., & Reichenbach, P. (2002) - Impact of mapping errors on the reliability of landslide hazard maps. *Natural Hazards and Earth System Sciences*, 2(1–2), 3–14. doi: 10.5194/nhess-2-3-2002.
- Armaghani, D. J., Tonnizam Mohamad, E., Momeni, E., Monjezi, M., & Sundaram Narayanasamy, M. (2016) - Prediction of the strength and elasticity modulus of granite through an expert artificial neural network. *Arabian Journal of Geosciences*, 9(1), 1–16. doi: 10.1007/s12517-015-2057-3.
- Arnone, E., Caracciolo, D., Noto, L. V., Preti, F., & R. L. Bras (2016) - Modeling the hydrological and mechanical effect of roots on shallow landslides. *Journal of the American Water Resources Association*, 5(3), 2–2. doi: 10.1111/j.1752-1688.1969.tb04897.x.
- Arrell, K. E., Fisher, P. F., Tate, N. J., & Bastin, L. (2007) - A fuzzy c-means classification of elevation derivatives to extract the morphometric classification of landforms in Snowdonia, Wales. *Computers and Geosciences*, 33(10), 1366–1381. doi: 10.1016/j.cageo.2007.05.005.
- Assunção, R. M., Neves, M. C., Câmara, G., & Da Costa Freitas, C. (2006) - Efficient regionalization techniques for socio-economic geographical units using minimum spanning trees. *International Journal of Geographical Information Science*, 20(7), 797–811. doi: 10.1080/13658810600665111.
- ASTM (2001) Standard test method for determination of rock hardness by rebound hammer method.

ASTM International.

- ASTM - D2937 (no date) - Standard Test Method for Density of Soil in Place by the Drive-Cylinder Method. Annual book of ASTM standards (7 pp.). ASTM International West Conshohocken, PA.
- ASTM D5873-14 (no date) Determination of Rock Hardness by Rebound Hammer Method. Available at: www.astm.org.
- Aufmuth, R. E. (1973) A systematic determination of engineering criteria for rock.
- Australian Standard (2002) Earth-retaining structures.
- Avanzi, G. D. A., Duchi, S., Galanti, Y., Giannecchini, R., & Lo Presti, D. (2010) - Geotechnical characterization of the Macigno Fm. debris by dynamic penetration tests in the Serchio River basin (Tuscany, Italy). *Rendiconti Online Societa Geologica Italiana*, 11(2), 579–580.
- Aydin, A. (2009) - ISRM Suggested method for determination of the Schmidt hammer rebound hardness: Revised version. *International Journal of Rock Mechanics and Mining Sciences*, 46(3), 627–634. doi: 10.1016/j.ijrmms.2008.01.020.
- Aydin, A., & Basu, A. (2005) - The Schmidt hammer in rock material characterization. *Engineering Geology*, 81(1), 1–14. doi: 10.1016/j.enggeo.2005.06.006.
- Barton, N. (1976) - The shear strength of rock and rock joints. *International Journal of Rock Mechanics and Mining Sciences and*, 13(9), 255–279. doi: 10.1016/0148-9062(76)90003-6.
- Barton, N., & Choubey, V. (1977) - The shear strength of rock joints in theory and practice. *Rock Mechanics Felsmechanik Mécanique des Roches*, 10(1–2), 1–54. doi: 10.1007/BF01261801.
- Basu, A., & Aydin, A. (2004) - A method for normalization of Schmidt hammer rebound values, 41, 1211–1214. doi: 10.1016/j.ijrmms.2004.05.001.
- Baum, R. L., Savage, W. Z., Godt, J. W., & others (2002) - TRIGRS—a Fortran program for transient rainfall infiltration and grid-based regional slope-stability analysis. US geological survey open-file report, 424, 38.
- Beck, H. E., Zimmermann, N. E., McVicar, T. R., Vergopolan, N., Berg, A., & Wood, E. F. (2018) - Present and future köppen-geiger climate classification maps at 1-km resolution. *Scientific Data*. The Author(s), 5, 1–12. doi: 10.1038/sdata.2018.214.
- van Beek, L. P. H. (2002) Assessment of the influence of changes in land use and climate on landslide activity in a Mediterranean environment. *Nederlandse Geografische Studies*.
- Beguería, S. (2006) - Validation and evaluation of predictive models in hazard assessment and risk management. *Natural Hazards*, 37(3), 315–329. doi: 10.1007/s11069-005-5182-6.
- Benito-Calvo, A., Pérez-González, A., Magri, O., & P. Meza (2009) - Assessing regional geodiversity: the Iberian Peninsula. *Earth Surface Processes and Landforms*, 34(March), 1433–1445. doi: 10.1002/esp.1840.
- Bernard, T., Sinclair, H. D., Gailleton, B., Mudd, S. M., & Ford, M. (2019) - Lithological control on the

- post-orogenic topography and erosion history of the Pyrenees. *Earth and Planetary Science Letters*. Elsevier B.V., 518, 53–66. doi: 10.1016/j.epsl.2019.04.034.
- Berti, M., Bertello, L., Bernardi, A. R., & Caputo, G. (2017) - Back analysis of a large landslide in a flysch rock mass. *Landslides*. *Landslides*, 14(6), 2041–2058. doi: 10.1007/s10346-017-0852-5.
- Beven, K. J., & Kirkby, M. J. (1979) - A physically based, variable contributing area model of basin hydrology. *Hydrological Sciences Bulletin*, 24(1), 43–69. doi: 10.1080/02626667909491834.
- Beverly, B. E., Schoenwolf, D. A., & Brierly, G. S. (1979) - Correlations of rock index values with engineering properties and the classification of intact rock. Federal Highway Administration, Washington DC, Technical Report, 228, 229.
- Bieniawski, Z. T. (1993) - Classification of rock masses for engineering: the RMR system and future trends. in *Rock Testing and Site Characterization*. Elsevier, 553–573.
- Binder, K., Heermann, D., Roelofs, L., Mallinckrodt, A. J., & McKay, S. (1993) - Monte Carlo simulation in statistical physics. *Computers in Physics*. American Institute of Physics, 7(2), 156–157.
- Bjerrum, L., & Simons, N. E. (1960) - Comparison of shear strength characteristics of normally consolidated clays, Norwegian Geotechnical Institute. Publication.
- Blahut, J., van Westen, C. J., & Sterlacchini, S. (2010) - Analysis of landslide inventories for accurate prediction of debris-flow source areas. *Geomorphology*. Elsevier B.V., 119(1–2), 36–51. doi: 10.1016/j.geomorph.2010.02.017.
- Blair, T. C., & McPherson, J. G. (1999) - Grain-size and textural classification of coarse sedimentary particles. *Journal of Sedimentary Research*, 69(1), 6–19. doi: 10.2110/jsr.69.6.
- Bolton, M. D. (1986) - The strength and dilatancy of sands. *Geotechnique*. Thomas Telford Ltd, 36(1), 65–78.
- Bone, C., Wulder, M. A., White, J. C., Robertson, C., & Nelson, T. A. (2013) - A GIS-based risk rating of forest insect outbreaks using aerial overview surveys and the local Moran's I statistic. *Applied Geography*. Elsevier Ltd, 40, 161–170. doi: 10.1016/j.apgeog.2013.02.011.
- Booth, A. M., Roering, J. J., & Perron, J. T. (2009) - Automated landslide mapping using spectral analysis and high-resolution topographic data: Puget Sound lowlands, Washington, and Portland Hills, Oregon. *Geomorphology*. Elsevier B.V., 109(3–4), 132–147. doi: 10.1016/j.geomorph.2009.02.027.
- Boruvka, O. (1926) - O jistém problému minimáln {\'i}m.
- Brardinoni, F., & Church, M. (2004) - Representing the landslide magnitude-frequency relation: Capilano River basin, British Columbia. *Earth Surface Processes and Landforms*, 29(1), 115–124. doi: 10.1002/esp.1029.
- Brideau, M. A., & Roberts, N. J. (2014) Mass Movement in Bedrock. *Landslide Hazards, Risks, and Disasters*. doi: 10.1016/B978-0-12-396452-6.00003-3.
- Brooker, E. W., & Ireland, H. O. (1965) - Earth pressures at rest related to stress history. *Canadian*

geotechnical journal. NRC Research Press, 2(1), 1–15.

- Brown, D. G., Lusch, D. P., & Duda, K. A. (1998) - Supervised classification of types of glaciated landscapes using digital elevation data. *Geomorphology*, 21(3–4), 233–250. doi: 10.1016/S0169-555X(97)00063-9.
- Brunetti, M., Guzzetti, F., & Rossi, M. (2009) - Probability distributions of landslide volumes. *Nonlinear Processes in Geophysics*, 16(2), 179–188. doi: 10.5194/npg-16-179-2009.
- BS 1377-2 (1990) - Methods of test for soils for civil engineering purposes-Part 2: Classification tests. London: UK: British Standard Institution.
- Burrough, P. A., Van Gaans, P. F. M., & MacMillan, R. A. (2000) - High-resolution landform classification using fuzzy k -means. *Fuzzy Sets and Systems*, 113(1), 37–52. doi: 10.1016/S0165-0114(99)00011-1.
- Cai, M., Kaiser, P. K., Uno, H., Tasaka, Y., & Minami, M. (2004) - Estimation of rock mass deformation modulus and strength of jointed hard rock masses using the GSI system. *International Journal of Rock Mechanics and Mining Sciences*, 41(1), 3–19. doi: 10.1016/S1365-1609(03)00025-X.
- Cai, M., Kaiser, P. K., Tasaka, Y., & Minami, M. (2007) - Determination of residual strength parameters of jointed rock masses using the GSI system. *International Journal of Rock Mechanics and Mining Sciences*, 44(2), 247–265. doi: 10.1016/j.ijrmms.2006.07.005.
- Caliński, T., & Harabasz, J. (1974) - Communications in Statistics - Theory and Methods. *Communications in Statistics*, 3(1), 1–27. doi: 10.1080/03610927408827101.
- Carmignani, L. . , Conti, P., Cornamusini, G., & Meccheri, M. (2004) - THE INTERNAL NORTHERN APENNINES , THE NORTHERN TYRRHENIAN SEA AND THE SARDINIA-CORSICA BLOCK C ARMIGNANI L . , C ONTI P . , C ORNAMUSINI G . , M ECCHERI M .
- Carmignani, L., Decandia, F. A., Fantozzi, P. L., Lazzarotto, A., Liotta, D., & Meccheri, M. (1994) - Tertiary extensional tectonics in Tuscany (Northern Apennines, Italy). *Tectonophysics*. Elsevier, 238(1–4), 295–315. doi: 10.1016/0040-1951(94)90061-2.
- Carmignani, L., Decandia, F. A., Disperati, L., Fantozzi, P. L., Kligfield, R., Lazzarotto, A., Liotta, D., & Meccheri, M. (2001) - Inner Northern Apennines. in Vai, G. B. and Martini, I. P. (eds) *Anatomy of an Orogen: the Apennines and Adjacent Mediterranean Basins*. Dordrecht: Springer Netherlands, 197–213. doi: 10.1007/978-94-015-9829-3_14.
- Carrara, A., Crosta, G., & Frattini, P. (2008) - Comparing models of debris-flow susceptibility in the alpine environment. *Geomorphology*, 94(3–4), 353–378. doi: 10.1016/j.geomorph.2006.10.033.
- Casagli, N., Cigna, F., Bianchini, S., Hölbling, D., Füreder, P., Righini, G., Del Conte, S., Friedl, B., Schneiderbauer, S., Iasio, C., Vlcko, J., Greif, V., Proske, H., Granica, K., Falco, S., Lozzi, S., Mora, O., Arnaud, A., Novali, F., & Bianchi, M. (2016) - Landslide mapping and monitoring by using radar and optical remote sensing: Examples from the EC-FP7 project SAFER. *Remote Sensing*

Applications: Society and Environment, 92–108. doi: 10.1016/j.rsase.2016.07.001.

- Cascini, L., Ciarleto, M., & Di Nocera, S. (2017) - Soil depth reconstruction for the assessment of the susceptibility to shallow landslides in fine-grained slopes. *Landslides*, 14(2), 459–471. doi: 10.1007/s10346-016-0720-8.
- Catani, F., Segoni, S., & Falorni, G. (2007) - Accurate basin scale soil depth modelling and its impact on shallow landslides prediction. in *Geophysical Research Abstracts*, 10828.
- Cervi, F., Berti, M., Borgatti, L., Ronchetti, F., Manenti, F., & Corsini, A. (2010) - Comparing predictive capability of statistical and deterministic methods for landslide susceptibility mapping: A case study in the northern Apennines (Reggio Emilia Province, Italy). *Landslides*, 7(4), 433–444. doi: 10.1007/s10346-010-0207-y.
- Chang, K. T., & Chiang, S. H. (2009) - An integrated model for predicting rainfall-induced landslides. *Geomorphology*. Elsevier B.V., 105(3–4), 366–373. doi: 10.1016/j.geomorph.2008.10.012.
- Chelli, A., Pappalardo, M., Llopis, I. A., & Federici, P. R. (2010) - The relative influence of lithology and weathering in shaping shore platforms along the coastline of the Gulf of La Spezia (NW Italy) as revealed by rock strength. *Geomorphology*. Elsevier B.V., 118(1–2), 93–104. doi: 10.1016/j.geomorph.2009.12.011.
- Chen, H. X., & Zhang, L. M. (2014) - A physically-based distributed cell model for predicting regional rainfall-induced shallow slope failures. *Engineering Geology*. Elsevier B.V., 176, 79–92. doi: 10.1016/j.enggeo.2014.04.011.
- Ching, J., Lin, G.-H., Chen, J.-R., & Phoon, K.-K. (2017) - Transformation models for effective friction angle and relative density calibrated based on generic database of coarse-grained soils. *Canadian Geotechnical Journal*. NRC Research Press, 54(4), 481–501.
- Ciarleto, M., Cascini, L., & Calvello, M. (2017) - A comparison of statistical and deterministic methods for shallow landslide susceptibility zoning in clayey soils. *Engineering Geology*. Elsevier, 223(April), 71–81. doi: 10.1016/j.enggeo.2017.04.023.
- Corominas, J., van Westen, C., Frattini, P., Cascini, L., Malet, J. P., Fotopoulou, S., Catani, F., Van Den Eeckhaut, M., Mavrouli, O., Agliardi, F., Pitilakis, K., Winter, M. G., Pastor, M., Ferlisi, S., Tofani, V., Hervás, J., & Smith, J. T. (2014) - Recommendations for the quantitative analysis of landslide risk. *Bulletin of Engineering Geology and the Environment*, 73(2), 209–263. doi: 10.1007/s10064-013-0538-8.
- Cruden, D. M. (1991) - A simple definition of a landslide. *Bulletin of the International Association of Engineering Geology - Bulletin de l'Association Internationale de Géologie de l'Ingénieur*, 43(1), 27–29. doi: 10.1007/BF02590167.
- Cruden, David M., & Varnes, D. J. (1996) - Landslide types and processes. Special Report - National Research Council, Transportation Research Board, 247(January 1996), 36–75.

- Cruden, David M, & Varnes, D. J. (1996) - Landslides, Investigation and Mitigation. Landslide types and processes Bussines Office. Washington, DC Transportation Research Board. Washington DC, USA, 36-75 p. Transportation research board special report, 247(February), 36–75.
- D’Addario, E., Trefolini, E., Mammoliti, E., Papasidero, M., & Disperati, L. (2018) - A new shallow landslides inventory for Southern Lunigiana (Tuscany, Italy) and analysis of predisposing factors. *Rend. Online Soc. Geol. It.*, 46, 149–154.
- D’Odorico, P. (2000) - A possible bistable evolution of soil thickness. *Journal of Geophysical Research: Solid Earth*. doi: 10.1029/2000jb900253.
- Deere, D. U., & Miller, R. P. (1966) - Engineering classification and index properties for intact rock. Report AWFL” FR—65416. Air Force Weapons Laboratory (WLDC) Kirtland Airforce base. New Mexico.
- Deng, Y. X., Wilson, J. P., & J. Sheng (2006) - Effects of Variable Attribute Weights on Landform Classification. *Earth Surface Processes and Landforms*, 31, 1452–1462. doi: 10.1002/esp.1401.
- DeWitt, J. D., Warner, T. A., Chirico, P. G., & Bergstresser, S. E. (2017) - Creating high-resolution bare-earth digital elevation models (DEMs) from stereo imagery in an area of densely vegetated deciduous forest using combinations of procedures designed for lidar point cloud filtering. *GIScience and Remote Sensing*. Taylor & Francis, 54(4), 552–572. doi: 10.1080/15481603.2017.1295514.
- Dietrich, W. E., Reiss, R., Hsu, M. -L, & Montgomery, D. R. (1995) - A process-based model for colluvial soil depth and shallow landsliding using digital elevation data. *Hydrological Processes*. doi: 10.1002/hyp.3360090311.
- Dietrich, W. E., Asua, R. R. de, Orr, J. C. B., & Trso, M. (1998) - A validation study of the shallow slope stability model, SHALSTAB, in forested lands of Northern California by Department of Geology and Geophysics University of California Berkeley, CA 94720 and Rafael Real de Asua Martin Trso Stillwater Ecosystem, W. *Land Use and Watersheds: Human Influence on Hydrology and Geomorphology in Urban and Forest Areas*, (June 1998), 59. doi: 10.1029/WS002p0195.
- Dikau, R. (1989) - The application of a digital relief model to landform analysis in geomorphology. Three dimensional applications in geographical information systems. Taylor & Francis London, 51–77.
- Disperati, L., Gregori, F., Perna, M., Manetti, F., Lavorini, G., & Villoresi, C. (2016) - Bi-temporal change analysis of satellite imagery to detect landslides triggered by intense rainfall events. *Rend. Soc. Geol. It. Rend. Soc. Geol. It.*, 39, 51–54.
- Disperati, L., Trefolini, E., D’Addario, E., Mammoliti, E., Papasidero, Michele Pio Vacca, V., & Viti, F. (2018) - Engineering geology characterization of slope deposits and physically-based assessment of shallow landslide susceptibility (Alpi. *Geophysical Research Abstracts*, 20, 19093.
- Donati, L., & Turrini, M. C. (2002) - An objective method to rank the importance of the factors

predisposing to landslides with the GIS methodology: Application to an area of the Apennines (Valnerina; Perugia, Italy). *Engineering Geology*, 63(3–4), 277–289. doi: 10.1016/S0013-7952(01)00087-4.

Drăguț, L., & Blaschke, T. (2006) - Automated classification of landform elements using object-based image analysis. *Geomorphology*, 81(3–4), 330–344. doi: 10.1016/j.geomorph.2006.04.013.

Duncan, J. M., Wright, S. G., & Brandon, T. L. (2014) *Soil strength and slope stability*. John Wiley & Sons.

Van Den Eeckhaut, M., Poesen, J., Govers, G., Verstraeten, G., & Demoulin, A. (2007) - Characteristics of the size distribution of recent and historical landslides in a populated hilly region. *Earth and Planetary Science Letters*. Elsevier, 256(3–4), 588–603. doi: 10.1016/j.epsl.2007.01.040.

Ehsani, A. H., Quiel, F., & Malekian, A. (2010) - Effect of SRTM resolution on morphometric feature identification using neural network-self organizing map. *GeoInformatica*, 14(4), 405–424. doi: 10.1007/s10707-009-0085-4.

Elter, P., Giglia, G., Trevisan, L., & Tongiorgi, M. (1975) - TENSIONAL AND COMPRESSIONAL AREAS IN THE RECENT (TORTONIAN TO PRESENT) EVOLUTION OF THE NORTHERN APENNINES.

ESRI (2013) - How Cluster and Outlier Analysis (Anselin Local Moran's I) works. Available at: <https://pro.arcgis.com/en/pro-app/tool-reference/spatial-statistics/h-how-cluster-and-outlier-analysis-anselin-local-m.htm>.

ESRI (2016) - How grouping analysis works. ArcGIS Pro | ArcGIS Deskt. <http://pro.arcgis.com/en/pro-app/tool-reference/spatial-statistics/how-grouping-analysis-works.htm>. Accessed, 7.

Evans, I. S. (1972) - General geomorphometry, derivatives of altitude, and descriptive statistics. *Spatial analysis in geomorphology*. Methuen, 17–90.

Evans, I. S. (2012) - Geomorphometry and landform mapping: What is a landform? *Geomorphology*. Elsevier B.V., 137(1), 94–106. doi: 10.1016/j.geomorph.2010.09.029.

Ewen, B. J., Parkin, G., & O'Connell, P. E. (2000) - Shetran : D Itributed R Iver B Asin F Low M Odelling S Ystem. *Journal of Hydrologic Engineering*, 5(JULY), 250–258.

Fannin, R. J., Eliadorani, A., & Wilkinson, J. M. T. (2005) - Shear strength of cohesionless soils at low stress. *Géotechnique*. Thomas Telford Ltd, 55(6), 467–478.

Farmer, I. W. (1983) - Discontinuities in Rock Masses. in *Engineering Behaviour of Rocks*. Dordrecht: Springer Netherlands, 143–167. doi: 10.1007/978-94-009-5978-1_6.

Fawcett, T. (2006) - An introduction to ROC analysis. *Pattern Recognition Letters*, 27(8), 861–874. doi: 10.1016/j.patrec.2005.10.010.

Fell, R., Corominas, J., Bonnard, C., Cascini, L., Leroi, E., & Savage, W. Z. (2008) - Guidelines for landslide susceptibility, hazard and risk zoning for land use planning. *Engineering Geology*. Elsevier

B.V., 102(3–4), 85–98. doi: 10.1016/j.enggeo.2008.03.022.

- Fener, M., Kahraman, S., Bilgil, A., & Gunaydin, O. (2005) - A comparative evaluation of indirect methods to estimate the compressive strength of rocks. *Rock Mechanics and Rock Engineering*, 38(4), 329–343. doi: 10.1007/s00603-005-0061-8.
- Ferrari, F. (2013) - Rock Mass Characterization and Spatial Estimation of Geomechanical Properties through Geostatistical Techniques, 233.
- Ferrari, F., Apuani, T., & Giani, G. P. (2014) - Rock Mass Rating spatial estimation by geostatistical analysis. *International Journal of Rock Mechanics and Mining Sciences*. Elsevier, 70, 162–176. doi: 10.1016/j.ijrmms.2014.04.016.
- Fisher, P., Wood, J., & Cheng, T. (2004) - Where is Helvellyn? Fuzziness of multi-scale landscape morphometry. *Transactions of the Institute of British Geographers*, 29(1), 106–128. doi: 10.1111/j.0020-2754.2004.00117.x.
- Florinsky, I. ., Eilers, R. ., Manning, G. ., & Fuller, L. . (2002) - Prediction of soil properties by digital terrain modelling. *Environmental Modelling & Software*, 17(3), 295–311. doi: 10.1016/S1364-8152(01)00067-6.
- Formetta, G., Capparelli, G., & Versace, P. (2016) - Evaluating performance of simplified physically based models for shallow landslide susceptibility. *Hydrology and Earth System Sciences*, 20(11), 4585–4603. doi: 10.5194/hess-20-4585-2016.
- Fowell, R. J., & McFeath Smith, I. (1976) - FACTORS INFLUENCING THE CUTTING PERFORMANCE OF A SELECTIVE TUNNELLING MACHINE.
- Fragaszy, R. J., Su, J., Siddiqi, F. H., & Ho, C. L. (1992) - Modeling strength of sandy gravel. *Journal of Geotechnical Engineering*. American Society of Civil Engineers, 118(6), 920–935.
- Francipane, A., Arnone, E., Lo Conti, F., Puglisi, C., & Noto, L. V. (2014) - A Comparison Between Heuristic, Statistical, And Data-Driven Methods In Landslide Susceptibility Assessment: An Application To The Briga And Giampileri Catchments. 11° International Conference on Hydroinformatics, 9. Available at: http://academicworks.cuny.edu/cc_conf_hic%0Ahttp://academicworks.cuny.edu/cc_conf_hic/ 150.
- Frattini, P., Crosta, G., Carrara, A., & Agliardi, F. (2008) - Assessment of rockfall susceptibility by integrating statistical and physically-based approaches. *Geomorphology*, 94(3–4), 419–437. doi: 10.1016/j.geomorph.2006.10.037.
- Frattini, P., & Crosta, G. B. (2013a) - The role of material properties and landscape morphology on landslide size distributions. *Earth and Planetary Science Letters*. Elsevier, 361, 310–319. doi: 10.1016/j.epsl.2012.10.029.
- Frattini, P., & Crosta, G. B. (2013b) - The role of material properties and landscape morphology on

- landslide size distributions. *Earth and Planetary Science Letters*. Elsevier, 361, 310–319. doi: 10.1016/j.epsl.2012.10.029.
- Galli, M., Ardizzone, F., Cardinali, M., Guzzetti, F., & Reichenbach, P. (2008) - Comparing landslide inventory maps. *Geomorphology*. doi: 10.1016/j.geomorph.2006.09.023.
- Gariano, S. L., & Guzzetti, F. (2016) - Landslides in a changing climate. *Earth-Science Reviews*. Elsevier, 162, 227–252. doi: 10.1016/j.earscirev.2016.08.011.
- Giannecchini, R., Galanti, Y., D'Amato Avanzi, G., & Barsanti, M. (2016) - Probabilistic rainfall thresholds for triggering debris flows in a human-modified landscape. *Geomorphology*, 257, 94–107. doi: 10.1016/j.geomorph.2015.12.012.
- Giannecchini, R., Galanti, Y., & D'Amato Avanzi, G. (2012) - Critical rainfall thresholds for triggering shallow landslides in the Serchio River Valley (Tuscany, Italy). *Natural Hazards and Earth System Science*. doi: 10.5194/nhess-12-829-2012.
- Giordan, D., Cignetti, M., Baldo, M., & Godone, D. (2017) - Relationship between man-made environment and slope stability: the case of 2014 rainfall events in the terraced landscape of the Liguria region (northwestern Italy). *Geomatics, Natural Hazards and Risk*. Taylor & Francis, 8(2), 1833–1852. doi: 10.1080/19475705.2017.1391129.
- Glaus, G., Delunel, R., Stutenbecker, L., Akçar, N., Christl, M., & Schlunegger, F. (2019) - Differential erosion and sediment fluxes in the Landquart basin and possible relationships to lithology and tectonic controls. *Swiss Journal of Geosciences*. Springer International Publishing, 112(2–3), 453–473. doi: 10.1007/s00015-019-00344-3.
- Goetz, J. N., Guthrie, R. H., & Brenning, A. (2011) - Integrating physical and empirical landslide susceptibility models using generalized additive models. *Geomorphology*. Elsevier B.V., 129(3–4), 376–386. doi: 10.1016/j.geomorph.2011.03.001.
- Goetz, J. N., Brenning, A., Petschko, H., & Leopold, P. (2015) - Evaluating machine learning and statistical prediction techniques for landslide susceptibility modeling. *Computers and Geosciences*. Elsevier, 81, 1–11. doi: 10.1016/j.cageo.2015.04.007.
- Goktan, R. M., & Ayday, C. (1993) - A suggested improvement to the Schmidt rebound hardness ISRM suggested method with particular reference to rock machineability. *INTERNATIONAL JOURNAL OF ROCK MECHANICS AND MINING & GEOMECHANICS ABSTRACTS*, 30(3).
- Gorsevski, P. V., Gessler, P. E., Boll, J., Elliot, W. J., & Foltz, R. B. (2006) - Spatially and temporally distributed modeling of landslide susceptibility. *Geomorphology*, 80(3–4), 178–198. doi: 10.1016/j.geomorph.2006.02.011.
- Goswami, R., Mitchell, N. C., & Brocklehurst, S. H. (2011) - Goswami et al., 2011, Distribution and causes of landslides in the eastern Peloritani of NE Sicily and western Aspromonte of SW Calabria,

Italy.pdf, 111–122.

- Goudie, A. S. (2004) *Encyclopedia of Geomorphology*. Routledge.
- Grelle, G., Revellino, P., Donnarumma, A., & Guadagno, F. M. (2011) - Bedding control on landslides : a methodological approach for computer-aided mapping analysis, 1395–1409. doi: 10.5194/nhess-11-1395-2011.
- Guimaraes, R. F., Montgomery, D. R., Greenberg, H. M., Fernandes, N. F., Gomes, R. A. T., & de Carvalho Junior, O. A. (2003) - Parameterization of soil properties for a model of topographic controls on shallow landsliding: Application to Rio de Janeiro. *Engineering Geology*, 69(1–2), 98–108. doi: 10.1016/S0013-7952(02)00263-6.
- Guth, P. L. (1995) - Slope and aspects calculations on gridded digital elevation models: examples from a geomorphometric toolbox for personal computers. *Zeitschrift für Geomorphologie. Supplementband*, (101), 31–52.
- Guthrie, R. H., & Evans, S. G. (2004) - Magnitude and frequency of landslides triggered by a storm event, Loughborough Inlet, British Columbia. *Natural Hazards and Earth System Science*, 4(3), 475–483. doi: 10.5194/nhess-4-475-2004.
- Guthrie, R. H., Deadman, P. J., Cabrera, A. R., & Evans, S. G. (2008) - Exploring the magnitude–frequency distribution: a cellular automata model for landslides. *Landslides*, 5(1), 151–159. doi: 10.1007/s10346-007-0104-1.
- Guzzetti, F., Mondini, A. C., Cardinali, M., Fiorucci, F., Santangelo, M., & Chang, K. T. (2012) - Landslide inventory maps: New tools for an old problem. *Earth-Science Reviews*. Elsevier B.V., 112(1–2), 42–66. doi: 10.1016/j.earscirev.2012.02.001.
- Guzzetti, F., Malamud, B. D., Turcotte, D. L., & Reichenbach, P. (2002) - Power-law correlations of landslide areas in central Italy. *Earth and Planetary Science Letters*, 195(3–4), 169–183. doi: 10.1016/S0012-821X(01)00589-1.
- Guzzetti, F., Ardizzone, F., Cardinali, M., Galli, M., Reichenbach, P., & Rossi, M. (2008) - Distribution of landslides in the Upper Tiber River basin, central Italy. *Geomorphology*, 96(1–2), 105–122. doi: 10.1016/j.geomorph.2007.07.015.
- Hack, R. (1997) - Rock mass strength by rock mass classification, (September), 346–356.
- Hanley, J. A., & McNeil, B. J. (1982) - The meaning and use of the area under a receiver operating characteristic (ROC) curve. *Radiology*, 143(1), 29–36.
- Haque, U., Blum, P., da Silva, P. F., Andersen, P., Pilz, J., Chalov, S. R., Malet, J. P., Auflič, M. J., Andres, N., Poyiadji, E., Lamas, P. C., Zhang, W., Peshevski, I., Pétursson, H. G., Kurt, T., Dobrev, N., García-Davalillo, J. C., Halkia, M., Ferri, S., Gaprindashvili, G., Engström, J., & Keellings, D. (2016) - Fatal landslides in Europe. *Landslides*, 13(6), 1545–1554. doi: 10.1007/s10346-016-0689-3.
- Haramy, K. Y., & DeMarco, M. J. (1985) - Use of the Schmidt hammer for rock and coal testing. in *The*

26th US Symposium on Rock Mechanics (USRMS).

- Head, K. H., & Epps, R. J. (1980) Manual of soil laboratory testing. Pentech Press London.
- Hebib, R., Belhai, D., & Alloul, B. (2017) - Estimation of uniaxial compressive strength of North Algeria sedimentary rocks using density, porosity, and Schmidt hardness. *Arabian Journal of Geosciences*. *Arabian Journal of Geosciences*, 10(17), 1–13. doi: 10.1007/s12517-017-3144-4.
- Heckman, K., & Rasmussen, C. (2011) - Lithologic controls on regolith weathering and mass flux in forested ecosystems of the southwestern USA. *Geoderma*. Elsevier B.V., 164(3–4), 99–111. doi: 10.1016/j.geoderma.2011.05.003.
- Hoek, E. (1994) - Strength of rock and rock masse. *NEWS JOURNAL OF INTERNATIONAL SOCIETY FOR ROCK MECHANICS*.
- Hoek, E. (2000) - Practical Rock Engineering, (1), 341. doi: 10.1007/s13398-014-0173-7.2.
- Hoek, E., & Brown, E. T. (1997) - Practical estimates of rock mass strength. *International Journal of Rock Mechanics and Mining Sciences*, 34(8), 1165–1186. doi: 10.7873/date2014.002.
- Hoek, E., & Brown, E. T. (2019) - The Hoek–Brown failure criterion and GSI – 2018 edition. *Journal of Rock Mechanics and Geotechnical Engineering*. Elsevier Ltd, 11(3), 445–463. doi: 10.1016/j.jrmge.2018.08.001.
- Hoek, E., Carranza-Torres, C., & Corkum, B. (2002) - Hoek-Brown failure criterion - 2002 Edition. *Proc. NARMS-TAC Conference, Toronto*, 1, 267–273.
- Hoek, E., Kaiser, P. K., & Bawden, W. F. (1995) - Support of underground excavations in hard rock. Rotterdam, Netherlands: AA Balkema Publishers.
- Holtz, W. G. (1961) Triaxial shear characteristics of clayey gravel soils. US Bureau of Reclamation.
- Hovius, N., Stark, C. P., & Allen, P. A. (1997) - Sediment flux from a mountain belt derived by landslide mapping. *Geology*, 25(3), 231–234. doi: 10.1130/0091-7613(1997)025<0231:SFFAMB>2.3.CO;2.
- Huang, C., Davis, L. S., & Townshend, J. R. G. (2002) - An assessment of support vector machines for land cover classification. *International Journal of Remote Sensing*. Taylor & Francis, 23(4), 725–749. doi: 10.1080/01431160110040323.
- Huang, C., Byrne, T. B., Ouimet, W. B., Lin, C. W., Hu, J. C., Fei, L. Y., & Wang, Y. B. (2016) - Tectonic foliations and the distribution of landslides in the southern Central Range, Taiwan. *Tectonophysics*. Elsevier B.V., 692, 203–212. doi: 10.1016/j.tecto.2016.06.004.
- Hungr, O., Leroueil, S., & Picarelli, L. (2014) - The Varnes classification of landslide types, an update. *Landslides*, 11(2), 167–194. doi: 10.1007/s10346-013-0436-y.
- Hurst, M. D., Ellis, M. A., Royse, K. R., Lee, K. A., & Freeborough, K. (2013) - Controls on the magnitude-frequency scaling of an inventory of secular landslides. *Earth Surface Dynamics*, 1(1), 67–78. doi: 10.5194/esurf-1-67-2013.
- Hurst, M. D., Mudd, S. M., Yoo, K., Attal, M., & Walcott, R. (2013) - Influence of lithology on hillslope

- morphology and response to tectonic forcing in the northern Sierra Nevada of California. *Journal of Geophysical Research: Earth Surface*, 118(2), 832–851. doi: 10.1002/jgrf.20049.
- Irvin, B. J., Ventura, S. J., & Slater, B. K. (1997) - Fuzzy and isodata classification of landform elements from digital terrain data in Pleasant Valley, Wisconsin. *Geoderma*, 77(2–4), 137–154. doi: 10.1016/S0016-7061(97)00019-0.
- ISRM (1978) - Suggested methods for determining hardness and abrasiveness of rocks. in.
- ISRM (2007) *The complete ISRM suggested methods for rock characterization, testing and monitoring: 1974-2006*. International Soc. for Rock Mechanics, Commission on Testing Methods.
- IUGS-International Working Group (1995) - A suggested method for describing the rate of movement of a landslide. *Bulletin of the International Association of Engineering Geology*, 52(1), 75–78. doi: 10.1007/BF02602683.
- Iwahashi, J., & Pike, R. J. (2007) - Automated classifications of topography from DEMs by an unsupervised nested-means algorithm and a three-part geometric signature. *Geomorphology*, 86(3–4), 409–440. doi: 10.1016/j.geomorph.2006.09.012.
- Jaboyedoff, M., Crosta, G. B., & Stead, D. (2011) - *Slope tectonics: a short introduction*. Geological Society, London, Special Publications, 351(1), 1–10. doi: 10.1144/sp351.1.
- Jaboyedoff, M., Oppikofer, T., Abellán, A., Derron, M. H., Loye, A., Metzger, R., & Pedrazzini, A. (2012) - Use of LIDAR in landslide investigations: A review. *Natural Hazards*, 61(1), 5–28. doi: 10.1007/s11069-010-9634-2.
- Jenness, J. (2006) - *Topographic Position Index (tpi_jen. avx) extension for ArcView 3. x, v. 1.3 a*. Jenness Enterprises.
- Johnson, B. L., & Johnston, C. A. (1995) - Relationship of Lithology and Geomorphology to Erosion of the Western Lake Superior Coast. *Journal of Great Lakes Research*, 21(1), 3–16. doi: [https://doi.org/10.1016/S0380-1330\(95\)71016-4](https://doi.org/10.1016/S0380-1330(95)71016-4).
- Joyce, K. E., Belliss, S. E., Samsonov, S. V., McNeill, S. J., & Glassey, P. J. (2009) - A review of the status of satellite remote sensing and image processing techniques for mapping natural hazards and disasters. *Progress in Physical Geography*. SAGE PublicationsSage UK: London, England, 33(2), 183–207. doi: 10.1177/0309133309339563.
- Kaewkongkaew, K., Phien-wej, N., & Kham-ai, D. (2015) - Prediction of rock mass along tunnels by geostatistics. *KSCE Journal of Civil Engineering*, 19(1), 81–90. doi: 10.1007/s12205-014-0505-3.
- Karaman, K., & Kesimal, A. (2015) - A comparative study of Schmidt hammer test methods for estimating the uniaxial compressive strength of rocks. *Bulletin of Engineering Geology and the Environment*. Springer Berlin Heidelberg, 74(2), 507–520. doi: 10.1007/s10064-014-0617-5.
- Karaman, S., Fener, M., & Gunaydin, O. (2002) - Predicting the Schmidt hammer values of in-situ intact rock from core sample values. *International Journal of Rock Mechanics and Mining Sciences*, 39(3),

395–399. doi: 10.1016/S1365-1609(02)00028-X.

- Kato, T. (2016) - Prediction of photovoltaic power generation output and network operation. in *Integration of Distributed Energy Resources in Power Systems*. Elsevier, 77–108.
- Katz, O., Reches, Z., & Roegiers, J.-C. (2000) - Evaluation of mechanical rock properties using a Schmidt Hammer. *International Journal of Rock Mechanics and Mining Sciences*, 37, 723–728.
- Kazi, A., & Al-Mansour, Z. R. (1980) - Empirical relationship between Los Angeles abrasion and Schmidt hammer strength tests with application to aggregates around Jeddah. *Quarterly Journal of Engineering Geology and Hydrogeology*. Geological Society of London, 13(1), 45–52.
- Kenney, T. C. (1959) - Geotechnical properties of glacial lake clays. *Journal of the Soil Mechanics and Foundations Division*, 84(3), 67–79.
- Kim, M. S., Onda, Y., Uchida, T., & Kim, J. K. (2016) - Effects of soil depth and subsurface flow along the subsurface topography on shallow landslide predictions at the site of a small granitic hillslope. *Geomorphology*. Elsevier B.V., 271, 40–54. doi: 10.1016/j.geomorph.2016.07.031.
- Kim, M. S., Onda, Y., Kim, J. K., & Kim, S. W. (2015) - Effect of topography and soil parameterisation representing soil thicknesses on shallow landslide modelling. *Quaternary International*. Elsevier Ltd, 384, 91–106. doi: 10.1016/j.quaint.2015.03.057.
- Kirby, E., & Whipple, K. X. (2012) - Expression of active tectonics in erosional landscapes. *Journal of Structural Geology*. Elsevier Ltd, 44, 54–75. doi: 10.1016/j.jsg.2012.07.009.
- Kılıç, A., & Teymen, A. (2008) - Determination of mechanical properties of rocks using simple methods. *Bulletin of Engineering Geology and the Environment*, 67(2), 237–244. doi: 10.1007/s10064-008-0128-3.
- Kohonen, T. (2012) *Self-organizing maps*. Springer Science & Business Media.
- Kolaiti, E., & Papadopoulos, Z. (1994) - Evaluation of Schmidt rebound hammer testing: a critical approach. *International Journal of Rock Mechanics and Mining Sciences & Geomechanics Abstracts*, 31(4), 182. doi: 10.1016/0148-9062(94)90970-9.
- Kong, F., & Shang, J. (2018) - A Validation Study for the Estimation of Uniaxial Compressive Strength Based on Index Tests. *Rock Mechanics and Rock Engineering*. Springer Vienna, 51(7), 2289–2297. doi: 10.1007/s00603-018-1462-9.
- Kruskal, J. B. (1956) - On the shortest spanning subtree of a graph and the traveling salesman problem. *Proceedings of the American Mathematical society*. JSTOR, 7(1), 48–50.
- Kühni, A., & Pfiffner, O. A. (2001) - The relief of the Swiss Alps and adjacent areas and its relation to lithology and structure: Topographic analysis from a 250-m DEM. *Geomorphology*, 41(4), 285–307. doi: 10.1016/S0169-555X(01)00060-5.
- Kulhawy, F. H., & Chen, J.-R. (2007) - Discussion of ‘Drilled Shaft Side Friction in Gravelly Soils’ by Kyle M. Rollins, Robert J. Clayton, Rodney C. Mikesell, and Bradford C. Blaise. *Journal of*

- Geotechnical and Geoenvironmental Engineering. American Society of Civil Engineers, 133(10), 1325–1328.
- Kuriakose, S. L., van Beek, L. P. H., & van Westen, C. J. (2009) - Parameterizing a physically based shallow landslide model in a data poor region. *Earth Surface Processes and Landforms*, 34(6), 867–881. doi: 10.1002/esp.1794.
- Kuriakose, S. L., Devkota, S., Rossiter, D. G., & Jetten, V. G. (2009) - Prediction of soil depth using environmental variables in an anthropogenic landscape, a case study in the Western Ghats of Kerala, India. *Catena*. Elsevier B.V., 79(1), 27–38. doi: 10.1016/j.catena.2009.05.005.
- Lambe, T. W., & Whitman, R. V (1991) *Soil mechanics*. John Wiley & Sons.
- Lancellotta, R. (2001) *Geotecnica*. Zanichelli.
- Lanni, C., Borga, M., Rigon, R., & Tarolli, P. (2012) - Modelling shallow landslide susceptibility by means of a subsurface flow path connectivity index and estimates of soil depth spatial distribution. *Hydrology and Earth System Sciences*, 16(11), 3959–3971. doi: 10.5194/hess-16-3959-2012.
- Lavorini, G., Villoresi, C., Bottai, L., Perna, M., Manetti, F., Capecchi, V., Betti, G., Bartolini, G., Crisci, A., & Corongiu, M. (2015) - Analisi dei dissesti associati ad alcuni fenomeni di precipitazione intensa in Toscana attraverso l'analisi di immagini satellitari multi-spettrali. *Il Geologo*, n.98/2015.
- Leopold, M., & Völkel, J. (2007) - Colluvium: Definition, differentiation, and possible suitability for reconstructing Holocene climate data. *Quaternary International*, 162–163, 133–140. doi: 10.1016/j.quaint.2006.10.030.
- Lezzerini, M., Franzini, M., Di Battistini, G., & Zucchi, D. (2008) - The «macigno» sandstone from Matraia and Pian di Lanzola quarries (north-western Tuscany, Italy). A comparison of physical and mechanical properties. *Atti della Società Toscana di Scienze Naturali, Memorie Serie A*, 113, 71–79.
- Li, L., Lan, H., & Wu, Y. (2016) - How sample size can effect landslide size distribution. *Geoenvironmental Disasters*. *Geoenvironmental Disasters*, 3(1), 18. doi: 10.1186/s40677-016-0052-y.
- Li, Z., Shi, W., Myint, S. W., Lu, P., & Wang, Q. (2016) - Semi-automated landslide inventory mapping from bitemporal aerial photographs using change detection and level set method. *Remote Sensing of Environment*. Elsevier Inc., 175, 215–230. doi: 10.1016/j.rse.2016.01.003.
- Liu, A., & Tang, G. (2006) - DEM based auto-classification of Chinese landform. *Geo-Information Science*, 4.
- Liu, C. N., & Wu, C. C. (2008) - Mapping susceptibility of rainfall-triggered shallow landslides using a probabilistic approach. *Environmental Geology*, 55(4), 907–915. doi: 10.1007/s00254-007-1042-x.
- Lu, N., & Godt, J. W. (2011) *Hillslope hydrology and stability*. Hillslope Hydrology and Stability. Cambridge University Press. doi: 10.1017/CBO9781139108164.
- MacMillan, R. A., & Shary, P. A. (2009) - Landforms and landform elements in geomorphometry.

- Developments in Soil Science, 33(C), 227–254. doi: 10.1016/S0166-2481(08)00009-3.
- Malamud, B. D., Turcotte, D. L., Guzzetti, F., & Reichenbach, P. (2004) - Landslide inventories and their statistical properties. *Earth Surface Processes and Landforms*, 29(6), 687–711. doi: 10.1002/esp.1064.
- Mammoliti, E. (2020) A new approach for engineering geological mapping of subsurface rock masses by means of fieldwork-based rebound hardness indexes and non-parametric Bayesian networks. University of Siena.
- Mangai, U. G., Samanta, S., Das, S., & Chowdhury, P. R. (2010) - The Institution of Electronics and Telecommunication Engineers A Survey of Decision Fusion and Feature Fusion Strategies for Pattern Classification, 27(4). Available at: www.ietejournals.org.
- Maracchi, G., Genesio, L., Magno, R., Ferrari, R., Crisci, A., & Bottai, L. (2005) - I diagrammi del clima in Toscana. Programma Interreg Iii B-Medoc-Asse, 4.
- Marchesini, I., Santangelo, M., Guzzetti, F., Cardinali, M., & Bucci, F. (2015) - Modeling Morpho-Structural Settings Exploiting Bedding Data Obtained Through the Interpretation of Stereoscopic Aerial Photographs. *Geotechnical Safety and Risk V*, 797–802. doi: 10.3233/978-1-61499-580-7-797.
- Marin, R. J., & Mattos, Á. J. (2019) - Physically-based landslide susceptibility analysis using Monte Carlo simulation in a tropical mountain basin. *Georisk*. Taylor & Francis, 0(0), 1–14. doi: 10.1080/17499518.2019.1633582.
- Marinos, P., & Hoek, E. (2000) - GSI: a geologically friendly tool for rock mass strength estimation. in ISRM international symposium.
- Marinos, P., & Hoek, E. (2001) - Estimating the geotechnical properties of heterogeneous rock masses such as flysch. *Bulletin of Engineering Geology and the Environment*, 60(2), 85–92. doi: 10.1007/s100640000090.
- Marinos, V. (2019) - A revised, geotechnical classification GSI system for tectonically disturbed heterogeneous rock masses, such as flysch. *Bulletin of Engineering Geology and the Environment*. *Bulletin of Engineering Geology and the Environment*, 78(2), 899–912. doi: 10.1007/s10064-017-1151-z.
- Martha, T. R., Kerle, N., van Westen, C. J., Jetten, V., & Vinod Kumar, K. (2012) - Object-oriented analysis of multi-temporal panchromatic images for creation of historical landslide inventories. *ISPRS Journal of Photogrammetry and Remote Sensing*. International Society for Photogrammetry and Remote Sensing, Inc. (ISPRS), 67(1), 105–119. doi: 10.1016/j.isprsjprs.2011.11.004.
- Marzini, L., D'Addario, E., Disperati, L., & Chianucci, F. (2019) - Relationships between vegetation cover characters and shallow landslides. in *Geophysical Research Abstracts*.
- Meisina, C., & Scarabelli, S. (2007) - A comparative analysis of terrain stability models for predicting

- shallow landslides in colluvial soils. *Geomorphology*, 87(3), 207–223. doi: 10.1016/j.geomorph.2006.03.039.
- Melesse, A. M., & Jordan, J. D. (2002) - A comparison of fuzzy vs. augmented-ISODATA classification algorithms for cloud-shadow discrimination from Landsat images. *Photogrammetric Engineering and Remote Sensing*, 68(9), 905–911.
- Michel, G. P., Kobiyama, M., & Goerl, R. F. (2014) - Comparative analysis of SHALSTAB and SINMAP for landslide susceptibility mapping in the Cunha River basin, southern Brazil. *Journal of Soils and Sediments*, 14(7), 1266–1277. doi: 10.1007/s11368-014-0886-4.
- Migoń, P., Jancewicz, K., Różycka, M., Duszyński, F., & Kasprzak, M. (2017) - Large-scale slope remodelling by landslides – Geomorphic diversity and geological controls, Kamienne Mts., Central Europe. *Geomorphology*, 289, 134–151. doi: 10.1016/j.geomorph.2016.09.037.
- Milledge, D. G., Bellugi, D., McKean, J. A., Densmore, A. L., & Dietrich, W. E. (2014) - A multidimensional stability model for predicting shallow landslide size and shape across landscapes. *Journal of Geophysical Research F: Earth Surface*. doi: 10.1002/2014JF003135.
- Miller, B. A., & Juilleret, J. (2020) - The colluvium and alluvium problem: Historical review and current state of definitions. *Earth-Science Reviews*. Elsevier, 209(November 2019), 103316. doi: 10.1016/j.earscirev.2020.103316.
- Mishra, D. A., & Basu, A. (2013) - Estimation of uniaxial compressive strength of rock materials by index tests using regression analysis and fuzzy inference system. *Engineering Geology*. Elsevier B.V., 160, 54–68. doi: 10.1016/j.enggeo.2013.04.004.
- Mitchell, A. (2005) - *The ESRI Guide to GIS Analysis (Volume 2)*. Redlands, CA: Esri Press.
- Mokarram, M., & Sathyamoorthy, D. (2018) - A review of landform classification methods. *Spatial Information Research*. Springer Singapore, 26(6), 647–660. doi: 10.1007/s41324-018-0209-8.
- Mokarram, M., Seif, A., & Sathyamoorthy, D. (2015) - Landform classification via fuzzy classification of morphometric parameters computed from digital elevation models: case study on Zagros Mountains. *Arabian Journal of Geosciences*, 8(7), 4921–4937. doi: 10.1007/s12517-014-1556-y.
- Montgomery, David R., & Dietrich, W. E. (1994) - A physically based model for the topographic control on shallow landsliding. *Water Resources Research*, 30(4), 1153–1171. doi: 10.1029/93WR02979.
- Montgomery, D R, & Dietrich, W. E. (1994) - A physically based model for the topographical control on shallow landsliding. *Water Resources Research*, 30(4), 1153–1171. doi: 10.1029/93WR02979.
- Montgomery, D. R., Sullivan, K., & Greenberg, H. M. (1998) - Regional test of a model for shallow landsliding, 955(November 1997).
- Moomivand, H. (2011) - Development of a New Method for Estimating the Indirect Uniaxial Compressive Strength of Rock Using Schmidt Hammer. *BHM Berg-und Hüttenmännische Monatshefte*, 156(4), 142–146. doi: 10.1007/ s00501-011-0644-5.

- Moran, P. A. P. (1948) - The interpretation of statistical maps. *Journal of the Royal Statistical Society. Series B (Methodological)*. JSTOR, 10(2), 243–251.
- Mudd, S. M., & Furbish, D. J. (2004) - Influence of chemical denudation on hillslope morphology. *Journal of Geophysical Research: Earth Surface*, 109(F2), n/a-n/a. doi: 10.1029/2003jf000087.
- Di Naccio, D., Boncio, P., Brozzetti, F., Pazzaglia, F. J., & Lavecchia, G. (2013) - Morphotectonic analysis of the Lunigiana and Garfagnana grabens (northern Apennines, Italy): Implications for active normal faulting. *Geomorphology*. Elsevier B.V., 201, 293–311. doi: 10.1016/j.geomorph.2013.07.003.
- NAVFAC, D. M. (1986) *Soil Mechanics, Design Manual*.
- Nicótina, L., Tarboton, D. G., Tesfa, T. K., & Rinaldo, A. (2011) - Hydrologic controls on equilibrium soil depths. *Water Resources Research*, 47(4), 1–11. doi: 10.1029/2010WR009538.
- Niemann, K. O., & Howes, D. E. (1991) - Applicability of digital terrain models for slope stability assessment. *ITC Journal*, 1991–3, 127–137. Available at: <https://www.scopus.com/inward/record.uri?eid=2-s2.0-0009563260&partnerID=40&md5=b2ba3f6da0eb56fc626d8deaae142842>.
- Nsangou Ngapna, M., Owona, S., Mvondo Owono, F., Mpesse, J. E., Youmen, D., Lissom, J., Mvondo Ondo, J., & Ekodeck, G. E. (2018) - Tectonics, lithology and climate controls of morphometric parameters of the Edea - Eseka region (SW Cameroon, Central Africa): Implications on equatorial rivers and landforms. *Journal of African Earth Sciences*, 138, 219–232. doi: 10.1016/j.jafrearsci.2017.11.008.
- O’Loughlin, E. M. (1986) - Prediction of Surface Saturation Zones in Natural Catchments by Topographic Analysis. *Water Resources*, 22(5), 794–804.
- Oliveira, S. C., Zêzere, J. L., Lajas, S., & Melo, R. (2016) - Combination of empirically-based and physically-based methods to assess shallow slides susceptibility at the basin scale. *Natural Hazards and Earth System Sciences Discussions*, (December), 1–37. doi: 10.5194/nhess-2016-381.
- Oliveira, S. C., Zêzere, J. L., Lajas, S., & Melo, R. (2017) - Combination of statistical and physically based methods to assess shallow slide susceptibility at the basin scale. *Natural Hazards and Earth System Sciences*, 17(7), 1091–1109. doi: 10.5194/nhess-17-1091-2017.
- Pack, R. T. ., Tarboton, D. G. ., & Goodwin, C. N. (1998) - The SINMAP Approach to Terrain Stability Mapping. 8th Congress of the International Association of Engineering Geology, 8.
- Palmstrom, A. (1982) - The volumetric joint count—a useful and simple measure of the degree of rock mass jointing. in *International Association of Engineering Geology. International congress. 4*, 221–228.
- Palmstrøm, A. (1996) - Characterizing rock masses by the R_{Mi} for use in practical rock engineering: Part 1: The development of the Rock Mass index (R_{Mi}). *Tunnelling and underground space technology*.

Elsevier, 11(2), 175–188.

- Papasidero, M. P. (2019) Caratterizzazione , modellazione predittiva e studio della variabilità locale e regionale delle proprietà idrologiche dei depositi di versante. University of Siena.
- Park, D. W., Nikhil, N. V., & Lee, S. R. (2013) - Landslide and debris flow susceptibility zonation using TRIGRS for the 2011 Seoul landslide event. *Natural Hazards and Earth System Sciences*, 13(11), 2833–2849. doi: 10.5194/nhess-13-2833-2013.
- Park, H. J., Lee, J. H., & Woo, I. (2013) - Assessment of rainfall-induced shallow landslide susceptibility using a GIS-based probabilistic approach. *Engineering Geology*. Elsevier B.V., 161, 1–15. doi: 10.1016/j.enggeo.2013.04.011.
- Pelletier, J. D. (1997) - Scale-invariance of soil moisture variability and its implications for the frequency-size distribution of landslides, 48. doi: 10.1016/S0013-7952(97)00041-0.
- Pelletier, J. D., & Rasmussen, C. (2009) - Geomorphically based predictive mapping of soil thickness in upland watersheds. *Water Resources Research*, 45(9). doi: 10.1029/2008WR007319.
- Pham, B. T., Pradhan, B., Tien Bui, D., Prakash, I., & Dholakia, M. B. (2016) - A comparative study of different machine learning methods for landslide susceptibility assessment: A case study of Uttarakhand area (India). *Environmental Modelling and Software*. Elsevier Ltd, 84, 240–250. doi: 10.1016/j.envsoft.2016.07.005.
- Pinheiro, M., Vallejos, J., Miranda, T., & Emery, X. (2016) - Geostatistical simulation to map the spatial heterogeneity of geomechanical parameters: A case study with rock mass rating. *Engineering Geology*. Elsevier B.V., 205, 93–103. doi: 10.1016/j.enggeo.2016.03.003.
- Plank, S., & Martinis, S. (2016) - Landslide Mapping in Vegetated Areas Using Change Detection Based on Optical and Polarimetric SAR Data. doi: 10.3390/rs8040307.
- Pradhan, A. M. S., & Kim, Y. T. (2016) - Evaluation of a combined spatial multi-criteria evaluation model and deterministic model for landslide susceptibility mapping. *Catena*. Elsevier B.V., 140, 125–139. doi: 10.1016/j.catena.2016.01.022.
- Priest, S. D. (2005) - Determination of shear strength and three-dimensional yield strength for the Hoek-Brown criterion. *Rock Mechanics and Rock Engineering*, 38(4), 299–327. doi: 10.1007/s00603-005-0056-5.
- Prim, R. C. (1957) - Shortest connection networks and some generalizations. *The Bell System Technical Journal*. Nokia Bell Labs, 36(6), 1389–1401.
- Raia, S., Alvioli, M., Rossi, M., Baum, R. L., Godt, J. W., & Guzzetti, F. (2014) - Improving predictive power of physically based rainfall-induced shallow landslide models: A probabilistic approach. *Geoscientific Model Development*, 7(2), 495–514. doi: 10.5194/gmd-7-495-2014.
- Regmi, A. D., Devkota, K. C., Yoshida, K., Pradhan, B., Pourghasemi, H. R., Kumamoto, T., & Akgun, A. (2014) - Application of frequency ratio, statistical index, and weights-of-evidence models and

- their comparison in landslide susceptibility mapping in Central Nepal Himalaya. *Arabian Journal of Geosciences*. Springer, 7(2), 725–742. doi: 10.1007/s12517-012-0807-z.
- Reichenbach, P., Rossi, M., Malamud, B. D., Mihir, M., & Guzzetti, F. (2018) - A review of statistically-based landslide susceptibility models. *Earth-Science Reviews*. Elsevier, 180(March), 60–91. doi: 10.1016/j.earscirev.2018.03.001.
- Rib, H. T., & Liang, T. (1978) - Recognition and identification. *Transportation Research Board Special Report*, (176).
- Roberts, B. D. W., Dowling, T. I., & Walker, J. (1997) - FLAG : A Fuzzy Landscape Analysis GIS Method for Dryland Salinity Assessment, (8), 1–23.
- Roering, J. J., Schmidt, K. M., Stock, J. D., Dietrich, W. E., & Montgomery, D. R. (2003) - Shallow landsliding, root reinforcement, and the spatial distribution of trees in the Oregon Coast Range.
- Rollins, K. M., Clayton, R. J., Mikesell, R. C., & Blaise, B. C. (2005) - Drilled shaft side friction in gravelly soils. *Journal of Geotechnical and Geoenvironmental Engineering*. American Society of Civil Engineers, 131(8), 987–1003.
- Saco, P. M., Willgoose, G. R., & Hancock, G. R. (2006) - Spatial organization of soil depths using a landform evolution model. *Journal of Geophysical Research: Earth Surface*, 111(2). doi: 10.1029/2005JF000351.
- Salciarini, D., Godt, J. W., Savage, W. Z., Conversini, P., Baum, R. L., & Michael, J. A. (2006) - Modeling regional initiation of rainfall-induced shallow landslides in the eastern Umbria Region of central Italy. *Landslides*, 3(3), 181–194. doi: 10.1007/s10346-006-0037-0.
- Schmertmann, J. H. (1978) *Guidelines for cone penetration test: performance and design*.
- Schmidt, J., & Hewitt, A. (2004) - Fuzzy land element classification from DTMs based on geometry and terrain position. *Geoderma*, 121(3–4), 243–256. doi: 10.1016/j.geoderma.2003.10.008.
- Schulz, W. H., Lidke, D. J., & Godt, J. W. (2009) - Modeling the spatial distribution of landslide-prone colluvium and shallow groundwater on hillslopes of Seattle, WA. *Earth Surface Processes and Landforms*, 34(March), 123–141. doi: 10.1002/esp.
- Schwarz, M., Preti, F., Giadrossich, F., Lehmann, P., & Or, D. (2010) - Quantifying the role of vegetation in slope stability : A case study in Tuscany (Italy), 36, 285–291. doi: 10.1016/j.ecoleng.2009.06.014.
- Scott, K. M., & Pain, C. F. (2008) *Regolith Science*. Springer Netherlands.
- Segoni, S., Rossi, G., & Catani, F. (2012) - Improving basin scale shallow landslide modelling using reliable soil thickness maps. *Natural Hazards*, 61(1), 85–101. doi: 10.1007/s11069-011-9770-3.
- Seibert, J., Stendahl, J., & Sørensen, R. (2007) - Topographical influences on soil properties in boreal forests. *Geoderma*, 141(1–2), 139–148. doi: 10.1016/j.geoderma.2007.05.013.
- Selçuk, L., & Yabalak, E. (2015) - Evaluation of the ratio between uniaxial compressive strength and Schmidt hammer rebound number and its effectiveness in predicting rock strength. *Nondestructive*

- Testing and Evaluation. Taylor & Francis, 30(1), 1–12. doi: 10.1080/10589759.2014.977789.
- Shalabi, F. I., Cording, E. J., & Al-hattamleh, O. H. (2007) - Estimation of rock engineering properties using hardness tests, 90, 138–147. doi: 10.1016/j.enggeo.2006.12.006.
- Sharpe, C. F. S. (1938) - Landslides and Related Phenomena. Geografiska Annaler. Columbia University Press, 20, 325. doi: 10.2307/520061.
- Shen, J., Priest, S. D., & Karakus, M. (2012) - Determination of Mohr-Coulomb shear strength parameters from generalized Hoek-Brown criterion for slope stability analysis. Rock Mechanics and Rock Engineering, 45(1), 123–129. doi: 10.1007/s00603-011-0184-z.
- Shokri, S., Shademan, M., Rezvani, M., Javankhoshdel, S., Cami, B., & Yacoub, T. (2020) - A review study about spatial correlation measurement in rock mass. Rock Mechanics for Natural Resources and Infrastructure Development- Proceedings of the 14th International Congress on Rock Mechanics and Rock Engineering, ISRM 2019, 360–366.
- Simoni, S., Zanotti, F., Bertoldi, G., & Rigon, R. (2008) - Modelling the probability of occurrence of shallow landslides and channelized debris flows using GEOtop-FS. Hydrological Processes. doi: 10.1002/hyp.6886.
- Sjöberg, J. (1997) Estimating rock mass strength using the Hoek-Brown failure criterion and rock mass classification - A review and application to the Aznalcollar open pit.
- Skempton, A. W., & Delory, F. A. (1984) - Stability of Natural Slopes in London Clay. in Selected Papers on Soil Mechanics, 70–73. doi: 10.1680/sposm.02050.0011.
- Soiltest Inc. (1976) - Operating instructions--concrete test hammer. Soiltest Inc. Evanston, IL.
- Sorensen, K. K., & Okkels, N. (2013) - Correlation between drained shear strength and plasticity index of undisturbed overconsolidated clays. 18th International Conference on Soil Mechanics and Geotechnical Engineering: Challenges and Innovations in Geotechnics, ICSMGE 2013, 1(1957), 423–428.
- Stark, C., & Hovius, N. (2001) - The characterization of landslide size distributions. Geophysical Research Letters, 28(6), 1091–1094.
- Stark, C. P., & Guzzetti, F. (2009a) - Landslide rupture and the probability distribution of mobilized debris volumes. Journal of Geophysical Research: Earth Surface. Blackwell Publishing Ltd, 114(2), 1–16. doi: 10.1029/2008JF001008.
- Stark, C. P., & Guzzetti, F. (2009b) - Landslide rupture and the probability distribution of mobilized debris volumes. Journal of Geophysical Research: Earth Surface, 114(2), 1–16. doi: 10.1029/2008JF001008.
- Stark, C. P., & Hovius, N. (2001) - The characterization of landslide size distributions. Geophysical Research Letters, 28(6), 1091–1094. doi: 10.1029/2000GL008527.
- Stead, D., & Wolter, A. (2015) - A critical review of rock slope failure mechanisms: The importance of

- structural geology. *Journal of Structural Geology*. Elsevier Ltd, 74, 1–23. doi: 10.1016/j.jsg.2015.02.002.
- Stepinski, T. F., Ghosh, S., & Vilalta, R. (2006) - Automatic Recognition of Landforms on Mars Using Terrain Segmentation and Classification. in Todorovski, L., Lavrač, N., and Jantke, K. P. (eds) *Discovery Science*. Berlin, Heidelberg: Springer Berlin Heidelberg, 255–266.
- Summerell, G. K., Vaze, J., Tuteja, N. K., Grayson, R. B., Beale, G., & Dowling, T. I. (2005) - Delineating the major landforms of catchments using an objective hydrological terrain analysis method. *Water Resources Research*, 41(12), 1–12. doi: 10.1029/2005WR004013.
- Sumner, P., & Nel, W. (2002) - The effect of rock moisture on Schmidt hammer rebound: Tests on rock samples from Marion Island and South Africa. *Earth Surface Processes and Landforms*, 27(10), 1137–1142. doi: 10.1002/esp.402.
- Szypuła, B., & Wiczorek, M. (2020) - Geomorphometric relief classification with the k-median method in the Silesian Upland, southern Poland. *Frontiers of Earth Science*, 152–170. doi: 10.1007/s11707-019-0765-9.
- Tarboton, D. G. (1997) - A new method for the determination of flow directions and upslope areas in grid digital elevation models. *Water Resources Research*, 33(2), 309–319. doi: 10.1029/96WR03137.
- Taylor, D. W. (1948) - *Fundamentals of Soil Mechanics*. *Soil Science*, 66(2), 161. doi: 10.1097/00010694-194808000-00008.
- Teixeira, M., Bateira, C., Marques, F., & Vieira, B. (2015) - Physically based shallow translational landslide susceptibility analysis in Tibo catchment, NW of Portugal. *Landslides*, 12(3), 455–468. doi: 10.1007/s10346-014-0494-9.
- Terzaghi, K., & Peck, R. B. (1967) *Soil Mechanics in Engineering Practice*. John Wiley & Sons.
- Terzaghi, K., Peck, R. B., & Mesri, G. (1996) *Soil mechanics in engineering practice*. John Wiley & Sons.
- Tesfa, T. K., Tarboton, D. G., Chandler, D. G., & McNamara, J. P. (2009) - Modeling soil depth from topographic and land cover attributes. *Water Resources Research*. doi: 10.1029/2008WR007474.
- Torabi, S., Ataei, M., & Javanshir, M. (2010) - Application of Schmidt rebound number for estimating rock strength under specific geological conditions. *Journal of Mining and Environment*, 0(0), 1–8. doi: 10.22044/jme.2011.9.
- Tou, J. T., & Gonzalez, R. C. (1974) - *Pattern recognition principles*.
- Trefolini, E. (2015) - *Engineering geologic characterization of slope deposits for the assessment of shallow landslides susceptibility*. PhD dissertation.
- Trefolini, E., Rindinella, A., & Disperati, L. (2015) - Cluster analysis applied to engineering geological mapping, 34, 70–73.
- Trigila, A., Iadanza, C., & Spizzichino, D. (2010) - Quality assessment of the Italian Landslide Inventory using GIS processing. *Landslides*, 7(4), 455–470. doi: 10.1007/s10346-010-0213-0.

- Tsai, C. C., Chen, Z. S., Duh, C. T., & Horng, F. W. (2001) - Prediction of soil depth using a soil-landscape regression model: a case study on forest soils in southern Taiwan. Proceedings of the National Science Council, Republic of China. Part B, Life sciences.
- Tüdeş, Ş., & Ceryan, N. (2011) - A comparative study on the estimation of shear strength of rock masses using rock SSPC system and Hoek-Brown criterion. Gazi University Journal of Science, 24(4), 855–865.
- USBR (1998) - Engineering Geology Field Manual. US Department of the Interior Bureau of Reclamation 2 vols Washington, DC.
- USDA (1987) - Soil mechanics level I. Module 3 - USDA textural soil classification study Guide. National Employee Development Staff, Soil Conservation Service, United~....
- Varnes, D. J. (1978) - Landslide Types and Processes. Highway Research Board Special Report.
- Varnes J, D. (1958) - Landslide Types and Processes. Highway Research Board Special Report.
- Vásárhelyi, B., & Kovács, D. (2017) - Empirical methods of calculating the mechanical parameters of the rock mass. Periodica Polytechnica Civil Engineering, 61(1), 39–50. doi: 10.3311/PPci.10095.
- Venturini, T., Trefolini, E., Patelli, E., Broggi, M., Tuliani, G., & Disperati, L. (2016) - Mapping slope deposits depth by means of cluster analysis: A comparative assessment. Rend. Soc. Geol. It., 39, 47–50. doi: 10.3301/ROL.2016.44.
- Viloria, J. A., Viloria-Botello, A., Pineda, M. C., & Valera, A. (2016) - Digital modelling of landscape and soil in a mountainous region: A neuro-fuzzy approach. Geomorphology. Elsevier B.V., 253, 199–207. doi: 10.1016/j.geomorph.2015.10.007.
- Vos, C., Don, A., Prietz, R., Heidkamp, A., & Freibauer, A. (2016) - Field-based soil-texture estimates could replace laboratory analysis. Geoderma. Elsevier B.V., 267, 215–219. doi: 10.1016/j.geoderma.2015.12.022.
- Wang, M., & Wan, W. (2019a) - A new empirical formula for evaluating uniaxial compressive strength using the Schmidt hammer test. International Journal of Rock Mechanics and Mining Sciences. Elsevier Ltd, 123(September), 104094. doi: 10.1016/j.ijrmms.2019.104094.
- Wang, M., & Wan, W. (2019b) - A new empirical formula for evaluating uniaxial compressive strength using the Schmidt hammer test. International Journal of Rock Mechanics and Mining Sciences, 123(July 2018). doi: 10.1016/j.ijrmms.2019.104094.
- Wang, S., Zhang, K., van Beek, L. P. H., Tian, X., & Bogaard, T. A. (2020) - Physically-based landslide prediction over a large region: Scaling low-resolution hydrological model results for high-resolution slope stability assessment. Environmental Modelling and Software. Elsevier Ltd, 124(September 2019), 104607. doi: 10.1016/j.envsoft.2019.104607.
- Watson, A., Phillips, C., & Marden, M. (2000) - Root strength, growth, and rates of decay: root reinforcement changes of two tree species and their contribution to slope stability. The Supporting

- Roots of Trees and Woody Plants: Form, Function and Physiology, 41–49. doi: 10.1007/978-94-017-3469-1_4.
- Wei, Y., Fu, W., & Ye, F. (2019) - Estimation of the equivalent Mohr–Coulomb parameters using the Hoek–Brown criterion and its application in slope analysis. *European Journal of Environmental and Civil Engineering*. Taylor & Francis, 0(0), 1–19. doi: 10.1080/19648189.2018.1538904.
- Weidner, L., Oommen, T., Escobar-Wolf, R., Sajinkumar, K. S., & Samuel, R. A. (2018) - Regional-scale back-analysis using TRIGRS: an approach to advance landslide hazard modeling and prediction in sparse data regions. *Landslides*. *Landslides*, 15(12), 2343–2356. doi: 10.1007/s10346-018-1044-7.
- van Westen, C. J., Castellanos, E., & Kuriakose, S. L. (2008) - Spatial data for landslide susceptibility, hazard, and vulnerability assessment: An overview. *Engineering Geology*, 112–131. doi: 10.1016/j.enggeo.2008.03.010.
- Van Westen, C. J., Rengers, N., & Soeters, R. (2003) - Use of Geomorphological expert knowledge in indirect landslide hazard assessment. *Natural Hazards*, 30, 399–419.
- Wieczorek, M., & Migoń, P. (2014) - Automatic relief classification versus expert and field based landform classification for the medium-altitude mountain range, the Sudetes, SW Poland. *Geomorphology*, 206, 133–146. doi: 10.1016/j.geomorph.2013.10.005.
- Wood, J. (1996) - Scale-based characterisation of digital elevation models. *Innovations in GIS*. Taylor and Francis London, 3, 163–175.
- Wu, W., & Sidle, R. C. (1995) - A Distributed Slope Stability Model for Steep Forested Basins. *Water Resources Research*, 31(8), 2097–2110. doi: 10.1029/95WR01136.
- Yaşar, E., & Erdoğlan, Y. (2004) - Estimation of rock physicochemical properties using hardness methods. *Engineering Geology*, 71(3–4), 281–288. doi: 10.1016/S0013-7952(03)00141-8.
- Yilmaz, I. (2009a) - A new testing method for indirect determination of the unconfined compressive strength of rocks. *International Journal of Rock Mechanics and Mining Sciences*, 46(8), 1349–1357. doi: 10.1016/j.ijrmms.2009.04.009.
- Yilmaz, I. (2009b) - Landslide susceptibility mapping using frequency ratio, logistic regression, artificial neural networks and their comparison: A case study from Kat landslides (Tokat-Turkey). *Computers and Geosciences*, 35(6), 1125–1138. doi: 10.1016/j.cageo.2008.08.007.
- Yin, K. L., & Yan, T. Z. (1988) - Statistical prediction models for instability of metamorphosed rocks. in *International symposium on landslides*. 5, 1269–1272.
- Zêzere, J. L., Pereira, S., Melo, R., Oliveira, S. C., & Garcia, R. A. C. (2017) - Mapping landslide susceptibility using data-driven methods. *Science of the Total Environment*. Elsevier B.V., 589, 250–267. doi: 10.1016/j.scitotenv.2017.02.188.
- Zhang, L., Scholz, M., Mustafa, A., & Harrington, R. (2009) - Application of the self-organizing map as a prediction tool for an integrated constructed wetland agroecosystem treating agricultural runoff.

Bioresource Technology. Elsevier Ltd, 100(2), 559–565. doi: 10.1016/j.biortech.2008.06.042.

Zhang, S., Huang, Y., Shen, C., Ye, H., & Du, Y. (2012) - Spatial prediction of soil organic matter using terrain indices and categorical variables as auxiliary information. *Geoderma*. Elsevier B.V., 171–172, 35–43. doi: 10.1016/j.geoderma.2011.07.012.

Zhong, T., Cang, X., Li, R., & Tang, G. (2009) - Landform classification based on hillslope units from DEMs. in Asian Conference on Remote Sensing (ACRS) proceedings.

Zizioli, D., Meisina, C., Valentino, R., & Montrasio, L. (2013) - Comparison between different approaches to modeling shallow landslide susceptibility: A case history in Oltrepo Pavese, Northern Italy. *Natural Hazards and Earth System Sciences*, 13(3), 559–573. doi: 10.5194/nhess-13-559-2013.